Thesis

Towards an Asymmetric Stall Model for the Fokker 100

E.H.P. De Meester

Thesis

Towards an Asymmetric Stall Model for the Fokker 100

by

E.H.P. De Meester

Student number: 4453190
Thesis supervisor: dr. ir. C.C. de Visser

TU Delft

List of Abbreviations

AoA	angle of attack
AoB	angle of bank
AoS	angle of sideslip
CFD	Computational Fluid Dynamics
CFIT	Controlled Flight into Terrain
CG	center of gravity
DoF	degree of freedom
EASA	European Union Aviation Safety Agency
EOM	equations of motion
FAA	Federal Aviation Authority
FPR	flight path reconstruction
FSTD	Flight Simulator Training Device
ICATEE	International Committee for Aviation Training in Extended Envelopes
IEKF	iterated extended kalman filter
IV	independent variables
LOC-I	Loss of Control in Flight
LOCART	Loss of Control Avoidance and Recovery Training
MAC	mean aerodynamic chord
MSE	mean squared error
ODE	ordinary differential equation
OEW	Operating Empty Weight
OLS	ordinary least squares
PSE	predicted squared error
SUPRA	Simulation of Upset Recovery in Aviation
TAWS	Terrain Awareness and Warning System
UKF	unscented kalman filter
UPRT	Upset Prevention and Recovery Training

List of Symbols

Symbol	Description	Unit
C_D	drag force coefficient	-
C_{L_0}	zero angle of attack lift coefficient	-
C_{L_α}	derivative lift coefficient with respect to the angle of attack	-
$C_{L_{\delta_e}}$	lift coefficient derivative with respect to elevator deflection	-
C_L	lift coefficient	-
C_Y	lateral force coefficient	-
C_{α_0}	coefficient to correct zero AoA measurement not aligned with aircraft geometry	rad
$C_{\alpha_{up}}$	Upwash coefficient of AoA measuring vane	-
C_l	roll moment coefficient	-
C_m	pitch moment coefficient	-
C_{n_β}	static directional stability derivative	-
C_n	yaw moment coefficient	-
V_{TAS}	true airspeed	m/s
X	internal flow separation point	-
$\dot{\alpha}$	rate of change of angle of attack	rad/s
$\dot{\beta}$	rate of change of angle of sideslip	rad/s
α	angle of attack	rad
α^*	stall angle of attack	rad
β	angle of sideslip	rad
δ_e	elevator deflection	degrees
μ_f	flank angle	rad
τ_1	time lag separation/reattachment time constant	s
τ_2	hysteresis time constant	s
a_1	stall abruptness	-
q	pitch rate	rad/s

List of Figures

List of Tables

Contents

I

Paper

Towards an Asymmetric Stall Model for the Fokker 100

E.H.P. De Meester*
Delft University of Technology, Delft, 2629HS, the Netherlands

Nomenclature

a_1	Stall abruptness parameter [-]	p_j	Candidate model term
a_i	Model parameter i	q	Pitch rate [rad/s]
C_L	Lift coefficient [-]	r	Yaw rate [rad/s]
C_l	Rolling moment coefficient [-]	X	Flow separation point [-]
C_n	Yawing moment coefficient [-]	$\mathbf{x}_0$	State variables
C_T	Thrust Coefficient [-]	α	Angle of attack [rad]
C_Y	Yaw force coefficient [-]	α^*	Stall angle of attack [rad]
C_{α_0}	Vane geometric coefficient [rad]	β	Angle of sideslip [rad]
$C_{\alpha_{up}}$	Vane upwash coefficient [-]	δ_a	Aileron deflection [rad]
J	Cost function	δ_e	Elevator deflection [rad]
M	Mach number [-]	δ_r	Rudder deflection [rad]
N	Number of data points	ϵ	Model error
n	Number of model terms	τ_1	Time delay due to flow inertia [s]
p	Roll rate [rad/s]	τ_2	Hysteresis effect [s]
		σ^2	Mean squared error (MSE)

I. Introduction

Loss of Control in Flight (LOC-I) accidents are the largest contributors to aviation fatalities [1, 2]. To enhance safety and minimise the amount of accidents, new regulations about pilot training for upset awareness, prevention, recognition and recovery have been established by the FAA and EASA [3, 4]. These regulations require training of pilots in flight simulators to handle upsets and avoid fatal accidents. This is often referred to as Upset Prevention and Recovery Training (UPRT)[3]. The aerodynamic models of current flight simulators are not sufficient to provide positive transfer of training as their fidelity is lacking [5]. The need to extend the flight envelopes in simulator training towards upsets, and stalls in specific, has therefore been receiving more attention lately. Improved extended aerodynamic flight envelopes will aid in giving pilots a realistic feel of the upset, leading to improved skill training that can help pilots to recover from an actual upset in real life [6].

Unlike the nominal angle of attack range for nominal flight conditions, high angles of attack close to and beyond stall, exhibit high non-linear behaviour [7]. Regular modelling methods are no longer sufficient to create high fidelity models to feed the simulators. Creating stall models for simulators therefore requires new approaches with respect to data gathering, processing and model identification. Kirchhoff's theory of flow separation has resulted into progress in flight test data based modelling techniques [8–12]. This theory captures the non-linearities from stall in a single flow separation variable that can be included in aerodynamic models [8]. The internal flow separation variable X can be estimated by solving an ordinary differential equation [13]. The research and development towards improved stall training for pilots is however far from completed. One of the current research gaps is the lack of high fidelity lateral-directional stall models for simulator training. As stall can be accompanied by lateral-directional divergence, requiring noticeable pilot input for safe recovery, there is a need to include this behaviour in the simulator stall models [14]. TU Delft has access to its own research aircraft, the Cessna Citation II, as well as flight test data of the Fokker 100.

*MSc Student, supervised by dr. ir. C.C. de Visser and dr.ir. D.M. Pool, Faculty of Aerospace Engineering, Control and Simulation Division, Email: emmademeester@hotmail.com.

The approach of using flight test data methodologies is therefore the most logic and feasible one.

This research intends to develop an asymmetric stall model from the certification flight test data of the Fokker 100 aircraft. The use of Kirchhoff's theory of flow separation will be extended to include multiple separation points to accommodate asymmetries in the flight data by modelling different flow separation points, and thus lift force, on each wing.

II. Flight Test Data

The Fokker 100 (F-28 MK-0100) is a regional twin jet aircraft. From 1986 till 1989, Fokker performed a series of flight tests including numerous stalls in different configurations. These served to evaluate the stall characteristics and stall speed. The data of these test flights will be used for the research into asymmetric stall behaviour. The selection of useful stalls was based on the reporting of asymmetries such as wing drops in the test cards accompanying the data as well as the presence of sufficient data to run the mass model and Kalman filter. The aircraft used for most stalls is the prototype aircraft.

Dimensions	
Wing Area	93.5 [m^2]
Wingspan	27.1 [m]
MAC	3.83 [m]

Table 1 Dimensions of the Fokker 100 prototype aircraft.

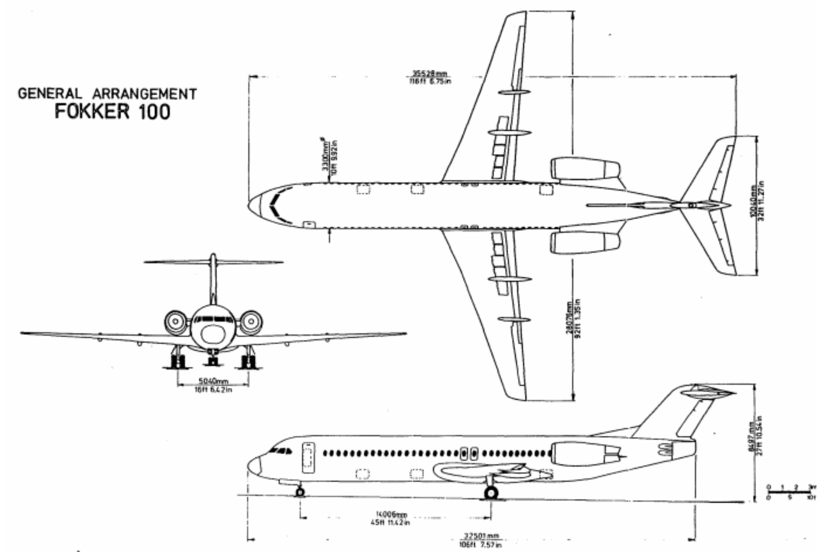

Fig. 1 The Fokker 100 aircraft (Drawing from Fokker).

The stall tests have been performed within the framework of certification of the aircraft as well as to generate supplementary aerodynamic data for simulation of aircraft behaviour. The supplementary data was used to improve and complement data gathered in wind tunnel experiments. Due to the certification nature of the flight test data, the data lacks deliberate excitation of the control surfaces in dedicated control manoeuvre sequences such as the doublet, 3-2-1-1, etc. Sufficient excitation is necessary for proper stall model identification [15, 16]. This data is however not available for the Fokker 100 aircraft. It therefore remains uncertain if a high fidelity stall model can be derived from the data. The only control surface deflections found in the flight test data are those required to perform the stall manoeuvre as well as to recover the aircraft if asymmetric behaviour occurs around the time of stall.

To identify an asymmetric stall model, some source of lateral-directional excitation should be present in the data. For this reason, only stalls with reported wing drops or noticeable angles of bank as a result of the stall, were selected for this research. This asymmetric behaviour and the use of control surface deflection by the pilot to recover the aircraft, will provide some excitation in the data to aid the identification process. About 200 stalls were selected based on this criterion. During the pre-processing phase, all stalls that had insufficient data to run the mass model or Kalman filter got dropped. 79 stalls remained available. These stalls cover a range of configurations. An overview is given by Table 2. In all stalls selected, aileron and rudder deflections are found related to the recovery of the aircraft after asymmetric behaviour occurred during the stall manoeuvre. The data sets are divided into training and validation sets (75/25).

Configuration	Stalls
Clean Configuration	29
6° Flaps	2
18° Flaps	23
25° Flaps and Gear Down	2
Landing Configuration	22

Table 2 Number of selected stalls for each configuration

III. Flight Path Reconstruction

Raw measurement data is subjected to sensor noise and bias. This will affect the fidelity of the stall identification model as the error progresses in the entire identification routine. Furthermore, some crucial aircraft states required for identification cannot be measured directly or lack accuracy. These issues can be limited by the application of the two-step method. This method will divide the identification process into a state reconstruction, followed by a model parameter estimation routine [16].

A. Iterated Extended Kalman Filter

A trade-off based on performance and computational expense resulted into the selection of the Iterated Extended Kalman Filter (IEKF) over the Unscented Kalman Filter to perform the state reconstruction of the two-step method. The IEKF reconstructs the aircraft states based on a weighted average between the predicted and measured state, with iterations to improve the filter's convergence. A necessary condition for convergence is full observability of the aircraft kinematics which allows the determination of aircraft states based on the output measurements on a certain time interval. The rank of the observability matrix needs to equal the number of states to be reconstructed. Lie derivatives are used to construct the observability matrix for the nonlinear aircraft kinematics of the Fokker 100 [17–19].

B. Airflow Angle Corrections

Aircraft behaviour is modelled for its centre of gravity (CG). Not all signals are however measured in the CG and their output is subjected to three-dimensional aircraft motions relative to the CG causing additional accelerations if we assume a rigid aircraft. Note that more influences occur in reality due to bending, vibrations, wind, dynamic vane response etc. These additional influences increase the complexity of the filter and can cause convergence issues as too many parameters are present to estimate [20]. For this research, rigid aircraft kinematics will be assumed.

Flow angle vanes measure the local flow angles that are subjected to both the movement of the aircraft's CG as well as the 3D movement. They do not necessarily correspond with the flow angles at the CG. The velocity components at the vane location are expressed in Equation 1. The velocity components at the CG, u,v and w receive an additional component consisting of angular rates p, q and r multiplied with the position of the vane (x_v, y_v and z_v) with respect to the CG [21]. The results are the velocity components u_v, v_v and w_v at the location of the vane.

$$\begin{bmatrix} u_v \\ v_v \\ w_v \end{bmatrix} = \begin{bmatrix} u \\ v \\ w \end{bmatrix} + \begin{bmatrix} 0 & -r & q \\ r & 0 & -p \\ -q & p & 0 \end{bmatrix} \begin{bmatrix} x_v \\ y_v \\ z_v \end{bmatrix} \tag{1}$$

Commonly, the flow angle corrections derived from Equation 1, are simplified under the assumption of small angle approximation and neglection of (small) angular rates. Grauer derived the full nonlinear corrections in 2017, see

Equation 2 and Equation 3[21]. Grauer concluded that these corrections improve identification results where the raw data has high amounts of noise and high values for flow angles and angular rates. For this research, stall behaviour is modelled and thus higher AoA's are obtained in correspondence with asymmetric roll behaviour. These conditions favour the use of Grauer's exact corrections as the validity of small angle approximations and angular rates becomes less accurate.

The derived full nonlinear flow angle corrections express the correct kinematics of the local flow which matches the raw measurements of the flow angle vanes. The kinematics are however expressed in body velocity components of the CG. These kinematics are used in the IEKF in favour of the widely used simplified version. Note that β vanes measure the flank angle μ rather than the side slip angle β. The AoS is obtained using Equation 4.

$$\alpha_v = \arctan\left(\frac{w_v}{u_v}\right) = \arctan\left(\frac{w - qx_v + py_v}{u - ry_v + qz_v}\right) \tag{2}$$

$$\mu_v = \arctan\left(\frac{v_v}{u_v}\right) = \arctan\left(\frac{v + rx_v - pz_v}{u - ry_v + qz_v}\right) \tag{3}$$

$$\beta = \arctan\left(\tan\mu\cos\alpha\right) \tag{4}$$

The flow angle corrections are also used to determine the local flow velocities and angles at a defined location with respect to the CG. This opens the door to panel methods in which more than one flow separation location point is used for the aircraft. In this research, a separate flow separation point for the left and right wing will be determined.

C. Flow Vane Coefficients

The Fokker 100 prototype aircraft is equipped with three different AoA vanes. Two of them are mounted on the fuselage. Their measurements are corrupted due to the upwash of the airflow around the aircraft. The third vane is mounted on a boom located further away from the fuselage and is therefore far less subjected to upwash of the flow. This vane is better aligned with the free stream velocity. Differences up to 5° were noted when measuring the AoA with the fuselage-mounted vanes compared to the boom-mounted vane. Boom measurement data is only available for a third of the stall manoeuvres selected for this research. Due to the large discrepancy in AoA, all the other stall manoeuvres cannot be used.

To make the boomless stall manoeuvres useable for this research, corrections can be applied to the vane measurements. A kalman filter can estimate the corrective coefficients together with the aircraft states if the aircraft kinematics system remains observable. The basic IEKF estimates 12 aircraft states whilst having an observability matrix of rank 12. Two vane corrective coefficients are required, an upwash coefficient $C_{\alpha_{up}}$ and a geometric coefficient C_{α_0}, which captures misalignment of the vane's zero AoA measurement. The observability matrix of the system must therefore increase to rank 14. To do so, additional kinematic relationships are required.

The three different AoA measurements and their corresponding kinematics can achieve this increase in observability rank. It is required to have three independent kinematic relationships for the vanes. Without using Grauer's full nonlinear vane corrections, this could not be achieved as both fuselage-mounted vanes would have the exact same kinematic relationship. By including their y-location, the rank of the observability matrix reached 14 and the necessary condition for convergence of the Kalman filter estimating the 12 states and both corrective vane coefficients, is met.

24 of the 79 stalls used in this research had measurements of all three vanes. The 14-state Kalman filter is applied to all 24 stalls. For 8 stalls, the estimation of the flow vane coefficients did not converge. The other 16 stalls converged to very similar values, see Figure 2. For each stall, a value was determined for both coefficients by taking the mean of the converged part. The mean of all these 16 values was used as final value for $C_{\alpha_{up}}$ and C_{α_0} and can be found in Table 3.

To validate the correctness and consistency of the found vane corrective coefficients, a comparison between the α-measurements from the boom vane and the corrected α-measurements from the fuselage-mounted vanes was made. The validation was performed on all 24 stalls of which measurement data of all three vanes was available, including the stalls to which the IEKF did not converge for the estimation of the vane corrective coefficients. The mean and median MSE are given in Table 3. A boxplot of the spread of the MSE of those 24 stalls is given by Figure 3. An order of magnitude of the MSE of 10^{-8} is reached, with 3 outliers that have still an order of magnitude of 10^{-6}. This order of magnitude is very small in relation to the order of magnitude of α, less than $1e^{-7}\%$. It can be concluded that the vane α-measurements can be corrected with high accuracy towards the measurements from the boom-mounted vane.

Table 3 Overview of the estimation results of the IEKF for the vane corrective coefficients $C_{\alpha_{up}}$ and C_{α_0}.

Coefficient	Value	mean MSE	median MSE
$C_{\alpha_{up}}$ [-]	0.4730	4.2379e-07	3.4838e-08
C_{α_0} [rad]	-0.1072		

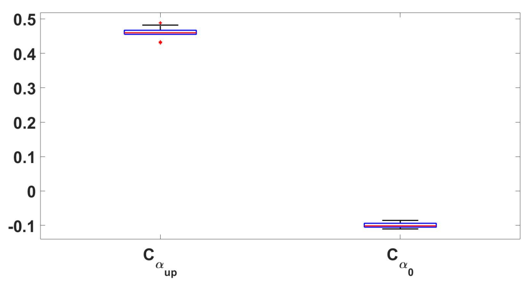

Fig. 2 Spread of the 16 estimates for the vane corrective coefficients.

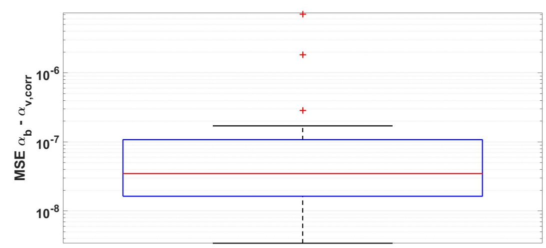

Fig. 3 Boxplot of the MSE between boom and vane corrected AoA measurement for all 24 stalls with 3 AoA vane measurements available.

D. Gramian Matrix for Determination Information Content

Observability of the aircraft kinematics is a necessary condition to guarantee convergence of the Kalman filter. It gives us more information if the Kalman filter can actually reconstruct the states based on the information captured in the kinematics describing the system. It is independent from the quality of measurements acquired during flight testing.

The Gramian observability matrix can be used to determine the minimum information content that should be present in the measured trajectory in order to reconstruct all system parameters. This is described by the invertibility of the nonlinear observability Gramian. The information content can be quantified by expressing how far the actual Gramian is away from its singular form. Taking the Euclidean distance from the Gramian towards its singular matrix form can be used to describe the information content present in the state trajectory. The minimum singular value or Eigenvalue is used as metric. The higher this value, thus the further it is from the zero value, the more information content is encoded in the flight measurement data of the trajectory. Higher accuracy for the parameter estimation can be obtained when the information content is high.

The nonlinear observability Gramian is defined by Equation 5. $\frac{\partial y}{\partial \mathbf{x}_0}$ is the Jacobian matrix of the state trajectory y with respect to the state variables $\mathbf{x}_0$. The derivation of this metric can be found in [22].

$$\int_0^T \left(\frac{\partial y}{\partial \mathbf{x}_0}\right)^T \frac{\partial y}{\partial \mathbf{x}_0} dt \tag{5}$$

IV. Asymmetric Stall Model Identification

A. Kirchhoff's Theory of Flow Separation

In 1992, Goman and Khrabrov introduced a new approach to stall modelling based on Kirchhoff's zone of constant pressure and linear cavitation theory assumptions. The state-space approach contains an internal variable, the flow separation location X, that represents the point of flow separation on the wing. X has a value between 0 (fully detached flow) and 1 (fully attached flow) [8]. This method has been further developed for aerodynamic model identification based on flight test data and resulted into an expression to estimate the lift coefficient C_L based on the chordwise location of flow separation, Equation 6. This location is determined using the ordinary differential equation (ODE) given by Equation 7. This has been referred to as Kirchhoff's theory of flow separation [13]. One can also estimate the flow separation location based on the C_L model. However, the C_L model parameter identification depends on the identified values for the parameters of Kirchhoff's ODE, whilst these parameters depend on their turn on the C_L model. An iterative process is required to identify both.

$$C_L = C_{L_\alpha} \left(\frac{1 + \sqrt{X}}{2} \right)^2 \alpha \tag{6}$$

$$\tau_1 \frac{dX}{dt} + X = \frac{1}{2} \left(1 - \tanh \left[a_1 (\alpha - \tau_2 \dot{\alpha} - \alpha^*) \right] \right) \tag{7}$$

Kirchhoff's ODE consists out of 4 parameters that need to be identified. τ_1 represents the time delay due to flow inertia, τ_2 models the effects of hysteresis, a_1 determines the abruptness of the stall and α^* sets the stall AoA. Kirchhoff's theory has been used in fight test data identification [10][11][23] as well as CFD semi-empirical methods [24][25] and its capability to model the nonlinear dynamics of stall has been validated in many scientific papers.

B. Multivariate Orthogonal Function modelling

Selecting a model structure can be done using thoughtful engineering judging. The aerodynamic coefficient models have to be built up by model terms consisting of the variables that influence the magnitude of the coefficient under consideration. A carefull selection is important, as adding too many terms leads to complex models prone to overfit. If two terms are too closely correlated, identification issues can arise in which it is better to drop one of them.

Morelli et al. introduced a mathematical approach to determine model structures for global aerodynamic modelling. The multivariate orthogonal function modelling technique starts from a pool of ordinary candidate regressor terms for the aerodynamic coefficients. All the candidate terms are made mutually orthogonal and therefore become decoupled. The multivariate orthogonal functions can now be individually assessed to quantify their contribution to the model fit. Only the best terms are added to the final model structure.

The multivariate orthogonal function takes the form of a linear combination of all multivariate orthogonal model terms $\tilde{p}_j$ and their parameters a_j, Equation 8. This approaches the computed values for the aerodynamic coefficients based on the measured signals $\tilde{z}$. The model terms are a function of the independent variables (IV).

$$\tilde{z} = a_1 \tilde{p}_1 + a_2 \tilde{p}_2 + ... a_n \tilde{p}_n + \tilde{\epsilon} = \tilde{P} \tilde{a} + \tilde{\epsilon} \tag{8}$$

A good model approximates the computed coefficients closely, keeping the model error $\tilde{\epsilon}$ as small as possible. $\tilde{\epsilon}$ will be minimised using a cost function that determines the values of model parameters a_i to achieve this minimisation. The cost function J to be minimised is a least squares function, Equation 9, where $\tilde{P}$ is the vector constituting of the different model terms $\tilde{p}_j$ and $\tilde{a}$ the vector with corresponding model parameters. This function reaches a minimum where its first derivative with respect to the model parameters a_i reaches 0, $\hat{\tilde{a}}$. The resulting output $\tilde{y}$ of the identified model is given by Equation 10.

$$J = \frac{1}{2} \tilde{\epsilon}^T \tilde{\epsilon} = \frac{1}{2} \left(\tilde{z} - \tilde{P} \tilde{a} \right)^T \left(\tilde{z} - \tilde{P} \tilde{a} \right) \tag{9}$$

$$\tilde{y} = \tilde{P}\hat{\tilde{a}} \tag{10}$$

Under the assumption of orthogonality (Equation 11), the cost function $\tilde{J}$ can be written as Equation 12. The parameter value to be estimated only depends on its corresponding model term $\tilde{p}_j$ and the measurement vector $\tilde{z}$, see Equation 13.

$$\tilde{p}_i \tilde{p}_j = 0 \quad for \quad i \neq j, \quad i, j = 1, 2, .., n \tag{11}$$

$$\tilde{J} = \frac{1}{2}\left[\tilde{z}^T \tilde{z} - \sum_{j=1}^{n} \frac{\left(\tilde{p}_j \tilde{z}\right)^2}{\tilde{p}_j^T \tilde{p}_j}\right] \tag{12}$$

$$\hat{a}_j = \frac{\tilde{p}_j \tilde{z}}{\tilde{p}_j^T \tilde{p}_j} \tag{13}$$

The contribution of each term is quantified in the PSE metric, see Equation 14. This metric quantifies the improvement in cost function $\tilde{J}$ minimisation whilst penalising the increased model complexity as a result of the additional term. The PSE metric uses the decoupled cost function $\tilde{J}$.

$$PSE = \frac{\left(\tilde{z} - \tilde{P}\hat{\tilde{a}}\right)^T \left(\tilde{z} - \tilde{P}\hat{\tilde{a}}\right)}{N} + \sigma_{max}^2 \frac{n}{N} = \frac{2\hat{J}}{N} + \sigma_{max}^2 \frac{n}{N} \tag{14}$$

$$\sigma_{max}^2 = \frac{1}{N-1} \sum_{i=1}^{N} \left[z_i - \bar{z}\right]^2 \tag{15}$$

$$\bar{z} = \frac{1}{N} \sum_{i=1}^{N} z_i \tag{16}$$

σ_{max}^2 is the upper-bound mean squared error, N the total number of data points for the data set under consideration, n being the number of model terms. The PSE metric is evaluated each time a model term is added to the cost function $\tilde{J}$. The order of addition must range from the most effective modelling term to the least effective one. Their effectiveness is quantified by Equation 17. Adding terms to the cost function will improve the model fit and therefore decrease the value of the cost function $\tilde{J}$. The model term is in fact subtracted from the measurement term $\tilde{z}^T \tilde{z}$. Adding an additional term will however increase the value of the model complexity penalty of the PSE. At a certain moment, the decrease in cost function value will not weigh against the increase in the model complexity penalty. A global minimum of the PSE has been reached. The corresponding model structure will become the final model structure as a result of the multivariate orthogonal function modelling approach. This global minimum will only be achieved if model terms are added with decreasing effectiveness [15]. The selection of terms will be counted for all manoeuvres in the data set and the most chosen terms will be added to the general model structure.

$$\left(\frac{2}{N}\right) \frac{\left(\tilde{p}_j \tilde{z}\right)^2}{\tilde{p}_j{}^T \tilde{p}_j} \tag{17}$$

The ordinary model terms used to build up the pool of candidate regressor terms are the following: a bias term, α, $\dot{\alpha}$, β, $\dot{\beta}$, p, q, r, δ_e, δ_a, δ_r, M, C_T and a series of terms related to Kirchhoff's point of flow separation X. The terms included depend on the model structure under consideration. The bias term is set as a fixed parameter and will always be included in each model structure.

C. Nonlinear Parameter Estimation of the Parameters of Kirchhoff's ODE

Kirchhoff's ODE, Equation 7, has 4 parameters that need to be identified for the Fokker 100 aircraft. Those parameters are τ_1, τ_2, a_1 and α^* . Nonlinear estimation techniques are required to identify their value. With the parameter values determined, the flow separation point X can be calculated by inputting the current angle of attack α and its derivative, $\dot{\alpha}$, and solving the ODE.

To identify the parameters of Kirchhoff's ODE (Equation 7), a nonlinear optimisation to a measured quantity needs to be performed. As the relation between X and C_L is widely documented in literature, Equation 6, this optimisation is performed to minimise the error between the measured and modelled C_L.

The modelled C_L structure will include one X-related term. The minimisation problem needs to estimate both the aerodynamic C_{L_i} parameters of the C_L model as the 4 parameters of Kirchhoff's ODE required to compute Kirchhoff's point of flow separation. To start the procedure, an initial C_L model structure with initial values for all parameters will need to be set up. From this point, multiple iterations will be required to improve the selection of the model structure, aerodynamic and Kirchhoff's ODE parameters.

Initial model structures and parameter values are iterated to improve the model fit. First, the model structure selection algorithm as proposed by Morelli et al. is applied to update the current model structure. A linear optimisation is run to estimate the aerodynamic parameters. Using linear optimisation is preferred wherever applicable due to the reduction in computational time as well as the guarantee towards convergence to the global minimum value. If the four parameters of Kirchhoff's ODE (Equation 7) are kept fixed during the estimation of the aerodynamic parameters, linear estimators such as the ordinary least squares method can be used. The last step of the iteration is to identify the Kirchhoff's ODE parameters using nonlinear optimisation techniques whilst conserving the previously identified model structure and aerodynamic parameters. Both optimisation routines can be iterated multiple times before reconsidering the model structure. Once the final C_L model and Kirchhoff's ODE parameters values are decided upon, all other model structures can be determined using the multivariate orthogonal function modelling algorithm and the parameters estimation can be performed using efficient linear solvers. An overview of the entire identification process is given in Figure 4.

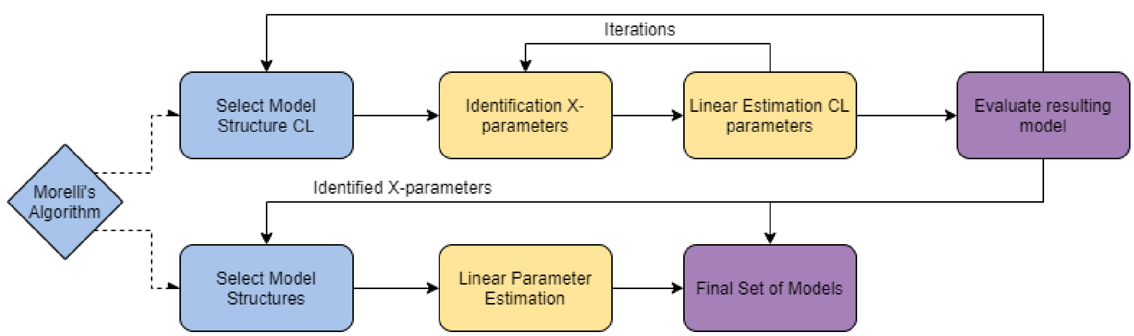

Fig. 4 Identification process of all model structures.

The nonlinear optimisation of Kirchhoff's ODE parameters is performed using the *fmincon* toolbox of Matlab [26]. The active set algorithm was selected on a trial-by-error base due to its relatively low computational time and optimisation results. The cost function used by the nonlinear optimisation procedure is a well-known mean squared error (MSE).

Nonlinear optimisation does not offer the guarantee of convergence to the global minimum of the cost function. The algorithm can converge to a local minimum instead. It is therefore advised to create a set of initial values within the physical and expected range of parameter values and run the optimisation for all these values. The lowest value will be taken as the optimal value, even though no certainty arises if this is the global optimum. Due to the computational expense and the lack of guarantee for global convergence, nonlinear parameter estimation should be avoided. Kirchhoff's ODE cannot be solved without nonlinear parameter estimation techniques.

V. Results

A. Lift Coefficient C_L model

A range of model terms related to the Kirchhoff point of flow separation X were tested as candidate regressor terms: $\left(\frac{1+\sqrt{X}}{2}\right)^2$, $(1 - X)$, X and $max(0.5, X)$. Running the multivariate orthogonal function modelling algorithm for the first time showed a strong dependence on different X-related terms. As $\left(\frac{1+\sqrt{X}}{2}\right)^2$ came out as the strongest dependent term, all other X-related terms were removed for the second run of the algorithm. The outcome of this second run is given by Figure 5. A dependence on pitch rate q, elevator deflection δ_e, aileron deflection δ_a, angle of sideslip β, angle of attack α and the Kirchhoff term $\left(\frac{1+\sqrt{X}}{2}\right)^2 \alpha$ is now observed. The latter combines the dependence on α and $\left(\frac{1+\sqrt{X}}{2}\right)^2$ and is widely used in literature. The Kirchhoff term is therefore added to the model structure.

Including the elevator deflection δ_e in the model structure caused problems in the identification of the Kirchhoff's ODE parameter α^* (Equation 7), even though this is generally considered as the easiest term to identify. An underestimation of its value was detected. The identified model flattened out to a steady C_L value when the AoA further increased towards a stall. The identified values did not vary noticeably for the different flap settings. It is a known fact that the stall angle of attack decreases with increasing flap setting. This fact was not observed if δ_e is included in the model. All values tended towards the lower bound of 0.3 rad, even though a value between 0.35 and 0.45 rad is expected.The elevator deflection was therefore not used in the model structure. The angle of side slip was removed based on engineering judgement.

The asymmetric aileron deflection term δ_a is an unexpected variable to occur in a symmetric model structure. The measured C_L curves however showed a 'wavy' behaviour that was only found in the asymmetric roll-related terms. δ_a captures this behaviour with the best model fit compared to the roll rate and roll angle and scores highest in the multivariate orthogonal function modelling algorithm. It is therefore included in the model structure by its absolute value. This is necessary to transform it into a symmetric variable. An aircraft rolling to the right or left both causes a decrease in lift due to the decrease in vertical component of the lift vector that stands perpendicular on the banked wings.

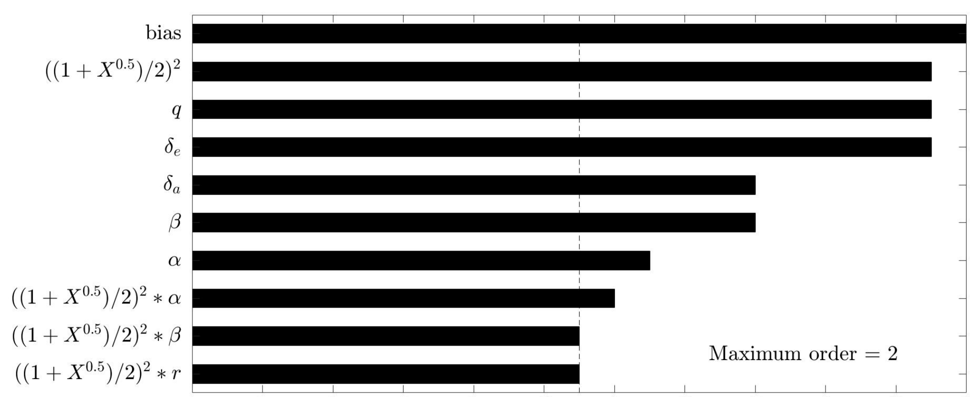

Fig. 5 Outcome of the 2nd run of the multivariate orthogonal function modelling algorithm for C_L of Fokker 100.

The model structure selected for C_L is

$$C_L = C_{L_0} + C_{L_\alpha} \left(\frac{1+\sqrt{X}}{2}\right)^2 \alpha + C_{L_{\delta_a}} |\delta_a| + C_{L_q} q. \tag{18}$$

The identification process of the parameters of Kirchhoff's ODE showed that τ_2 had no visual influence on the C_L curve, see Figure 6. Too little dynamic stall information is present in the Fokker 100 stall data set to identify this value. It was therefore left out from Kirchhoff's ODE. The other three parameters, especially a_1 and α^* have an influence on the behaviour of the model for C_L. There is no correlation between the parameters that could cause bad identification, Figure 7. Similar behaviour is obtained for the different flap settings investigated.

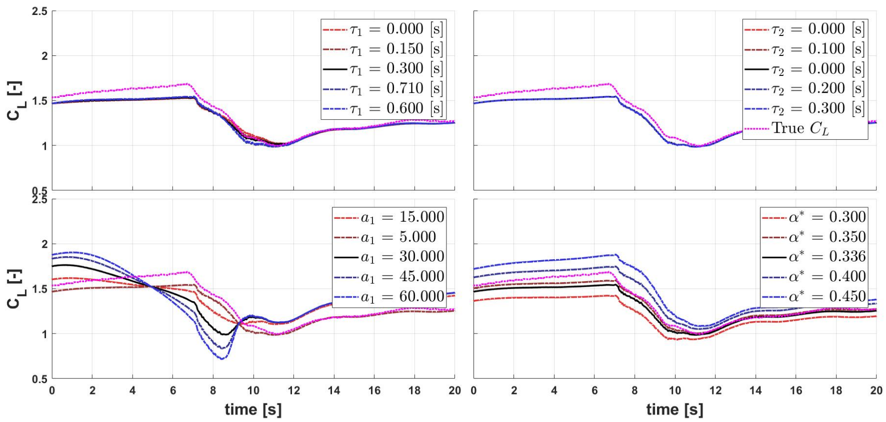

Fig. 6 Influence of varying the parameters of Kirchhoff's ODE on the C_L model, compared to the measured/true C_L, flaps = 0°, Fokker 100

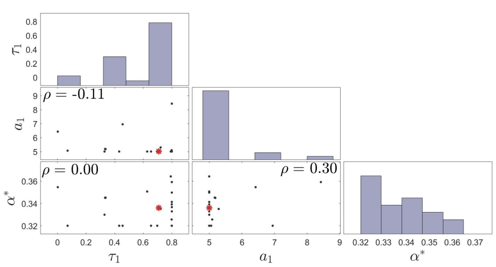

Fig. 7 Spread and correlation of the different parameters of Kirchhoff's ODE (Equation 7), flaps = 42°

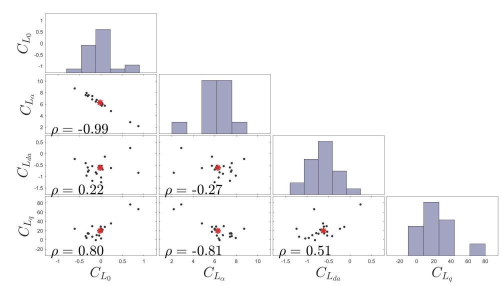

Fig. 8 Spread and correlation of the C_L parameters, flaps = 0°, Fokker 100

Fixing the identified parameters of Kirchhoff's ODE (Equation 7), allows linear optimisation of the aerodynamic C_L-model parameters. An overview of the outcome of this optimisation for all flap settings can be found in Table 5. As the lift curve shifts towards the origin with increasing flap setting, the C_{L_0} value should increase as well. This behaviour is observed in the results. Values of -0.0218, 0.1980 and 0.9870 are estimated for 0°, 18° and 42° flap setting, respectively.

The model fit is not very accurate. Different phenomena are observed when comparing the flight data with the identified C_L model. For certain stalls, an underestimation of the maximum C_L value is noticeable, Figure 9. The model flattens out even though the AoA is still rising. A too low value for α^* causes this behaviour, as the effect of higher α^*, as seen in Figure 6, is desirable in this case. Figure 7 shows that the identified α^* values for each stall manoeuvre are quite evenly spread between 0.30 and 0.37. Taking the median value inherently implies that for some stalls, the value will be too low, leading to the flattening out phenomenon observed in Figure 9. For a_1 and τ_1, Figure 7 shows a lower variation around the median value with a few outliers.

The stall with the best mean squared error (MSE) from the 18° flaps (MSE= 0.0016) set is given by Figure 10. The effect of adding the absolute value of the aileron deflection is especially visible from time = 7-11 s. The drop in C_L is

Table 4 Results of identifying the parameters of Kirchhoff's ODE.

Parameter		Results			
Name	Unit	$\hat{\theta}$	θ_{lb}	θ_{ub}	$\frac{s(\hat{\theta})}{\hat{\theta}}$
Flaps = 0°					
τ_1	[s]	**0.7098**	0.001	0.80	0.3528
a_1	[-]	**5.0**	5.000	80.00	0.1689
α^*	[rad]	**0.3359**	0.30	0.45	0.0426
Flaps = 18°					
τ_1	[s]	**0.198**	0.001	0.80	1.5270
a_1	[-]	**5.8971**	5.000	80.00	0.6389
α^*	[rad]	**0.3734**	0.300	0.45	0.1208
Flaps = 42°					
τ_1	[s]	**0.6989**	0.001	0.80	0.4248
a_1	[-]	**18.106**	5.000	80.00	0.6237
α^*	[rad]	**0.3165**	0.300	0.45	0.0806

followed by the model and is only observed clearly in the graph of δ_a. Without adding the term, the model would go linearly from peak to peak in that time frame. An overview of the MSE, relative MSE (percentage of mean C_L) and Root Mean Squared (RMS) are given in Table 5.

Figure 9 and Figure 10 should have been almost identical manoeuvres for their certification purpose. Different flap settings and configurations are however used. Figure 9 is performed in landing configuration (gear down and flaps = 42°). Figure 10 is performed with gear up and flaps = 18°. The manoeuvres are performed by human pilots, making them prone to differences in execution. Furthermore, only stalls were selected with asymmetric behaviour during the stall manoeuvre. This behaviour is widely considered as unpredictable due to its nonlinear nature and reduced lateral-directional stability. None of the stall manoeuvres considered is therefore alike and large differences can be observed[27].

In general, the model follows the trend of the flight data quite well. This is confirmed by inspecting the Variance Accounted For (VAF) of the different stalls. Each stall, both training and validation data sets, has a VAF higher than 99%, except for two stalls that have a VAF of 98.75% and 98.80%.

The model has especially difficulties to follow the flight data if the data contains more dynamical behaviour. Insufficient information content is present in the flight data to achieve high levels of accuracy. This is a consequence of the nature of the flight tests. They were performed with certification purposes and therefore lack any source of deliberate control surface excitation. The limits of this data gathering method has become visible. Simulation models built from certification data will not reach the level of fidelity compared to those where excitation of control surfaces has been applied meticulously [10]. It remains yet to be investigated what level of fidelity is required for pilot training.

A metric to express the information content in flight test data is the Gramian matrix [22]. The minimum Eigenvalues obtained for the different stall manoeuvres range in the order of magnitude of $10^{-9} - 10^{-11}$. Values as high as 113 are reached for the wind box calibration manoeuvre by Moszczynski et al.[22]. The wind box calibration manoeuvre is dedicated towards acquiring data which allows accurate parameter identification and is therefore known to have a very high information content. Simple straight stall manoeuvres (Moszczynski et al.) reached Gramian minimum Eigenvalues of 0.04, which are still much higher than those obtained from the Fokker 100 data.

B. Rolling moment C_l model

To select the asymmetric rolling moment model c_l, a set of X-related parameters has been selected as candidate regressor terms for the multivariate orthogonal function modelling algorithm. Asymmetric terms were chosen, based on a different

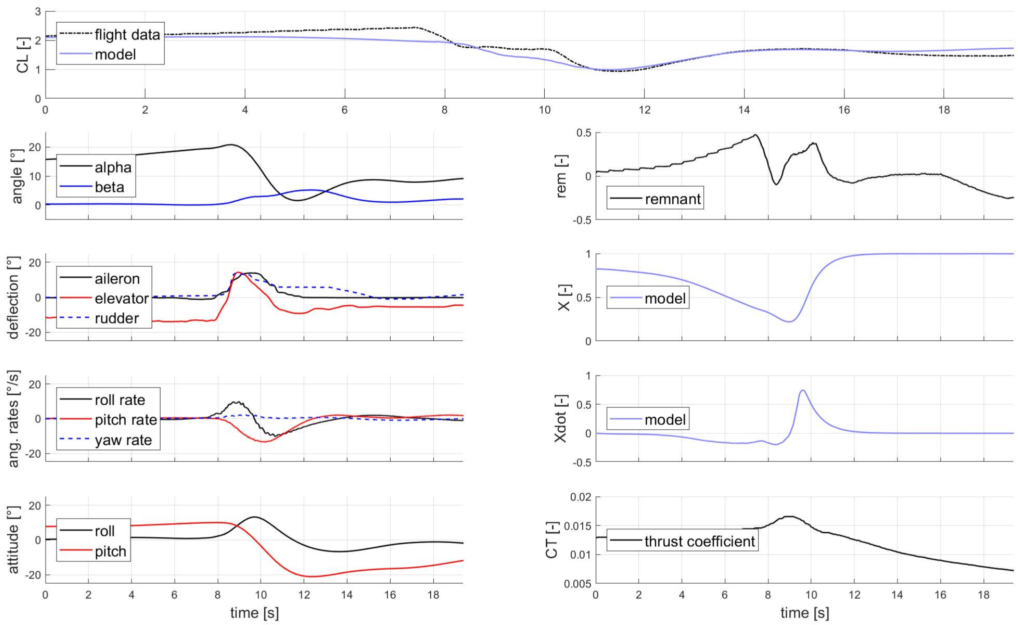

Fig. 9 Stall with the worst MSE of the C_L model for flaps = 42°, MSE = 0.0344.

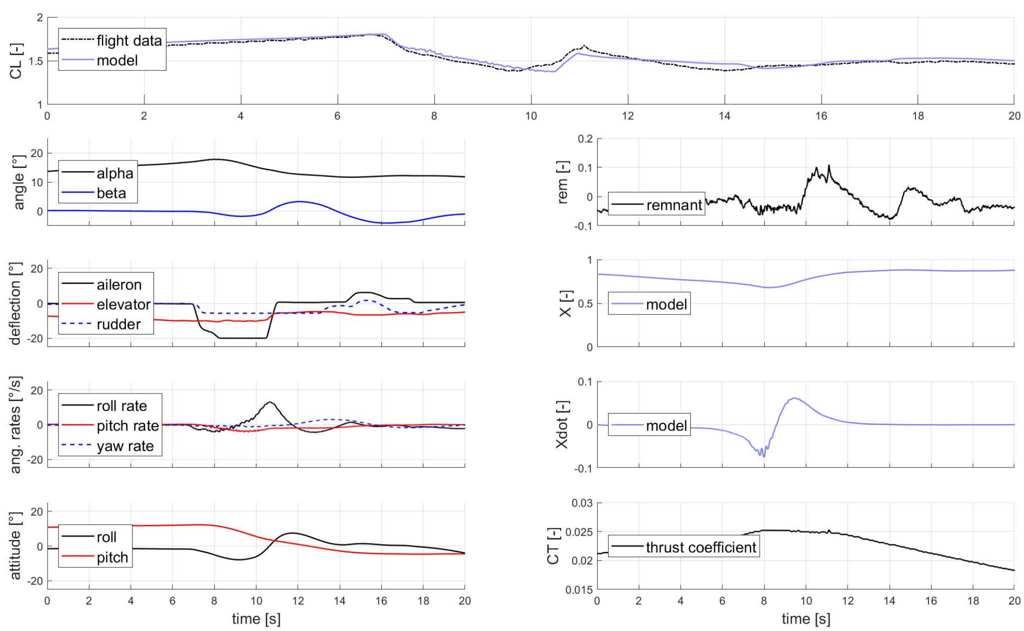

Fig. 10 Stall with the best MSE of the C_L model for flaps = 18°, MSE = 0.0016.

Table 5 Results of identifying the C_L-parameters and some performance evaluating metrics. The relative MSE is expressed in function of the average value of C_L during the flight tests for the flapping setting under consideration. The RMS (0 % for perfect fit) is averaged for all stall manoeuvres in the training or validation data set.

Parameter		Results			Verification data set			Validation data set		
Name	Unit	$\hat{\theta}$	$\frac{s(\hat{\theta})}{\hat{\theta}}$	$CRLB$	MSE	rel. MSE	RMS	MSE	rel. MSE	RMS
Flaps = 0°										
C_{L_0}	[-]	**-0.0218**	-15.1065	5.3e-04	0.0049	1.78 %	15 %	0.0051	1.85 %	10 %
C_{L_α}	[-]	**6.2771**	0.2428	0.0103						
$C_{L_{\delta_a}}$	[-]	**-0.6189**	-0.5983	0.3803						
C_{L_q}	[-]	**19.7334**	0.9609	4.2945						
Flaps = 18°										
C_{L_0}	[-]	**0.1980**	0.5301	7.2e-04	0.0092	3.5 %	15 %	0.0052	2.14 %	22 %
C_{L_α}	[-]	**5.0102**	0.2446	0.0131						
$C_{L_{\delta_a}}$	[-]	**-0.6779**	-0.7228	0.3837						
C_{L_q}	[-]	**24.7203**	0.5321	5.1844						
Flaps = 42°										
C_{L_0}	[-]	**0.9870**	0.1582	3.6e-04	0.012	4.6 %	14 %	0.024	9.2 %	13 %
C_{L_α}	[-]	**4.4580**	0.1919	0.007						
$C_{L_{\delta_a}}$	[-]	**-0.5377**	-0.7375	0.2113						
C_{L_q}	[-]	**20.3092**	3.5366	18.8847						

flow separation point or angle of attack on both wings. This difference is indicated by the subscripts r (right) and l (left). The terms are the differential flow separation point / differential X-term $(X_r - X_l)$, the differential angle of attack $(\alpha_r - \alpha_l)$ and the differential Kirchhoff term $\left(\left(\frac{1+\sqrt{X_r}}{2}\right)^2 \alpha_r - \left(\frac{1+\sqrt{X_l}}{2}\right)^2 \alpha_l\right)$, as well as the symmetric terms X and $(1 - X)$. Applying the algorithm for model structure selection combined with a check of minimum MSE resulted into three different model structures, depending on the flap setting, Equation 19 - Equation 21. Besides the outcome of the selection algorithm, Figure 11 and Figure 12, the MSE and correlation between the different measured signals were taken into account to fine-tune the models.

The C_l data shows to be dependent on the aileron deflection, difference in left and right flow separation point and the differential Kirchhoff term $\left(\left(\frac{1+\sqrt{X_r}}{2}\right)^2 \alpha_r - \left(\frac{1+\sqrt{X_l}}{2}\right)^2 \alpha_l\right)$. Even though the last two might seem very similar terms, no correlation was found between them. Between the flap settings, the difference in flow separation is either multiplied by the pitch rate q or the overall flow separation point X, the selection was based on the outcome of the multivariate orthogonal function modelling algorithm and verified by computing the MSE. The differential lift and roll rate p can be seen to exhibit very similar trends (Figure 13) as they are correlated, $\rho = 0.94$. Only for the 18° flaps case, the roll rate performed better as a regressor term. For the other flap settings, the differential lift term was selected. Adding at least two separate flow separation points as a term for asymmetric modelling as well as a differential Kirchhoff term, show their importance in improving the model quality.

Table 6 gives an overview of the found parameter values combined with some performance evaluating metrics. Low values for the MSE error and RMS are found for all data sets, but the low values for the VAF (0.10 - 0.57) indicate that the model is not capturing the trend of the flight data. Compared to the order of magnitude of C_l, the Cramèr-Rao Lower Bounds (CRLB) indicate a parameter variance that is rather high. As the CRLB indicate the theoretical lower boundary for this parameter variance, it can be concluded that the data cannot reconstruct the flight data with very high accuracy. The ratio between the standard deviation and parameter estimate, $\frac{s(\hat{\theta})}{\hat{\theta}}$, shows the parameters where difficulties can arise to estimate an accurate value, such as δ_a.

$$C_{l_{F0}} = C_{l_0} + C_{l_{\delta_a}}\delta_a + C_{l_{\delta_r}}\delta_r + C_{l_{\Delta X}}\left(X_r - X_l\right)X + C_{l_{\Delta L}}\left(\left(\frac{1+\sqrt{X_r}}{2}\right)^2\alpha_r - \left(\frac{1+\sqrt{X_l}}{2}\right)^2\alpha_l\right) \tag{19}$$

$$C_{l_{F18}} = C_{l_0} + C_{l_p}p + C_{l_{\dot\beta}}\dot\beta + C_{l_{\delta_a}}\delta_a + C_{l_{\Delta X}}\left(X_r - X_l\right)X \tag{20}$$

$$C_{l_{F42}} = C_{l_0} + C_{l_{\delta_a}}\delta_a + C_{l_{\delta_r}}\delta_r + C_{l_{\Delta X}}\left(X_r - X_l\right)q + C_{l_{\Delta L}}\left(\left(\frac{1+\sqrt{X_r}}{2}\right)^2\alpha_r - \left(\frac{1+\sqrt{X_l}}{2}\right)^2\alpha_l\right) \tag{21}$$

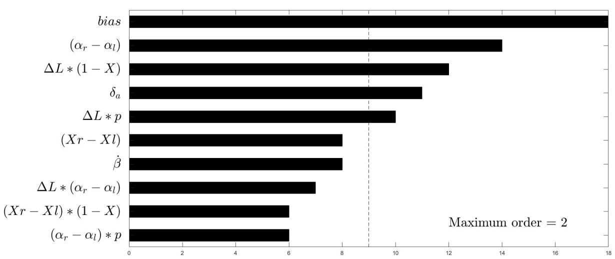

Fig. 11 C_l **model structure selection algorithm outcome, Flaps = 18°**

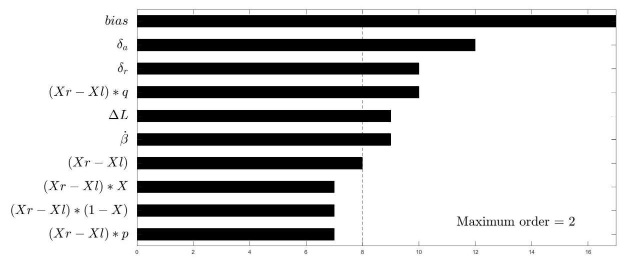

Fig. 12 C_l **model structure selection algorithm outcome, Flaps = 42°**

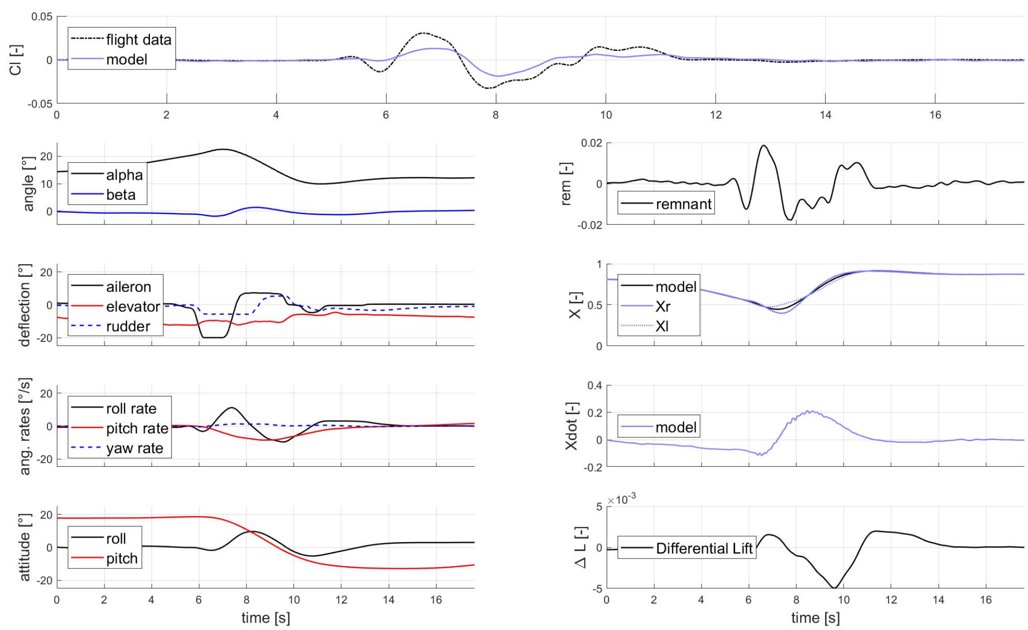

Fig. 13 Example of C_l **flight data and model for the Fokker 100, flaps = 18°.**

C. Yawing moment C_n model

The set of the X-related parameters for the yawing moment C_n model is the same as for the rolling moment model. The results of the algorithm proposed by Morelli (Figure 14 and Figure 15) in combination with a correlation and MSE analysis were used to determine the final model structure per flap setting, Equation 22 - Equation 24.

Table 6 Results of estimating the C_l-parameters and some performance evaluating metrics. The relative MSE is expressed in function of the maximum value obtained for c_l during the flight tests for the flap setting under consideration. The RMS (0 % for perfect fit) is averaged for all stall manoeuvres in the data set.

Parameter		Results			Training				Validation			
Name	Unit	$\hat{\theta}$	$\frac{s(\hat{\theta})}{\hat{\theta}}$	CRLB	MSE	rel. MSE	VAF	RMS	MSE	rel. MSE	VAF	RMS
Flaps = 0°												
C_{l_0}	[-]	-4.4e-04	-1.1608	-								
$C_{l_{\delta_a}}$	[-]	-0.0126	-4.1806	0.0278								
$C_{l_{\delta_r}}$	[-]	0.0182	5.0055	0	1.179e-05	0.05%	0.48	11 %	1.425e-05	0.05%	0.38	12 %
$C_{l_{\Delta X \cdot X}}$	[-]	0.5699	0.3437	0.0016								
$C_{l_{\Delta L}}$	[-]	3.111	0.3797	0.0016								
Flaps = 18°												
C_{l_0}	[-]	-6e-04	-3.9987	-								
$C_{l_{\delta_a}}$	[-]	-0.0636	-10.0721	0.0394								
C_{l_β}	[-]	-0.0108	-3.9617	0	4.537e-05	0.08%	0.10	14 %	1.585e-05	0.03%	0.57	13 %
$C_{l_{\Delta X \cdot X}}$	[-]	0.7595	0.8967	0.0058								
C_{l_p}	[-]	0.8966	1.0603	0.3289								
Flaps = 42°												
C_{l_0}	[-]	-8.2e-04	-8e-04	-								
$C_{l_{\delta_a}}$	[-]	-0.0379	-0.0379	0								
$C_{l_{\delta_r}}$	[-]	0.0612	0.0612	0.001	6.164e-05	0.1%	0.33	13 %	4.842e-05	0.08%	0.37	12 %
$C_{l_{\Delta X \cdot q}}$	[-]	-12.1077	-12.1077	4.9979								
$C_{l_{\Delta L}}$	[-]	0.1061	0.1061	0.0295								

$$C_{n_{F0}} = C_{n_0} + C_{n_\beta}\beta + C_{n_{\delta_a}}\delta_a + C_{n_{\Delta\dot{\alpha}}}(\dot{\alpha_r} - \dot{\alpha_l}) + C_{n_{\Delta\alpha}}(\alpha_r - \alpha_l) \tag{22}$$

$$C_{n_{F18}} = C_{n_0} + C_{n_\beta}\beta + C_{n_{\dot\beta}}\dot{\beta} + C_{n_{\Delta\alpha}}(\alpha_r - \alpha_l) \tag{23}$$

$$C_{n_{F42}} = C_{n_0} + C_{n_\beta}\beta + C_{n_{\delta_a}}\delta_a + C_{n_{\Delta\alpha}}(\alpha_r - \alpha_l) + C_{n_{\Delta X(1-X)}}(X_r - X_l)(1 - X) + C_{n_{\Delta L}}\left(\left(\frac{1+\sqrt{X_r}}{2}\right)^2 \alpha_r - \left(\frac{1+\sqrt{X_l}}{2}\right)^2 \alpha_l\right) \tag{24}$$

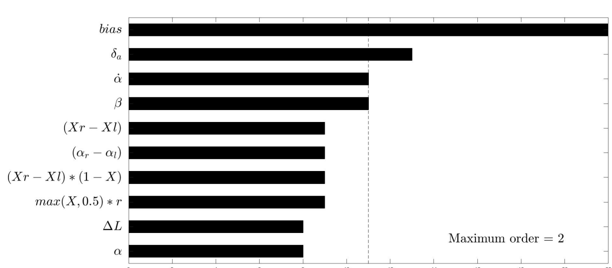

Fig. 14 C_n model structure selection algorithm outcome, Flaps = 0°

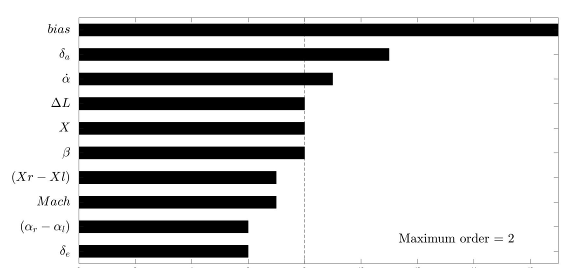

Fig. 15 C_n model structure selection algorithm outcome, Flaps = 42°

Except for some returning model terms, the structures selected show a wide variety over the flap settings. The yawing moment showed a mutual dependence on the side slip angle and difference in local AoA for all flap settings. For the case where the flaps = 42° (landing configuration), a rather lengthy model is found where three differential terms are chosen: differential Kirchhoff, AoA and X. None of the terms are correlated to each other in this data set, even though this is the case for the other flap settings (ρ = 0.95 for $\Delta\alpha$ and ΔL for flaps = 0° and 18°, ρ = 0.58 for flaps 42°).

Terms found for a specific flap setting were also tested for improvement in MSE for the other settings. $(X_r - X_l)(1 - X)$ showed up in the algorithm for flaps = 0°, but was only used for the flaps = 42° as it did contribute to a reduction in MSE. The multivariate orthogonal function modelling algorithm can serve as an indication, but its outcome is dependent on which model terms are in the pool, the value of the model complexity penalty, matrices close to singular values, etc. Adding model terms based on engineering judgement or even trial and error, could aid to improve the model structures quality by adapting the results of the algorithm.

Table 7 shows better results for the CRLB compared to the model for C_l. Good values for the MSE and relative MSE are again observed, but the VAF again indicates that the flight data trend is not followed by the model, as shown in Figure 16. In fact, the selection of three totally different model structures for the different flap settings indicates that the information content in the flight test data is lacking to identify an accurate stall model, valid for all flap settings. The VAF and RMS show less good results for the C_n models compared to the more consistent model structures found for C_l.

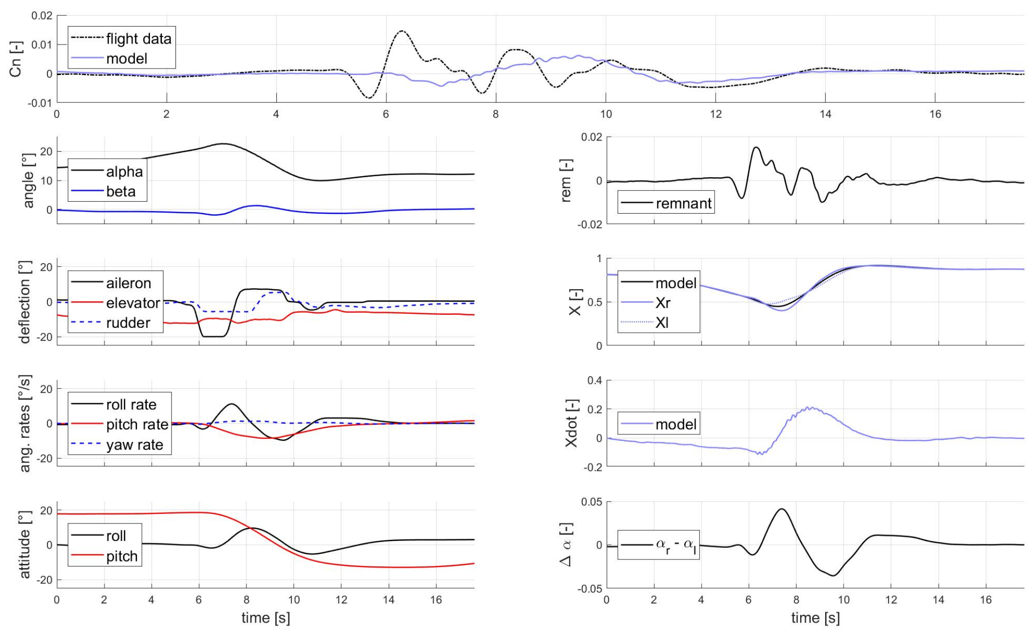

Fig. 16 Example of c_n flight data and model for the Fokker 100, flaps = 18°. Same stall manoeuvre as Figure 13

D. Yaw Force C_Y model

The same candidate regressor pool is used as for all other asymmetric model terms. The results of the multivariate orthogonal function algorithm are shown in Figure 17 and Figure 18. The chosen model structures are given by Equation 25-Equation 27.

Table 7 Results of estimating the C_n-parameters and some performance evaluating metrics. The relative MSE is expressed in function of the maximum value obtained for C_n during the flight tests for the flap setting under consideration. The RMS (0 % for perfect fit) is averaged for all stall manoeuvres in the data set.

Parameter		Results			Training				Validation			
Name	Unit	$\hat{\theta}$	$\frac{s(\hat{\theta})}{\hat{\theta}}$	CRLB	MSE	rel. MSE	VAF	MSE	rel. MSE	VAF		
Flaps = 0°												
C_{n_0}	[-]	-4e-05	-22.0605	-	8.223e-06	0.09%	0.30	15 %	1.496e-05	0.16%	0.26	15 %
C_{n_β}	[-]	0.0965	0.6942	0.0002								
$C_{n_{\delta_a}}$	[-]	-0.0141	-1.3199	0								
$C_{n_{\Delta\dot{\alpha}}}$	[-]	0.9160	1.9334	0.0460								
$C_{n_{\Delta\alpha}}$	[-]	-0.0855	-2.2676	0.0003								
Flaps = 18°												
C_{n_0}	[-]	6e-04	2.3412	-	1.403e-05	0.12%	0.27	16 %	1.625e-05	0.14%	0.23	17 %
C_{n_β}	[-]	0.0382	1.3981	0.0002								
$C_{n_{b\dot{e}ta}}$	[-]	0.5516	0.7301	0.0357								
$C_{n_{\Delta\alpha}}$	[-]	-0.2326	-0.5828	0.0045								
Flaps = 42°												
C_{n_0}	[-]	3.05e-05	-8e-04	-	3.352e-05	0.19%	0.33	16 %	3.542e-05	0.2%	0.08	17 %
C_{n_β}	[-]	0.0480	-0.0379	0.0029								
$C_{n_{\delta_a}}$	[-]	-0.0289	0.0612	0.004								
$C_{n_{\Delta X\cdot(1-X)}}$	[-]	0.2291	-12.1077	0.2877								
$C_{n_{\Delta\alpha}}$	[-]	0.5782	0.1061	1.0654								
$C_{n_{\Delta L}}$	[-]	-3.4910	0.1061	31.0265								

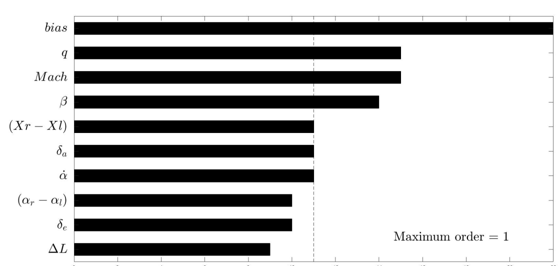

Fig. 17 C_Y model structure selection algorithm outcome, Flaps = 0°

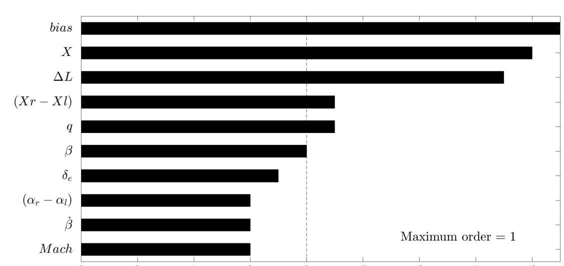

Fig. 18 C_Y model structure selection algorithm outcome, Flaps = 42°

$$C_{Y_{F0}} = C_{Y_0} + C_{Y_\beta}\beta + C_{Y_{\delta_a}}\delta_a + C_{Y_{\Delta\alpha}}(\alpha_r - \alpha_l) \tag{25}$$

$$C_{Y_{F18}} = C_{Y_0} + C_{Y_\beta}\beta + C_{Y_{\delta_a}}\delta_a + C_{Y_{\Delta X}}(X_r - X_l) \tag{26}$$

$$C_{Y_{F42}} = C_{Y_0} + C_{Y_\beta}\beta + C_{Y_{\delta_a}}\delta_a + C_{Y_{\Delta X}}(X_r - X_l) \tag{27}$$

The yaw force model C_Y has three very similar models for the three different flap settings. Only for flaps = 0°, the difference in AoA is preferred over the difference in flow separation location. Furthermore, β was selected for all three flap settings by the multivariate orthogonal function modelling algorithm, the aileron deflection was selected for flaps = 0° and 18°, but also improved model fit for flaps = 42°. Adding the differential Kirchhoff term, as suggested by the model structure selection algorithm, did not improve the VAF nor the MSE.

Analysing the performance of the models for C_Y indicates improved results compared to the other asymmetric models. Lower CRLB values are found and the VAF shows improved capabilities to model the trend of the flight data. Figure 19

Table 8 Results of estimating the C_Y-parameters and some performance evaluating metrics. The relative MSE is expressed in function of the maximum value obtained for C_Y during the flight tests for the flap setting under consideration. The RMS (0 % for perfect fit) is averaged for all stall manoeuvres in the data set.

Parameter		Results			Training				Validation			
Name	Unit	$\hat{\theta}$	$\frac{s(\hat{\theta})}{\hat{\theta}}$	CRLB	MSE	rel. MSE	VAF	RMS	MSE	rel. MSE	VAF	RMS
Flaps = 0°												
C_{Y_0}	[-]	-0.0032	-0.8465	-	5.692e-05	0.20%	0.56	14 %	8.108e-05	0.28%	0.17	15 %
C_{Y_β}	[-]	-0.5566	-0.3521	0.0002								
$C_{Y_{\delta_a}}$	[-]	0.0053	10.0566	0								
$C_{Y_{\Delta\alpha}}$	[-]	0.2009	1.8090	0.0460								
Flaps = 18°												
C_{Y_0}	[-]	-0.0035	-1.1399	-	1.902e-04	0.34%	0.63	15 %	3.026e-04	0.54%	0.58	16 %
C_{Y_β}	[-]	-0.4961	-0.6171	0.0030								
$C_{Y_{\delta_a}}$	[-]	-0.0191	-5.6077	0.0002								
$C_{Y_{\Delta X}}$	[-]	0.0054	49.5843	0.0012								
Flaps = 42°												
C_{Y_0}	[-]	2.772e-04	18.7954	-	4.96e-04	0.51%	0.61	23 %	5.23e-04	0.53%	0.29	16 %
C_{Y_β}	[-]	-0.4720	-0.5934	5.196e-04								
$C_{Y_{\delta_a}}$	[-]	-0.0092	-19.1434	2.614e-04								
$C_{Y_{\Delta X}}$	[-]	0.0768	2.3173	4.841e-04								

suggest that the peak in C_Y model is related to the peak found in $(X_r - X_l)$. Its coefficient is however too low to sufficiently scale up the differential X peak. Taking a closer look shows an apparent time lag between the peaks, which was also found in other data sets and models. The filters applied on certain time signals to remove high frequency components caused by the stall buffet, were chosen carefully to not alter or lag the trend of the data. A more detailed investigation might offer insight to improve the model fit.

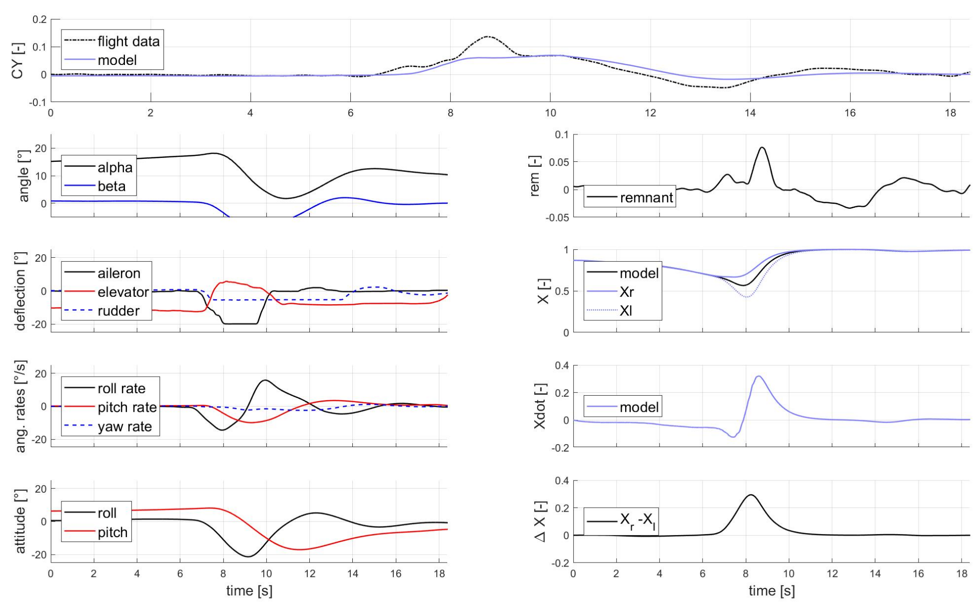

Fig. 19 Example of C_Y flight data and model for the Fokker 100, flaps = 42°

VI. Conclusion

The Fokker 100 data set originates from a flight characteristics certification campaign. As a result, the stalls performed for that campaign lack any sort of deliberate pilot excitation of the control surfaces. Only control deflections to recover the aircraft from the stall and resulting asymmetric responses are applied. The necessity of control surface excitation for proper stall model parameter identification has been widely suggested in literature ([11, 15]). This research intended to investigate the use of multiple Kirchhoff separation points to model asymmetric aircraft behaviour. Stalls exhibiting noticeable roll-off during stall, as reported in the flight test cards of Fokker 100, were selected to test whether enough information was present in this data to perform proper stall model identification.

The nonlinear identification of Kirchhoff's ODE parameters showed that the dynamic parameter τ_2 had no effect on the model structure of C_L. Furthermore, the identification of the most predictable parameter α^* did not meet with the expectations based on knowledge of the stall angle of attack, visual inspection of the C_L model and flight data and the behaviour in function of flap setting. The data set contains not enough information to identify the Kirchhoff's ODE parameters for a high fidelity simulation model. The Gramian matrix, a metric to quantify this information content, did output very small values compared to those obtained in dedicated identification flight manoeuvres.

The information content of the Fokker 100 stall data set is insufficient to accurately model its stall behaviour. For the C_n model three different model structures were identified, not showing clear consistency between the different flap settings. This can be an indication that not enough information content is present in the data sets to properly identify a good model. It might also indicate non-linearities in the aerodynamic behaviour attributed to the flap setting. More dedicated data sets including control surface excitation in specific sequences (doublet, 3-2-1-1, etc.) are required to build high fidelity stall models for pilot training in flight simulators. The Fokker 100 data set is not suited for those high fidelity models. It is yet unknown what level of fidelity the simulators models should achieve. The Fokker 100 data set should therefore not be discarded.

Including differential flow separation points and related terms into the asymmetric stall model structures can increase the model fit to the flight data. The selection of such terms by the multivariate orthogonal function modelling algorithm, combined with an improvement of MSE and VAF of the model fit show their importance in asymmetric stall modelling. Kirchhoff's theory includes more possibilities than just modelling the lift coefficient. Extending this methodology to multiple separation points for each wing could even further improve the stall modelling for asymmetric behaviour.

References

[1] Airbus, "A Statistical Analysis of Commercial Aviation Accidents 1958-2018," Tech. rep., 2019.

[2] Boeing, "Statistical Summary of Commercial Jet Airplane Accidents Worldwide Operations | 1959 – 2017," Tech. rep., Boeing Commercial Airplanes, 2018. URL `www.boeing.com/news/techissues/pdf/statsum.pdf`.

[3] FAA, "Advisory Circular Subject: Upset Prevention and Recovery Training," Tech. rep., 2017.

[4] EASA, "Easy Access Rules for Aircrew (Regulation (EU) No 1178/2011)," Tech. rep., 2019. URL `http://eur-lex.europa.eu/,`.

[5] Advani, S., and Field, J., "Upset Prevention and Recovery Training in Flight Simulators," *AIAA Modeling and Simulation Technologies Conference 08-11 August 2011, Portland, Oregon*, Portland, 2011. https://doi.org/10.2514/6.2011-6698, URL http://arc.aiaa.org.

[6] Crider, D. A., "The Need for Upset Recovery Training," *AIAA Modeling and Simulation Technologies Conference and Exhibit 18 - 21 August 2008, Honolulu, Hawaii*, Honolulu, 2008. https://doi.org/10.2514/6.2008-6864, URL http://arc.aiaa.org.

[7] Kay, J., Ralston, J. N., and Lash, S. F., "Development of Non-Linear, Low-Speed Aerodynamic Model for the F-16/Vista," *American Institute of Aeronautics and Astronautics*, 1997. https://doi.org/10.2514/6.1997-3576, URL http://arc.aiaa.org.

[8] Goman, M., and Khrabrov, A., "State-Space Representation of a Aerodynamic Characteristics of an Aircraft at High Angles of Attack," *Astrodynamics Conference, 1992*, American Institute of Aeronautics and Astronautics, Reston, Virigina, 1992, pp. 759–766. https://doi.org/10.2514/3.46618, URL http://arc.aiaa.org/doi/10.2514/6.1992-4651.

[9] Deiler, C., and Kilian, T., “Dynamic Aircraft Simulation Model Covering Local Icing Effects,” *CEAS Aeronautical Journal*, Vol. 9, No. 3, 2018, pp. 429–444. https://doi.org/10.1007/s13272-018-0291-6.

[10] Van Ingen, J., “Dynamic Stall Modeling for the Cessna Citation II,” , No. October, 2017, p. 145. URL http://resolver.tudelft.nl/uuid:f76439ef-ab2a-4173-8d78-3122a2696e91.

[11] Dias, J. N., “Unsteady and Post-Stall Model Identification Using Dynamic Stall Maneuvers,” *Proceedings of the AIAA Atmospheric Flight Mechanics Conference, Dallas (TX)*, American Institute of Aeronautics and Astronautics (AIAA), Dallas, 2015. https://doi.org/10.2514/6.2015-2705.

[12] Grant, P. R., Liu, S., Luo, Z. Z., and Moszczynski, G., “Development of Post-Stall Flight Models from Certification Flight Test and Wind-Tunnel Data,” *AIAA Modeling and Simulation Technologies Conference, 2017*, American Institute of Aeronautics and Astronautics Inc, AIAA, 2017. https://doi.org/10.2514/6.2017-1549.

[13] Singh, J., and Jategaonkar, R. V., “Identification of Lateral-Directional Behavior in Stall From Flight Data,” *Journal of Aircraft*, Vol. 33, No. 3, 1996, pp. 627–630. https://doi.org/10.2514/3.46993.

[14] Ralston, J. N., Gingras, D. R., Wilkening, C., and Desrochers, P., “The Application of Potential Data Sources for Simulator Compliance with ICATEE Recommended Stall Modeling Requirements,” *AIAA Modeling and Simulation Technologies Conference 2012*, 2012, pp. 1–22. https://doi.org/10.2514/6.2012-4568.

[15] Morelli, E. A., Cunningham, K., and Hill, M. A., “Global Aerodynamic Modeling for Stall/Upset Recovery Training Using Efficient Piloted Flight Test Techniques,” *AIAA Atmospheric Flight Mechanics Conference; August 19, 2013 - August 22, 2013; Boston, MA; United States*, 2013. URL https://ntrs.nasa.gov/search.jsp?R=20140002791.

[16] Mulder, J. A., Chu, Q. P., Sridhar, J. K., Breeman, J. H., and Laban, M., “Non-Linear Aircraft Flight Path Reconstruction Review and New Advances,” *Progress in Aerospace Sciences*, Vol. 35, No. 7, 1999, pp. 673–726. https://doi.org/10.1016/S0376-0421(99)00005-6.

[17] Walcott, B. L., Corless, M. J., and Żak, S. H., “Comparative study of non-linear state-observation techniques,” *International Journal of Control*, Vol. 45, No. 6, 1987, pp. 2109–2132. https://doi.org/10.1080/00207178708933870.

[18] Hwang, M., and Seinfeld, J. H., “Observability of Nonlinear Systems 1,” Tech. Rep. 2, 1972.

[19] Welch, G., and Bishop, G., “An Introduction to the Kalman Filter,” Tech. rep., 2001. https://doi.org/10.1.1.117.6808, URL http://www.voluntarybenefitsmagazine.com/article/population-risk-management-and-workplace-health-centers.html{%}5Cninternal-pdf://1153/population-risk-management-and-workplace-health-centers.html.

[20] Laban, M., “Laban - 1994 - On-Line Aircraft Aerodynamic Model Identification,” Ph.D. thesis, 1994.

[21] Grauer, J., “Position Corrections for Airspeed and Flow Angle Measurements on Fixed-Wing Aircraft,” Tech. Rep. November, 2017.

[22] Moszczynski, G. J., Giamou, M., Leung, J. M., Kelly, J., and Grant, P. R., “An Observability-Based Approach to Flight Path Reconstruction of Uninformative Coupled Aircraft Trajectories: A Case Study Considering Stall Maneuvers for Aircraft Certification,” *AIAA Scitech 2019 Forum*, American Institute of Aeronautics and Astronautics Inc, AIAA, 2019. https://doi.org/10.2514/6.2019-0012.

[23] Fischenberg, D., and Jategaonkar, R. V., “Identification of Aircraft Stall Behavior from Flight Test Data,” *Proceedings of the RTO SCI Symposium on System Identification for Integrated Aircraft Development and Flight Testing, Madrid, Spain*, Madrid, 1998, pp. 17–1—-17–8.

[24] Nie, Y., Kampen, E.-j. V., and Chu, P., “Geometry Based Quick Aircraft Modeling Method for Upset Recovery Applications,” *AIAA SciTech 5 - 9 January 2015, Kissimee, Florida AIAA Modeling and Simulation Technologies Conference*, 2015, pp. 1–16.

[25] Luchtenburg, D. M., Rowley, C. W., Lohry, M. W., Martinelli, L., and Stengel, R. F., “Unsteady High-Angle-of-Attack Aerodynamic Models of a Generic Jet Transport,” *Journal of Aircraft*, Vol. 52, No. 3, 2015. https://doi.org/10.2514/1.C032976, URL http://arc.aiaa.org.

[26] The Mathworks Inc., “fmincon,” , 2020.

[27] Chambers, J. R., and Grafton, S. B., “Aerodynamic Characteristics of Airplanes at High Angles of Attack,” Tech. rep., 1977. URL https://ntrs.nasa.gov/search.jsp?R=19780005068.

II

Preliminary Report

1

Literature Review

1.1. Introduction

Loss of Control in Flight (LOC-I) accidents are the largest contributors to aviation fatalities [8]. To enhance safety and minimise these accidents, new regulations about pilot training for upset awareness, prevention, recognition and recovery have been established by the Federal Aviation Authority (FAA) and European Union Aviation Safety Agency (EASA)[42][39]. These regulations require training of pilots in flight simulator to handle upsets and avoid fatal accidents. This is often referred to as Upset Prevention and Recovery Training (UPRT). The aerodynamic models of current flight simulators are not sufficient to provide positive transfer of training as their fidelity is lacking [5]. The need to extend the flight envelopes in simulator training towards upset, and stalls in specific, has therefore been receiving more attention lately.

Significant progress in modeling techniques based on actual flight test data has been made already using Kirchhoff's theory of flow separation. There is however still work to do to provide improved stall training to the pilots. One of the current research gaps is the lack of high fidelity lateral-directional stall models. Up until today, the existing lateral stall models are not very accurate and are often estimated together with the longitudinal model [46, 87]. No specific approaches have been applied with focus on the lateral-directional characteristics. As a stall can be accompanied by lateral-directional divergence, requiring noticeable pilot input for safe recovery, there is a need to include this behaviour in the simulator stall models. TU Delft has access to its own research aircraft, the Cessna Citation II, as well as flight test data of the Fokker 100. The approach of using flight test data methodologies is therefore the most logic and feasible one.

Chapter 1.2 provides background information to this problem statement, whilst section 1.3 provides an overview of the early efforts made to create high angle of attack stall models for fighters and airliners. Chapter 1.4 discusses the state-of-the-art modeling approaches towards aerodynamic stall modeling. The chapter ends with the research objective and questions to be answered during the MSc thesis.

1.2. Background

This chapter gives a background towards the performed literature review. In subsection 1.2.1 and subsection 1.2.2, the phenomenon of aerodynamic stall and corresponding aircraft characteristics will be discussed. Section 1.2.4 gives insight in aviation accidents and how to improve safety, followed by subsection 1.2.5 where analysis and recommendations are given to enhance safety by pilot simulator training for aircraft upset conditions.

1.2.1. Aerodynamic Stall

An aircraft produces lift to overcome the gravitational force directed towards the center of the earth. A combination of Bernoulli's law and Newton's third law of motion, action-reaction, allow a wing to generate lift. The amount of lift is linearly related to the angle of attack (AoA) of the wing chord with respect to the relative wind. This linear relationship only holds to a certain AoA, after which it becomes non-linear and a stall is entered. A stall occurs when the maximum AoA with corresponding C_L, is exceeded. No matter what flight condition the aircraft is in, descending or climbing, low or high altitude, etc. If this AoA is exceeded, a stall will occur. The stall will cause a sudden decrease of lift and the aircraft will lose altitude. A typical lift curve slope is represented by the solid black line on the left image in Figure 1.1.

A distinction must be made between static and dynamic stall. Static stall can be investigated using wind tunnel tests in which the AoA is varied slowly and measurements are only taken after the change in AoA has stabilised. If an aircraft has a positive increasing rate in AoA, $\dot{\alpha}$, higher C_L values can be obtained compared to static stalls as the flow separation lags the increase in AoA [3][14][86]. We speak of dynamic stall due to the additional effects of stall hysteresis [83]. Quasi-steady stall is a dynamic stall in which the increase in AoA is small enough to neglect the dynamic effects. This depends on the rate of change of the AoA. If this rate is low, the flow field can follow these changes without noticeable time lags. Making this assumption, is case dependent.

1.2.2. High Angle of Attack Flight Characteristics

The aerodynamics of aircraft at high AoA close to the stall angle is different compared to the nominal AoA flight regime. Stability derivatives change, leading to different aircraft behaviour at these AoAs. A short overview of the altered stability derivatives and aircraft behaviour is given below.

Stability Derivatives

Generally speaking, aircraft at high AoAs experience reduced lateral and directional stability as well as reduced control effectiveness. This is due to the flow separation that occurs in the stall flight regime [90]. The stability derivatives exhibit nonlinear behaviour as the AoA approaches the critical AoA. Furthermore, different values for stability derivatives occur for static and dynamic stall, making it hard to have a single model covering both stall types [82].

As flow separation starts to occur, it covers (parts) of the vertical tail with its wake, making the vertical tail less effective due to this adverse side wash. This affects the static directional stability derivative (C_{n_β}), also known as weathercock stability. Furthermore, we see a decrease in effective dihedral and roll damping. The desired behaviour of both derivatives is based on restoring moments if differential lift on both wings occurs caused by side slipping and rolling respectively. However, this restoring lift increase can in fact cause the exceedance of the critical AoA of that wing, causing the wing to drop rather than restoring the equilibrium. Aircraft in stall experience altered pitching behaviour. If this is an increase or decrease depends on the aircraft configuration[21][82][50].

Aircraft Behaviour

The changing stability derivatives cause the aircraft to behave and fly differently near stall than in the low AoA regime. The exhibited behaviour is nonlinear and impossible to predict using just theory [21]. The first undesired reaction is a pitch-up due the changed pitch stability. The pitch-up does not happen for all aircraft and is mainly dependent on the sweep and aspect ratio of the wing and the location of the horizontal tail with respect to the wing wake. This pitch-up can lead to a deep stall if not countered in time. Once in a deep stall, insufficient nose-down authority is present to recover the aircraft.

The reduced lateral-directional stability can cause asymmetric stalls, with rolling and yawing moments upon stall as a consequence. The asymmetry starts from differential lift on both wings and instability in roll damping. This can cause the aircraft to auto-rotate, if not stopped in time, leads to a developed spin with unstable roll damping [21][90].

At stall, flow separation causes buffet of the aircraft. The intensity and frequency of this buffet depends on the aircraft configuration. Buffet onset does provide a good initial cue for pilots to recognise a stall, just like the sudden asymmetric behaviour like roll-off. It is therefore important to include buffet in future stall models as well. Knowledge of the buffet frequency also allows to filter its influence on the instrumentation before the system identification algorithm is thrown on the data [67].

1.2.3. Icing effects

An aircraft always stall at its critical AoA. This is however only the case if the wing is free of any substance or particles that alter the smoothness and/or shape of the airfoil profile like dust, rain or insects. A major concern is icing. The presence of icing on the wing can severely alter its capability to produce lift. The wing stalls at lower AoAs and has increased drag. Iced wings can in fact stall at AoAs far lower than clean wings. Pilots are thrown off as the stall warning system based on AoA do not go off and they do not expect stall in these attitudes. The startle factor is present and pilots do not always recognise in time for a successful recovery. Furthermore, asymmetric icing is easily achieved, causing uncommanded roll-offs [29].

The type of icing has an influence on the change of dynamic behaviour. Leading edge icing causes much more severe premature stalling and increased drag. This is represented in Figure 1.1.

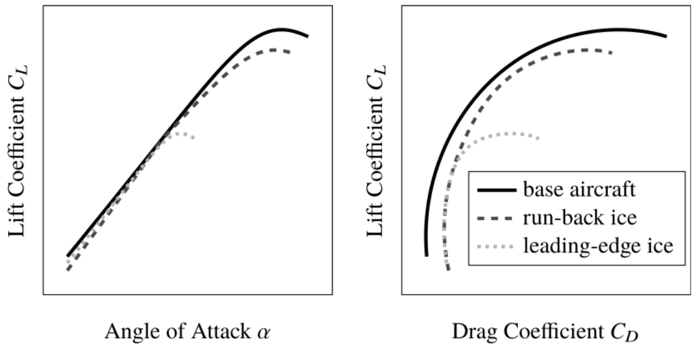

Figure 1.1: Lift and drag curves under influence of icing [29]

1.2.4. LOC-I accidents

Aviation is a fast-growing industry, doubling in magnitude about every 15 years. Safety is a key aspect and much attention is paid towards improving aviation safety and minimising fatalities. The amount of incidents and accidents does not follow the growing trend, rather it is slowly decreasing . This is the result of many efforts to increase safety and technological advances aiding in their prevention. The introduction of the Terrain Awareness and Warning System (TAWS) and its widespread use resulted into a reduction of Controlled Flight into Terrain (CFIT) accidents by a factor 7 over the last 2 decades. The most fatal cause of accidents,LOC-I, did only reduce by a factor 2 in the same time span. It therefore remains the largest contributor towards fatalities. From 2008 till 2017, LOC-I caused 1,131 fatalities, CFIT 636 being the second largest contributor. All other causes resulted into another 619 fatalities [8] [11] [55].

The question remains on how LOC-I incidents and accidents can in fact be effectively reduced. The major technological advance that already contributed to this is the fly-by-wire system which allowed the development of flight envelope protection systems. However, this is not sufficient. LOC-I is a general term for all sorts of lost of control events. Further investigation of the specific causes of these LOC-I accidents shows that from 1993 - 2007, a total of 74 LOC-I accidents occurred. 27 of them were due to stalling, 20 due to icing of which 9 ended up in a stall and 8 due to spatial disorientation, those three being the major causes. In total, 3241 people died in those 74 accidents. In 10 accidents, incorrect recovery techniques performed by the pilots actually worsened the situation. It must be said that none of the aircraft involved in those 74 accidents was equipped with flight envelope protection [61]. This system is only present in 4th generation jets, which perform about 50 % of all flights nowadays [8].

Technological advances are currently not sufficient for LOC-I prevention and recovery. Improved pilot training can aid towards a safer aviation industry. In-flight training has risks and is expensive [49]. This is where ground-based flight simulator come into play. Pilots of aircraft without envelope protection have access to this mean of safety enhancement, but all pilots can benefit from this[16]. Besides simulator training, awareness of conditions and situations that can lead to upsets should be improved. In this research, the focus will be on the prevention, recognition and recovery of stalls by means of ground-based simulator training.

Regulatory frameworks were set-up based on recommendations published by specialised working groups. ICATEE [1] and Loss of Control Avoidance and Recovery Training (LOCART) were founded specifically to tackle this problem and investigate new ways of training pilots in order to reduce the amount of LOC-I accidents. The result is an advisory circular that was published by the FAA based on the recommendations of the working groups [42]. Same holds for EASA, who have incorporated the recommendations in their aviation rules [39]. As by March 2019, air carriers must provide stall training to all their pilots. The need for improved high fidelity stall training in simulators has therefore notably been receiving more attention all around the world.

1.2.5. Stall Mitigation and Recovery Training in Flight Simulators

Part of the solution to reduce the amount of LOC-I accidents, is dedicated training for stall recognition, prevention and recovery in flight simulators. Pilots should be trained to prevent the aircraft diverging from its intended flight path. If the aircraft does so anyways, pilots should be able to timely recognise this divergence and restore the intended flight path before the situation unfolds to an actual upset condition. In case an actual upset is encountered, pilots should of course be able to take manual control of the aircraft to resolve the upset condition in a safely manner, without damaging the aircraft [42].

For stall upsets, the aircraft is however partly flying outside the aerodynamic flight envelope with which the simulator is equipped. In order to allow pilots to actually benefit from simulator stall training and improving their manual flying skills restoring from upset conditions, accurate extended flight envelopes have to be developed. The fidelity of current aerodynamic flight envelopes for stall is too low to provide positive transfer of training [5]. If the fidelity of the simulation is too low for accurate and realistic training, a suggestion would be to change the color of the visual outside view, to warn pilots that the simulation will differ from real life behaviour of the aircraft. This makes pilots aware that they cannot fully rely on their simulator experience if they encounter a similar situation in actual flight. It thus avoids giving pilots a false sense of security. If pilots are not aware of the limited fidelity, negative transfer of training occurs, which can actually lead to accidents rather than preventing them [23]. The ideal case however still remains having high fidelity simulators to train with.

Simulators can provide all sorts of cues helping pilots recognise an upset condition. Those cues can come from the visual system, including instrumentation, motion or sound (stall warning for example). A good mathematical model of the aircraft is required to be able to provide these cues accurately. Some notes must be made with respect to motion cueing. Upsets usually involve unusual attitude of the aircraft, including high pitch and roll attitudes. Motion systems such as hexapods are however limited in their motion and cannot always provide motion cues that large for upset recovery training. Rather, incorrect or insufficient motion cueing can lead to a negative transfer of training, possibly causing accidents rather than mitigating them due to the introduction of false information. Contradicting statements about motion cueing relevance are found in literature. Some claim that motion cueing does not necessarily add to a positive transfer of training [63] [23], whilst others claim the opposite [49]. If motion could be left out, it would be beneficial for stall training, as less complex simulators could be used for this purpose, making this training more accessible.

Another important consideration in stall mitigation in flight simulators is icing. Icing of the aircraft wings changes it aerodynamic shape and can cause abrupt stalls at angles of attack much lower than those for clean wings. If an aircraft is equipped with a stall warning system based on angle of attack, those will not go off, while pilots might consider this as the most important cue for stalling. It is therefore very important that pilots learn to recognise other aircraft specific cues such as roll off as well. Simulator training should therefor include these scenarios as well, as well as degraded flight controls [57][23].

ICATEE published a list of stall characteristics that should be present in extended aerodynamic stall models for simulator training [82]. This covers the high AoA effects described in subsection 1.2.2 and subsection 1.2.2 with some additional requirements.

- Degradation of lateral-directional stability, both in static as dynamic stall
- Degraded control effectiveness for all aircraft axes
- Uncommanded roll-off, requiring significant control deflection to counteract
- Randomness and non-repeatably
- Changing pitch stability
- Effects of Mach number

- Effects of buffeting

The manoeuvres that should be included in the qualification procedure of the FSTD are listed below [82].

- Wings level stall
- Turning stall with an angle of bank (AoB) of at least 25°
- Power-on stall
- Stall at cruise altitude
- Demonstration of at least two flap settings during stall

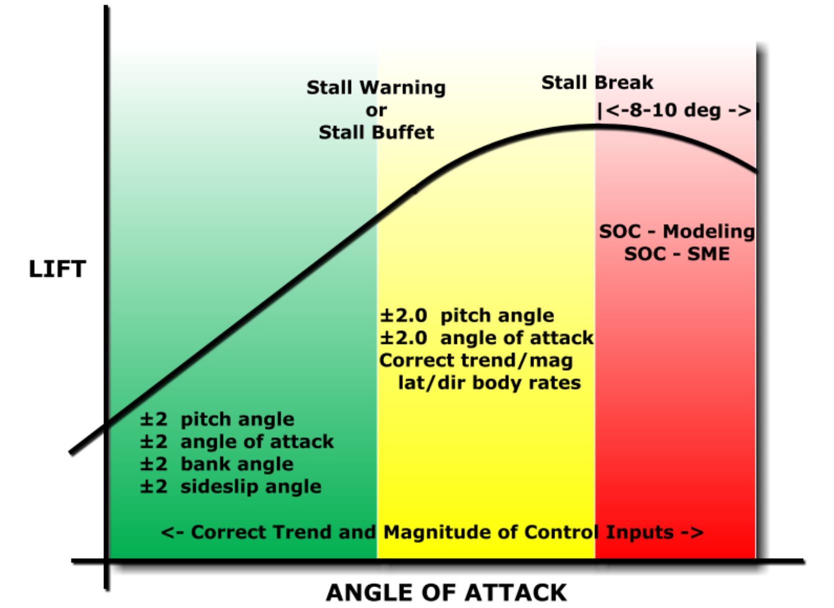

Figure 1.2: ICATEE variable fidelity requirements for proof of match of FSTD [82]

As stall incidents most often occur in the approach and landing phases, as well as take-off and initial climb, special attention should be paid to these conditions in pilot training[36] [8]. It is therefore also important to model stall behaviour in take-off and landing configuration. The CG location also has an influence on the stall behaviour. Aft CG often leads to lateral departures, pitch-up manoeuvres exceeding the nose down authority of the horizontal tail, etc. Forward CG puts the tail at high down force creating angles to keep the nose up, increasing the risk of tail plane stall, especially with full flaps [12].

Another important consideration is the surprise or startle factor [5]. Training results into rote-memorising of skills, learning through the act of repetition. If a similar situation occurs as the one that has been trained, pilots exhibit correct responses in the recovery of the familiar upset. If an unexpected event occurs, pilots seem to forget what they learned or cannot apply it to the new situation, although the response should be the same [17]. Including surprise factors in the training will help pilots apply the correct recovery techniques in all circumstances, not only in those they recognise from training. Simulation of icing conditions is a good example of how this surprise factor can be incorporated. No stall warnings will go off, as the stall happens at a lower AoA than expected. Not all expected stall cues will thus be present, even though the aircraft is in fact stalling.

1.3. Early Stall Modeling Efforts

This chapter gives a historical perspective on the evolution of stall modeling in the history of aviation. The early methods were used for fighter design and are elaborated upon insubsection 1.3.1. The application of these methods on commercial aviation is found in subsection 1.3.2, followed by a comparison of data sources for modeling in subsection 1.3.3.

1.3.1. Research: Fighter Methods

Research into high angle of attack aerodynamics and the corresponding phenomena such as stall and spin, has started already in the early days of aviation in the beginning of the 20th century. Little was known about these complex, nonlinear aerodynamic motions. The fundamental research was however halted during the second world war. The war took most resources and the emphasis was on creating new designs to beat the enemy, rather than on fundamental research. It was only during the sixties that interest in this research field took a leap again [18]. The Vietnam war showed to need for highly manoeuvrable aircraft, including in the stall flight regime [13]. Most research during the following decades focused on military fighter jets. The modeling methods developed are therefor referred to as fighter methods.

The main reasons for the research and development for fighter methods is from a design point of view. Engineers benefit from predicting control and stability behaviour in all flight regimes in early design phases [13], as well as preventing unwanted high angle of attack phenomena such as wing rock, nose slice, etc. by making adjustment to the aircraft design. Therefore, safety can be improved [20] [22].

The fighter methods in the 60s and 70s mainly rely on data gathered during various kinds of wind tunnel experiments on scale models of the aircraft under consideration. The experiments serve to determine the control and stability derivatives as input values for the selected aerodynamic model structure. The experiments also allow identification of the aerodynamic phenomena near and in the stall flight regime[50] [21]. From the 90s onward, parameter estimation based on flight data entered the research field [59] [13], wind tunnel experiments remained to major source of stall data and was used in comparison with flight data models [58] [35]. A final applied method in this research field for fighter aircraft is piloted simulation. Existing models are flown by pilots to include their input in flying combat maneuvers and reflect upon the results of the actual flight tests [68][21] [13]. Fighter methods focus on the avoidance of unwanted behaviour in the stall flight regime through design and not so much on the creation of an accurate stall model for simulation purposes. Furthermore, the fact that they rely strongly on wind tunnel data, makes this methodology rather expensive and subjected to scaling effects, as is further elaborated upon in 1.3.3.

1.3.2. Research: Commercial Aviation

Recently, the developed fighter methods have also been applied to commercial aircraft to enhance safety [4]. Wind tunnel test data in combination with Computational Fluid Dynamics (CFD) generated data are used to create aerodynamic models of commercial aircraft in the stall flight regime to build simulations for pilot training. The Simulation of Upset Recovery in Aviation (SUPRA) project, based on recommendations of the ICATEE, is an example of this [49]. The SUPRA aerodynamic model combines data from different wind tunnel set-ups and CFD towards a model extending the normal flight envelope.

1.3.3. Overview of High AoA Modeling Data Sources

As discussed in subsection 1.3.1 and subsection 1.3.2, many different methods to gather data for modeling are out there. Three major groups can be considered: wind tunnel experiments, CFD simulations and flight tests. Each data gathering method has its advantages and disadvantages and will be discussed here.

Wind Tunnel
Wind tunnels allow data gathering for extremely large AoA and angle of sideslip (AoS) ranges [35]. They also allow the investigation of individual contributions of aircraft parts, as well as static and dynamic motions. This however requires many different test set-ups, often requiring a range of different wind tunnels to complete the large test matrix to have a comprehensive data picture. Wind tunnel testing also requires downscaling, which causes Reynolds and Mach number discrepancies. This affects the results and corrections need to be applied. The scaling issues form an important limitation for this data gathering method. Wind tunnel testing is on top of that an expensive option [82].

CFD
Using the advanced CFD methods to solve the Navier-Stokes equation could result into models with high predictive capability. It is a promising method, but current application methods and computational power capabilities simply aren't there yet [82]. Simpler semi-analytical CFD methods can be solved now, but lack predictive power and cannot create full stall models. For accurate stall models, CFD methods can only be used to polish the models based on wind tunnel and flight testing techniques, rather than creating them from scratch [90]. The strength of CFD is its endless experimental possibilities. Any manoeuvre can be flown, all

Reynolds number, Mach number, AoA ranges etc. can be investigated once the right methods and sufficient computational power are available [44]. As this is not the case at time of this research, CFD methods are not considered for this research.

Flight Test
Flight test data is gathered using the actual aircraft. There are no down-scaling issues with Reynolds number and it is in fact cheaper than wind tunnel experiments. There are however human lives at stake, limiting the range of AoA and AoS that can be investigated due to unacceptable risks [74]. This is especially the case for commercial aircraft, less for fighters. Working with (down-scaled) unmanned vehicles can be a solution, jet you still do not want to crash your test vehicle. For down-scaled vehicles, the same scaling issues arise as for wind tunnel testing. Flight testing requires lots of data to create accurate and complete models and must therefore be handled with care [45].

Aerodynamic Stall Model
Creating an accurate aerodynamic model with high predictive power, requires the complementary use of the methods described above. Accurate flight test data in the pre-stall to stall regime can be complemented with wind tunnel data in the post-stall regime, whilst the entire model can be polished with CFD results. CFD and wind tunnel data can also make generic models type specific, as is proposed in [90]. This poses challenges in how all this data can correctly be blended to create the best possible stall model for pilot stall training. Other fields of research can also benefit from these modeling techniques.

1.4. Stall Model Identification

This chapter discusses the idea behind flight path reconstruction to correct for process and measurement noise in flight test data is introduced, subsection 1.4.1, followed by a discussion on proper flight test manoeuvres to aid in this flight path reconstruction and model identification, see subsection 1.4.2. Different aerodynamic model structures for identification from flight test data are discussed in subsection 1.4.3. This section includes Kirchhoff's theory of flow separation, a new methodology of including the nonlinearities of flow separtion and stall in aircraft models, 1.4.3.The chapter ends with the research gap of lateral stall models and the corresponding research objective and questions for this thesis research, in section 1.5 and subsection 1.5.1.

1.4.1. Flight Path Reconstruction

Flight test data is both subjected to process and measurement noise. For accurate model identification, both sources of noise should be addressed. Parameter estimation techniques used for identification can usually only handle one of the two sources. Equation-error methods are based on the assumption that no measurement noise is present, whilst output error methods assume the absence of process noise [47].

Mulder et al. elaborates on the successful technique of decomposition of the problem in a nonlinear state estimation routine, followed by a linear parameter estimation of the identification model. This is the so-called two-step method. The first step, nonlinear state estimation/reconstruction is called flight path reconstruction (FPR). Many FPRs methods exist, each one with their own advantages and disadvantages and areas of application. For the purpose of aircraft model identification from flight data, Kalman filters and maximum likelihood methods are the most popular. Kalman filtering and smoothing can deal with both measurement and process noise and exhibits improvement by smoothing in reverse direction as well, which is only possible if the application is not in real-time.

Successful FPR depends on the tests that have been performed. For nonsteady test data of a dynamic object such as an aircraft, sufficient excitation signals must be fed to the aircraft [73]. The importance is further discussed in subsection 1.4.2. FPR has been used and advised in many recent stall identification research based on flight test data [93][32][30][47][71].

1.4.2. Flight Test Manoeuvres

Good design of flight tests and the manoeuvres to be flown is essential for obtaining accurate stall models. Safety and financial considerations limit the amount of flight conditions to be flown as well as their location within the aircraft's flight envelope. It is therefore important to determine the best way to spend the available flight hours, whilst not taking unnecessary risks. Furthermore, the manoeuvres should be performed in a way to obtain high quality data to create high fidelity models.

A key element for aircraft identification through flight tests is proper excitation of all aircraft axes. This aids in proper reconstruction of the measured aircraft states [70]. Dias recognises the importance of proper excitation. He suggests performing doublets before stall entry on both the elevator and ailerons. The oscillations of this action should be completely disappeared before the actual stall has commenced. The excitation helps in FPR but does not influence the gathered stall data. Many simulator requirements talk about a stall speed reduction of 1 kts. Dias argues that this is in fact too steady for proper FPR. This can be overcome by taking the entire stall manoeuvre into account for stall identification.

Morelli et al. suggest both excitation in and outside the stall flight regime, with input on all axis at the same time in a non-correlated fashion with varying frequency. In addition, non-excited stalls are added to the data to capture clean stall behaviour. Van Ingen recommends the use of doublets or 3-2-1-1 manoeuvres before and during stall for dynamic stall identification as well as control effectiveness degradation. Excitation during the stall manoeuvre makes the stall dynamic, making the identified model less suitable for quasi-steady stall estimation [32].

Moszczynski et al. has investigated the use of the Gramian matrix to assess observability of different flight test manoeuvres. This observability metric has been well proven in different research fields, but is new in FPR. It provides insight in the information content contained in the dynamics of the manoeuvre flown. Good information content allows FPR with high fidelity. Moszczynski et al. showed that turning stalls have higher information content than straight, dynamic or accelerated stalls. Combining information of different stall manoeuvres creates an information content close the that of the wind box manoeuvre, a manoeuvre known to contain lots of information and ideal for sensor calibration.

1.4.3. Stall Identification Models based on Flight Test Data

The use of Kirchhoff's theory for modeling stall behaviour based on flight test data is widely spread in state-of-the-art research. It is a simple way of presenting the nonlinear behaviour of flow separation in a comprehensive way. Variations in aerodynamic model structure and parameter estimation techniques are however found in the approaches of the different research institutions working on this topic.

Kirchhoff's Theory

In 1992, Goman and Khrabrov introduced a new approach to stall modeling based on Kirchhoff's zone of constant pressure and linear cavitation theory assumptions. They used a state-space approach instead of the common Taylor series expansion approach for aerodynamic aircraft modeling. The state-space contains an internal variable, the X, that represents the point of flow separation on the wing. X has a value between 0 (fully detached flow) and 1 (fully attached flow) [46]. This method has been further developed for aerodynamic model identification based on flight test data and resulted into an expression to estimate the lift coefficient C_L based on the chordwise location of flow separation, Equation 1.1. This location is determined using the ODE given by Equation 1.2. This has been referred to as Kirchhoff's theory of flow separation [87]. Due to the made assumptions, this theory is only applicable to trailing edge flow separation.

$$C_L = C_{L_\alpha}\left(\frac{1+\sqrt{X}}{2}\right)^2 \alpha \tag{1.1}$$

$$\tau_1 \frac{dX}{dt} + X = \frac{1}{2}\left(1 - \tanh\left[a_1(\alpha - \tau_2\dot{\alpha} - \alpha^*)\right]\right) \tag{1.2}$$

The ODE consists out of 4 parameters that need to be identified. τ_1 represents the time delay due to flow inertia, τ_2 models the effects of hysteresis, a_1 determines the abruptness of the stall and α^* sets the stall AoA. The effect of varying the last two parameters is visualised in Figure 1.3. Kirchhoff's theory has been used in fight test data identification [93][32][43] as well as CFD semi-emperical methods [77][64] and its capability to model the nonlinear dynamics of stall has been validated in many scientific papers.

Equation 1.2 is the expression to find the flow separation point based on data from flight tests. It can model unsteady flow separation and stalls. In case of steady stall, the rate of change of AoA, $\dot{\alpha}$, equals zero. Both

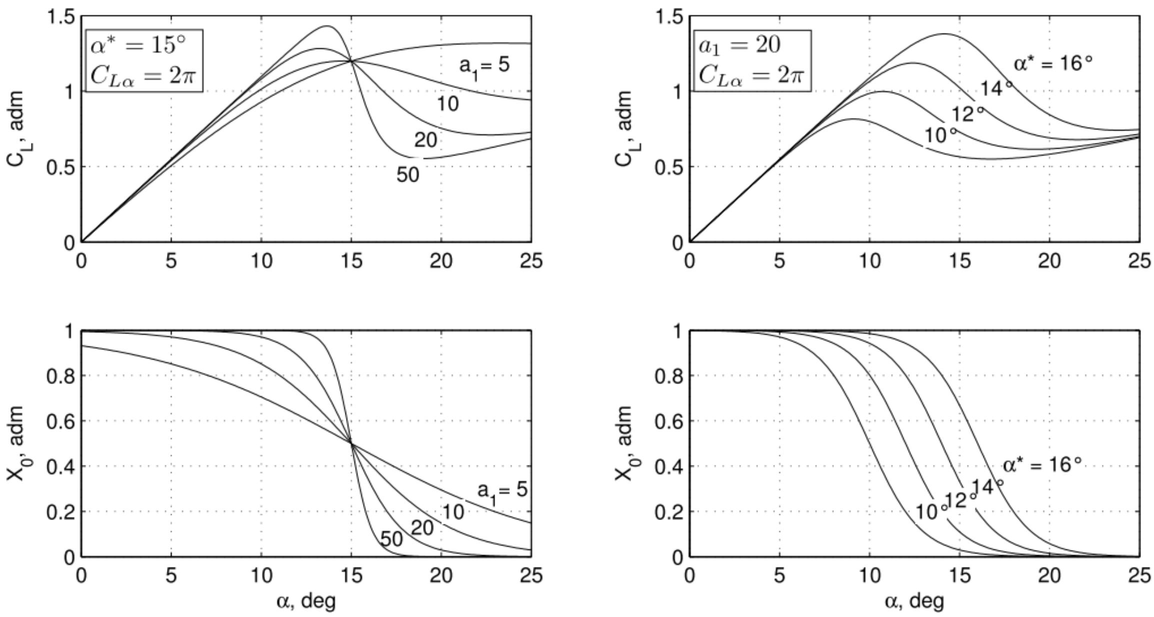

(a) Effect of parameter a_1.

(b) Effect of parameter α^*.

Figure 1.3: Influence of varying a_1 and α^* in the Kirchhoff ODE on the lift curve slope and internal separation variable X [32] [43]

time related parameters, τ_1 and τ_2 drop out of the equation. This also implies that the identification of those two parameters can only be done using dynamic stall manoeuvres [43]. Identifying a single stall model for both quasi-steady and dynamic stall is therefore difficult [87].

Smets et al. investigated the influence of the 4 parameters of Kirchhoff's ODE on stall perception by pilots in a simulator. The stall model developed by Van Ingen was tested in the Simona research simulator of TU Delft using a staircase data approach. Only symmetric degree of freedom (DoF) were taken into account. As τ_2 has little effect on the model output and α^* is easy to determine as it is not a dynamic parameter, only τ_1 and a_1 were considered in the experiment. Smets et al. concluded that emphasis should be put on the determination of a_1. The experiment took only a few factors into account, further investigation including an improved buffet model, asymmetric stall, work load for the pilots, different stall models, etc. should be performed to make stronger statements about this result.

Global Model Structures

The basic idea for aerodynamic model structures is to represent aircraft behaviour in 6 DoF using 6 non-dimensional coefficients for the 3 forces and 3 moments models (C_L,C_D,C_Y,C_l,C_m,C_n). This is a common approach in aerodynamic modeling. The 6 equations are constituted of stability and control derivatives multiplied with common aircraft states such as velocities, flow angles and angular accelerations. If limited to linear aircraft estimation, only first order terms of the aircraft states are present. For global aerodynamic models, the values of the identified derivatives remain constant throughout a large range of aircraft states values.

Van Ingen and Dias use this idea to identify the components constituting each coefficient. As the stall flight regime can no longer be assumed linear, modifications to the common structure of aerodynamic equations have to be performed. Aircraft states can be present in higher order versions, as well as cross-coupled. Furthermore, the Kirchhoff term X will pop-up to capture the non-linearities accompanying flow separation in stall. An example including Kirchhoff is given by Equation 1.3, Equation 1.4 and Equation 1.5, which is the model structure for a 3 DoF longitudinal model by Dias. Both models lack estimation of lateral behaviour and loss of control effectiveness, but exhibit clear information about data gathering, pre-processing and model identification as well as thorough validation.

$$C_L = C_{L0} + C_{L\alpha}\left(\frac{1+\sqrt{X}}{2}\right)^2 \alpha + C_{L\dot{\alpha}}\frac{\dot{\alpha}\bar{c}}{2V_0} + C_{Lq}\frac{q\bar{c}}{2V_0} + C_{L\delta_e}\delta_e \tag{1.3}$$

$$C_D = C_{D0} + \frac{1}{e\pi\Lambda}C_L^2 + \frac{\partial C_D}{\partial X}(1-X) \tag{1.4}$$

$$C_m = C_{m0} + C_{m\alpha}\alpha + C_{m\dot{\alpha}}\frac{\dot{\alpha}\bar{c}}{2V_0} + C_{mq}\frac{q\bar{c}}{2V_0} + C_{m\delta_e}\delta_e + \frac{\partial C_m}{\partial X}(1-X) \tag{1.5}$$

Model structures can be selected based on literature and common sense. Morelli et al. suggest the use of multivariate orthogonal function to create the model structure. This structure is suited for nonlinear modeling, whilst providing a comprehensive physical meaning. Yet it is complex enough to accurately describe functional dependencies within the model. Working with mutually orthogonal functions rather than polynomials, allows evaluation of the contribution of each individual function to the model fit with the data sets.

This approach has been used by Van Ingen to select a model structure from a pool of candidate regressor terms. The terms were first orthogonalised to decouple the problem and investigate which terms improved the quality of fit of the aerodynamic model. As higher order terms can capture the variations of a specific data set, tailoring the model to that specific set only, these terms are penalised in the selection procedure to avoid over-fit.

Data Partitioning
Global models can lead to compromises as fitting non-linearities affects the entire data range [34]. Adding spline terms allows tailoring the model in the regions where increased model fit is required. Global models often require complex model structures, which can result into problems to identify all parameters, especially if no data with a high information content is available.

Data partitioning will divide the data range domain into several smaller parts. Each subdomain will have its own estimated parameter values. The main advantage is that more simple model structures can be used, solving the identifiability issue. Grant et al. opted for this method as the usability of certification data is investigated. This data has not been specifically gathered for identification purposes and thus lacks excitation. The idea behind this paper is interesting as stall models could be build using data available for every type of aircraft from certification. However, many of the proposed methods to increase the fidelity of the resulting model have not been incorporated in the actual model due to time constraints. Data partitioning also poses some issues. Sufficient data in each intervals must be present whilst the intervals must be small enough to eliminate dependencies on the parameter upon which the division is made [47].

Δ add-on modeling
The Δ add-on modeling method has many interesting (possible) applications. The method allows extending or adjusting existing aerodynamic models. The original parameter coefficients are linearly adjusted by simple addition of the Δ terms. There's no need to develop the new model from scratch. The methodology is visualised in Figure 1.4 and its general mathematical expression is given by Equation 1.6 [26].

Deiler et al. apply this methodology to add the effects of icing to a pre-identified aircraft model for the longitudinal DoF [28]. The added model for icing is based on altered parameter of Kirchhoff's theory (α^* and a_1). Aircraft with similar degradation due to icing could benefit from this add-on model as it could simply be added to those aircraft models as well. This has however not been tested nor validated. Teng et al. use this methodology to create representative aircraft models from a single baseline model. The Δ terms serve to add the effects of specific aircraft configuration changes compared to the baseline model. An accurate baseline model could like this be easily and cost-effectively extended to several representative models for pilot stall training.

$$C_{(\cdot)}(P) = C_{(\cdot)}(P_{base} + \Delta P_{add-on}) = \left(C_{(\cdot)}\left(P_{base}\right)\right)_{base} + \Delta\left(C_{(\cdot)}\left(P_{base+\Delta P_{add-on}}\right)\right)_{add-on} \tag{1.6}$$

The Δ add-on terms can be generated from wind tunnel testing, flight testing or CFD, which makes it an interdisciplinary tool that can contribute to combining the best of all worlds into a single model. It can help

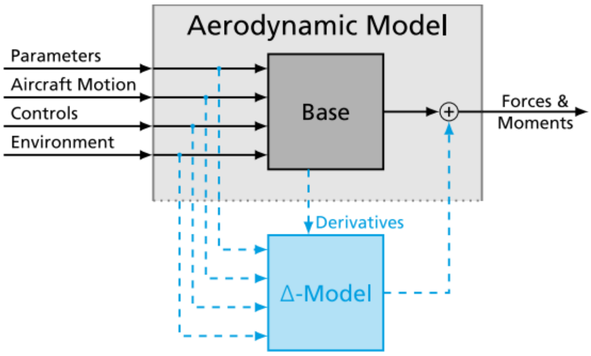

Figure 1.4: The Δ add-on modeling principle [26]

improving existing simulation models, without altering the original and underlying aerodynamic data. It can just be incorporated as an additional module in the simulation. Other applications can include the effects of damaged aircraft, reduced control effectiveness, etc. As generating a complete aircraft model based on flight test can require quite some flight hours, it must also be investigated if generic model can be sufficient for pilot stall training [45][56]. The Δ add-on principle can then also be used to make these generic models type-specific if necessary.

Two-point model
The basic models based on Kirchhoff model stall of the entire aircraft. Another approach, still using Kirchhoff, is to model both the wing-body contribution and the horizontal tail separately. The AoA of the horizontal tail is in function of the downwash from the main wing. It is proposed by Dias to deal with the identifiability issues for $\dot{\alpha}$ and pitch rate q. Both parameters are correlated, often leading to neglecting one of them although both have an important influence on the stall behaviour of aircraft. Proper excitation of the longitudinal axis is one way to improve, the two-point model is suggested to be another one. This modeling methodology is also used by Deiler to deal with the nonlinearities in downwash and flow transit time between the main wing and the horizontal tail.

Neural Networks
Neural networks can also be used as a model structure. These structures do not use any of the a priori information about the system, even if it is available. Saderla et al. use this approach and claim equivalent behaviour to a classic maximum likelihood estimation technique. They recognise the need for additional data for a more complete validation with regards to consistency. The paper exhibits low quality validation graphs. As more data is in fact required to validate consistency of the neural network method, it might not be suited for this stall modeling application, as focus is put on cost-efficient generation of high fidelity models.

Parameter Estimation
To perform the actual parameter estimation step with the carefully gathered and reconstructed flight measurements, a model structure must be selected, followed by the parameter estimation. A cost function is to be minimised by changing the parameter values. Many different structures and estimation techniques exist. Kirchhoff introduces nonlinearity in the model, requiring nonlinear estimation techniques. These techniques are complicated and challenging. For linear model structures, many efficient estimation methods are available. Van Ingen only uses a gradient based nonlinear estimation methods to solve Kirchhoff's ODE and once those parameters are known, linear estimation of all other aerodynamic parameters take place to estimate the entire model.

1.5. Lateral Stall Modeling

Identification of lateral stall models remains a rather unexplored area of the research field. In the works of Goman and Khrabrov, Fischenberg and Jategaonkar, Singh and Jategaonkar, lateral models based on Kirchhoff's theory are proposed. The models assume a different separation point on the left and right wing due to sideslip. This leads to a normal force difference resulting in rolling and yawing moments. The moments due to differential lift are added to the dimensionless roll and yaw moment coefficient through the moment arm between the mean aerodynamic chord (MAC) and the CG. These works are however outdated ('90s), lack information about how the data was gathered and pre-processed, how identification was done and have limited validation. These works introduce interesting ideas and methodologies, but are rather vague in supporting their claims. New research into to the possibilities of this reasoning and adapting the current models with more recent findings should be done in order to further explore this methodology for lateral modelling whilst providing improved and more transparent validation.

Suggestions have been made to increase the accuracy of lateral-directional stall models. The derivatives based on rate of change in sideslip ($\dot{\beta}$) are negligible in the nominal AoA range, but become important near stall [75][22]. Furthermore, cross and cross-coupling derivatives also have an increased influence in the higher AoA range and their importance should therefore also be investigated [87].

Deiler and Kilian uses the Δ add-on principle to include degradation due to icing on existing models. The approach includes asymmetric modeling due to asymmetric degradation on both wings. It also includes the use of segment-wise estimation of all relevant parameters, including Kirchhoff, using the division of the wing into 20 segments. This approach is only used for icing effects, but shows potential to improve the current use of Kirchhoff in which a single separation point is used for the entire aircraft. Asymmetric modeling requires at least two separation points.

1.5.1. Research Objective and Questions

Based on the performed literature review, research towards to development of a high fidelity lateral model will be performed. It is clear that many work is yet to be done in this part of the research field to create high fidelity stall models for pilot simulator training, minimising the number of LOC-I accidents.

The research objective is therefore formulated as follows: Identify, verify and validate a lateral-directional stall model for the Fokker 100 by using flight test data and Kirchhoff's theory of flow separation.

Several sub-goals are also formulated:

- Investigate possible ways to obtain differential flow angle estimates on at least two wing sections by using the available measurements of aircraft states.
- Extend the use of Kirchhoff to identify an asymmetric stall model by using multiple Kirchhoff separation points.
- Evaluate the usefulness of different flight test manoeuvres for asymmetric stall identification by assessing their information content using available metrics.
- Select a suitable model structure for asymmetric stall modeling for the available stall data by extending state-of-the-art model structures towards lateral-directional stall.
- Validate the generalisation of the developed asymmetric stall model by applying it to stall data of the Cessna Citation II.

The main research question is stated as follows: How can Kirchhoff be used to create a high fidelity lateral-directional stall model based on flight test data?

- Which available aircraft states measurements can contribute to the reconstruction of the flow angles at the different span-wise wing locations?
- Which flight test manoeuvres are especially suitable for proper asymmetric stall identification?
- Which model structure can incorporated lateral-directional characteristics of asymmetric stalls?
- Can the developed model by generalised for other aircraft such as the Cessna Citation II?

1.5.2. Methodology

Theoretical Content/Methodology
Kirchhoff's theory of flow separation will be used as central methodology within this research, see Equation 1.1 and Equation 1.2. The identification methodology of van Ingen [93] will be further developed to create a lateral-directional stall model structure using multivariate orthogonal functions. The parameter estimation will be done using a Matlab build-in non-linear solver for the ODE and an efficient OLS linear solver for the remainder of the parameters.

The novelty in this research will be the extension of the available methodologies towards an asymmetric stall model. The Fokker 100 test aircraft was equipped with two angle of attack vanes. This data will be exploited to help reconstruct differential lift on both wings using Kirchhoff.

Results, Outcome and Relevance
The available data from flight test measurements consists out of GPS data for position determination, including the rate of change of location. Furthermore, air flow angle data on angle of attack and sideslip will be used. Inertial measurements and accelerometers will provide the aircraft's Euler angles, accelerations and roll, yaw and pitch rates. Finally, airspeed measurements are also present. This data will be used to identify an aerodynamic model in terms of 6 dimensionless force and moment equations. An example of such an equation for the lift coefficient can be found in Equation 1.7[32]. The parameters are the coefficients $C_{\cdot}$.

$$C_L = C_{L0} + C_{L\alpha}\left(\frac{1+\sqrt{X}}{2}\right)^2 \alpha + C_{L\dot{\alpha}}\frac{\dot{\alpha}\bar{c}}{2V_0} + C_{Lq}\frac{q\bar{c}}{2V_0} + C_{L\delta_e}\delta_e \tag{1.7}$$

Identification of the parameters will lead to a stall model. Focus will be put on the asymmetric force and moments coefficients, namely C_Y, C_m and C_n. Verification of the basic scripts for Kalman filtering will be done as follows. Metrics are available to assess the convergence of Kalman filters such as innovation, covariance matrix, etc. These will be assessed. Furthermore, the basic coding verification procedures will be applied (debugging, unit and system tests). Adaptions of an already existing and verified Kalman filter will be done. These adaptions should not lead to significantly different results, unless clear and thorough explanations are available. Comparison towards the verified Kalman filter is seen as verification.

Not all data of the Fokker 100 will be used for identification. Some of it will be kept asides to perform the validation of the identified model. The validation can consider model-error based and statistical approaches such as auto-correlation of the resulting variables, (co)variance plots of the estimated parameter showing areas with lacking information content or the correlation between the different parameters.

The resulting model will give answers about the theoretical level of fidelity that can be reached using the applied methodology. Further research will however be necessary in which the model is actually tested in a simulator and evaluated by pilots, but this is outside the scope of this thesis and is in fact a thesis subject on its own. It will contribute to the knowledge about stall modeling and aid towards the creation of many high fidelity stall models used to train pilots. In the future, these models should help in the avoidance of LOC-I incidents and accidents and hopefully save human lives.

2

Flight Test Data

The Fokker 100 (F-28 MK-0100) is a regional twin jet aircraft. From 1986 till 1989, Fokker performed a series of flights test including numerous stalls in different configurations. These served to evaluate the stall characteristics and stall speed. The data of these test flights will be used for the research into asymmetric stall behaviour. The selection of useful stalls was based on the reporting of asymmetries such as wing drops in the test cards accompanying the data as well as the presence of sufficient data to run the mass model and Kalman filter. The aircraft used for most stalls is the prototype aircraft.

Dimensions	
Wing Area	93.5 [m^2]
Wing Span	27.1 [m]
MAC	3.83 [m]

Table 2.1: Dimensions of the Fokker 100 prototype aircraft.

2.1. Stall Test Data of the Fokker 100

The stall tests have been performed within the framework of certification of the aircraft as well as to generate supplementary aerodynamic data for simulation of aircraft behaviour. The supplementary data was used to improve and complement data gathered in wind tunnel experiments. Due to the certification nature of the flight test data, the data lacks excitation of the control surfaces. Sufficient excitation is necessary for proper stall model identification [70, 73]. This data is however not available for the Fokker 100 aircraft. It therefore remains uncertain if a high fidelity stall model can be derived from the data.

In order to still be able to identify a lateral stall model, only stalls were selected where the flight test card explicitly mentioned a wing drop or noticeable angle of bank caused by the stall. About 200 stalls were selected based on this criterion. During the pre-processing phase, all stalls that had insufficient data to run the mass model or Kalman filter got dropped. 79 stalls remained available. These stalls cover a range of configurations. An overview is given by Table 2.2.

Configuration	Stalls
Clean Configuration	24
6° Flaps	2
18° Flaps	23
25° Flaps and Gear Down	2
Landing Configuration	22

Table 2.2: Number of selected stalls for each configuration

2.2. Mass Model

To create a high fidelity aircraft model, accurate data is required. The more accurate the data is, the better the aircraft model will become. This holds for all measured variables, but also for the mass and balance and inertial data of the aircraft at the moment of stall. The Fokker database does contains some information regarding these properties, but insufficient to calculate the CG and inertial tensor accurately. No existing algorithms or models have been found for this purpose. Luteijn therefore created an accurate mass model for the prototype aircraft of the Fokker 100. Most stall test available in the extensive database have been performed using this specific prototype aircraft. The mass model has only been validated for the prototype. Only stalls performed using this aircraft are therefore used for this research.

The mass model has three major contributors: the Operating Empty Weight (OEW), fuel and water ballast. The OEW is build up from all structural elements (engines, fuselage, empennage, undercarriage,etc.), the flight instrumentation, all wiring, unusable fuel and oil, cabin items, crew and crew related items, etc. The mass model is build up by discretising separate aircraft elements as points masses (see Figure 2.1) and determine their relative CG location within a fixed reference frame. The overall CG can be calculated within this frame and becomes the origin of the conventional body reference frame. The relative location of each element can now be expressed in terms of the body reference frame to determine the inertial data. Figure 2.2 gives a schematic overview of the different steps undertaken by the mass model to calculate the required data.

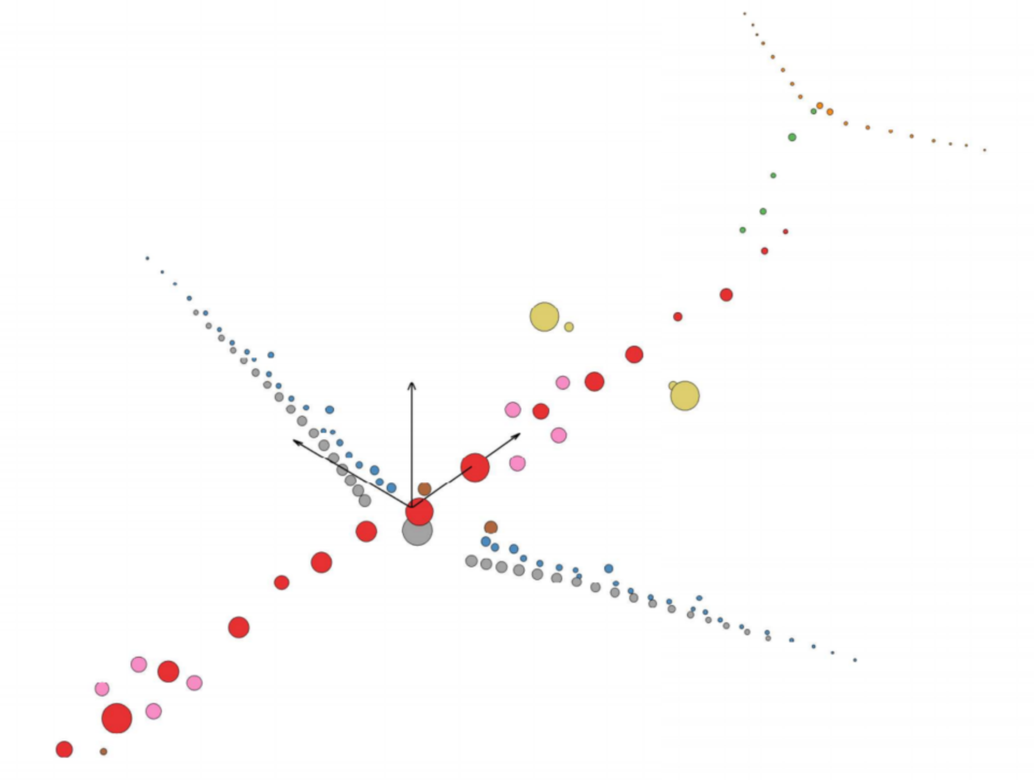

Figure 2.1: Overview of the discretised mass distribution of the Fokker 100 prototype aircraft by Luteijn[65]. The pink dots represent the filled water ballast tanks, the grey dots filled fuel tanks.

Detailed information is available for all aircraft elements. Their location is given with respect to an origin for the aircraft section to which the element belongs. To calculate the overall CG, the mass model algorithm starts by determining the local CG data of each section including all elements.The mass and arm of each element within the local reference frame, are multiplied and summed together. Next, this term gets divided by the total mass of all elements of the specific section (Equation 2.1, N being the total number of elements for the section). The result is the CG location of each section. The arm to the sectional CG within the fixed vehicle-nose reference frame is determined. The datum point of the vehicle-nose reference frame is located at the

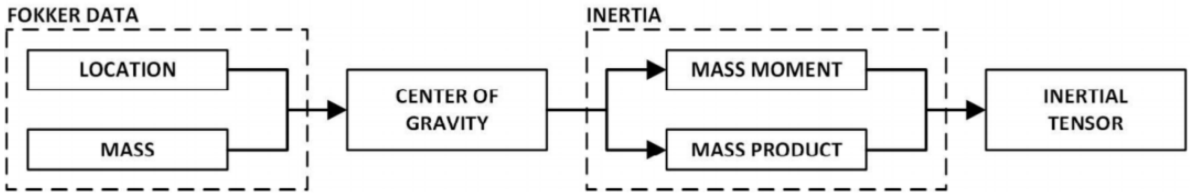

Figure 2.2: Different steps taken by the mass model to calculate the CG and inertial tensor, figure by Luteijn[65]

front of the aircraft, Table B.1 in Appendix B. The same procedure is applied to find the overall CG within the vehicle-nose reference frame. The mass of each section is multiplied with the corresponding arm from the origin of the vehicle-nose reference frame to the sectional CG and summed for all sections. This sum is then divided by the sum of all sectional masses. The overall CG is now determined.

$$\bar{r}_{cg} = \frac{\sum_{i=1}^{N} \bar{r}_i m_i}{\sum_{i=1}^{N} m_i} \quad , \quad \bar{r} = \begin{bmatrix} x \\ y \\ z \end{bmatrix} \tag{2.1}$$

With the CG defined, the inertial terms of the Fokker 100 aircraft can be computed. Their value depends on the CG location and the mass division of the aircraft at the moment of stall. Each aircraft element has its own inertial moments (six in total per element). The inertial values per (cross-)axis must be summed for all elements. Besides the sum of inertial moments, the parallel axis theorem is applied. This theorem quantifies inertia due to the presence of a mass element located at a certain distance away from the aircraft's CG. The arms from the center of the element to the aircraft's CG are computed in order to calculate the value for the parallel axis theorem. This is done for all elements and for each (cross-)axis. An example of inertial moment calculation around the x-axis is given by Equation 2.2. Note that the same procedure applies as for the CG. First, the total inertial moments per section are calculated. Then the sections are combined to yield the overall inertial moments. The inertial tensor can be created from these six inertial moments, see Equation 2.3.

$$I_{xx}^{b} = \sum_{i=1}^{N} I_{xx}^{i} + \sum_{i=1}^{N} m_i \cdot \left(y_i^2 + z_i^2\right) \tag{2.2}$$

$$I_{cg}^{b} = \begin{bmatrix} I_{xx}^{b} & -I_{xy}^{b} & -I_{xz}^{b} \\ -I_{yx}^{b} & I_{yy}^{b} & -I_{yz}^{b} \\ -I_{zx}^{b} & -I_{zy}^{b} & I_{zz}^{b} \end{bmatrix} \tag{2.3}$$

The weight distribution for the main components have been listed in Table 2.3. Figure 2.3 shows the division of the three major mass components as part of the total aircraft mass in case of fully filled water ballast and fuel tanks.

2.2.1. Fuel Tanks

The fuel tanks can contribute to almost $\frac{1}{4}$ of the total aircraft weight. During flight, fuel is consumed making the fuel tanks a dynamic component of the aircraft mass and balance. The inertial values are also dynamically influenced by the fuel burn. Accurately modeling the dynamic fuel weights, moment arms and inertial tensors has received special attention in the creation of the mass model for the Fokker 100 [65].

The fuel distribution system consists out of three major fuel tanks: two main wing tanks, one in each aircraft wing and a center tank in the fuselage. All three tanks are bottom-draining. Each main wing tanks is further divided into 17 smaller sub-tanks, divided by the wing's rib-stations. The two sub-tanks located closest to the fuselage are the so-called collector tanks. All fuel will first pass by the collector tanks before proceeding the the aircraft engines.The collector tanks are therefore always fully filled as long as there is still fuel left in the remaining wing sub-tanks and the center wing tank. The center tank is always the first tank that gets

Section	Mass [kg]
Fuselage	16954.8
Wings (2x)	4369.0
Vertical Stabilizer	506.5
Horizontal Stabilizer (2x)	630.8
Engines (2x)	5149.9
Nose Undercarriage	124.0
Main Undercarriage (2x)	955.6
Operating Empty Weight (OEW)	28690.5
Fuel Tanks (left, right & center)	10306.0
Water Ballast Tanks (8x)	5300.0
Total	44296.5

Table 2.3: Fokker 100 prototype maximum section masses, based on the Fokker prototype load case documentation.

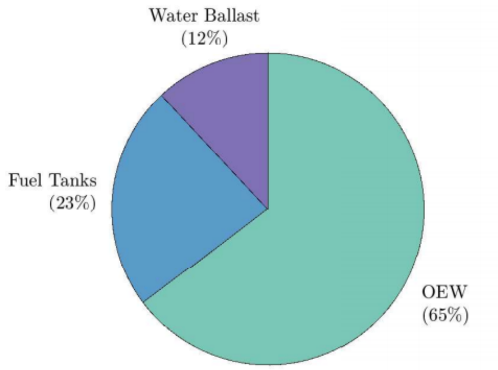

Figure 2.3: Division of aircraft weight components in case of fully filled water ballast tanks and fuel tanks.

emptied, followed by the main wing tanks and finally the collector tanks. Fuel pumping from tank to tank is always done such that the fuel is symmetrically distributed along the aircraft's lateral axis.

Fuel loading data is available from Fokker. A combination of their supplied emperical method combined with the derived tank dimensions lead to an interpolation of available data points towards functions expressing the CG data in terms of fuel level. This data is represented by Figure 2.4. The figure shows how the fuel tanks are emptied during flight. A color scheme shows where the fuel is located if a certain amount of fuel is still available.

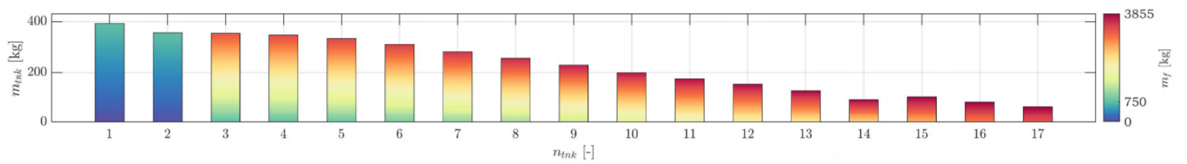

Figure 2.4: Fuel distribution as function of the amount of fuel available for the Fokker 100 prototype aircraft. The data is shown for a single main wing tank, where 1 and 2 are the collector tanks, 3-17 are the other 15 sub-tanks.

The center fuel tank inside the fuselage is a simple rectangular box. Interpolation between given datapoints is again performed to create a CG as function of the fuel level within the center tank. Appendix B contains figures of the distribution and location of the fuel tanks within the aircraft's wings.

2.2.2. Water Ballast Tanks

Detailed information about the water ballast tank location within the aircraft as well as their CG as function of the amount of water, has been made available by Fokker. This data was again interpolated with a least squares method to create a smooth function. For both fuel and water ballast tanks, the assumption has been made that the water or fuel is seen as a solid object within the tank. The moving of fuel and water due to aircraft movement has not been taken into account. Water ballast is seen as a static quantity. Some flight test report pumping fuel from one tank to another or dumping it. This is taken into account by the mass model as it calculates all aircraft mass and inertia related data for each stall again.

3

Flight Path Reconstruction

Raw measurement data is subjected to sensor noise and bias. This will affect the fidelity of the stall identification model as the error progresses in the entire identification routine. Furthermore, some crucial aircraft states required for identification can not be measured directly or lack accuracy. These issues can be limited by the application of the two step method. This method will divide our identification process into a state reconstruction, followed by a model parameter estimation routine [73]. In this chapter, the first part, also known as flight path reconstruction (FPR), will be discussed. The research performed in the context of stall model identification at the TU Delft has served as a basis for the FPR of the current research.

3.1. Iterated Extended Kalman Filter

Kalman filters are widely used as a tool for FPR. Kalman filters can filter out sensor noise and estimate sensor bias of the aircraft states. Futhermore, they can reconstruct system states that cannot be measured directly based on available measurement data and their known kinematics in relation to the system states and inputs [73].

Many different Kalman filters exist. As the kinematic system used to describe the aircraft behaviour is nonlinear, the linear kalman filter cannot be used. Both the IEKF and unscented kalman filter (UKF) have been tested before on both the Fokker 100 and the Cessna Citation II data [93]. Their performance was very similar, but the UKF has a much higher computational cost. As the benefit is negligible, the choice was made to stay with the IEKF.

3.1.1. Methodology

The IEKF will reconstruct the aircraft state based on a weighted average between the predicted and the measured state. It exhibits an iteration part to improve convergence of the filter compared to a simple extended kalman filter.

Based on the selected aircraft kinematics, the IEKF process will make a prediction of the next state $\underline{\hat{x}}_{k+1,k}$ by implementing the previous optimal state estimate $\underline{\hat{x}}_{k,k}$ in the kinematics equation, Equation 3.1. For nonlinear systems, this often involves solving an integral of the state equation. The Runge Kutta 4th order scheme is used to perform this calculation within the Matlab environment.

$$\underline{\hat{x}}_{k+1,k} = \underline{\hat{x}}_{k,k} + \int_{t_k}^{t_{k+1}} f(\underline{\hat{x}}_{k,k}, u_h^*, t)dt \tag{3.1}$$

The weighted average is determined based on the certainty we have about the correctness of our measurements and predictions. This part is iterated to improve convergence of the Kalman filter. Therefore, the state prediction covariance matrix $P_{k+1,k}(\bullet)$ is created as the expectancy of the state prediction error. As the system is nonlinear, this error comes as a linearised pertubation equation, requiring the calculation and discretisation of the Jacobians of both the state and observation equations of the aircraft kinematics. The Kalman gain matrix, Equation 3.2 quantifies the (un)certainty. If $P_{k+1,k}(\bullet)$ goes towards zero during the Kalman filtering, this indicates that the filter becomes more certain about the correctness of the predicted output. This influences the Kalman gain such that it favors the predicted output over the actual measured output.

The Kalman gain matrix is built using the state prediction covariance matrix $P_{k+1,k}(\bullet)$ and the measurement noise matrix R_{k+1}. R_{k+1} represents how certain we are about the correct output of our measuring devices. Furthermore, the Jacobian of the state equation $H_x^T(\bar{\eta}_i)$ is also required. It is calculated for $\bar{\eta}_i$, which is the current state estimate in the iteration of the IEKF. The Kalman gain is recalculated in every local iteration.

$$K_{k+1}(\bar{\eta}_i) = P_{k+1,k}(\bullet)H_x^T(\bar{\eta}_i)[H_x(\bar{\eta}_i)P_{k+1,k}(\bullet)H_x^T(\bar{\eta}_i) + R_{k+1}]^{-1} \tag{3.2}$$

With the Kalman gain known, the weighted average is obtained using Equation 3.3. This state estimation update is put in the state equation jacobian to recalculate the Kalman gain to obtain an improved measurement. The iteration process is halted when the number of iterations exceeds 25 or the difference between the last two measurement updates is less than $1e^{-10}$.

$$\bar{\eta}_{i+1} = \hat{\bar{x}}_{k+1,k} + K_{k+1}(\bar{\eta}_i)(\bar{z}_{k+1} - \bar{h}(\bar{\eta}_i, \bar{u}_{k+1}) - H_x(\bar{\eta}_i)(\hat{\bar{x}}_{k+1,k} - \bar{\eta}_i)) \tag{3.3}$$

The final state estimation update $\hat{\bar{x}}_{k+1,k+1}$ becomes the initial value for the next measurement point that will be evaluated by the filter. The correspoding covariance matrix of this state estimate, $P_{k+1,k+1}(\bullet)$ becomes the initial covariance matrix for the next point [95].

3.1.2. Kinematic Relations

The IEKF requires knowledge about the aircraft kinematics to produce state predictions. The more knowledge, the greater the accuracy of the Kalman filter will be.

The nonlinear kinematics of the state equations are given by Equation 3.4. The kinematics are described in terms of measured accelerations and angular rates and the system states to be estimated, namely the body velocities, body rates and the biases λ. The nonlinear system observation equations can be found in Equation 3.5. These are expressed in terms of state (Equation 3.6) and input (Equation 3.7) variables as well as constants.

Not all states can be measured directly. Therefore, the observation equation for true airspeed V_{TAS} is expressed in terms of body velocities that are incorporated into the aircraft state vector. Same holds for the flow angles. The angle of sideslip (AoS) is only measured when the aircraft was equipped with a boom during the specified flight test. The vane does not measure angle of sideslip (β), but the flank angle (μ_f). The corresponding kinematics $\arctan\left(\frac{v_b + r_m x_{\beta,boom} - p_m z_{\beta,boom}}{u_b - r_m y_{\beta,boom} + q_m z_{\beta,boom}}\right)$ are used in that case. However, not all stalls have boom data. The Fokker 100 data therefore contains reconstructed β data. The kinematics are found in the last row of the observability equation given by Equation 3.5.

$$f(x(t), u(t)) = \begin{bmatrix} (r_m - \lambda_r)v_b + (\lambda_q - q_m)w_b + Ax_m - \lambda_x - g_0\sin(\theta) \\ (\lambda_r - r_m)u_b + (p_m - \lambda_p)w_b + g_0\cos(\theta)\sin(\phi) + Ay_m - \lambda_y \\ (q_m - \lambda_q)u_b + (\lambda_p - p_m)v_b + g_0\cos(\theta)\cos(\phi) + Az_m - \lambda_z \\ (q_m - \lambda_q)\sin(\phi)\tan(\theta) + (r_m - \lambda_r)\cos(\phi)\tan(\theta) + p_m - \lambda_p \\ (\lambda_r - r_m)\sin(\phi) + (q_m - \lambda_q)\cos(\phi) \\ ((q_m - \lambda_q)\sin(\phi))/\cos(\theta) + (r_m - \lambda_r)\cos(\phi)/\cos(\theta) \\ 0 \\ 0 \\ 0 \\ 0 \\ 0 \\ 0 \end{bmatrix} \tag{3.4}$$

$$h(x(t),u(t)) = \begin{bmatrix} \phi \\ \theta \\ \psi \\ (u_b^2+v_b^2+w_b^2)^{1/2} \\ \arctan(\frac{w_b}{u_b}) - \frac{(q_m x_\alpha)}{\sqrt{(u_b^2+v_b^2+w_b^2)}} \\ \arctan(\frac{v_b}{(\sqrt{u_b^2+w_b^2})}) \end{bmatrix} \tag{3.5}$$

$$x = \begin{bmatrix} u_b & v_b & w_b & \phi & \theta & \psi & \lambda_x & \lambda_y & \lambda_z & \lambda_p & \lambda_q & \lambda_r \end{bmatrix} \tag{3.6}$$

$$u = \begin{bmatrix} Ax_m & Ay_m & Az_m & p_m & q_m & r_m \end{bmatrix} \tag{3.7}$$

$$z = \begin{bmatrix} \phi & \theta & \psi & V_{TAS} & \alpha & \beta \end{bmatrix} \tag{3.8}$$

3.1.3. Observability

Kalman filters reconstruct system states based on kinematics and system output knowledge. A necessary requirement for convergence of the Kalman filter is that the kinematics are fully observable and that the states can thus be determined from the output on a certain time interval. Determining the observability of the system is therefore an essential step in the Kalman filter process. As the aircraft kinematics of this research exhibits nonlinear behaviour, the observability analysis cannot be performed globally. Local observability analysis using the Lie derivative, defined in Equation 3.9, has therefore been performed. The Lie derivative of the observation equation $h(x)$ is defined as its Jacobian multiplied with the state equation $f(x)$, both of them evaluated at a specified state [51, 94].

$$L_f h(x) = \frac{\partial h(x)}{\partial x} f(x) \tag{3.9}$$

For analysis, a recursive matrix of n Lie derivatives is constructed for n states. The result is the observability matrix $\mathcal{O}(x)$, see Equation 3.10. If the rank of this matrix corresponds to the number of states, the system is said to be locally observable around the combination of states values entered in $h(x)$.

$$\mathcal{O}(x) = \begin{bmatrix} L_f^0 h(x) \\ L_f^1 h(x) \\ L_f^2 h(x) \\ \vdots \\ L_f^{n-1} h(x) \end{bmatrix} = \begin{bmatrix} \frac{\partial h(x)}{\partial x} \\ L_f h(x) \\ L_f L_f h(x) \\ \vdots \\ L_f \left(L_f^{n-2} h(x) \right) \end{bmatrix} \tag{3.10}$$

The full observability of the system is a necessary condition for convergence. It does not guarantee actual convergence. This convergence will need to be assessed by different metrics that are determined after the completion of the Kalman filtering process.

3.1.4. Results

The outcome of the IEKF on the 6 states and 6 bias terms can be found in Figure 3.1. The local observability was assessed for each measurement point and showed full rank (12) at each point. This is no proof of global observability, rather it is a good indication. The Kalman filter can converge. The corresponding innovation is shown in Figure 3.2. Innovation is a metric that shows the difference between the predicted measurement and the actual measurement. The innovation values are small and show that the predicted and actual measurements are not very different, therefore indicating convergence of the Kalman filter as the prediction does not diverge from the actual measurements [95].

The covariance matrix of the state estimates error is displayed in Figure 3.3. The covariances of all states converge during the estimation process of the Kalman filter. This indicates that each new step (data point) of the IEKF, more certainty arises about our predicted measurement. Furthermore, the bias terms also converge fairly quickly to a steady value, indicating that the Kalman filter has quickly identified those values. This is visible in Figure 3.1.

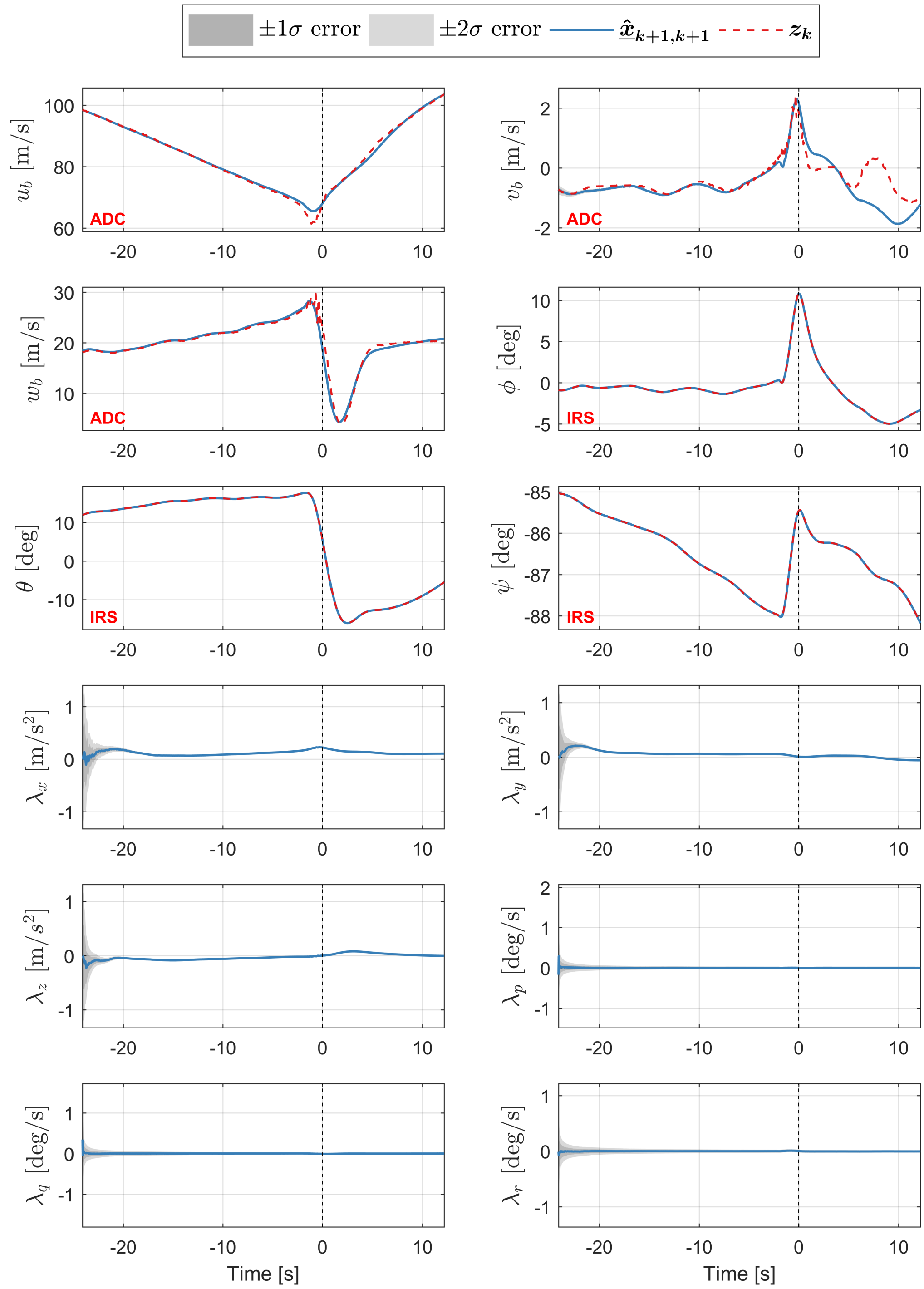

Figure 3.1: Results of the IEKF on the measurement data of the F100.

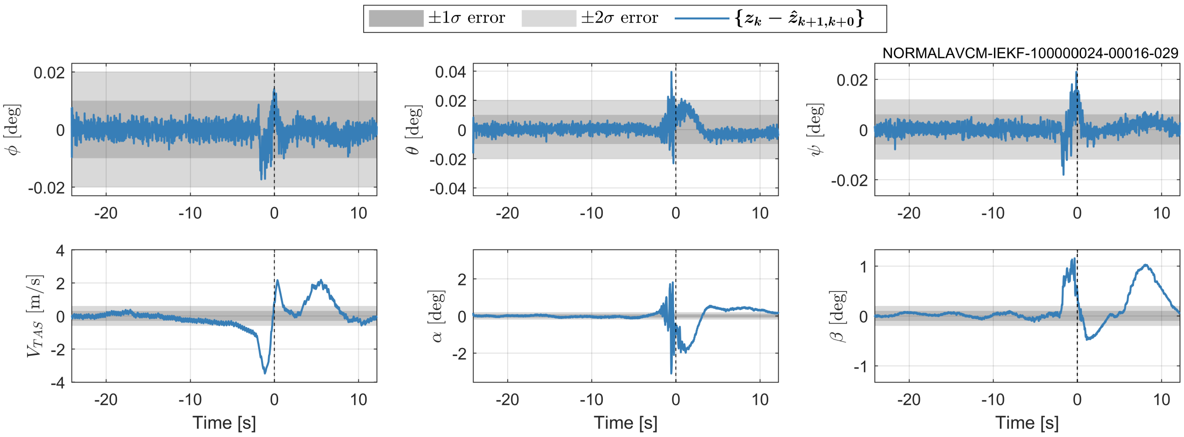

Figure 3.2: Innovation of the state estimation of the F100 using the IEKF.

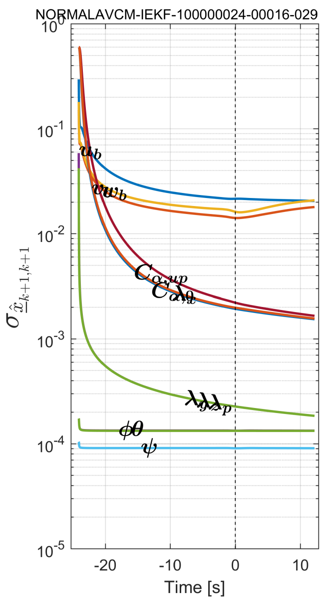

Figure 3.3: covariance matrix of the state estimate error.

3.2. Flow Measurement Corrections

Aircraft behaviour is modelled for its center of gravity (CG). Not all signals are however measured in the CG and their output is subjected to three dimensional aircraft behaviour if we assume a rigid aircraft. Note that more influences occur in reality due to bending, vibrations, wind, dynamic vane response etc. These additional influences increase the complexity of the filter and can cause convergence issues as too many parameters are present to estimate [60]. For this research, rigid aircraft kinematics will be assumed. Only the effects of location outside the CG will therefore be taken into account for now.

The angular accelerations cause an offset in the measured signals not located in the CG. For the flow angles AoA and AoS, corrections are applied to remove these influences and estimate their values at the CG. The common simplified corrections have been used in the kinematics found in subsection 3.1.2. These corrections incorporate small angle approximations and neglection of small angular rates. Grauer derived to full nonlinear corrections in 2017. Grauer concluded that these corrections improve identification results with high amounts of noise and at high values for flow angles and angular rates. For this research, stall behaviour is modelled and thus higher AoA are obtained in correspondence with asymmetric roll behaviour. These conditions favour the use of Grauer's exact corrections as the validity of small angle approximations and angular rates becomes less accurate. The proposed idea was implemented in the IEKF and will be discussed in this section.

3.2.1. Grauer's Exact Position Corrections

Flow angles vanes measure the local flow angles that are subjected to both the movement of the aircraft's CG as well as the 3D movement. The velocity components experienced at the vane location are expressed in Equation 3.11. The velocity components at the CG, u,v and w receive an additional component consisting of angular rates multiplied with the position of the vane with respect to the CG [48].

$$\begin{bmatrix} u_v \\ v_v \\ w_v \end{bmatrix} = \begin{bmatrix} u \\ v \\ w \end{bmatrix} + \begin{bmatrix} 0 & -r & q \\ r & 0 & -p \\ -q & p & 0 \end{bmatrix} \begin{bmatrix} x_v \\ y_v \\ z_v \end{bmatrix} \tag{3.11}$$

Flow angles can be expressed in terms of velocity components in the body reference system. The vanes measure local flow angles and thus require local velocity components to have the correct kinematic expression in our system. Using Equation 3.11, these local velocity components can be replaced by the velocity components in the CG with corrections for the position of the vanes. These expressions (Equation 3.12,Equation 3.13) capture the kinematics at the vane location, matching the raw measurement data, but expressed in body velocity components of the CG. These components are referred to in the complete kinematics and are used in the IEKF. Note that beta vanes measure the flank angle rather than the side slip angle. The AoS is then obtained using Equation 3.14.

$$\alpha_v = \arctan\left(\frac{w_v}{u_v}\right) = \arctan\left(\frac{w - qx_v + py_v}{u - ry_v + qz_v}\right) \tag{3.12}$$

$$\mu_f = \arctan\left(\frac{v_f}{u_f}\right) = \arctan\left(\frac{v + rx_f - pz_f}{u - ry_f + qz_f}\right) \tag{3.13}$$

$$\beta = \arctan\left(\tan\mu\cos\alpha\right) \tag{3.14}$$

Conventionally, these expressions are simplified by small angle approximations and low angular rates resulting in some terms dropping out. For this work, it was however decided to work with the full expressions rather than the simplified ones.

3.2.2. Results

Applying the full flow vane measurement corrections has only a slight effect on the outcome of the Kalman filter. In Figure 3.4 the results of the IEKF for the simplified and full corrections in the observation equations are represented together with the decomposed raw measurement data. The bottom 6 graphs show the difference between both kinematic systems. The largest difference can in fact be found in v_b. The deviation increases near the stall angle of attack (represented by the black dotted line) and decreases again once the stall is more or less recovered. As Grauer claimed, the simplification error gets more pronounced at higher AoA, thus near stall and for larger angular rates as observed in the recovery of the stall manoeuvre. For this thesis research, special attention is paid towards the accurate filtering and estimating of the AoA related measurements due to the importance of this variable for the research objective. Figure 3.5 and Figure 3.6 show the behaviour of the AoA for both kinematic system. It is visible in Figure 3.6 that the largest deviation is again located at and beyond the actual stall.

As the exact position corrections are only applied to the flow angles, only the innovation of angle of attack (α) and angle of sideslip (β) is affected the most by the adapted kinematics. The magnitude of the innovation remains largely within the 2 σ bounds and is zero-mean. Both covariance matrices show convergence of the system. The rate of convergence is slightly different though. In general, all parameters indicate convergence for the IEKF with exact position corrections.

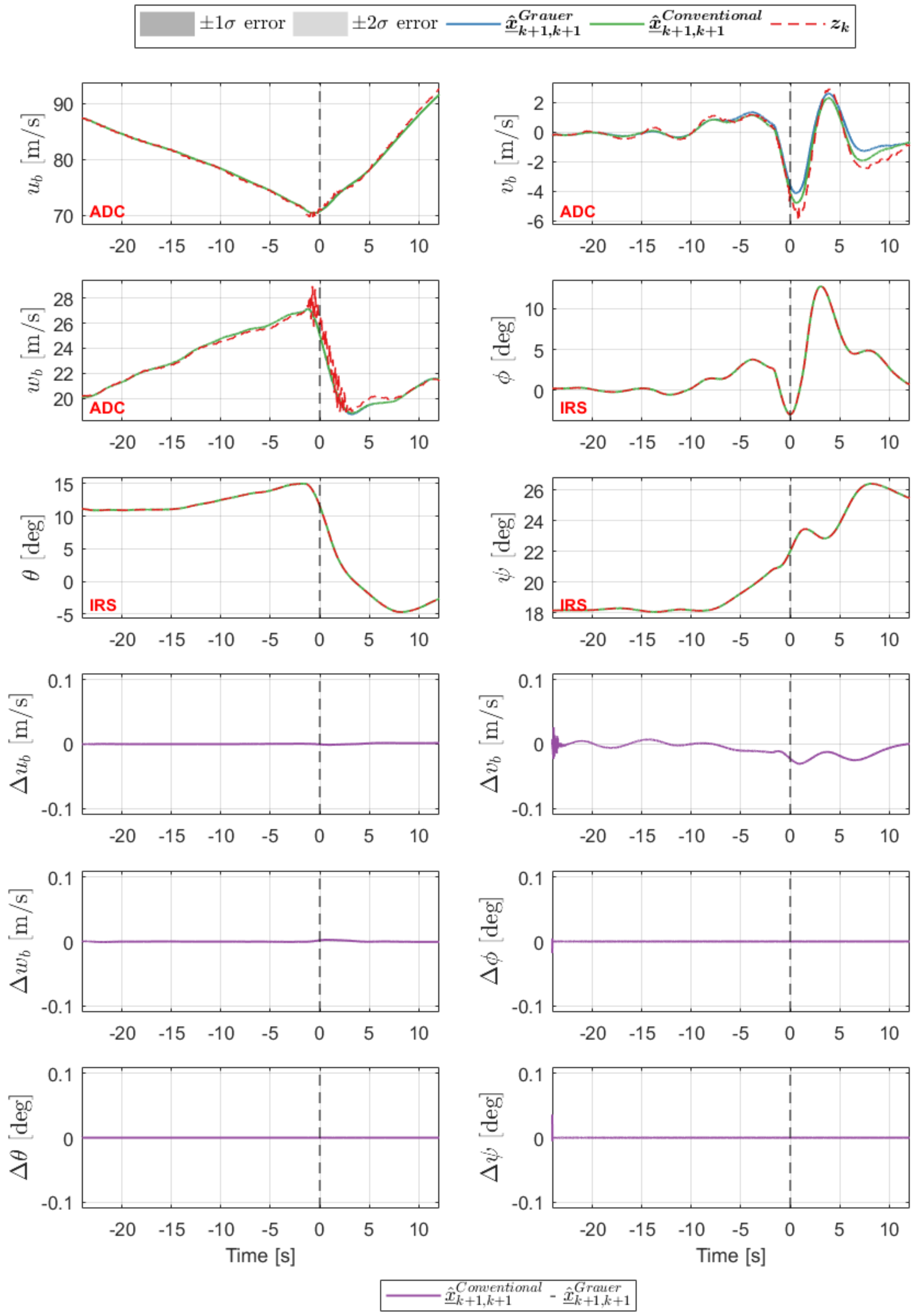

Figure 3.4: Comparison of the IEKF performances using conventional flow angle correction kinematics and those using Grauer's full nonlinear corrections.

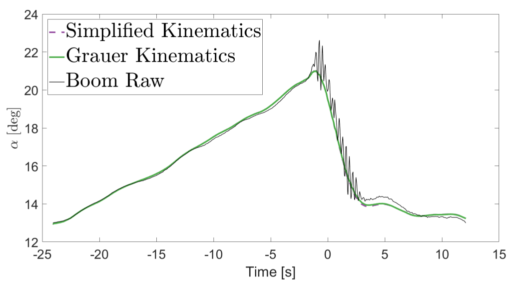

Figure 3.5: Angle of attack estimation from the IEKF for the conventional and Grauer flow corrections.

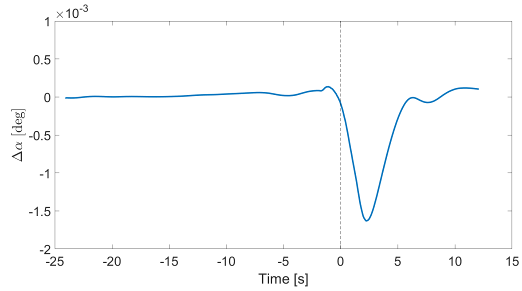

Figure 3.6: Deviation from Grauer flow angle kinematics from the conventional kinematics.

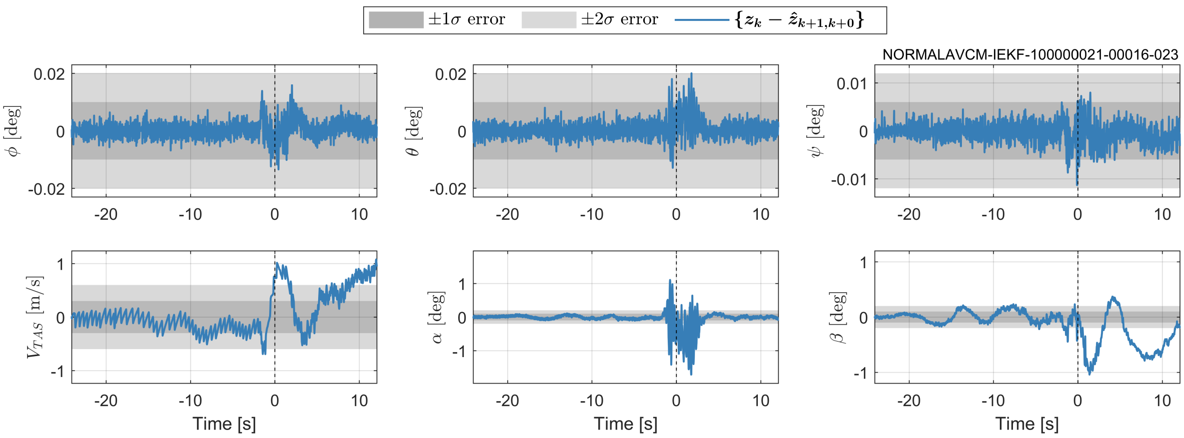

Figure 3.7: Innovation of the IEKF with simplified position correction kinematics

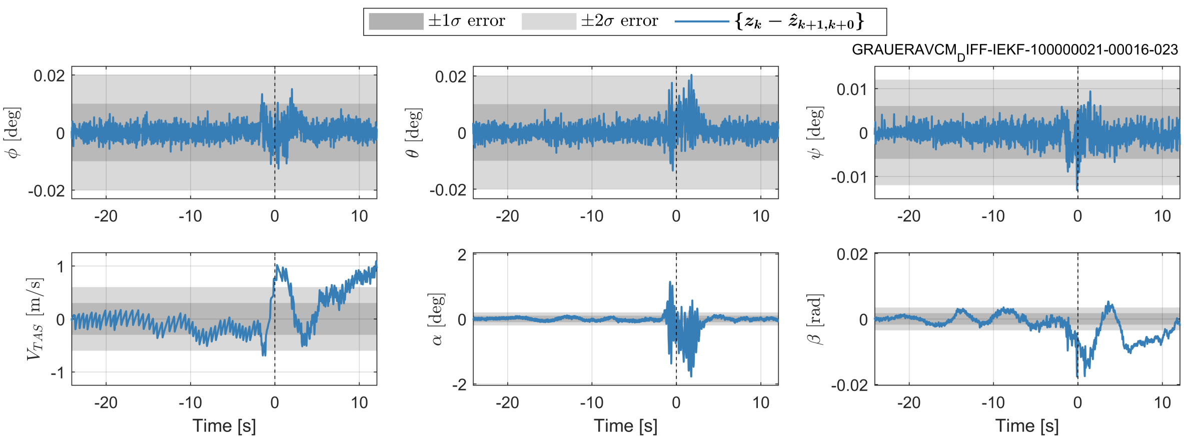

Figure 3.8: Innovation of the IEKF with exact position correction kinematics

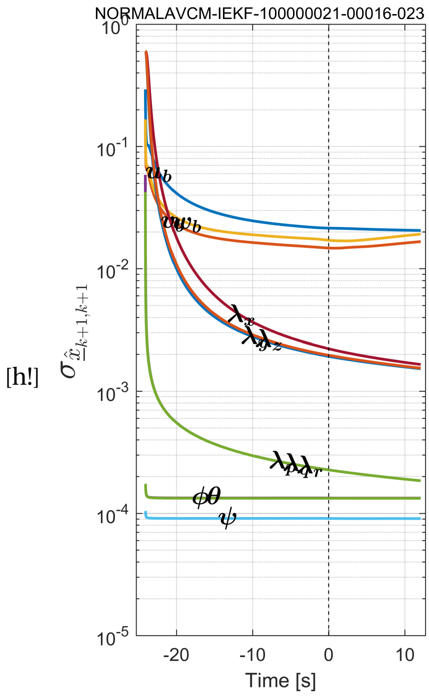

Figure 3.9: Covariance matrix of the state estimation error for the simplified position corrections.

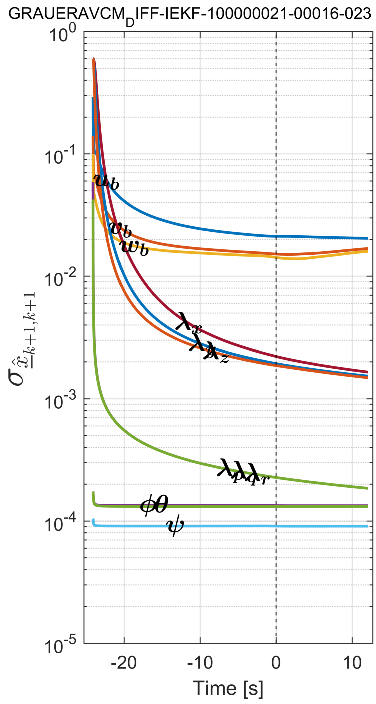

Figure 3.10: Covariance matrix of the state estimation error for the exact position corrections.

3.3. Upwash and Geometry Offset Coefficients for the Alpha Vanes

Upon investigation of the different stalls selected for this research, a large discrepancy was discovered on the measurement of the AoA. For some stalls, the test aircraft was equipped with a boom located below and in front of the aircraft measuring both α and β. The α measurements resulted into different values compared to those measured by the fuselage mounted vanes. The difference went up to 5° at the moment of stall. As not all stall manoeuvres recorded contain boom data (only a third of the stalls selected for this research), this discrepancy in AoA poses problems to identify an accurate and generic model using all the available data. In this section, two constant coefficients will be estimated to correct the vane AoA data and minimise the difference with respect to the boom data.

3.3.1. Boom AoA versus Vane AoA

The AoA vanes are located next to the cockpit of the aircraft. As they are mounted on the fuselage, they are subjected to the upwash around this fuselage and the measurement data is therefore corrupted. The boom is located in front of the aircraft and its vane measurements are far less influenced by the presence of the aircraft and the boom itself. If both measurements are available, preference goes to using the boom data rather than the fuselage mounted vanes. In order to be able to also use stall data where no boom measurements are available, the fuselage mounted vanes measurements can be corrected by estimating their upwash coefficient $C_{\alpha_{up}}$ and C_{α_0}. C_{α_0} takes into account that the vane's zero α measurement is not aligned with the aircraft's longitudinal axis. A kalman filter can be used to estimate these coefficients together with the other states.

These adapted kinematics have to be fully observable in order to estimate the vane coefficients. If this is not the case, the Kalman filter will not converge. The regular kinematic system described in subsection 3.1.2 does not allow this. The rank of its observability matrix is 12, only allowing the estimation of the regular 12 states. In order to estimate both coefficients, the observability rank must go up to 14.

3.3.2. Increasing Observability for Estimation of $C_{\alpha_{up}}$ and C_{α_0}

Increasing the rank of the observability matrix can be done by including more measurement signals. Up until now, only a single AoA measurement signal has been included in the aircraft observation equations. For the Fokker 100 aircraft equipped with a flow measurement boom, up to 3 signals are available: 2 vanes near the cockpit and 1 vane on the boom. Instead of using the boom measurement or the average of the two regular vanes, all three signals and their corresponding kinematics were included into the observation equation. The result is an increase of observability rank by 2 towards a total of 14. Next to the 12 regular states, 2 more coefficients can be estimated whilst the necessary condition for convergence is met.

The application of Grauer's full nonlinear flow measurement corrections is essential for increased observability. The simplified corrections exhibit the same kinematics for the left and right fuselage mounted α vanes. This causes both fuselage vanes entries into the matrix to be linearly dependent and thus not contributing to an additional increase in the dimension of the vector space spanned by the matrix columns. The rank of the observability matrix is only 13 in this case. Using the exact flow measurement corrections distinguishes the y-location of the vane making the kinematic relations linearly independent. This results into a rank of 14 allowing the estimation of both the $C_{\alpha_{up}}$ and C_{α_0} coefficient.

New kinematics can now be set up to estimate both coefficients. Both coefficients are added to the state vector, Equation 3.17. Just like the bias terms, a zero pop-ups in the state equation for these coefficients. The new observation equation and measurement vector are given by Equation 3.15 and Equation 3.16 respectively. Grauer's exact flow measurement corrections are applied to both vane and boom flow angles, including the flank angle. This kinematics system will only be used to estimate the value for both coefficients.

$$H = \begin{bmatrix} \phi \\ \theta \\ \psi \\ (u_b^2 + v_b^2 + w_b^2)^{1/2} \\ \arctan\left(\frac{w_b - q_m x_\alpha + p_m y_{\alpha,r}}{u_b + q_m z_\alpha - r_m y_{\alpha,r}}\right)(C_{\alpha,up} + 1) + C_{\alpha,0} \\ \arctan\left(\frac{w_b - q_m x_\alpha + p_m y_{\alpha,l}}{u_b + q_m z_\alpha - r_m y_{\alpha,l}}\right)(C_{\alpha,up} + 1) + C_{\alpha,0} \\ \arctan\left(\frac{w_b + p_m y_{\alpha,boom} - q_m x_{\alpha,boom}}{u_b + q_m z_{\alpha,boom} - r_m y_{\alpha,boom}}\right) \\ \arctan\left(\frac{v_b + r_m x_{\beta,boom} - p_m z_{\beta,boom}}{u_b - r_m y_{\beta,boom} + q_m z_{\beta,boom}}\right) \end{bmatrix} \tag{3.15}$$

$$z = \begin{bmatrix} \phi & \theta & \psi & V_{TAS} & \alpha_{vane,r} & \alpha_{vane,l} & \alpha_{boom} & \mu_f \end{bmatrix} \tag{3.16}$$

$$x = \begin{bmatrix} u_b & v_b & w_b & \phi & \theta & \psi & C_{\alpha,up} & C_{\alpha,0} & \lambda_x & \lambda_y & \lambda_z & \lambda_p & \lambda_q & \lambda_r \end{bmatrix} \tag{3.17}$$

The IEKF including the coefficient estimation kinematics have been applied on all selected stalls that include boom data. A total of 28 stalls were included, 4 of them were removed due to unreliable data. Of the 24 remaining stall data sets, 8 did not converge to constant values for $C_{\alpha_{up}}$ and C_{α_0}. However, the 16 converging data sets, did converge to about the same values. A bump however shows up at the moment of stall, disturbing the convergence of the coefficients. It was decided to average this out in the determination of the coefficient values.

Each data set did require some time to converge, see Figure 3.11. The average value of each data set was determined. Only the converged part was included. All these values were then averaged out for all data set resulting into the following two values for $C_{\alpha_{up}}$ and C_{α_0}:

$C_{\alpha_{up}}$ [-]	C_{α_0} [rad]
0.4730	-0.1072

On an average value for the AoA of 0.23 rad, an average mean squared error (MSE) of $4.23e^{-7}$ was reached. All MSE had a similar order of magnitude, with 3 outliers going towards $7e^{-6}$ as the largest MSE of the set of stalls with boom measurements.

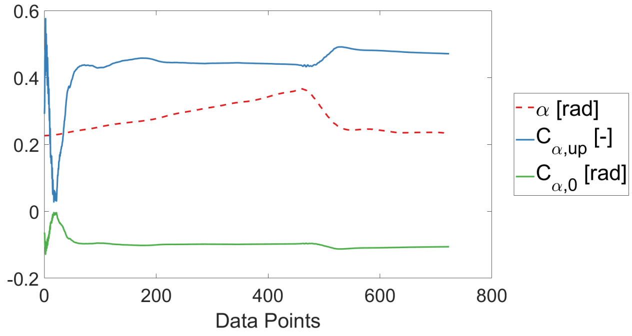

Figure 3.11: Convergence of $C_{\alpha_{up}}$ and C_{α_0} for a F100 stall data set.

3.4. Fokker 100 Kalman Filter

The insides gained regarding the use of the full nonlinear flow measurement corrections as derived by Grauer [48] has lead to the identification of the fuselage mounted vanes upwash coefficient $C_{\alpha_{up}}$ and C_{α_0}. The final kinematics system for the iterated extended kalman filter (IEKF) for the F100 aircraft stall data can now be constructed and evaluated.

3.4.1. Kinematics

Adding the vane coefficients $C_{\alpha_{up}}$ and C_{α_0}, together with the exact flow measurement corrections to the IEKF results into the final kinematics system. The state equation, Equation 3.18 is the same as the first system represented in this chapter. For the observation equation, a distinction has to be made between stall data sets without boom data, Equation 3.20, and stall data sets that do have boom measurements available, Equation 3.21. The process and measurement noise has also been included in the equations.

$$\dot{x} = \begin{bmatrix} \dot{u}_b \\ \dot{v}_b \\ \dot{w}_b \\ \dot{\phi} \\ \dot{\theta} \\ \dot{\psi} \\ \dot{\lambda}_x \\ \dot{\lambda}_y \\ \dot{\lambda}_z \\ \dot{\lambda}_p \\ \dot{\lambda}_q \\ \dot{\lambda}_r \end{bmatrix} = \begin{bmatrix} (r_m-\lambda_r)v_b + (\lambda_q - q_m)w_b + Ax_m - \lambda_x - g_0\sin(\theta) \\ (\lambda_r - r_m)u_b + (p_m-\lambda_p)w_b + g_0\cos(\theta)\sin(\phi) + Ay_m - \lambda_y \\ (q_m-\lambda_q)u_b + (\lambda_p - p_m)v_b + g_0\cos(\theta)\cos(\phi) + Az_m - \lambda_z \\ (q_m-\lambda_q)\sin(\phi)\tan(\theta) + (r_m-\lambda_r)\cos(\phi)\tan(\theta) + p_m - \lambda_p \\ (\lambda_r - r_m)\sin(\phi) + (q_m-\lambda_q)\cos(\phi) \\ ((q_m-\lambda_q)\sin(\phi))/\cos(\theta) + (r_m-\lambda_r)\cos(\phi)/\cos(\theta) \\ 0 \\ 0 \\ 0 \\ 0 \\ 0 \\ 0 \end{bmatrix} + G \begin{bmatrix} w_{Ax} \\ w_{Ay} \\ w_{Az} \\ w_p \\ w_q \\ w_r \end{bmatrix} \tag{3.18}$$

with

$$G = \begin{bmatrix} 1 & 0 & 0 & 0 & -w_b & v_b \\ 0 & 1 & 0 & w_b & 0 & -u_b \\ 0 & 0 & 1 & -v_b & u_b & 0 \\ 0 & 0 & 0 & 1 & \tan(\theta)\sin(\phi) & \cos(\phi)\tan(\theta) \\ 0 & 0 & 0 & 0 & \cos(\phi) & -\sin(\phi) \\ 0 & 0 & 0 & 0 & \sin(\phi)/\cos(\theta) & \cos(\phi)/\cos(\theta) \\ 0 & 0 & 0 & 0 & 0 & 0 \\ 0 & 0 & 0 & 0 & 0 & 0 \\ 0 & 0 & 0 & 0 & 0 & 0 \\ 0 & 0 & 0 & 0 & 0 & 0 \\ 0 & 0 & 0 & 0 & 0 & 0 \\ 0 & 0 & 0 & 0 & 0 & 0 \\ 0 & 0 & 0 & 0 & 0 & 0 \\ 0 & 0 & 0 & 0 & 0 & 0 \end{bmatrix} \tag{3.19}$$

$$z_{noboom} = \begin{bmatrix} \phi \\ \theta \\ \psi \\ V_{TAS} \\ \alpha_{vane,r} \\ \alpha_{vane,l} \\ \beta \end{bmatrix} = \begin{bmatrix} \phi \\ \theta \\ \psi \\ (u_b^2 + v_b^2 + w_b^2)^{1/2} \\ \arctan\left(\frac{w_b - q_m x_\alpha + p_m y_{\alpha,r}}{u_b + q_m z_\alpha - r_m y_{\alpha,r}}\right)(C_{\alpha,up} + 1) + C_{\alpha,0} \\ \arctan\left(\frac{w_b - q_m x_\alpha + p_m y_{\alpha,l}}{u_b + q_m z_\alpha - r_m y_{\alpha,l}}\right)(C_{\alpha,up} + 1) + C_{\alpha,0} \\ \arctan(\frac{v_b}{(\sqrt{u_b^2 + w_b^2})}) \end{bmatrix} + \bar{v} \tag{3.20}$$

$$z_{boom} = \begin{bmatrix} \phi \\ \theta \\ \psi \\ V_{TAS} \\ \alpha_{boom} \\ \mu_f \end{bmatrix} = \begin{bmatrix} \phi \\ \theta \\ \psi \\ (u_b^2 + v_b^2 + w_b^2)^{1/2} \\ \arctan\left(\frac{w_b + p_m y_{\alpha,boom} - q_m x_{\alpha,boom}}{u_b + q_m z_{\alpha,boom} - r_m y_{\alpha,boom}}\right) \\ \arctan\left(\frac{v_b + r_m x_{\beta,boom} - p_m z_{\beta,boom}}{u_b - r_m y_{\beta,boom} + q_m z_{\beta,boom}}\right) \end{bmatrix} + \bar{v} \tag{3.21}$$

with

$$\bar{v} = \begin{bmatrix} w_\phi & w_\theta & w_\psi & w_{V_{TAS}} & w_\alpha & w_\beta \end{bmatrix} \tag{3.22}$$

3.4.2. Results

The estimation of the vane coefficients aimed at correcting the measurements for the presence of the fuselage, influencing the airflow measured at the vanes. Without corrections, the discrepancy between these measurements and those from the more reliable boom were simply too large, reducing the accuracy of the next step in the system identification process, namely the model parameter identification. One could choose to only use stall data sets containing boom measurements, seriously limiting the number of data sets that are useable. Two correcting coefficients have been identified and their influence on the vane measurements can now be assessed. The assessment will be done based on the reconstructed AoA. The output states of the kalman filter can be used to reconstruct the AoA from that specific IEKF, as by Equation 3.23.

$$\alpha = atan\left(\frac{w}{u}\right) \tag{3.23}$$

Adding both $C_{\alpha_{up}}$ and C_{α_0} to the observation equation, as in Equation 3.20, results into a very clear improvement on the estimation of the AoA if only fuselage mounted vane measurements are used. Figure 3.12 shows this. The upper two lines represent the raw vane measurement plot of α as well as the outcome of the Kalman filter if the boom data is left out and no vane coefficients are included. The Kalman filter models the raw vane data. For this data set, boom data of α is however available, represented by the noisy line. This is the result of stall buffet related vibrations on the boom. Note that they only occur after stall and disappear when the aircraft is recovered. If the Kalman filter gets this boom α data as single input, it filters out the vibrations and reconstructs the AoA following the trend of the raw boom data. Finally, a third Kalman filter is applied using only vane data, but adding the determined vane coefficients. The result is an AoA that follows the trend of the boom and the boom-based Kalman filter output. This is the case even though not a single boom measurement is used in this filter. This proofs that the upwash coefficient $C_{\alpha_{up}}$ and C_{α_0} determining IEKF has converged to the actual coefficient values for the fuselage mounted vanes on the Fokker 100.

A similar analysis is applied to a stall with boom for which the estimation of the vane coefficients did not converge. The results are given by Figure 3.13. In the process of estimating the vane coefficients $C_{\alpha_{up}}$ and C_{α_0}, the IEKF diverges, negatively affecting the estimation of the body velocities and therefore the corresponding AoA. The AoA does not follow the trend of the boom nor the vanes. No reason has been found why some stall data sets did not converge. Local observability analysis showed full rank for at all data points. If the final vane coefficients are however included in the observation equation and the diverging data set enters this altered kalman filter, the results are very similar as the case discussed above. For α measurement data

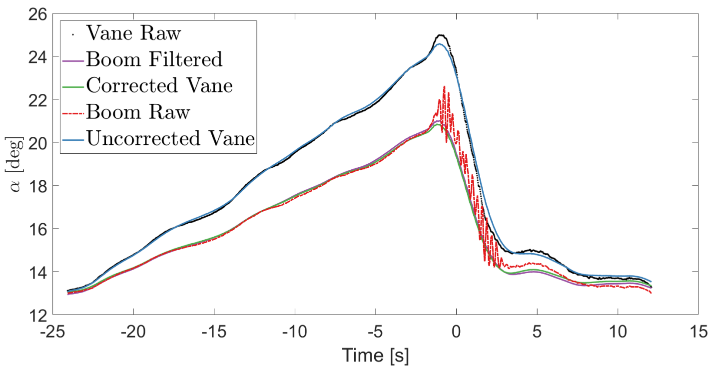

Figure 3.12: Result of the Kalman filter for boom data and vane data, both with and without vane coefficients.

coming only from the fuselage mounted vanes, corrected with the coefficients, the trend of the boom data and boom filtered IEKF is again closely followed. All stalls including boom data have been evaluated and not a single stall exhibited different behaviour. This confirms the correctness of the vane coefficient values.

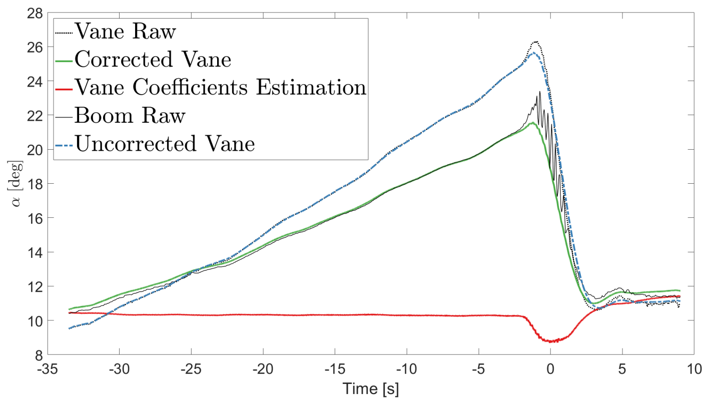

Figure 3.13: Result of the Kalman filter for boom data and vane data, both with and without vane coefficients. Coefficient estimation process diverted for this stall.

With the determined values for $C_{\alpha_{up}}$ and C_{α_0}, all stalls without boom AoA data can now be corrected. The less reliable output from the fuselage mounted vanes can be corrected to closely resemble the more reliable boom output. This saves more than two thirds of the stalls selected for the next part of the research. Without corrections, having only vane data would have made the filtered data not accurate enough to enter the model parameter estimation process. The result of using the IEKF including the determined vane coefficients is shown in Figure 3.14.

Based on the investigation of the behaviour of the AoA, the final IEKF kinematics system with $C_{\alpha_{up}}$ and C_{α_0} shows very promising behaviour. It remains to further assess its observability and convergence. The rank of the observability matrix remains 12, thus the necessary condition for observability is matched for all data points. The innovation of all outputs remains small, Figure 3.16. An offset from zero-mean is observed for the AoA's. The offset can be explained by the fact that two separate AoA signals are measured, one by each vane. As the vanes are located on opposite sides of the fuselage, different values for α are recorded. Both signals are used in the IEKF to reconstruct u and w, which are the velocity components building up the angle of attack. This means that a single AoA is reconstructed by the filter. This value will lay in the middle of both measured signals. The innovation detects this as a bias. One vane will be located below the estimated average, the other one above. The innovation of the β is influenced by the fact that β is not measured directly as no boom data is available for this stall. It has been reconstructed by Fokker itself.

The covariance matrix of the state estimation error converges as well, Figure 3.17. All observed metrics indi-

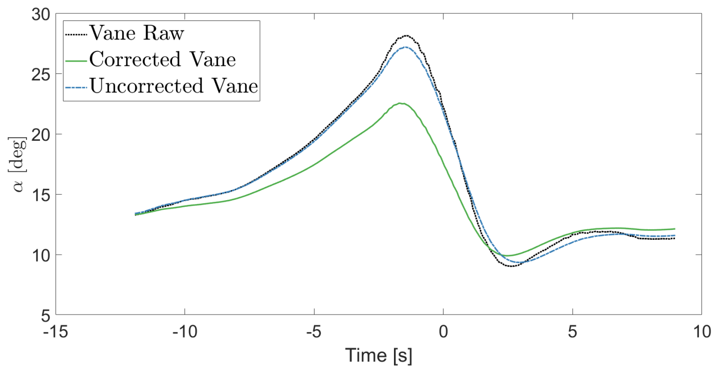

Figure 3.14: Result of the Kalman filter for vane data only, with and without vane coefficients.

cate that the Kalman filter converges for the newly introduced kinematics.

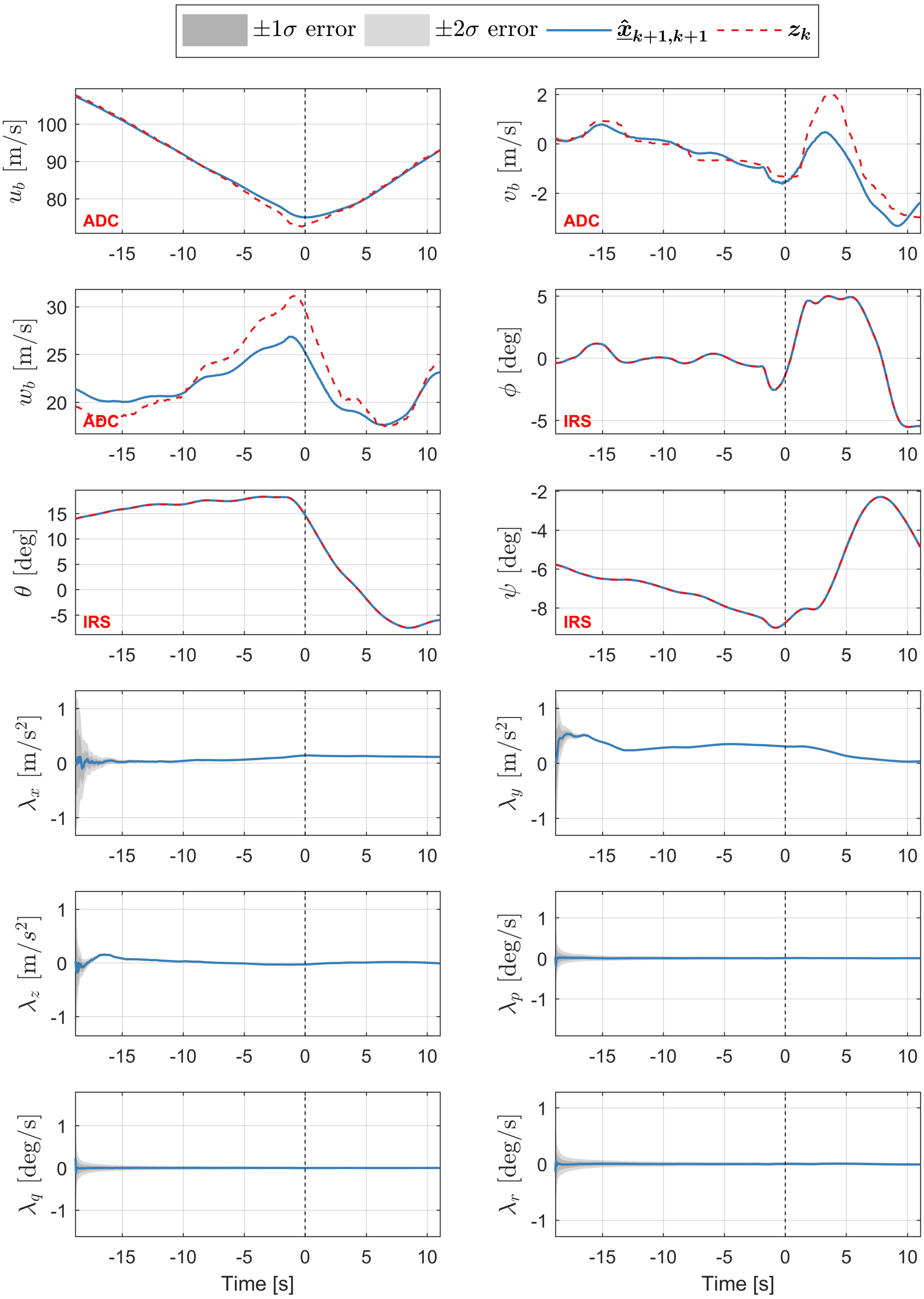

Figure 3.15: Result of the states estimation for a stall without boom, using kinematics including $C_{\alpha_{up}}$ and C_{α_0}

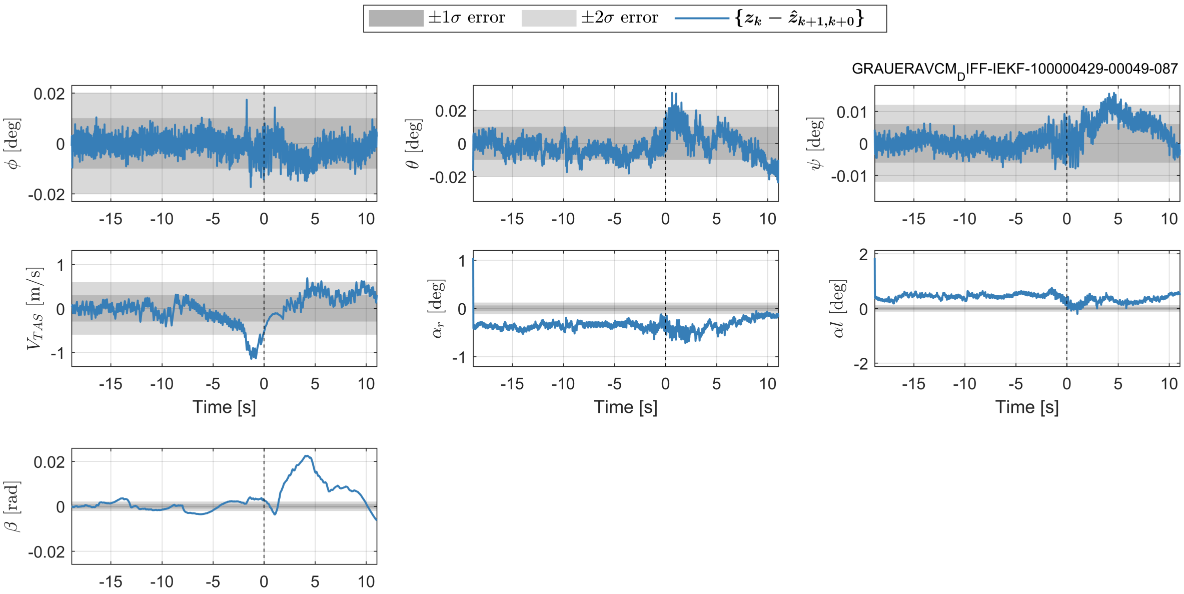

Figure 3.16: Innovation of the output of a stall without boom, prediction model using kinematic including $C_{\alpha_{up}}$ and C_{α_0}

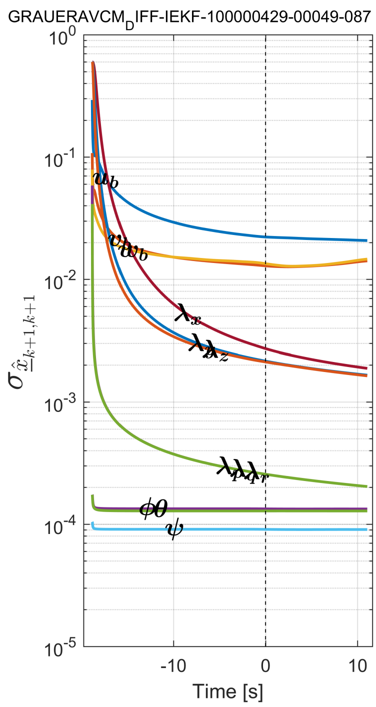

Figure 3.17: Covariance matrix of the state estimation error for a stall without boom, prediction model using kinematic including $C_{\alpha_{up}}$ and C_{α_0}

4

Model Structure

Due to the nonlinear behaviour and characteristics of aircraft motion near and during stall, the conventional model structures do not suffice to accurately model aircraft stalls. For this research, a new model structure will be derived to fit the training data as good as possible, while attempting to keep the structure simple. This chapter will introduce the theoretical background on the creation of the stall adjusted model structure for the Fokker 100.

4.1. Aircraft Equations of Motion

To model aircraft behaviour, its equations of motion (EOM) have to be solved. In most cases, Equation 4.1 and Equation 4.2 are used to represent the aircraft. These equations have been derived under the following assumptions:

- The aircraft is a rigid body
- The aircraft mass remains constant throughout the stall manoeuvre under consideration
- Flat and non-rotating Earth
- Body fixed reference frame with $X_b Z_b$ plane being a plane of symmetry
- No rotating masses

$$m\begin{bmatrix}\dot{u}+qw-rv\\ \dot{v}+ru-pw\\ \dot{w}+pv-qu\end{bmatrix}=mg_0\begin{bmatrix}-\sin\theta\\ \sin\phi\cos\theta\\ \cos\phi\sin\theta\end{bmatrix}+\begin{bmatrix}X\\ Y\\ Z\end{bmatrix} \tag{4.1}$$

$$\begin{bmatrix}I_{xx} & 0 & I_{xz}\\ 0 & I_{yy} & 0\\ -I_{xz} & 0 & I_{xz}\end{bmatrix}\begin{bmatrix}\dot{p}\\ \dot{q}\\ \dot{r}\end{bmatrix}=\begin{bmatrix}l\\ m\\ n\end{bmatrix}-\begin{bmatrix}p\\ q\\ r\end{bmatrix}\times\begin{bmatrix}I_{xx} & 0 & I_{xz}\\ 0 & I_{yy} & 0\\ -I_{xz} & 0 & I_{xz}\end{bmatrix}\begin{bmatrix}p\\ q\\ r\end{bmatrix} \tag{4.2}$$

To solve Equation 4.1 and Equation 4.2, the aerodynamic forces X, Y, Z and aerodynamic moments l, m, n have to be available. Once these are known, the aircraft behaviour can be calculated using the EOM. The magnitude of these forces and moments strongly dependent on the aircraft type, speed, weight, etc. To make comparisons more straightforward, the forces and moments are non-dimensionalised, removing their dependence on aircraft velocity and size. What remains are 6 aerodynamic coefficients. Their values will be determined in a system identification process. Their model structure needs to be selected for proper fitting to create stall models with high fidelity.

4.2. Conventional Model Structure

For the identification of aircraft models in normal flight conditions, the model structures for the 6 aerodynamic coefficients are formulated as first order expansions of the Taylor's series. These expansions are centered around a specified trim condition. Common parameters to build up the model are the flow angles α and β and their time derivatives, the non-dimensionalised angular velocities $\tilde{p}, \tilde{q}, \tilde{r}$ and the control surface deflections δ. These variables are also known as independent variables (IV). An example of this conventional model structure is given by Equation 4.3.

$$
\begin{aligned}
C_L &= C_{L_0} + C_{L_\alpha}\alpha + C_{L_q}\tilde{q} + C_{L_{\dot{\alpha}}}\dot{\alpha} \\
C_D &= C_{D_0} + C_{D_\alpha}\alpha + C_{D_q}\tilde{q} + C_{D_{\dot{\alpha}}}\dot{\alpha} \\
C_Y &= C_{Y_0} + C_{Y_\beta}\beta + C_{Y_p}\tilde{p} + C_{Y_r}\tilde{r} + C_{Y_{\dot{\beta}}}\dot{\beta} \\
C_l &= C_{l_0} + C_{l_\beta}\beta + C_{l_p}\tilde{p} + C_{l_r}\tilde{r} + C_{l_{\dot{\beta}}}\dot{\beta} + C_{l_{\delta_a}}\delta_a + C_{l_{\delta_r}}\delta_r \\
C_m &= C_{m_0} + C_{m_\alpha}\alpha + C_{m_q}\tilde{q} + C_{m_{\dot{\alpha}}}\dot{\alpha} + C_{m_{\delta_e}}\delta_e \\
C_n &= C_{n_0} + C_{n_\beta}\beta + C_{n_p}\tilde{p} + C_{n_r}\tilde{r} + C_{n_{\dot{\beta}}}\dot{\beta} + C_{n_{\delta_a}}\delta_a + C_{n_{\delta_r}}\delta_r
\end{aligned}
\tag{4.3}
$$

The notation is specific to aerodynamic model structures. The IV are given as deviation from the trimmed condition as they come from a first order Taylor's series expansion. Their conventional notation is however leaving out the Δ sign in front of them that represents this fact. The C_{i_j} coefficients are partial derivatives from the aerodynamic force or moment i to the IV j. These are the so called control and stability derivatives.

4.3. Kirchhoff Model Terms

The conventional model structure is applied for normal flight conditions, in which linearity is assumed and the model starts from a trimmed condition. These assumptions do not hold for stalls, as they are subjected to nonlinear behaviour and the region of validity around the trimmed condition is small compared to normal flight. The model would only be valid for small regions of the flight envelope. It would therefore require the creation of many models to cover the entire flight envelope, making it a very expensive and lengthy process. This approach is simply not sufficient to create stall models.

One can however extend these models with terms that can capture the nonlinear characteristics and extend the area of applicability within the flight envelope. The use of Kirchhoff's theory of flow separation has proven to be able to do so and has been widely applied in the research towards the creation of stall models [27, 32, 47, 87, 93]. Goman and Khrabrov introduced this theory in 1992. Four Kirchhoff parameters have to be estimated to solve an ODE. This ODE solves for the internal flow separation point (X), which is a number between 0 and 1 representing the location of flow separation along the wing's chord. The four Kirchhoff parameters (τ_1, τ_2,a_1 and α^*) have to be identified for the specific aircraft under consideration and allow the modeling of the specific stall behaviour as function of the AoA. For a given AoA α, the ODE can be solved for X. Equation 4.5 can now be solved to achieve lift coefficient (C_L) based on the AoA, C_{L_α} and X [46].

$$
\tau_1 \frac{dX}{dt} + X = \frac{1}{2}\left(1 - \tanh\left[a_1(\alpha - \tau_2\dot{\alpha} - \alpha^*)\right]\right) \tag{4.4}
$$

$$
C_L = C_{L_\alpha}\left(\frac{1+\sqrt{X}}{2}\right)^2 \alpha \tag{4.5}
$$

τ_1 represents the time delay due to flow inertia, τ_2 models the effects of hysteresis, a_1 determines the abruptness of the stall and α^* sets the stall AoA. Smets et al. investigated the influence of varying all four parameters on the subjective noticeability of pilots in the simulator. Some parameters are easy to determine accurately whilst others have little influence on how pilots experience the stall. Smets et al. therefore suggested to put the emphasis on correct estimation of a_1 [89]. The effect of varying the four parameters on the lift coefficient (C_L) is given by Figure 4.1-Figure 4.4. The effect on X is given by Figure 4.5-Figure 4.8.

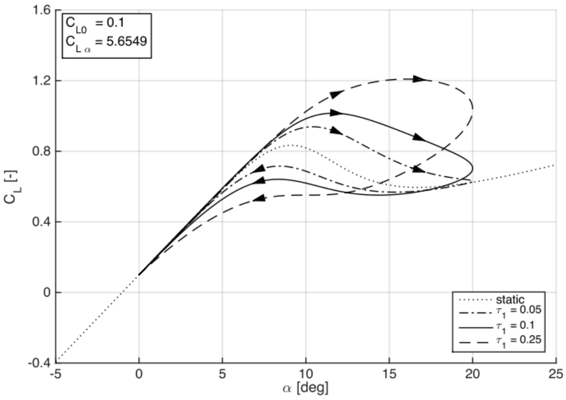

Figure 4.1: Effect of varying τ_1 on the lift coefficient curve [93]

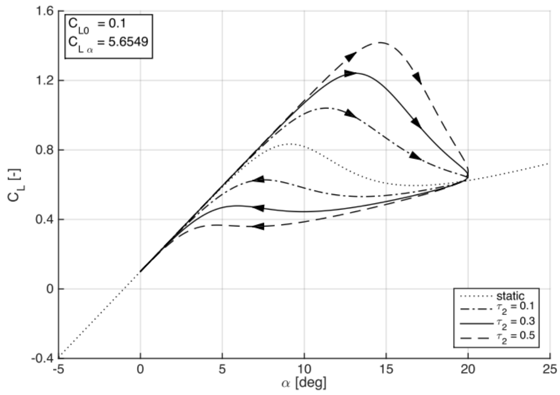

Figure 4.2: Effect of varying τ_2 on the lift coefficient curve [93]

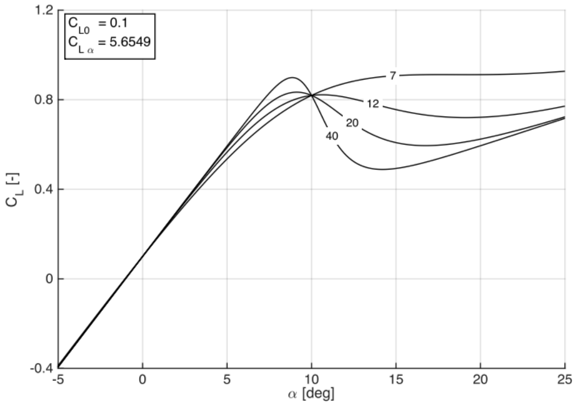

Figure 4.3: Effect of varying a_1 on the lift coefficient curve [93]

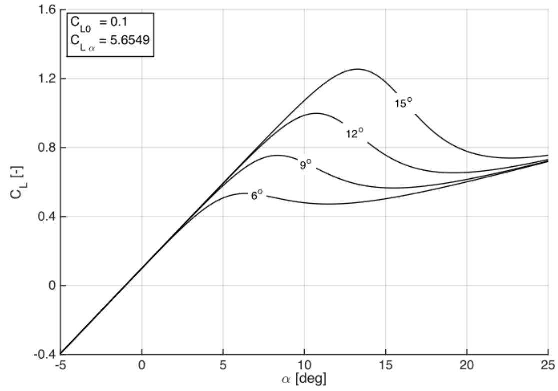

Figure 4.4: Effect of varying α^* on the lift coefficient curve [93]

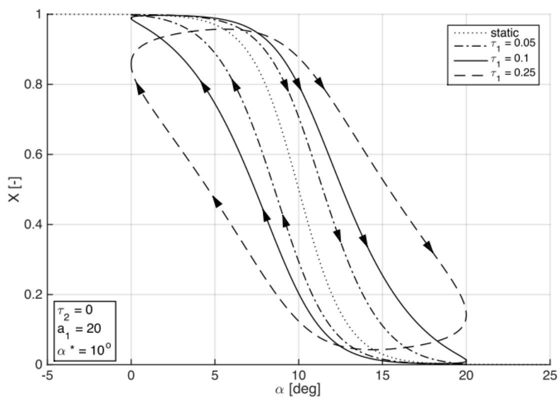

Figure 4.5: Effect of varying τ_1 on the point of flow separation X [93]

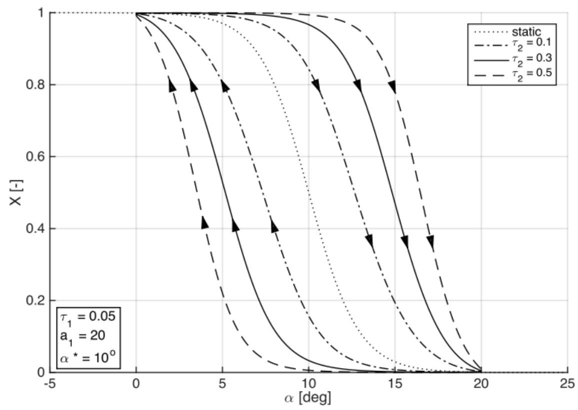

Figure 4.6: Effect of varying τ_2 on the point of flow separation X [93]

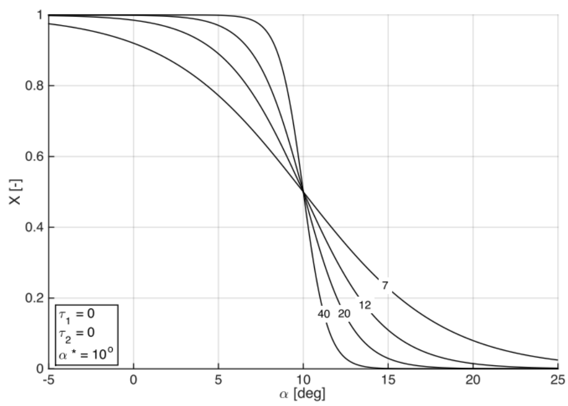

Figure 4.7: Effect of varying a_1 on the point of flow separation X [93]

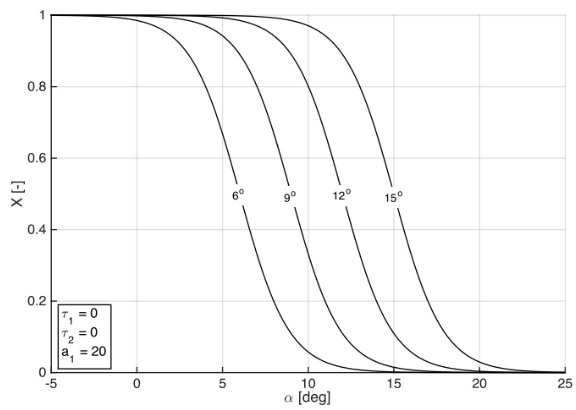

Figure 4.8: Effect of varying α^* on the point of flow separation X [93]

4.4. Local Model Terms

The disadvantage of using global model structures is that capturing a severe local nonlinearity affects the entire domain. One can therefore choose to split the domain in several subdomains and estimate a separate model on that subdomain. To identify a model, sufficient data is required. Splitting the domain in multiple subdomains increases the amount of data required. This amount of data is not always available and acquiring it requires additional flight test that can be very expensive and time consuming. It is not an ideal solution for aerodynamic model identification using flight test data.

Spline terms offer a better alternative. Spline terms are terms that are only defined on a part of the domain, as shown by Equation 4.6. They complement the global model structure in a specific domain to assist in capturing severe local nonlinearities, without affecting the remainder of the domain. No additional flight test data is required to identify its parameters.

$$(x - x_i)_+^m = \begin{cases} 0 & \text{when } x < x_i \\ (x - x_i)^m & \text{when } x > x_i. \end{cases} \tag{4.6}$$

4.5. Multivariate Orthogonal Function Modeling

Selecting a model structure can be done using thoughtful engineering judging. The aerodynamic coefficient models have to be build up by model terms consisting of the variables that influence the magnitude of the coefficient under consideration. The selection must be wise, as adding too many terms leads to complex models prone to overfit. If two terms are too closely correlated, identification issues can arise in which it is better to drop one of them.

Morelli et al. introduced a mathematical approach to determine model structures for global aerodynamic modeling. The multivariate orthogonal function modeling technique will start from a pool of candidate regressor terms for the aerodynamic coefficients. All the candidate terms are orthogonalised and therefore they become decoupled. The multivariate orthogonal functions can now be individually assessed to quantify their contribution to the model fit. Only the best terms are added to the final model structure.

4.5.1. Theory behind Multivariate Orthogonal Function Modeling

For all 6 aerodynamic coefficients, the multivariate orthogonal function takes the form of a linear combination of all multivariate orthogonal model terms, Equation 4.7. This approaches the computed values for the aerodynamic coefficients based on the measured signals. The model terms are a function of the independent variables (IV).

$$\tilde{z} = a_1 \tilde{p}_1 + a_2 \tilde{p}_2 + ... a_n \tilde{p}_n + \tilde{\epsilon} = \tilde{P}\tilde{a} + \tilde{\epsilon} \tag{4.7}$$

A good model approximates the computed coefficients closely, keeping the model error $\tilde{\epsilon}$ as small as possible. $\tilde{\epsilon}$ will be minimised using a cost function that determines the values of model parameters a_i to achieve this minimisation. The cost function to be minimised is a least squares function, Equation 4.8. This function reaches a minimum where its first derivative with respect to the model parameters a_i reaches 0. The values that correspond with the lowest model error, $\hat{\tilde{a}}$, can be found by rewriting the derivative to Equation 4.9. The resulting output y of the identified model is given by Equation 4.10.

$$J = \frac{1}{2}\tilde{\epsilon}^T\tilde{\epsilon} = \frac{1}{2}\left(\tilde{z} - \tilde{P}\tilde{a}\right)^T\left(\tilde{z} - \tilde{P}\tilde{a}\right) \tag{4.8}$$

$$\hat{\tilde{a}} = \left[\tilde{P}^T\tilde{P}\right]^{-1}\tilde{P}^T\tilde{z} \tag{4.9}$$

$$\tilde{y} = \tilde{P}\hat{\tilde{a}} \tag{4.10}$$

The corresponding estimated covariance matrix is given by

$$\tilde{\Sigma}_{\hat{\tilde{a}}} = E\left[\left(\hat{\tilde{a}} - \tilde{a}\right)\left(\hat{\tilde{a}} - \tilde{a}\right)^T\right] = \sigma^2\left(\tilde{P}^T\tilde{P}\right)^{-1} \tag{4.11}$$

where σ^2 represents the fit error covariance. This covariance can be estimated based on the computation of the residuals between each measurement and the corresponding model prediction as below

$$\tilde{v} = \tilde{z} - \tilde{P}\hat{\tilde{a}} \tag{4.12}$$

The estimation of the fit error covariance is done as follows

$$\hat{\sigma}^2 = \frac{1}{N-n}\left[\left(\tilde{z} - \tilde{P}\hat{\tilde{a}}\right)^T\left(\tilde{z} - \tilde{P}\hat{\tilde{a}}\right)\right] = \frac{\tilde{v}^T\tilde{v}}{N-n} \tag{4.13}$$

With this equation, the standard errors of the parameters can be assessed by taking the square root of the corresponding diagonal elements of the fit error covariance matrix.

The multivariate orthogonal function modeling differs from conventional function modeling. The conventional approach uses ordinary multivariate polynomials or spline terms to build up the model structure. The multivariate orthogonal function modeling only uses multivariate polynomials or spline terms that are mutually orthogonal to each other. The main advantage of using this method is the individual evaluation of adding each term to the model. Due to the mutual orthogonality, the contribution of each single model term towards improvement of model fit can be assessed. The modeling process is decoupled. Under the assumption of orthogonality (Equation 4.14), the cost function $\tilde{J}$ can now be written as Equation 4.15. The parameter value to be estimated only depends on its corresponding model term and the measurement vector $\tilde{z}$, see Equation 4.16.

$$\tilde{p}_i\tilde{p}_j = 0 \quad for \quad i \neq j, \quad i,j = 1,2,..,n \tag{4.14}$$

$$\tilde{J} = \frac{1}{2}\left[\tilde{z}^T\tilde{z} - \sum_{j=1}^{n}\frac{\left(\tilde{p}_j\tilde{z}\right)^2}{\tilde{p}_j{}^T\tilde{p}_j}\right] \tag{4.15}$$

$$\hat{a}_j = \frac{\tilde{p}_j\tilde{z}}{\tilde{p}_j{}^T\tilde{p}_j} \tag{4.16}$$

The contribution of each term is quantified in the predicted squared error (PSE) metric, see Equation 4.17. This metric quantifies the improvement in minimising the cost function $\tilde{J}$ whilst penalising the increased model complexity as a result of the additional term. The PSE metric uses the decoupled cost function $\tilde{J}$.

$$PSE = \frac{\left(\tilde{z} - \tilde{P}\hat{\tilde{a}}\right)^T \left(\tilde{z} - \tilde{P}\hat{\tilde{a}}\right)}{N} + \sigma^2_{max}\frac{n}{N} = \frac{2\hat{J}}{N} + \sigma^2_{max}\frac{n}{N} \tag{4.17}$$

$$\sigma^2_{max} = \frac{1}{N-1}\sum_{i=1}^{N}\left[z_i - \bar{z}\right]^2 \tag{4.18}$$

$$\bar{z} = \frac{1}{N}\sum_{i=1}^{N} z_i \tag{4.19}$$

Here, σ^2_{max} is the upper-bound mean squared error, N the total number of data points for the data set under consideration, n being the number of model terms. The PSE metric is evaluated each time a model term is added to the cost function $\tilde{J}$. The order of addition must range from the most effective modeling term to the least effective one. Their effectiveness is quantified by Equation 4.20. Adding terms to the cost function will improve the model fit and therefore decrease the value of the cost function $\tilde{J}$. The model term is in fact subtracted from the measurement term $\tilde{z}^T\tilde{z}$. Adding an additional term will however increase the value of the model complexity part of the PSE. At a certain moment, the decrease in cost function value will not weigh against the increase in the model complexity penalty. A global minimum of the PSE has been reached. The corresponding model structure will become the final model structure as a result of the multivariate orthogonal function modeling approach. This global minimum will only be achieved if model terms are added with decreasing effectiveness [70].

$$\left(\frac{2}{N}\right)\frac{\left(\tilde{p_j}\tilde{z}\right)^2}{\tilde{p_j}^T\tilde{p_j}} \tag{4.20}$$

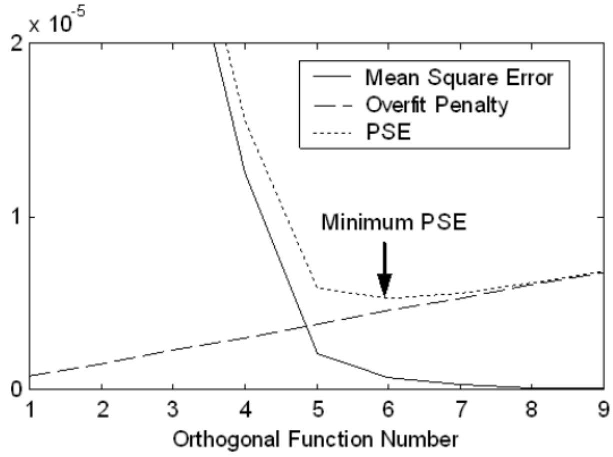

Figure 4.9: predicted squared error (PSE) metric exhibiting a global minimum as a result of decreasing cost function value and increasing model complexity penalty

4.5.2. Gram-Schmidt Orthogonalising of Ordinary Polynomial Functions

The procedure to create mutually orthogonal functions is according to Gram-Schmidt.The initial set of candidate regressor terms are ordinary multivariate polynomials and splines. All of them need to be orthogonalised with respect to all other functions. To start the procedure, a first ordinary multivariate model term is selected. A second term gets selected. The selection can be random. This second term needs to be orthogonalised with respect to the first term. The orthogonalisation is done according to Equation 4.21. From the ordinary multivariate model term $\tilde{\xi}_j$, the sum from the previously added mutual orthogonal multivariate terms p_k gets subtracted. Each previous orthogonal functions gets a specific scalar factor γ_{j_k}. This scalar invokes the mutual orthogonality by definition, see Equation 4.22.

$$\tilde{p_j} = \tilde{\xi}_j - \sum_{k=1}^{j-1} \gamma_{k_j} \tilde{p_k} \quad j = 2, 3, ..., n \tag{4.21}$$

$$\gamma_{k_j} = \frac{\tilde{p_k}^T \tilde{\xi}_j}{\tilde{p_k}^T \tilde{p_k}} \tag{4.22}$$

The procedure is repeated for all model terms. The summation however grows as it contains all previously orthogonalised functions to make sure the current function becomes mutually orthogonal to all model terms added before. The orthogonalised function $\tilde{p_j}$ is expressed as a linear expansion of the original ordinary multivariate function. No information or characteristics have been lost in the Gram-Schmidt orthogonalisation procedure. The orthogonalised function can also be de-orthogonalised towards the original ordinary function. After the model structure selection, the functions can be decomposed again to their ordinary form restoring the physical meaning to our model structure [70].

4.6. Evaluation of Multivariate Orthogonal Function Modeling

The procedure described above has been implemented applied to all individual stall manoeuvres of the Fokker 100 data set under consideration. The selected terms differed from stall to stall. The terms that got selected the most were included in the specific model. Some observations were made during the application of the procedure.

The outcome of the algorithm is subjected to the model terms included in the pool. Adding or removing candidate regressor terms altered the count of previously present terms and could therefore alter the ranking of model terms. The algorithm used by Van Ingen was slightly altered, reducing the subjectivity of the algorithm to the candidate pool. All candidate regressor terms are made mutually orthogonal to the entire set of candidate terms before the PSE metric is computed. Van Ingen used a stepwise orthogonalisation method instead, adding one term at a time.

Full decoupling of the model terms was however not achieved. The rank of the matrix containing all orthogonalised terms is slightly lower than full rank, indicating that there is still some dependence between a few orthogonalised model terms. This denies one of the assumptions of the multivariate orthogonal modelling algorithm. Yet, the outcome of the algorithm can serve as a good starting point. The algorithm was furthermore extended with a check to see if the term actually contributed to reducing the RMS of the model. If that was not the case, the term will be removed even though initially being selected.

During the quest to select the best possible model structure, it turned out that the multivariate orthogonal function modelling is not the 'holy grail'. A good sense of engineering judgement, evaluations of the RMS values, etc. is still required to tune the model structure towards the desired results.

4.7. Model Structure Selection

Using a pool of candidate regressor terms, a model structure for the 6 force and moment coefficients is selected. All 6 models for the Fokker 100 are discussed below.

4.7.1. Lift Coefficient C_L

The pool of candidate regressor terms for the lift coefficient (C_L) consists out of a bias term, α, $\dot{\alpha}$,$\left(\frac{1+\sqrt{X}}{2}\right)^2$, $(1-X)$, X, $max(0.5, X)$, p,q,r, δ_e, δ_a, δ_r, β and the second order combinations of the terms. Some unrealistic second order terms were manually removed based on engineering judgement. The bias term is set as a fixed parameter and will always be included in the model structure. A strong dependence on different X-related parameters is observed, Figure 4.10 .

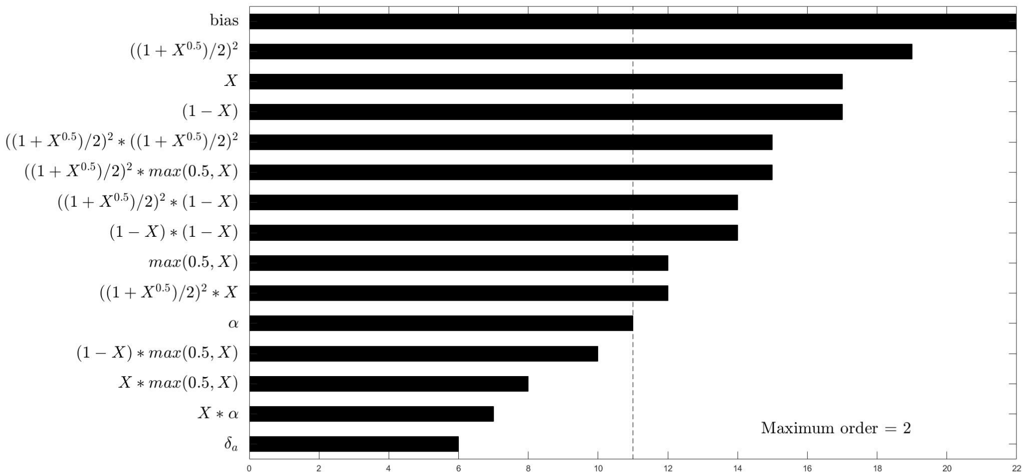

Figure 4.10: Result of the Multivariate Orthogonal Function Modeling Algorithm for the data set with flaps = 0° and different X-terms included in the pool.

Only one X-related term should be included in the model structure. As the Kirchhoff term $\left(\frac{1+\sqrt{X}}{2}\right)^2$ comes out as the highest ranked X-related term, combined with the extensive use found in literature, it was selected for the model structure. The other X-related terms are removed from the pool. Their presence influences the visibility of other good candidate regressor terms within the algorithm.

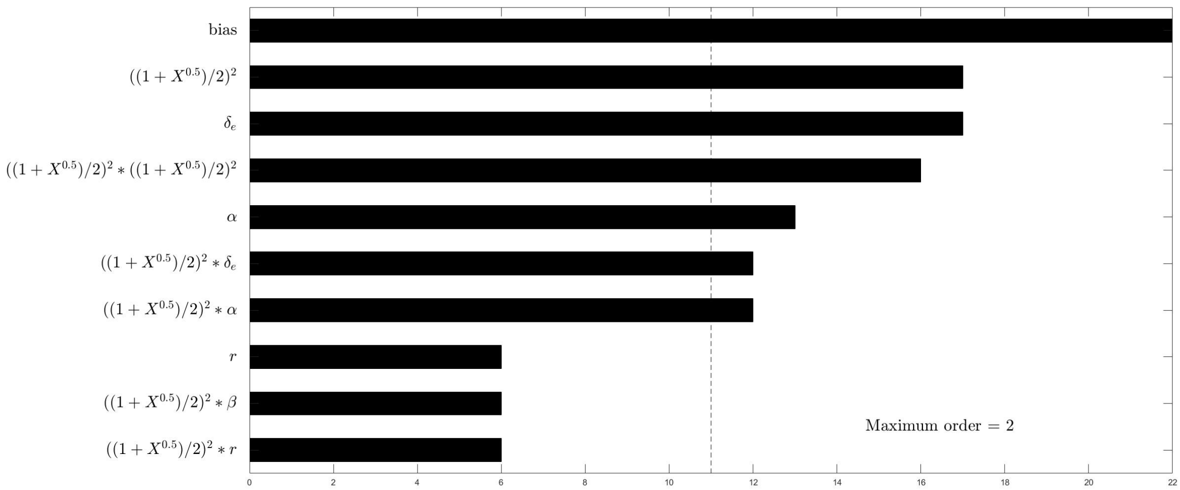

Figure 4.11: Result of the Multivariate Orthogonal Function Modeling Algorithm for the data set with flaps = 0° where only one X-related term (Kirchhoff term) is left in the pool.

The Fokker 100 data set intended certification of the aircraft. No specific excitation has been applied during stall. The information content of the data sets is therefore considered low. visual inspection of several measured C_L graphs, showed some wavy behaviour Looking further into the different measured signals also shows this behaviour in the aileron input and therefore also in the roll. As the data set has been selected for asymmetric behaviour at stall, this is a logic fact. It was therefore decided to include one of the two parameters in the model to capture this wavy behaviour. The multivariate orthogonal modeling algorithm favoured the inclusion of the aileron deflection δ_a. As lift coefficient (C_L) is a symmetric model, whilst δ_a is an asymmetric term, the absolute value of δ_a was used. If the aircraft wings are banked, the lift vector banks as well causing a decrease in vertical lift component, independent to which side the aircraft banks.

The insight delivered by the multivariate orthogonal function modeling algorithm created a starting point for the further derivation of the aircraft lift coefficient model and the identification of the model parameters.

5

Parameter Estimation

5.1. Kirchhoff Parameter Estimation

Kirchhoff's ODE, Equation 4.4, has 4 parameters that need to be estimated for the Fokker 100 aircraft. Those parameters are τ_1, τ_2, α^* and a_1. As they are part of the ODE, nonlinear estimation techniques are required to estimate their value. With their estimated value, the ODE can be solved with input of α to obtain the flow separation point X. X is part of a few model terms in the pool of candidate regressor terms for the final model structure. The four Kirchhoff parameters will therefore need to be estimated before the multivariate orthogonal function modelling algorithm is applied to select a model structure for the stall model of the F100.

The flow separation point X is closely related to the amount of lift produced and its relation to the lift coefficient C_L is well described by Equation 4.5. The estimation of Xwill therefore be done through the model for C_L. A model structure for C_L will therefore have to be assumed first and adapted by means of iterations later on if this is required to improve the model fit. Van Ingen performed a similar method for a longitudinal stall model of the Cessna Citation II. His identified C_L model structure will be used as initial model structure. The focus in this work will be put on the identification of the asymmetric stall model.

Nonlinear parameter estimation is a complex and challenging procedure. It is beyond the scope of this research to develop an estimation routine. Matlab contains an extensive nonlinear optimisation toolbox *fmincon* that will be used for the parameter estimation of the four kirchhoff terms. Nonlinear parameter estimation comes down on an optimisation routine minimising a cost function. This is exactly what the *fmincon* toolbox does. It computes a minimum for a constrained nonlinear multivariate function [91]. For this research, the mean squared error between the measured C_L and estimated C_L will be minimised. The estimated C_L must depend on Kirchhoff's X parameter in order to estimate the four Kirchhoff ODE parameters.

Nonlinear optimisation unfortunately does not offer the guarantee of convergence to the global minimum of the cost function. Chances are that a local minimum will be found. It is therefore advised to create a set of initial values within the physical and expected range of parameter values and run the optimisation for all these initial values. The lowest value will be taken as the optimal value, even though no certainty arises if this is actually the global optimum. Due to the computational expense and the lack of guarantee for global optimum convergence, nonlinear parameter estimation should be avoided. Only where absolutely necessary, it should be used. Kirchhoff's ODE cannot be solved without nonlinear parameter estimation techniques.

The Matlab *fmincon* has a series of algorithms to perform the minimisation. Further research has to be performed to select the best option. Van Ingen used trial-and-error to select the active set algorithm. All possible algorithms are listed below. The active set algorithm is also selected as algorithm for the Fokker 100 Kirchhoff parameter identification.

- Interior Point
- Thrust Region Reflection

- Sequential Quadratic Programming
- Sequential Quadratic Programming Legacy
- Active Set

The algorithms use the function gradient at each iteration to improve their estimate and move towards the (local) minimum. Computing gradients can be expensive. If the gradient of the function is known, it should be given as an input to the nonlinear solver toolbox of Matlab to increase the computational speed and reliability. If no gradient is supplied, Matlab will use the finite difference method to compute it.

5.2. Aerodynamic Model Parameter Estimation

Once τ_1, τ_2, a_1 and α^* have been set, the six models for the aerodynamic force and moment equation can be determined. Note that changes in the model structure for C_L requires re-estimation of τ_1, τ_2, a_1 and α^*. The multivariate orthogonal function modeling explained in section 4.5 must be applied to determine the five other aerodynamic force and moment coefficient model structures. As the Kirchhoff parameters are assigned a fixed value eventually, the non-linearity in the model structure dissolves and the remainder of the parameter estimation routine can be solved using efficient linear solvers. convergence to global minima is guaranteed.

The stall model can schematically be written as

$$\hat{y}(\theta) = A\theta \tag{5.1}$$

where $\hat{y}(\theta)$ is the estimated model output, A the matrix with regressor terms that have been selected using the multivariate orthogonal function modeling and θ the vector of parameters to be estimated. A cost function must be selected to determine the parameter vector $\hat{\theta}$ that minimises the error between the measured output and the model output. The well-known ordinary least squares (OLS) method will be used here, Equation 5.2.

$$J(\theta) = \frac{1}{2}\left(y - \hat{y}(\theta)\right)^T \left(y - \hat{y}(\theta)\right) = \frac{1}{2}\left(y - A\theta\right)^T \left(y - A\theta\right) \tag{5.2}$$

Taking the derivative of the cost function $J(\theta)$ towards the parameters θ and setting it to zero results in the minimum values for $\hat{\theta}$. The equation to be solved is given by Equation 5.4.

$$\frac{\partial J(\hat{\theta})}{\partial \theta} = 0 \tag{5.3}$$

$$\hat{\theta} = \left[A^T A\right]^{-1} A^T y \tag{5.4}$$

The OLS method is derived under the assumption that errors between the actual and modeled output are normally distributed. This assumption may become invalid for significant modeling errors above the sensor noise.

5.3. Evaluating Model Quality

Once the optimisation routine has been performed on the selected model structure, the results will be validated. Only a part of the 79 stalls selected will be used for identification. For each configuration, with the exception of 6° and 25° flap setting, a division will be made between identification data sets and validation data set. The input data of the validation data sets will be fed to the identified model structure and the output of the model will be compared with the measured output of the validation set. The quality of the model can be evaluated using mean squared error (MSE) as well as looking into the parameter covariance to discover parameters that are too tightly coupled to each other and therefore cause identification issues. In such cases, it might be better to leave out one term to improve the model fit. Further research is to be performed to find other metrics that are useful in quantification of the validation.

The identification of parameter values is again performed separately for each data set. This will lead to variances in their value. For the identification of the X-parameters, several runs with varying initial conditions will be done for each data set. This is required as nonlinear optimisation does not guarantee the convergence to the global minimum. Statistical tests will be used to evaluate the distribution and deviation from normal distribution of parameter value outcomes for the different data sets used for identification. Further research is yet to be performed to determine which statistical tests will be used and how to interpret their results and possibly use them to improve the model quality.

5.4. Model Parameter Identification

5.4.1. Kirchoff Parameters Identification

The identification of the Kirchhoff parameters was performed synchronously with the selection and parameter identification of the C_L model. Starting from a initial model structure and parameter values, an iteration is started in which the X-parameters and aerodynamic C_L parameters are identified separately. The X-parameters are identified using the *fmincon* nonlinear optimisation toolbox and the *active set* algorithm of Matlab. The identified values are kept fixed to allow a linear optimisation of the aerodynamic parameters with global minimum convergence guarantees. These found parameters are kept fixed to iterate over the X-parameters again. This iteration holds until no visual improvements in model fit are observed.

Many attempts have been made to find a suitable model for C_L. A dozen of model structure have been tested. The structures were based on the outcome of the multivariate orthogonal function modeling, engineering judging, visual comparison between curve behaviour of C_L and different measured parameters and comparison to model structures found in literature. The limits of the information content of the Fokker 100 stall database were however encountered. The certification data contains too little excitation and information to identify a proper model.

The initial selected model included the elevator deflection. This caused problems in the identification of α^*, although being generally considered as an easy-to-identify parameter. α^* determines the stall angle of attack and therefore can be easily related to the maximum C_L value observed. It is furthermore known that the stall angle of attack decreases for increasing flap setting. The lift curve shifts to the origin for simple flap systems. For complex slotted flap system, the curve tilts backwards as well, further decreasing the stall angle of attack, Figure 5.1. As the Fokker 100 database contains stalls at different flap settings, a decrease in α^* is expected for increasing flap settings.

$$C_L = C_{L0} + C_{L_\alpha}\left(\frac{1+\sqrt{X}}{2}\right)^2 \alpha + C_{L_{\delta_a}}|\delta_a| + C_{L_{\delta_e}}\delta_e \tag{5.5}$$

The inclusion of elevator deflection δ_e resulted into underestimation of α^*, whilst having very similar values for the range of flap settings. The underestimation of α^* is visible in Figure 5.2. The bottom graph shows the effect of varying α^* values on the baseline C_L model. The black line is the identified model, whilst the full magenta line is the measured baseline model. To capture the peak in C_L, occurring at maximum AoA, the value of α^* should go towards 0.35 rad (about 20°). Inspecting raw AoA plots also indicates that the maximum AoA reached lies somewhere between 20 - 25°. The identified value of α^* is however just above the lower bound of 0.3 rad set in the *fmincon* toolbox. Values slightly above 0.3 rad are found for all flap settings.

From Figure 5.2, it is also visible that τ_2 has no visual effect on the C_L curve. Identifying the correct value is therefore unimportant as the value does not affect the C_L curve. It is therefore decided to set its value to 0 and thus leave out the τ_2-related term from the Kirchhoff ODE.

The spread of the parameters estimated for the data set with flaps = 0°, is given by Figure 5.3. There is a strong correlation between C_{L_0} and C_{L_α}, $\rho = -0.98$. As both parameter are essential parts of the model, none of both

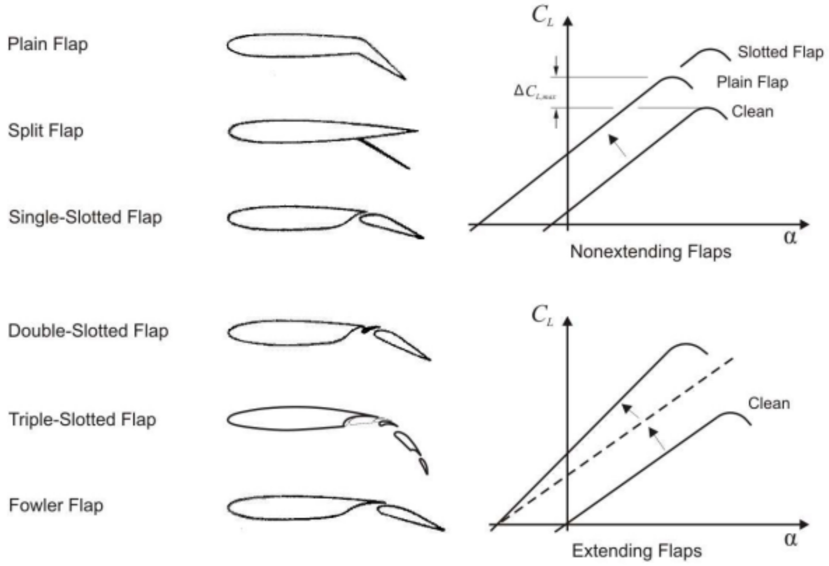

Figure 5.1: Effect of flap setting on lift curve slope, DATCOM 1978

can be removed due to their correlated behaviour. Furthermore, a less strong correlation can be observed between C_{L_α} and $C_{L_{\delta_e}}$, $\rho = 0.82$.

Removing the δ_e term from the C_L model improved the identification of α^*, its behaviour over ranging flap settings as well as the RMS value of both training and validation data set. Replacing the δ_e-term by the pitching moment q improved the RMS values again. The final model used is given by Equation 5.6.

$$C_L = C_{L_0} + C_{L_\alpha}\left(\frac{1+\sqrt{X}}{2}\right)^2 \alpha + C_{L_{\delta_a}}|\delta_a| + C_{L_q} q \tag{5.6}$$

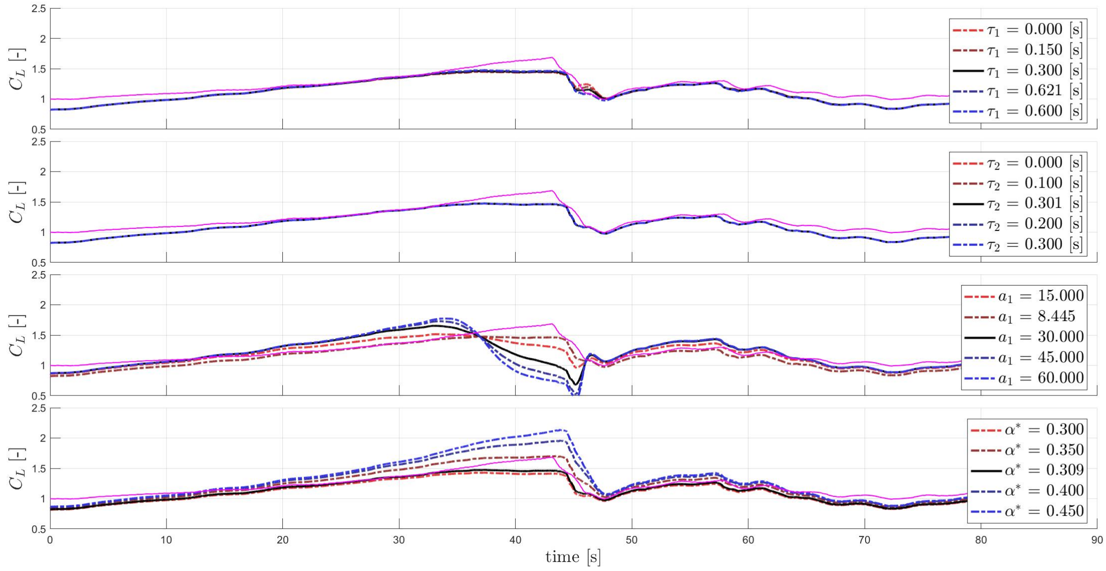

Figure 5.2: Effect of ranging value of the X-parameters on the baseline C_L curve (thin full magenta line) for Equation 5.5, flaps = 0°.

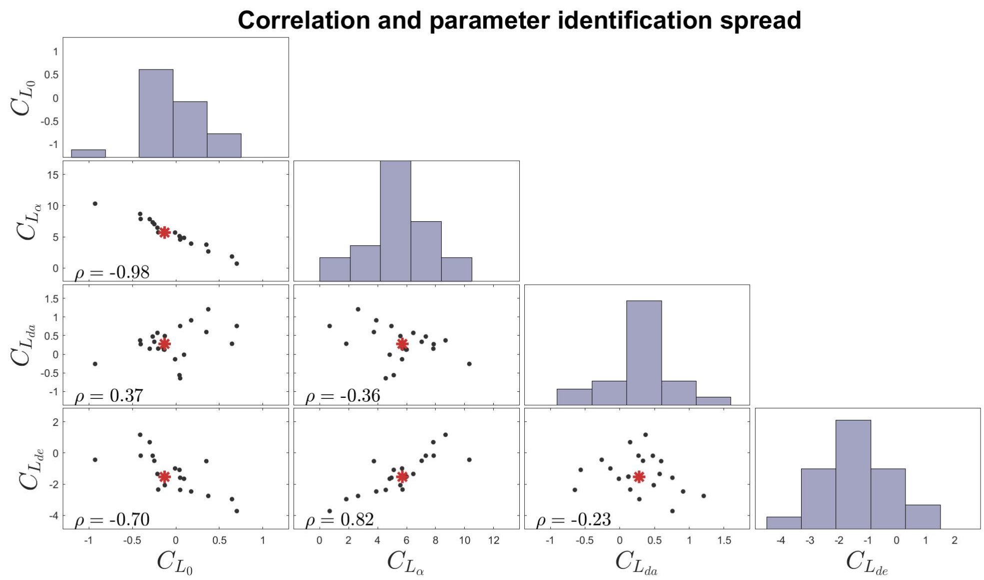

Figure 5.3: Correlation and spread of the identified aerodynamic parameters for Equation 5.5, flaps = 0°.

A

Time Series

A.1. Clean Configuration

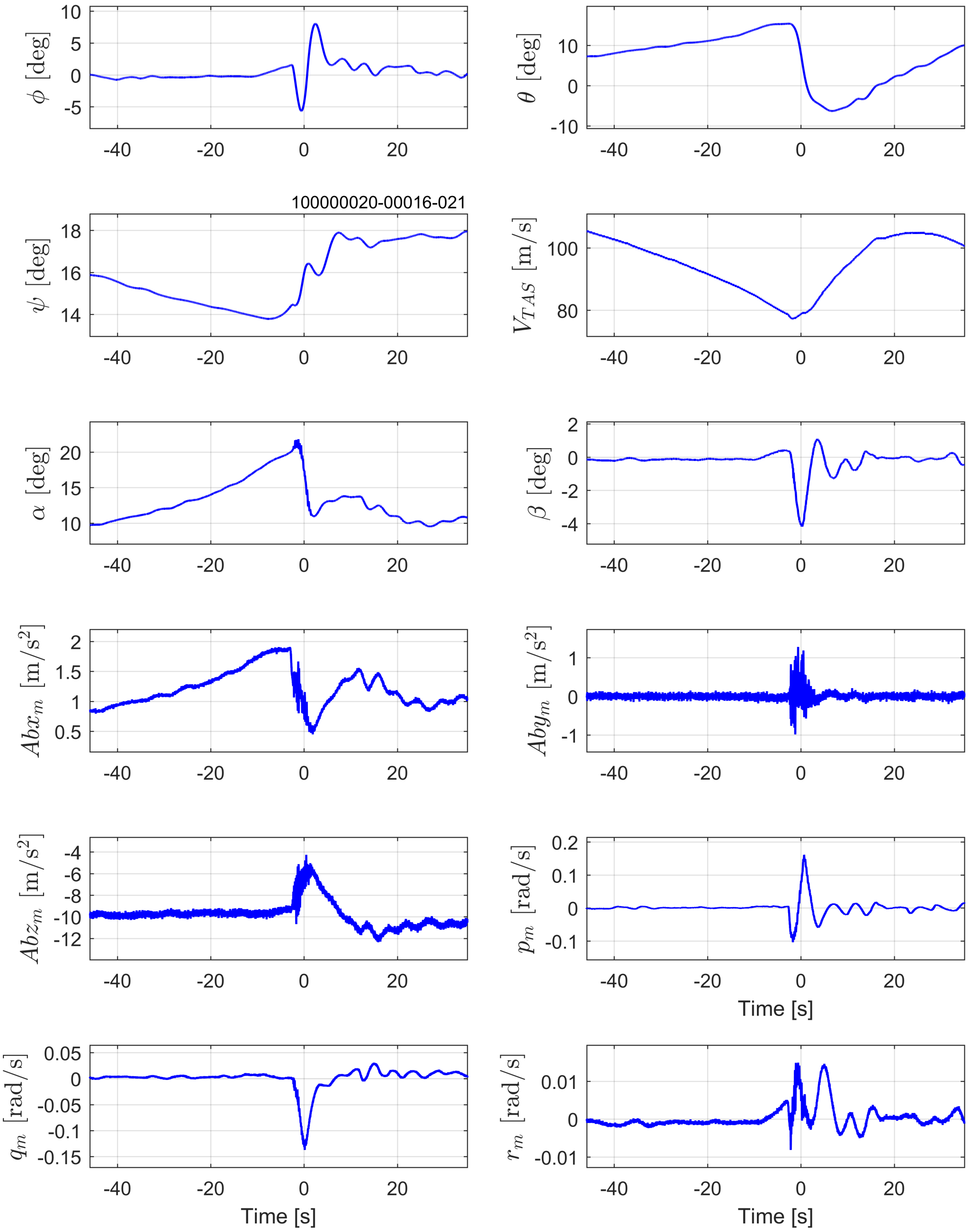

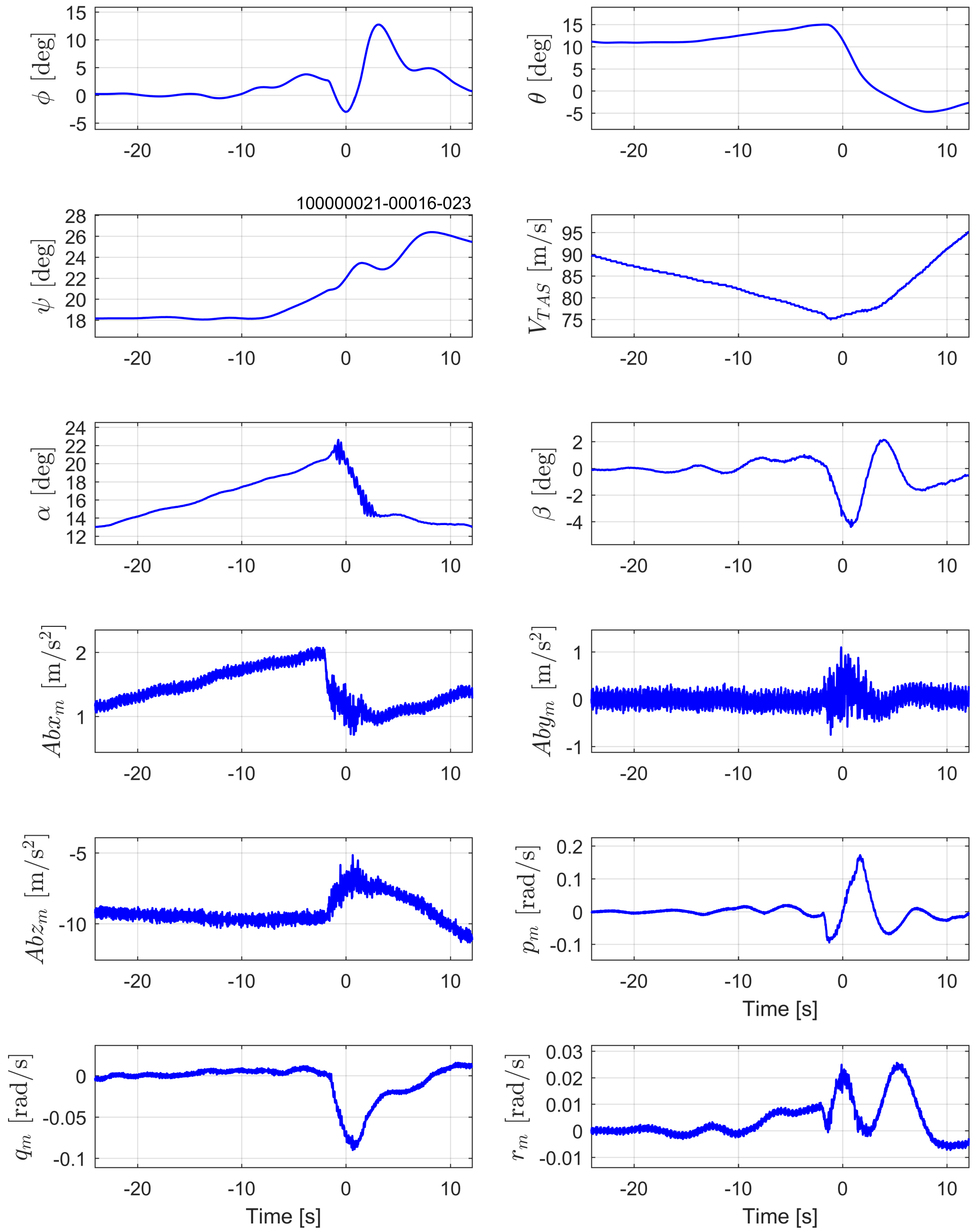

100000021-00016-023
ϕ [deg]
θ [deg]
ψ [deg]
V_TAS [m/s]
α [deg]
β [deg]
Abx_m [m/s²]
Aby_m [m/s²]
Abz_m [m/s²]
p_m [rad/s]
q_m [rad/s]
r_m [rad/s]
Time [s]

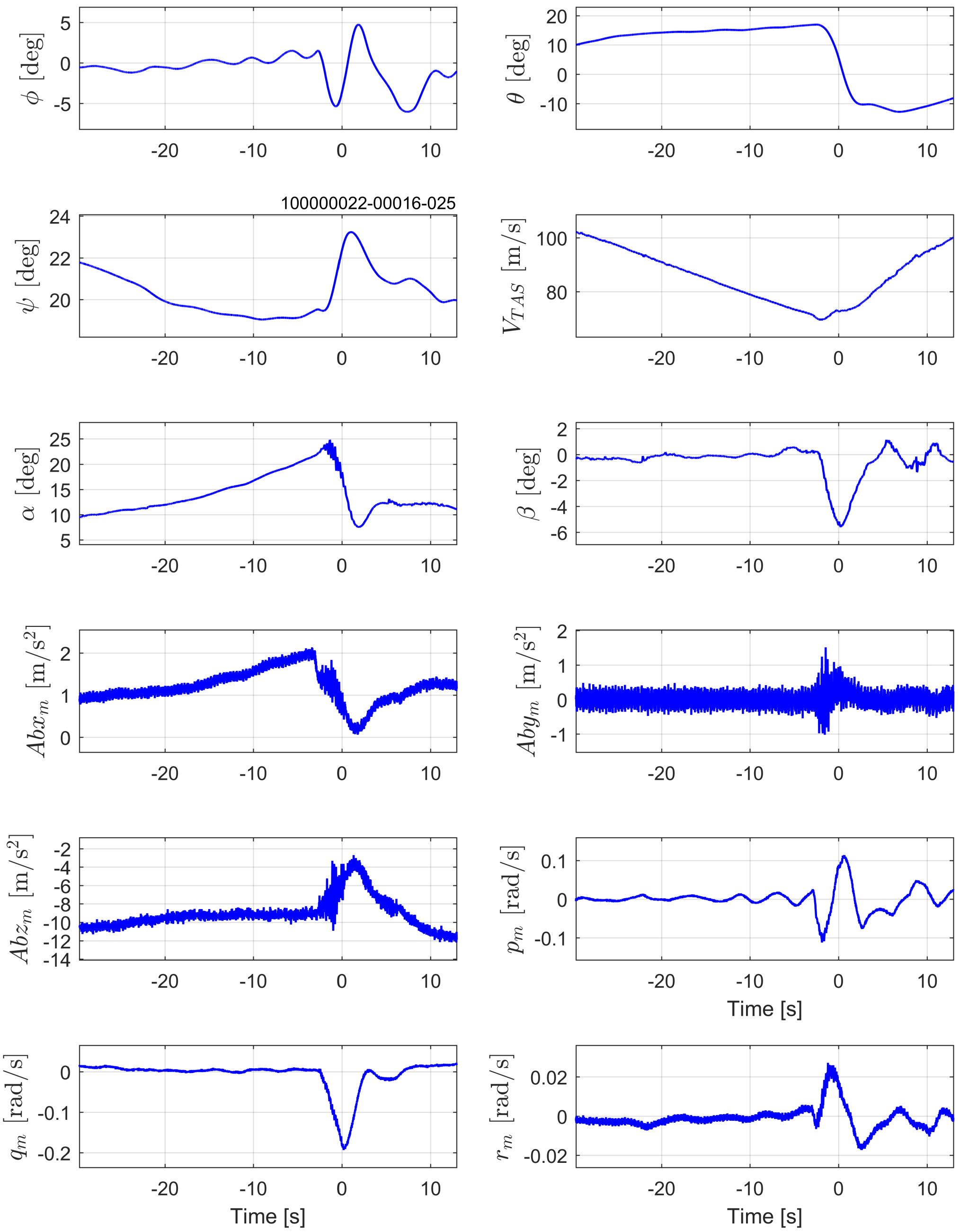

100000022-00016-025
ϕ [deg]
θ [deg]
ψ [deg]
V_{TAS} [m/s]
α [deg]
β [deg]
Abx_m [m/s^2]
Aby_m [m/s^2]
Abz_m [m/s^2]
p_m [rad/s]
q_m [rad/s]
r_m [rad/s]
Time [s]
Time [s]
Time [s]

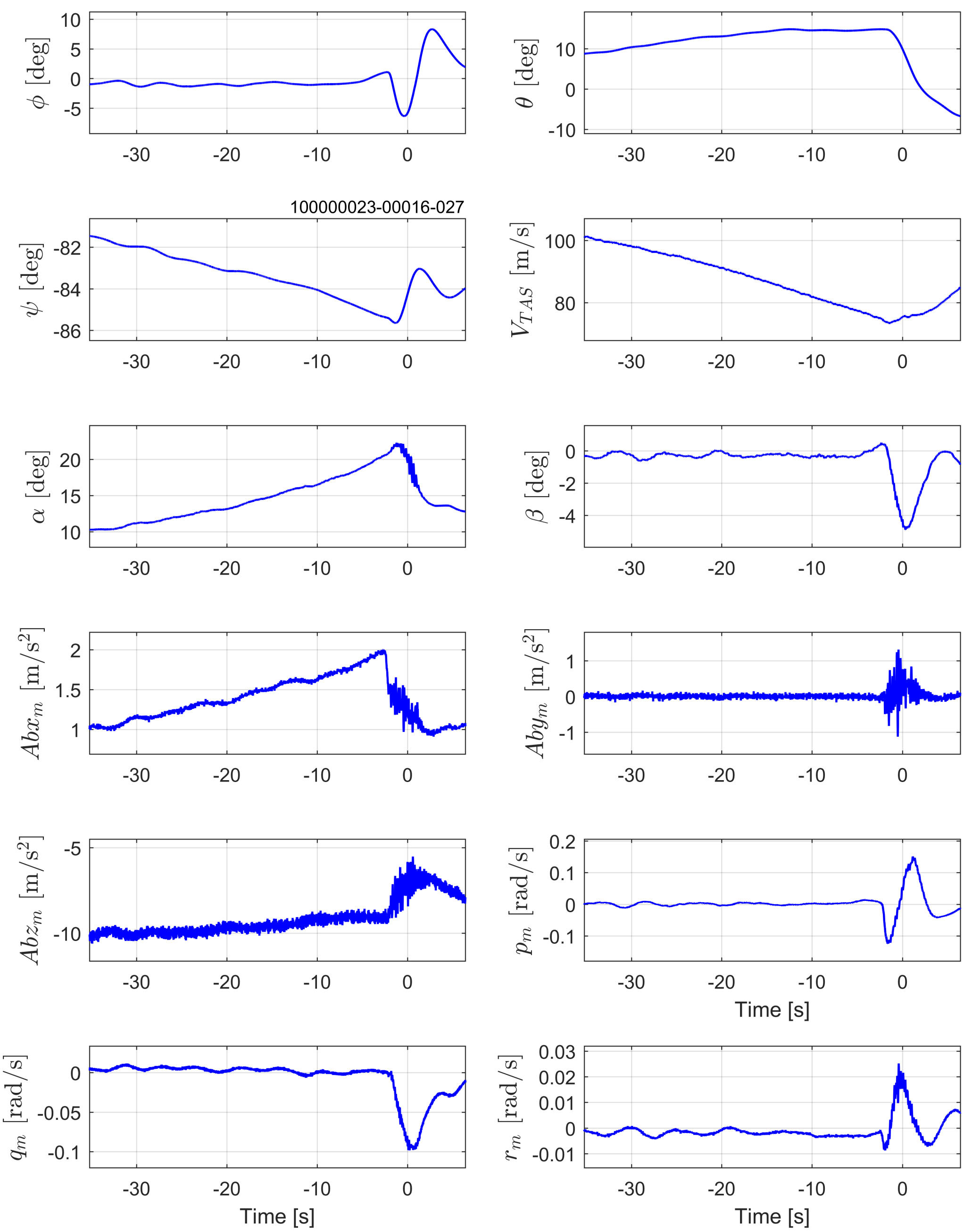
100000023-00016-027
φ [deg]
θ [deg]
ψ [deg]
V_TAS [m/s]
α [deg]
β [deg]
Abx_m [m/s²]
Aby_m [m/s²]
Abz_m [m/s²]
p_m [rad/s]
q_m [rad/s]
r_m [rad/s]
Time [s]
Time [s]
Time [s]

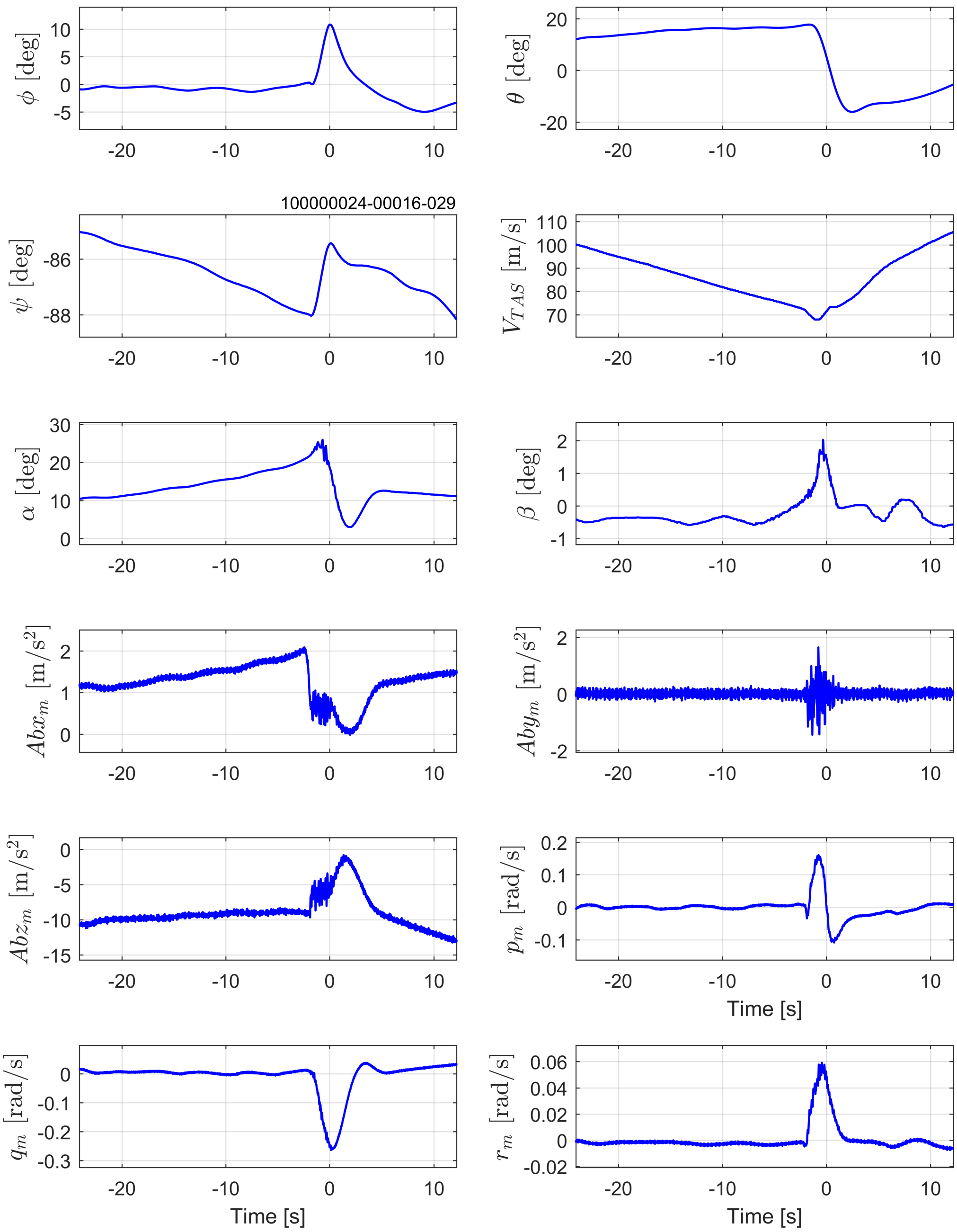

ϕ [deg]
θ [deg]
100000024-00016-029
ψ [deg]
V_{TAS} [m/s]
α [deg]
β [deg]
Abx_m [m/s^2]
Aby_m [m/s^2]
Abz_m [m/s^2]
p_m [rad/s]
q_m [rad/s]
r_m [rad/s]
Time [s]

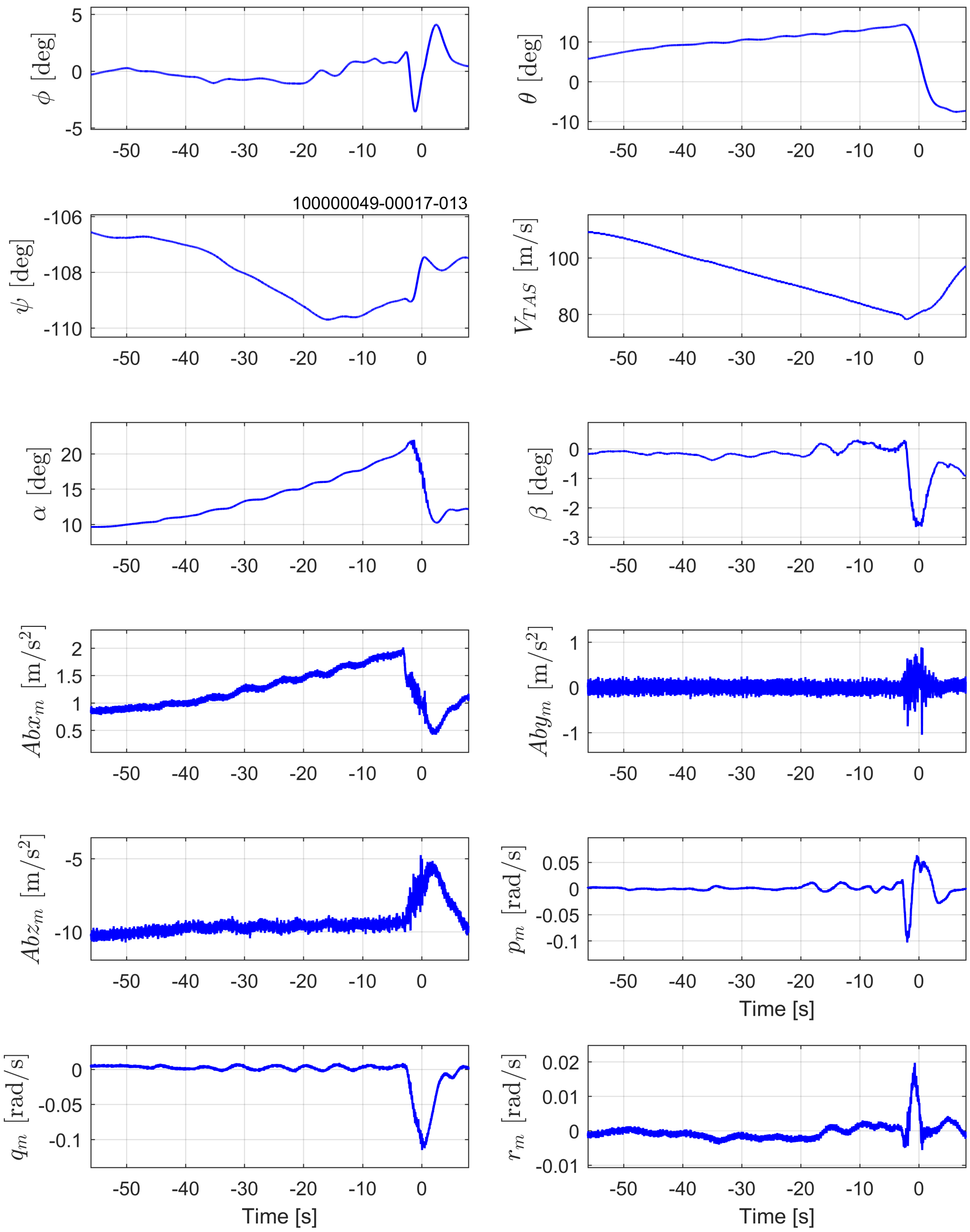

100000049-00017-013
ϕ [deg]
θ [deg]
ψ [deg]
V_{TAS} [m/s]
α [deg]
β [deg]
Abx_m [m/s^2]
Aby_m [m/s^2]
Abz_m [m/s^2]
p_m [rad/s]
q_m [rad/s]
r_m [rad/s]
Time [s]

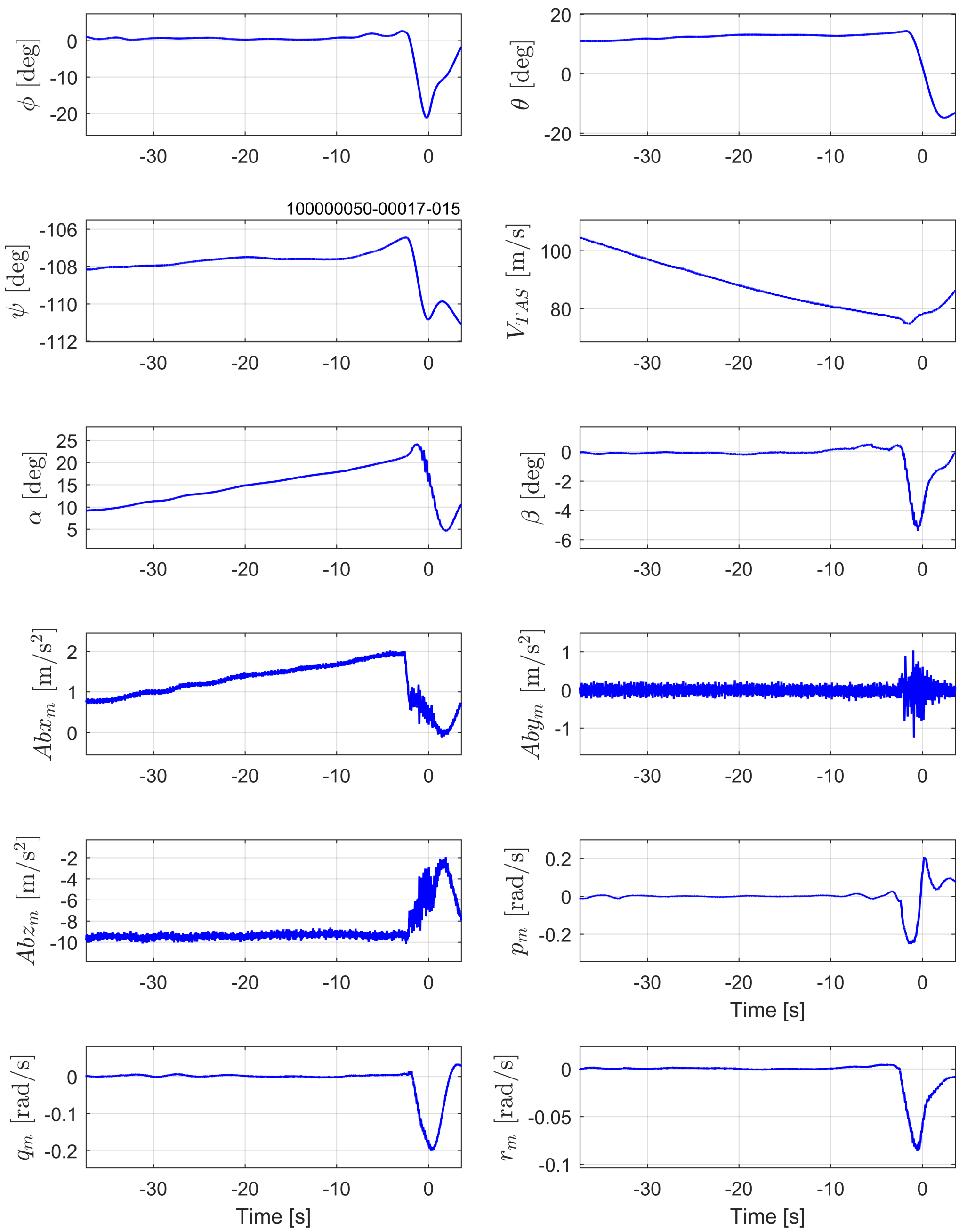

100000050-00017-015
ϕ [deg]
θ [deg]
ψ [deg]
V_{TAS} [m/s]
α [deg]
β [deg]
Abx_m [m/s^2]
Aby_m [m/s^2]
Abz_m [m/s^2]
p_m [rad/s]
q_m [rad/s]
r_m [rad/s]
Time [s]

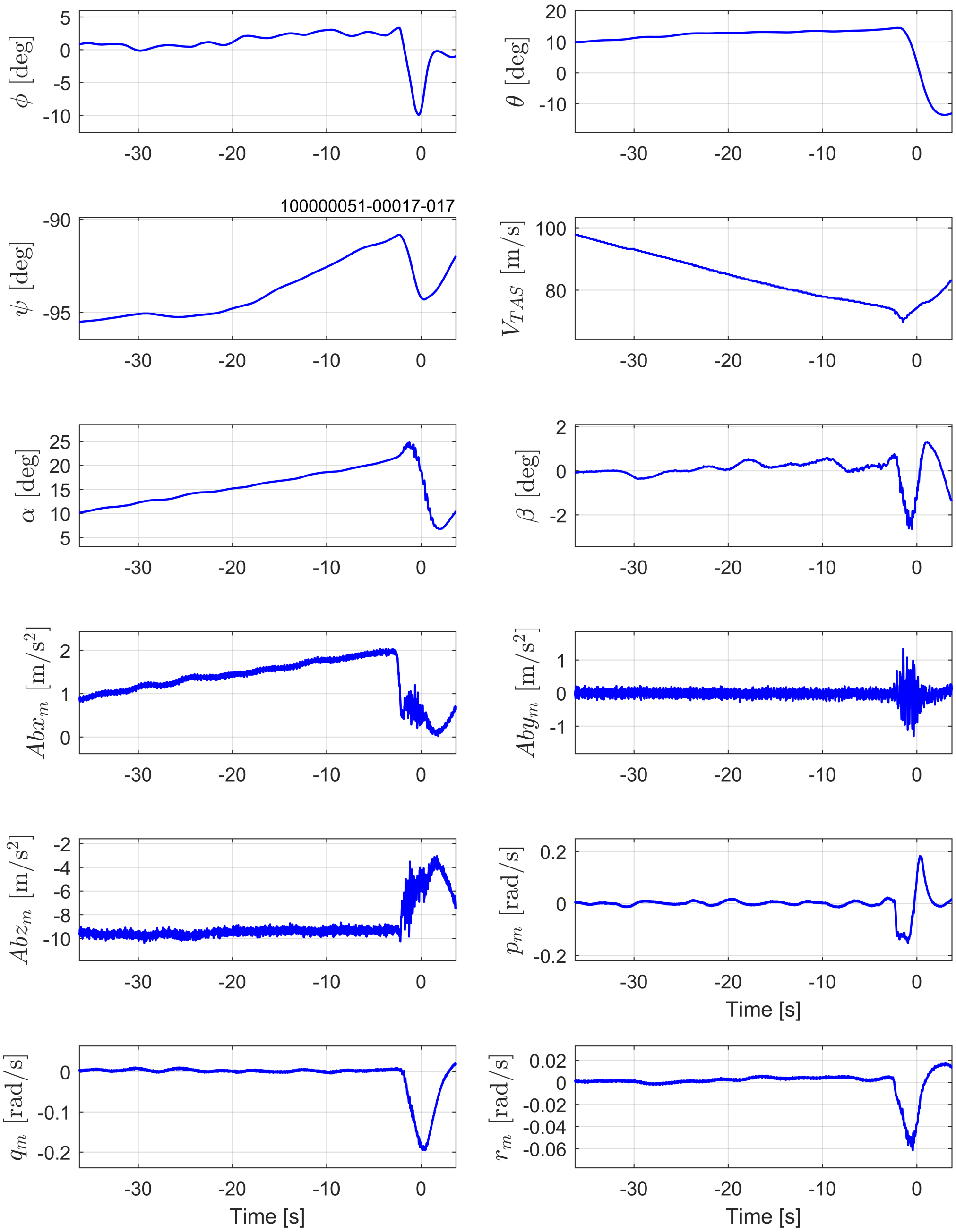
ϕ [deg]
θ [deg]
100000051-00017-017
ψ [deg]
V_{TAS} [m/s]
α [deg]
β [deg]
Abx_m [m/s^2]
Aby_m [m/s^2]
Abz_m [m/s^2]
p_m [rad/s]
q_m [rad/s]
r_m [rad/s]
Time [s]
Time [s]
Time [s]

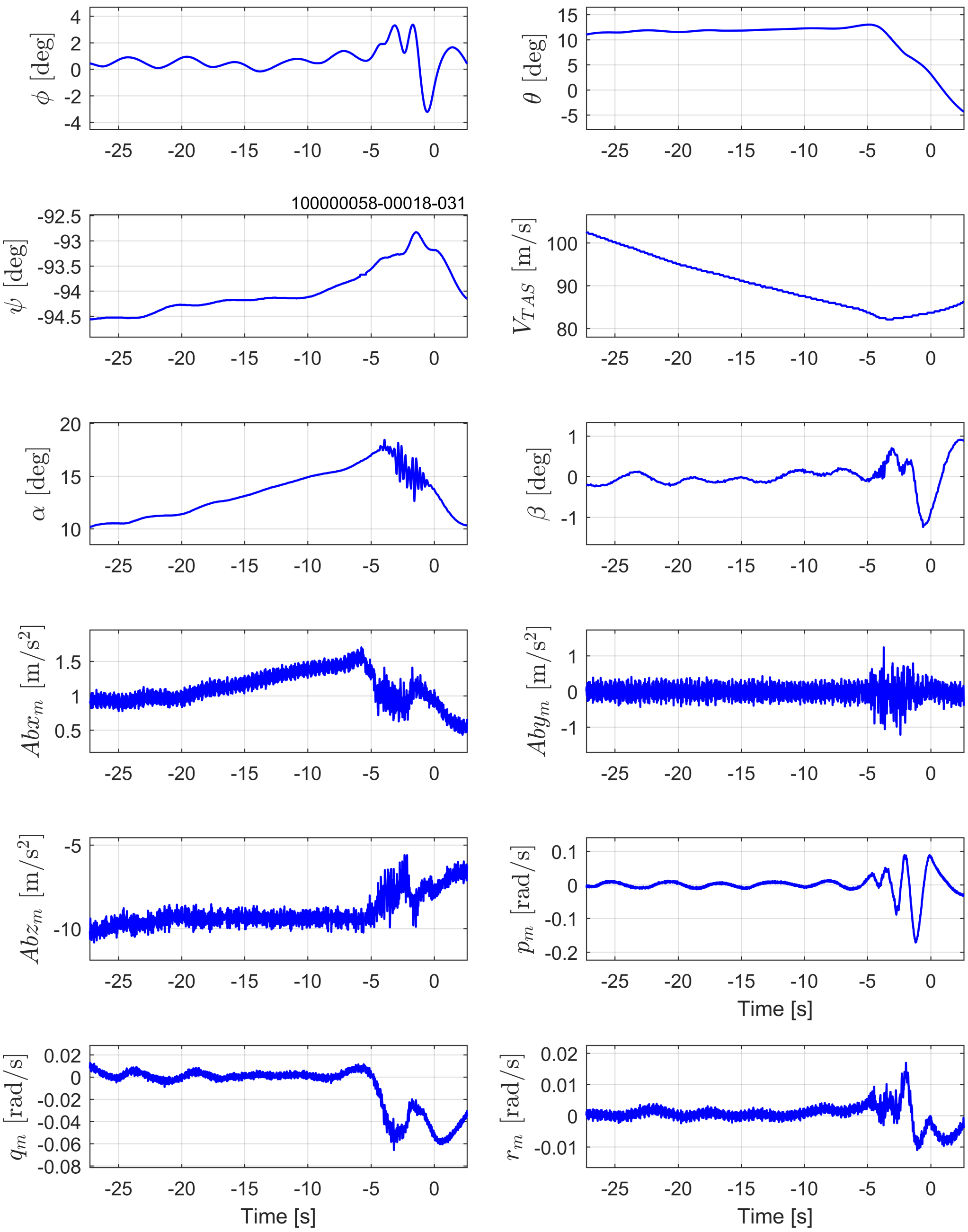

ϕ [deg]
θ [deg]
100000058-00018-031
ψ [deg]
V_{TAS} [m/s]
α [deg]
β [deg]
Abx_m [m/s^2]
Aby_m [m/s^2]
Abz_m [m/s^2]
p_m [rad/s]
q_m [rad/s]
r_m [rad/s]
Time [s]
Time [s]
Time [s]

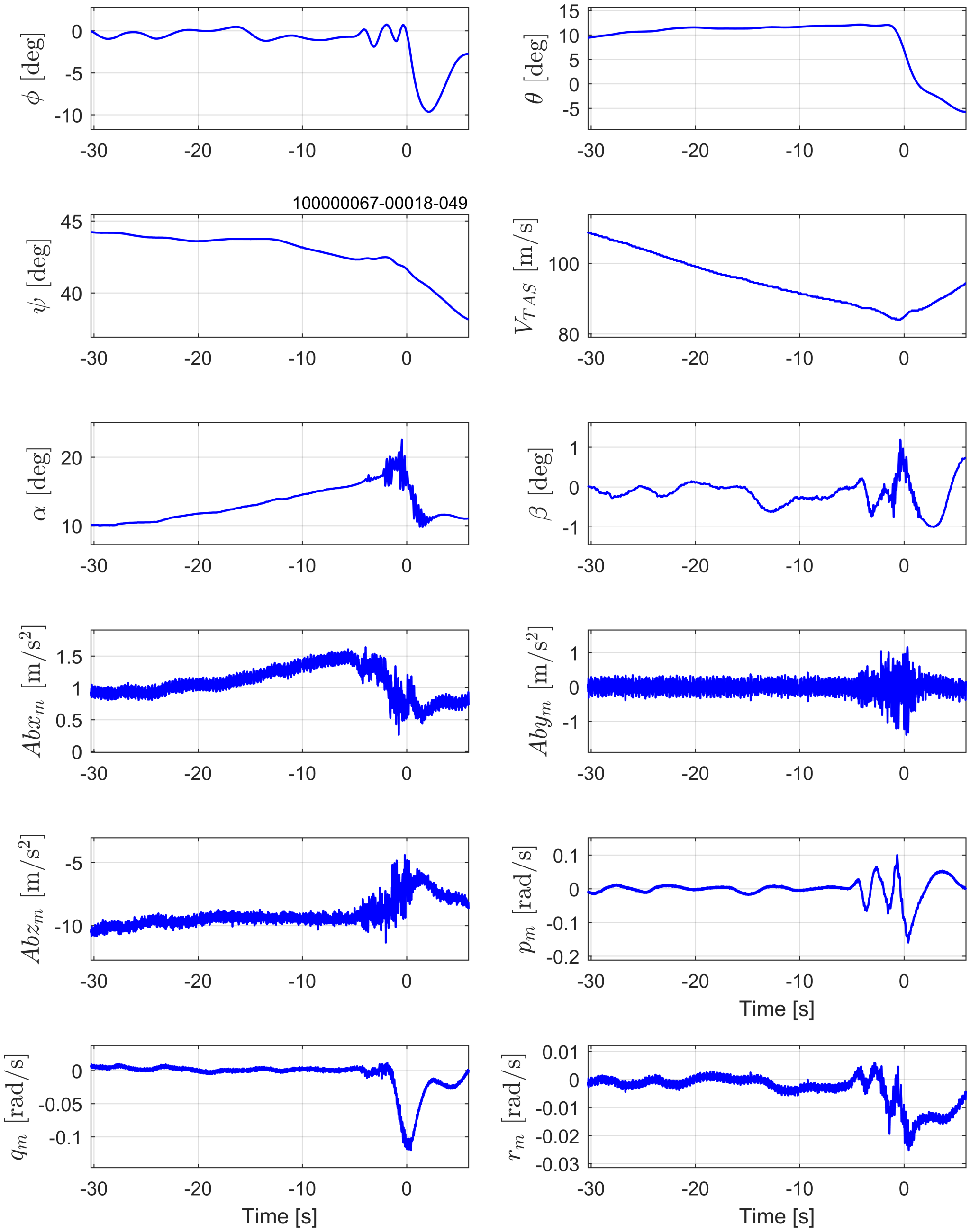
100000067-00018-049
ϕ [deg]
θ [deg]
ψ [deg]
V_{TAS} [m/s]
α [deg]
β [deg]
Abx_m [m/s^2]
Aby_m [m/s^2]
Abz_m [m/s^2]
p_m [rad/s]
q_m [rad/s]
r_m [rad/s]
Time [s]

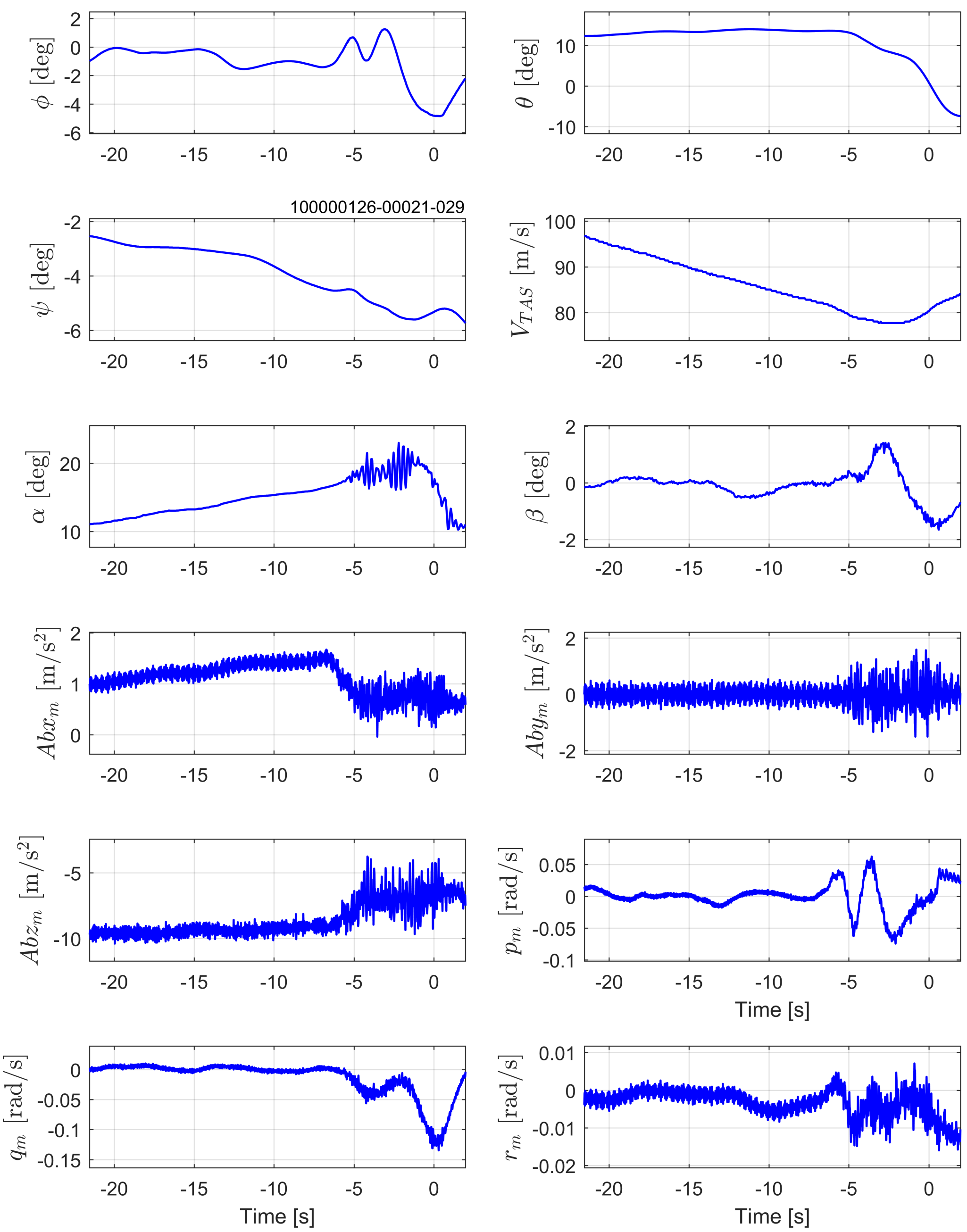
100000126-00021-029
ϕ [deg]
θ [deg]
ψ [deg]
V_{TAS} [m/s]
α [deg]
β [deg]
Abx_m [m/s^2]
Aby_m [m/s^2]
Abz_m [m/s^2]
p_m [rad/s]
q_m [rad/s]
r_m [rad/s]
Time [s]

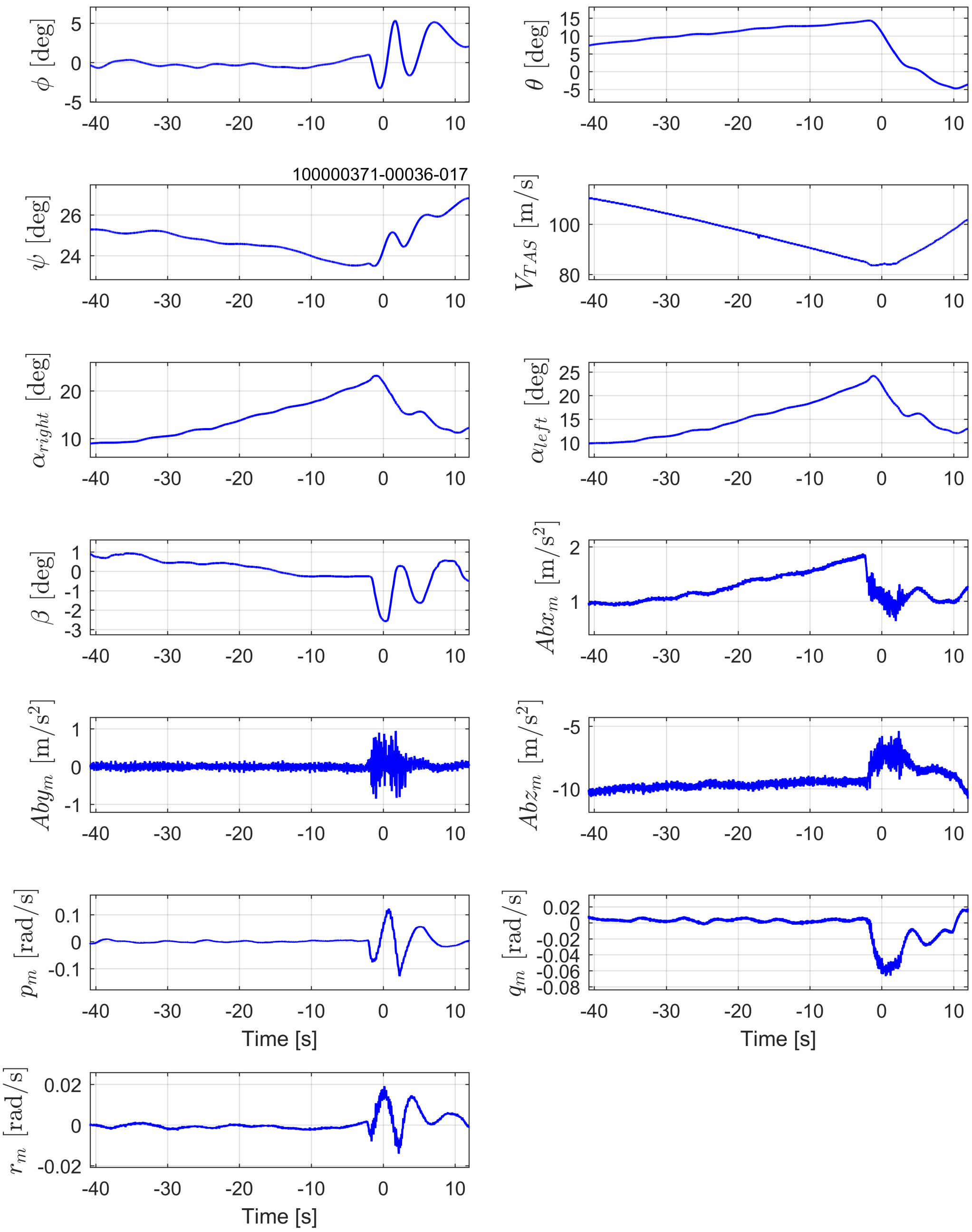
ϕ [deg]
θ [deg]
100000371-00036-017
ψ [deg]
V_{TAS} [m/s]
α_{right} [deg]
α_{left} [deg]
β [deg]
Abx_m [m/s^2]
Aby_m [m/s^2]
Abz_m [m/s^2]
p_m [rad/s]
q_m [rad/s]
r_m [rad/s]
Time [s]

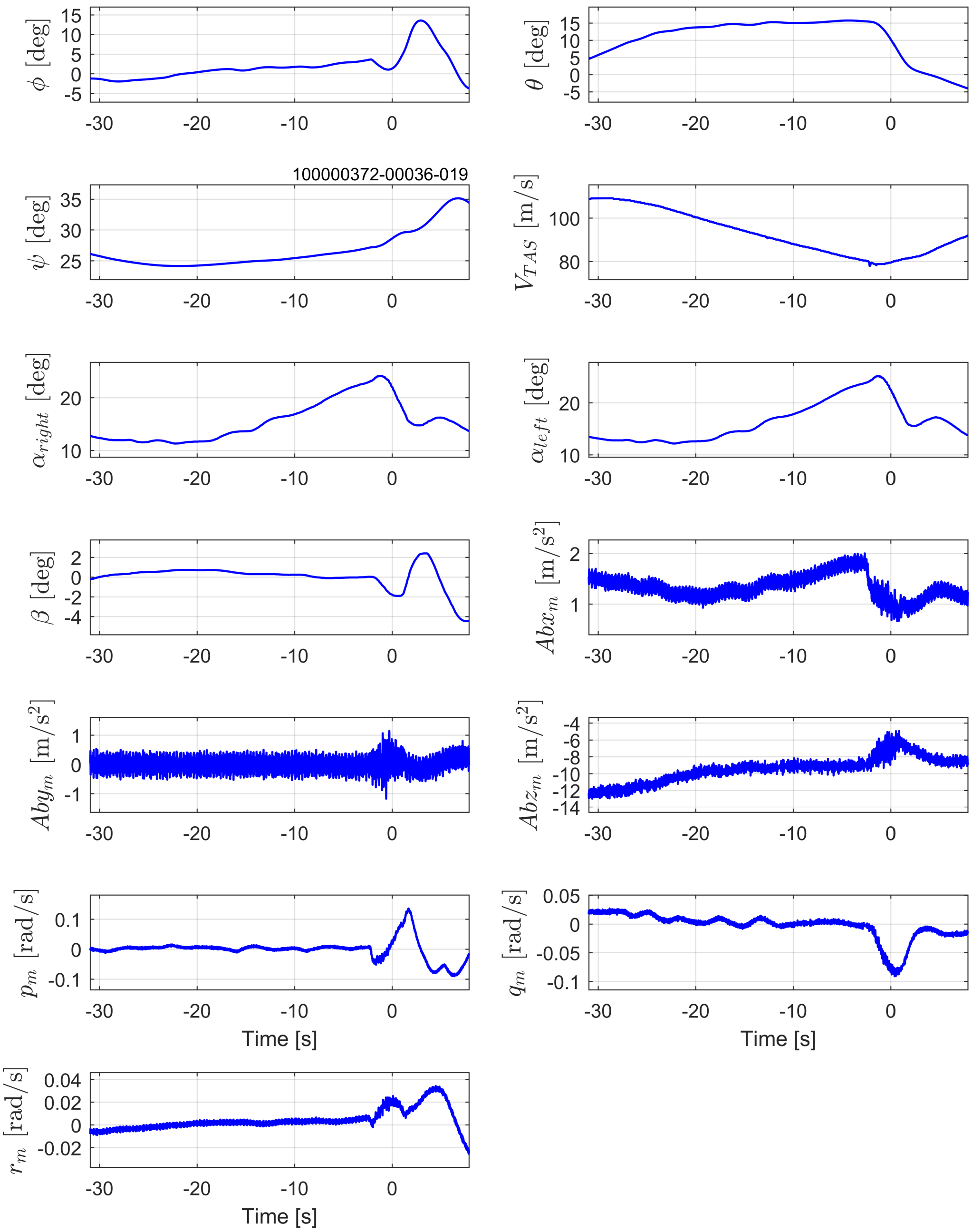
ϕ [deg]
θ [deg]
100000372-00036-019
ψ [deg]
V_{TAS} [m/s]
α_{right} [deg]
α_{left} [deg]
β [deg]
Abx_m [m/s^2]
Aby_m [m/s^2]
Abz_m [m/s^2]
p_m [rad/s]
q_m [rad/s]
r_m [rad/s]
Time [s]

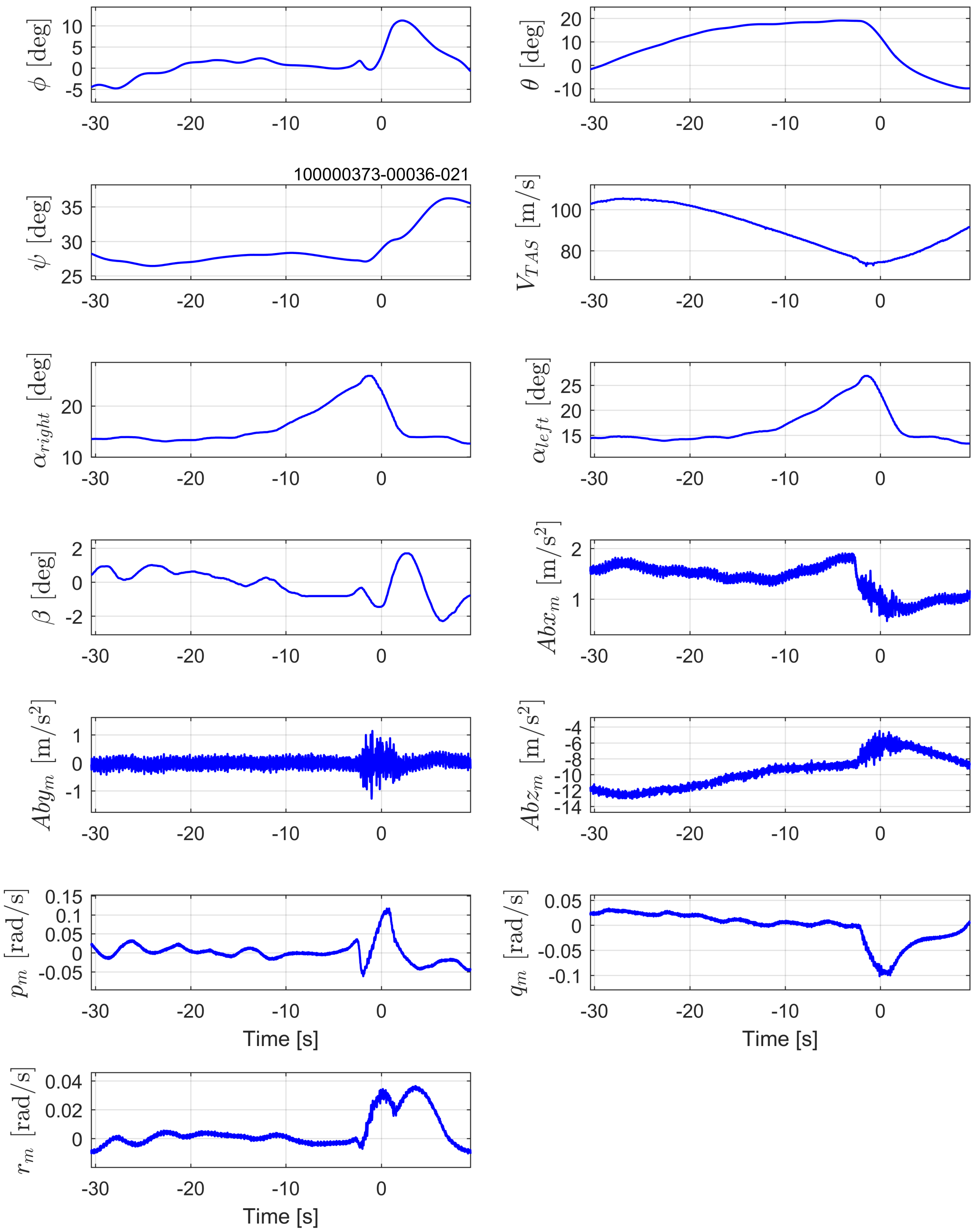

100000373-00036-021
ϕ [deg]
θ [deg]
ψ [deg]
V_{TAS} [m/s]
α_{right} [deg]
α_{left} [deg]
β [deg]
Abx_m [m/s^2]
Aby_m [m/s^2]
Abz_m [m/s^2]
p_m [rad/s]
q_m [rad/s]
r_m [rad/s]
Time [s]

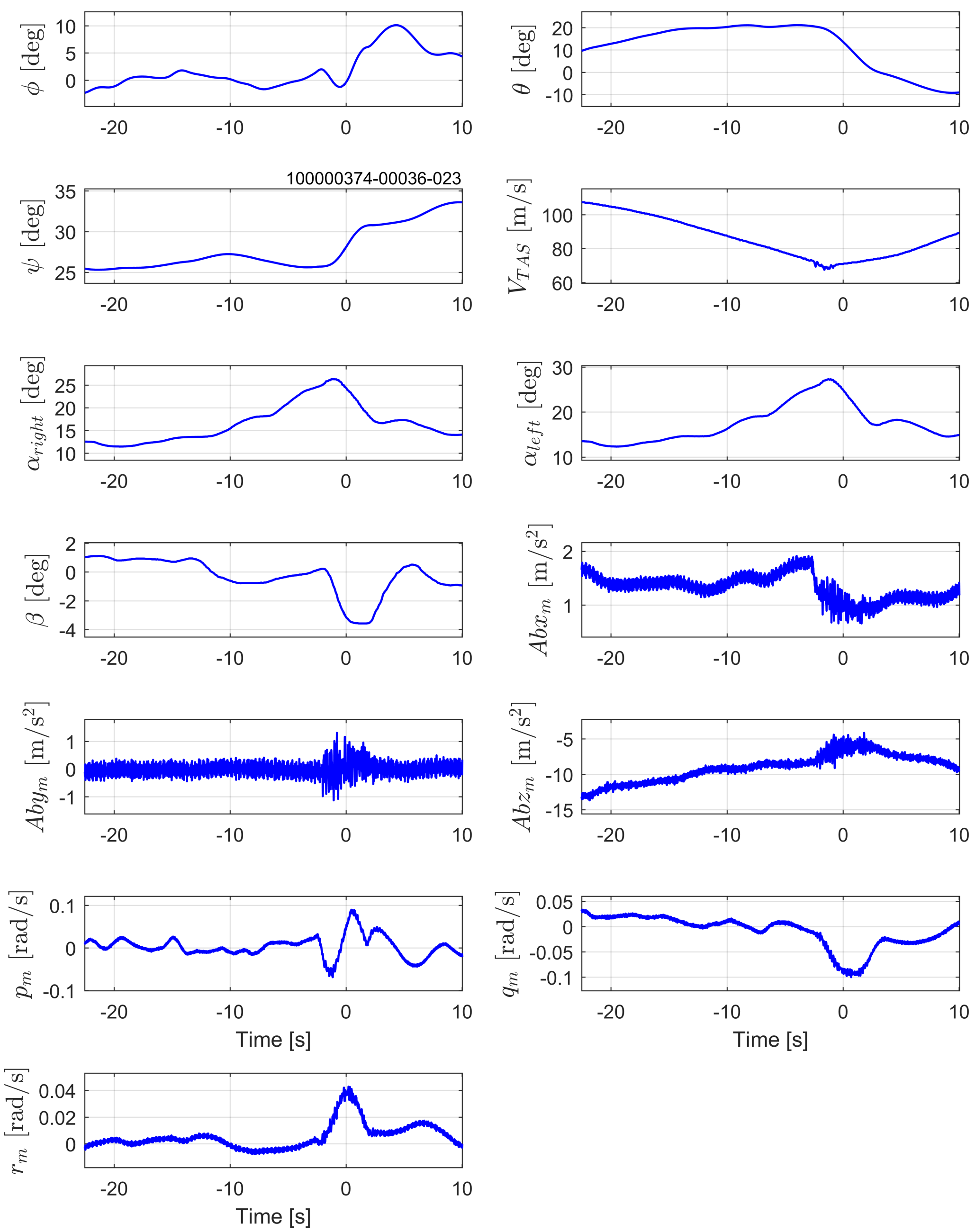

ϕ [deg]
θ [deg]
100000374-00036-023
ψ [deg]
V_{TAS} [m/s]
α_{right} [deg]
α_{left} [deg]
β [deg]
Abx_m [m/s^2]
Aby_m [m/s^2]
Abz_m [m/s^2]
p_m [rad/s]
q_m [rad/s]
r_m [rad/s]
Time [s]

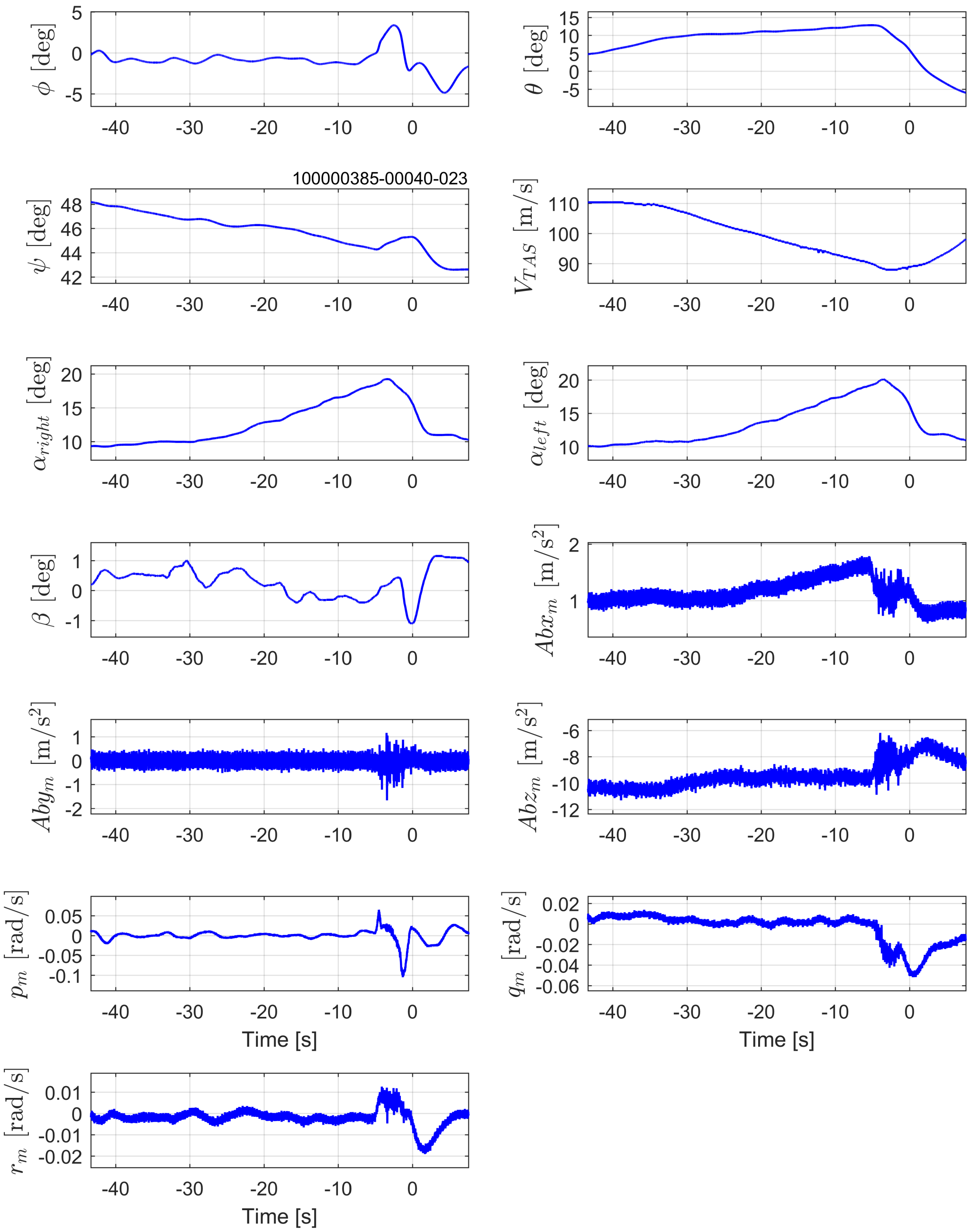

ϕ [deg]
θ [deg]
100000385-00040-023
ψ [deg]
V_{TAS} [m/s]
α_{right} [deg]
α_{left} [deg]
β [deg]
Abx_m [m/s^2]
Aby_m [m/s^2]
Abz_m [m/s^2]
p_m [rad/s]
q_m [rad/s]
r_m [rad/s]
Time [s]

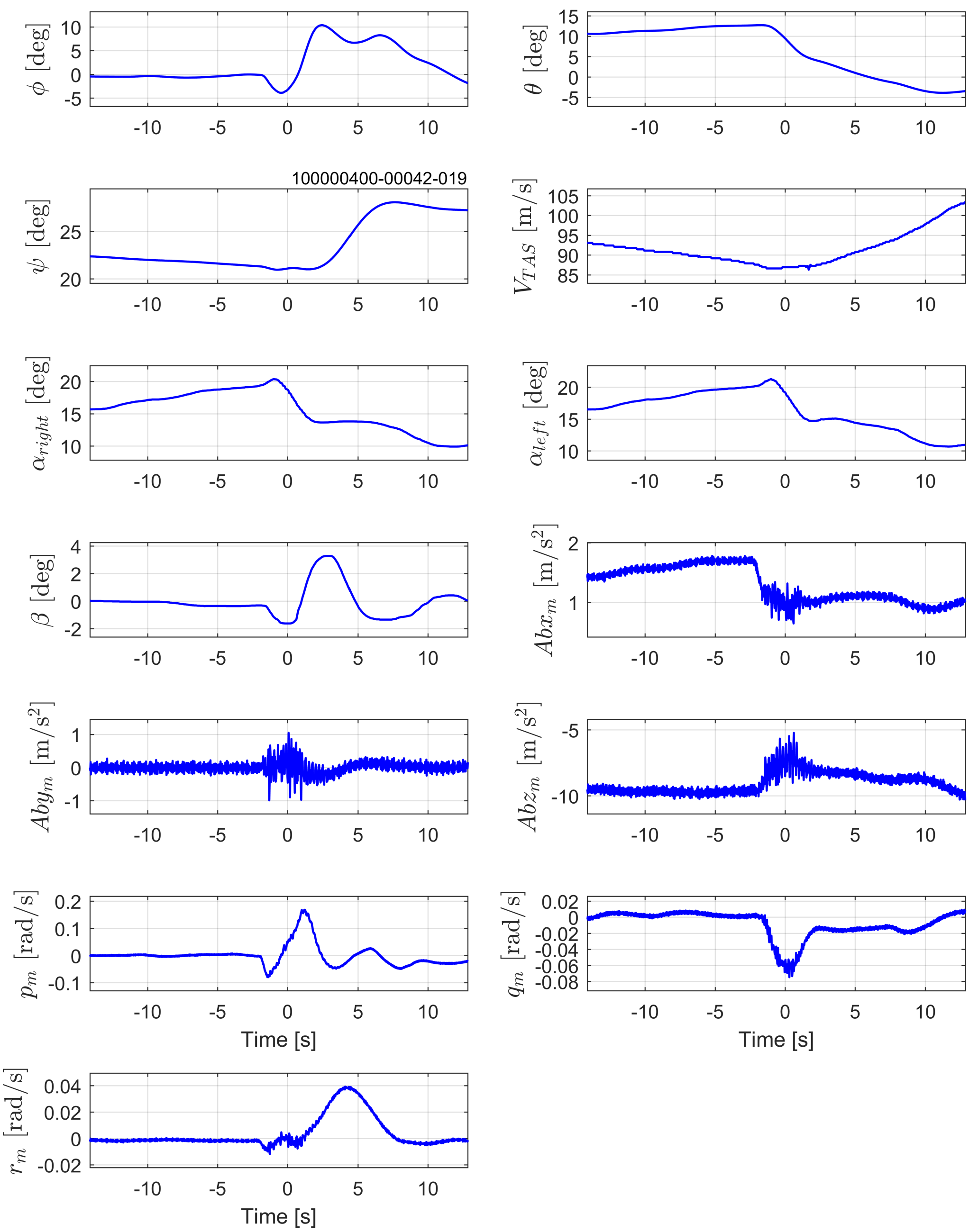

ϕ [deg]
θ [deg]
100000400-00042-019
ψ [deg]
V_{TAS} [m/s]
α_{right} [deg]
α_{left} [deg]
β [deg]
Abx_m [m/s^2]
Aby_m [m/s^2]
Abz_m [m/s^2]
p_m [rad/s]
q_m [rad/s]
r_m [rad/s]
Time [s]

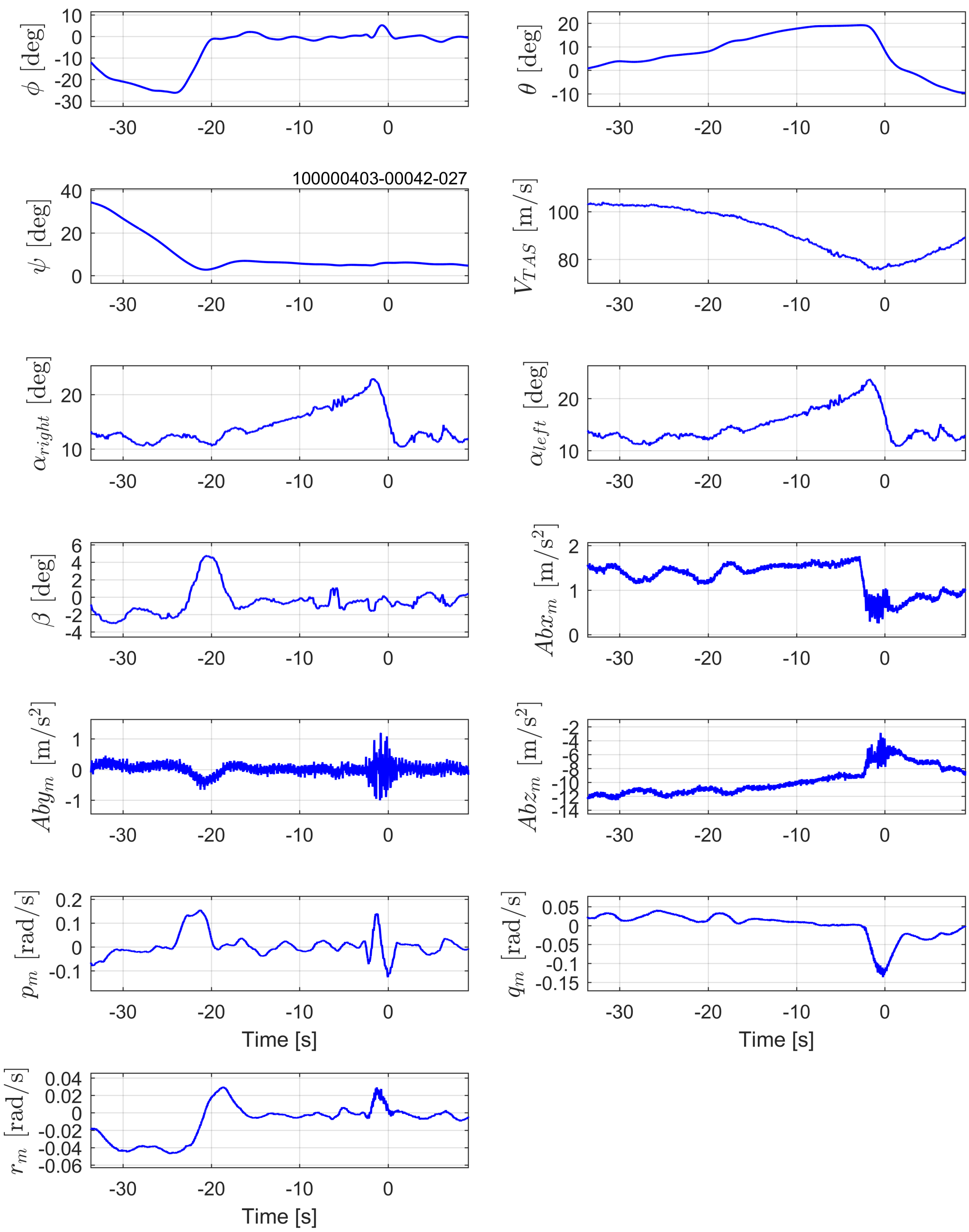
100000403-00042-027
ϕ [deg]
θ [deg]
ψ [deg]
V_{TAS} [m/s]
α_{right} [deg]
α_{left} [deg]
β [deg]
Abx_m [m/s^2]
Aby_m [m/s^2]
Abz_m [m/s^2]
p_m [rad/s]
q_m [rad/s]
r_m [rad/s]
-30 -20 -10 0
Time [s]

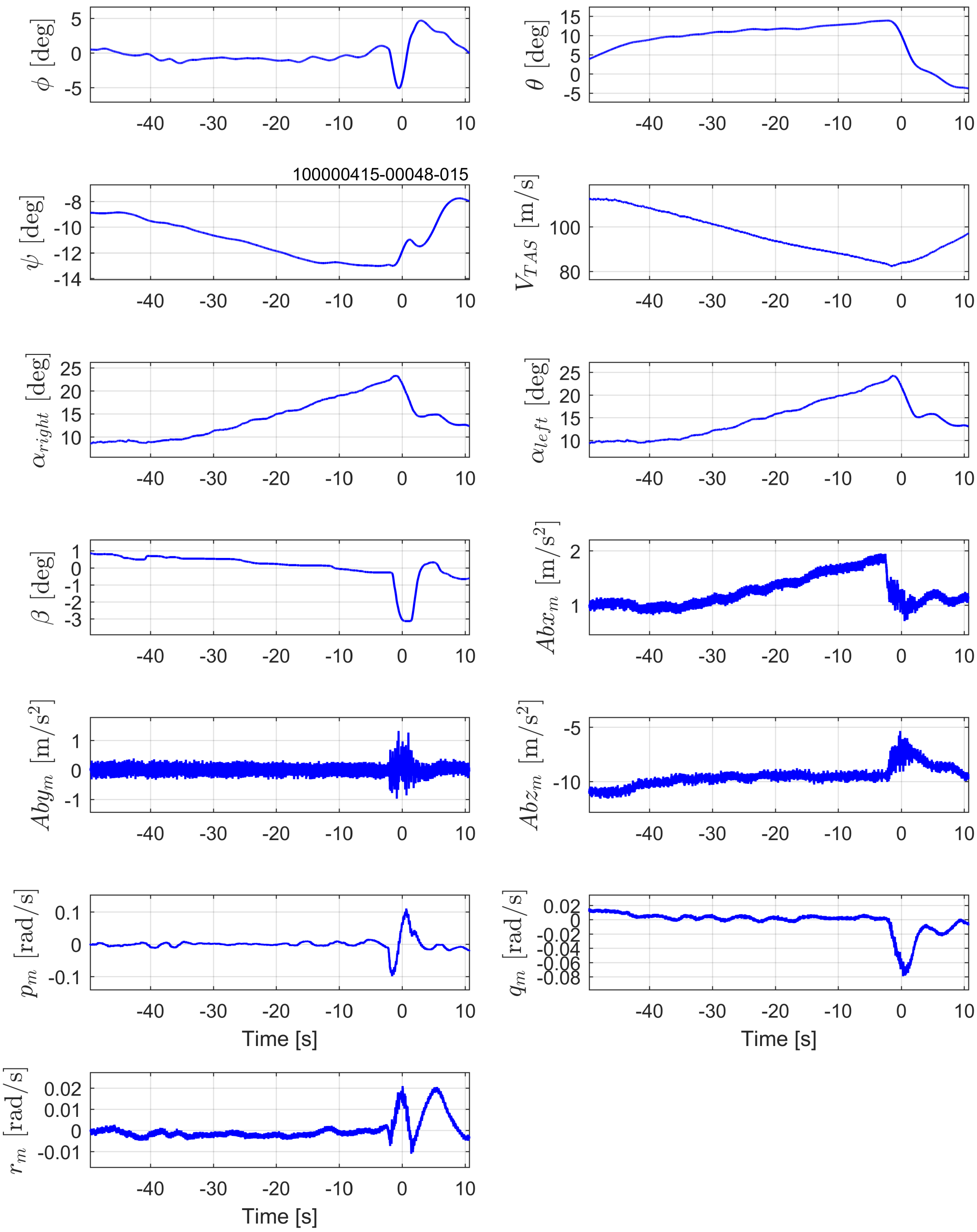

ϕ [deg]
θ [deg]
100000415-00048-015
ψ [deg]
V_{TAS} [m/s]
α_{right} [deg]
α_{left} [deg]
β [deg]
Abx_m [m/s^2]
Aby_m [m/s^2]
Abz_m [m/s^2]
p_m [rad/s]
q_m [rad/s]
r_m [rad/s]
Time [s]

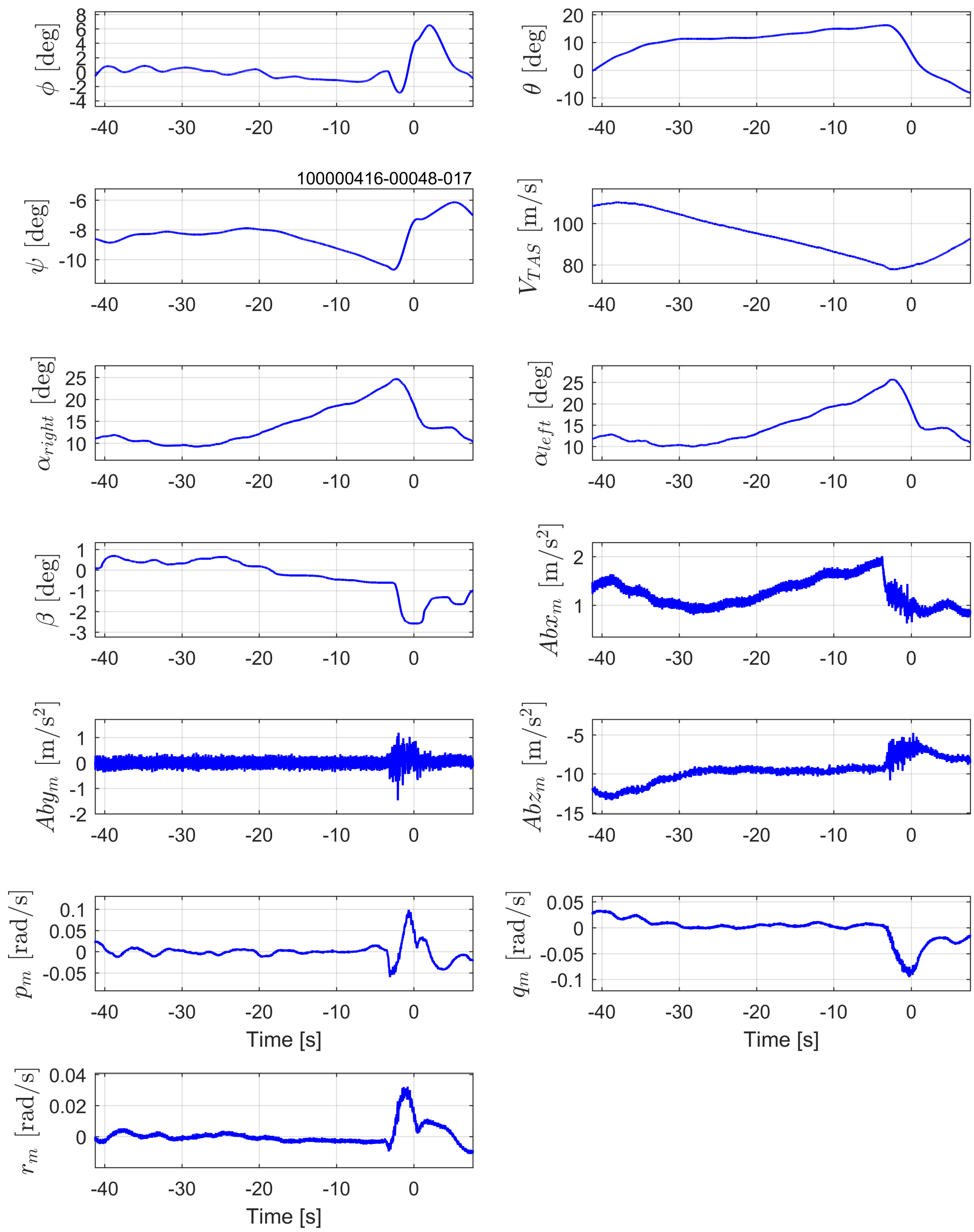

ϕ [deg]
θ [deg]
100000416-00048-017
ψ [deg]
V_{TAS} [m/s]
α_{right} [deg]
α_{left} [deg]
β [deg]
Abx_m [m/s^2]
Aby_m [m/s^2]
Abz_m [m/s^2]
p_m [rad/s]
q_m [rad/s]
r_m [rad/s]
Time [s]
Time [s]
Time [s]

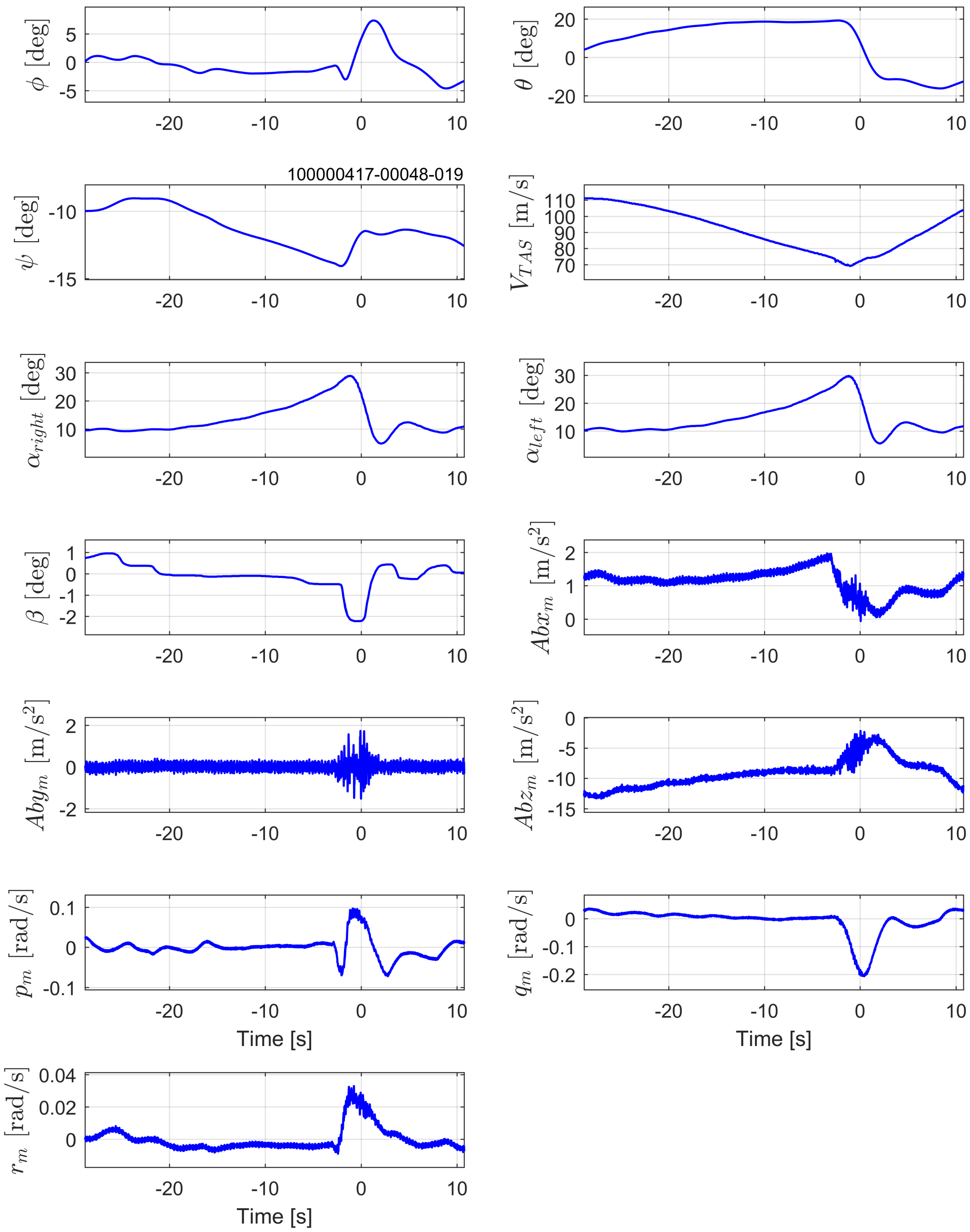

100000417-00048-019
ϕ [deg]
θ [deg]
ψ [deg]
V_{TAS} [m/s]
α_{right} [deg]
α_{left} [deg]
β [deg]
Abx_m [m/s^2]
Aby_m [m/s^2]
Abz_m [m/s^2]
p_m [rad/s]
q_m [rad/s]
r_m [rad/s]
Time [s]
Time [s]
Time [s]

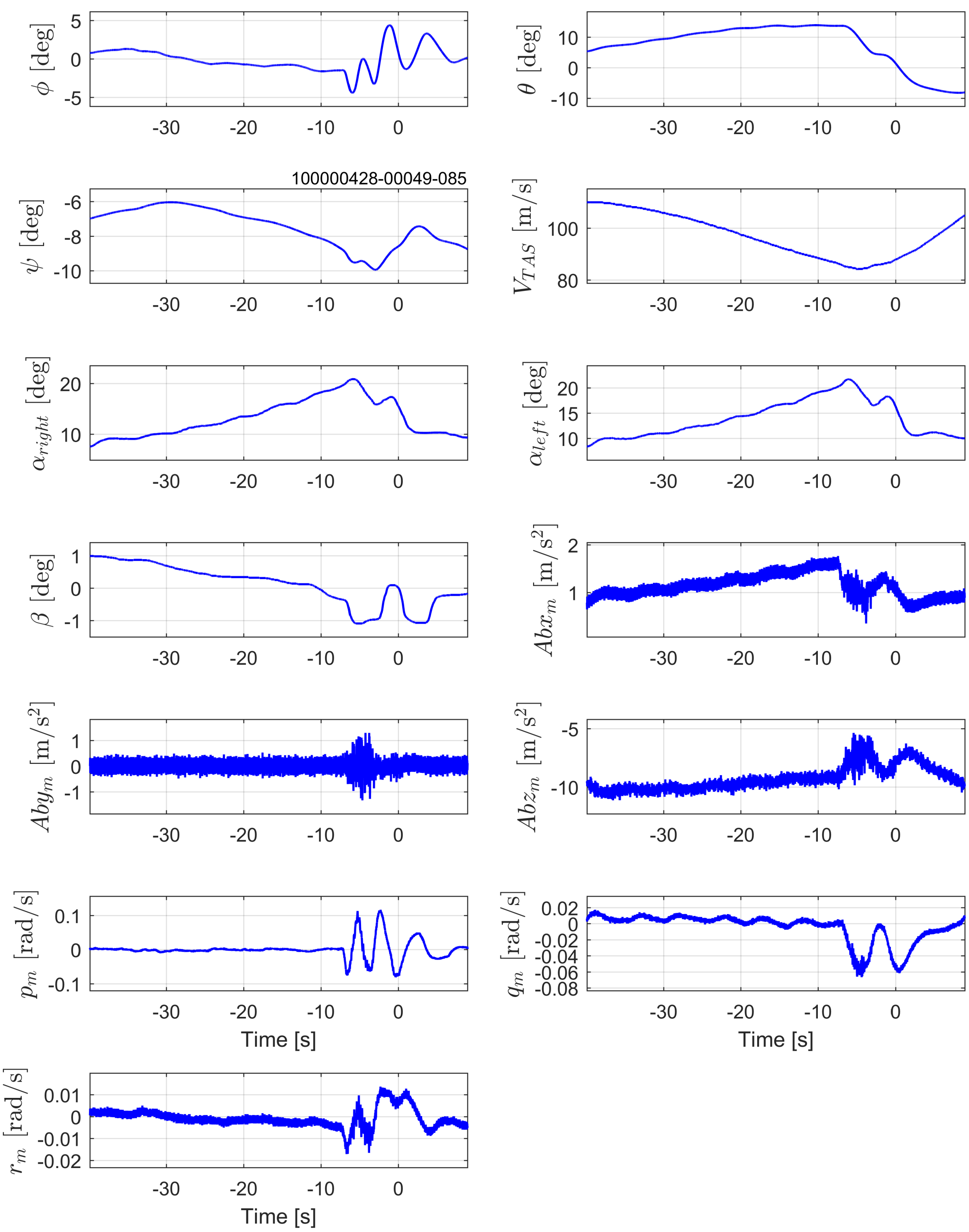

100000428-00049-085
ϕ [deg]
θ [deg]
ψ [deg]
V_{TAS} [m/s]
α_{right} [deg]
α_{left} [deg]
β [deg]
Abx_m [m/s^2]
Aby_m [m/s^2]
Abz_m [m/s^2]
p_m [rad/s]
q_m [rad/s]
r_m [rad/s]
Time [s]

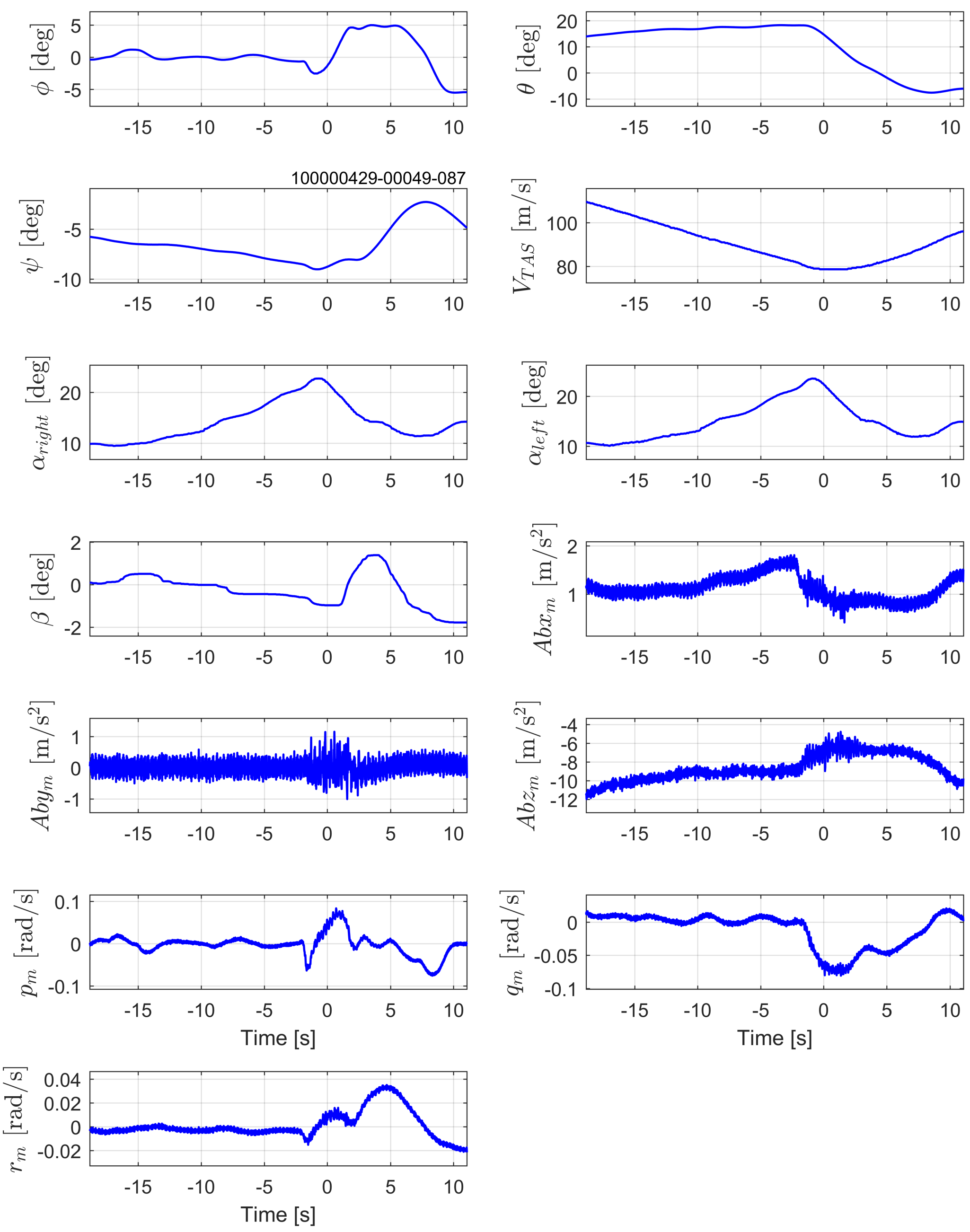

ϕ [deg]
θ [deg]
100000429-00049-087
ψ [deg]
V_{TAS} [m/s]
α_{right} [deg]
α_{left} [deg]
β [deg]
Abx_m [m/s^2]
Aby_m [m/s^2]
Abz_m [m/s^2]
p_m [rad/s]
q_m [rad/s]
r_m [rad/s]
Time [s]

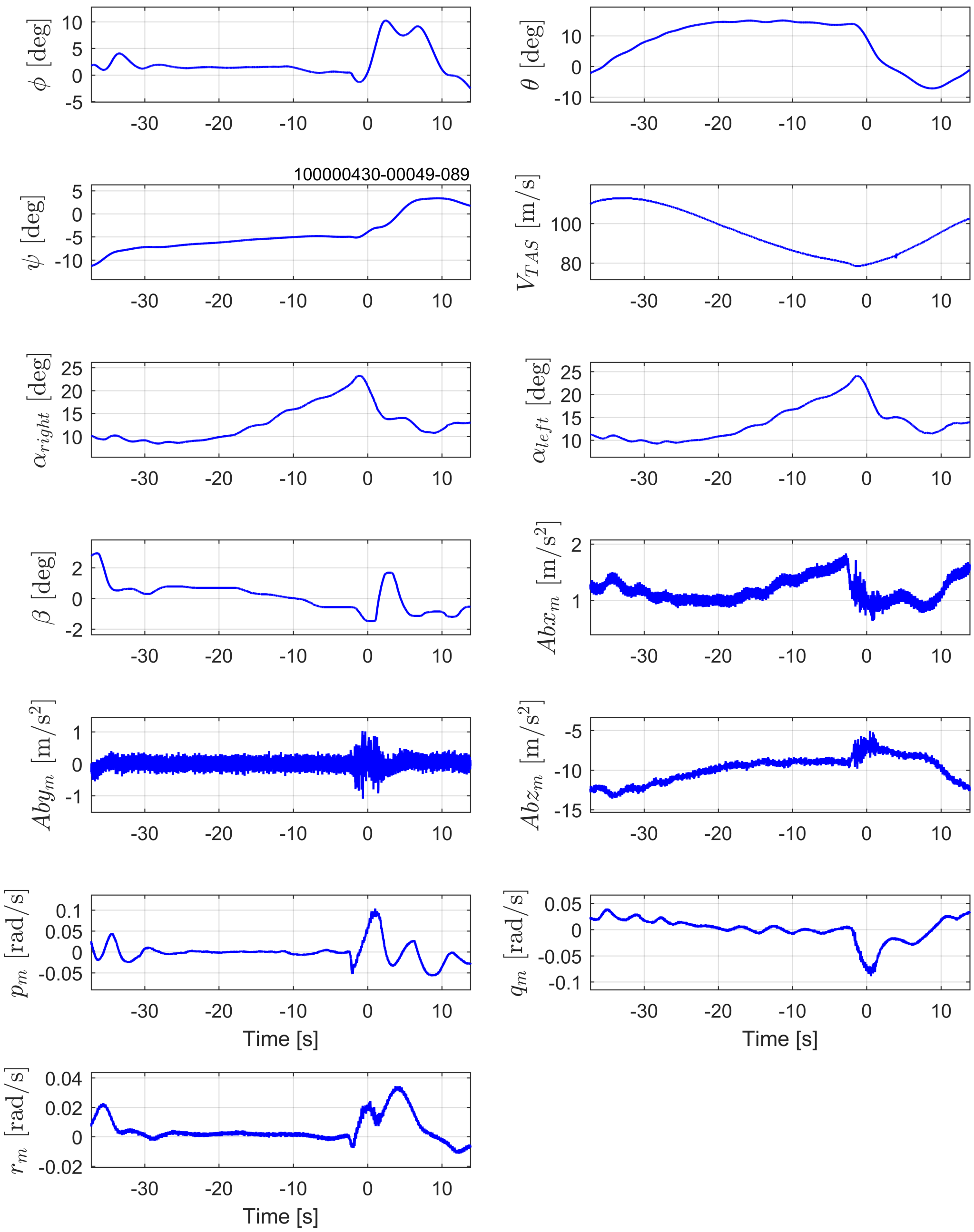
100000430-00049-089
ϕ [deg]
θ [deg]
ψ [deg]
V_{TAS} [m/s]
α_{right} [deg]
α_{left} [deg]
β [deg]
Abx_m [m/s^2]
Aby_m [m/s^2]
Abz_m [m/s^2]
p_m [rad/s]
q_m [rad/s]
r_m [rad/s]
Time [s]

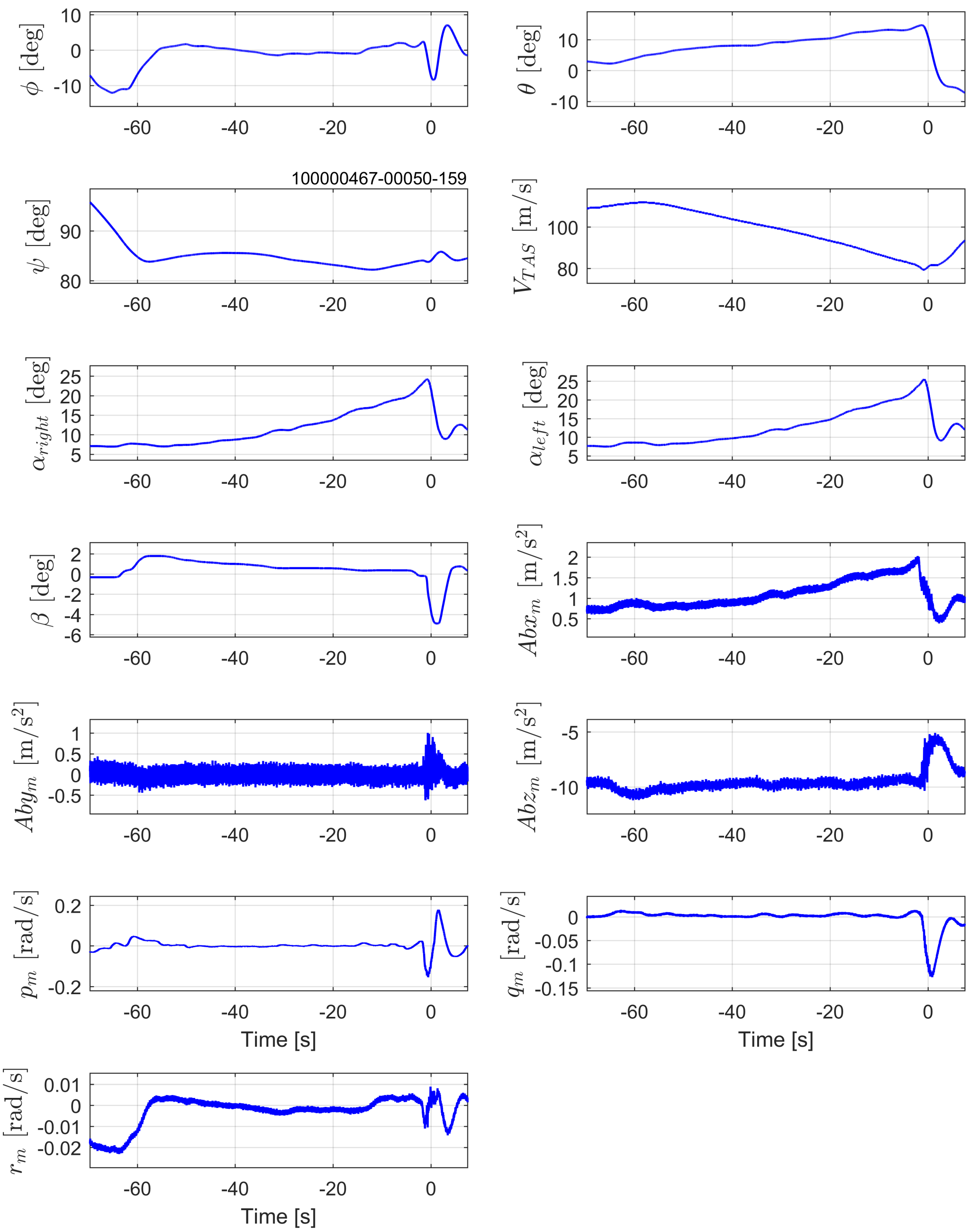
100000467-00050-159
ϕ [deg]
θ [deg]
ψ [deg]
V_{TAS} [m/s]
α_{right} [deg]
α_{left} [deg]
β [deg]
Abx_m [m/s^2]
Aby_m [m/s^2]
Abz_m [m/s^2]
p_m [rad/s]
q_m [rad/s]
r_m [rad/s]
Time [s]

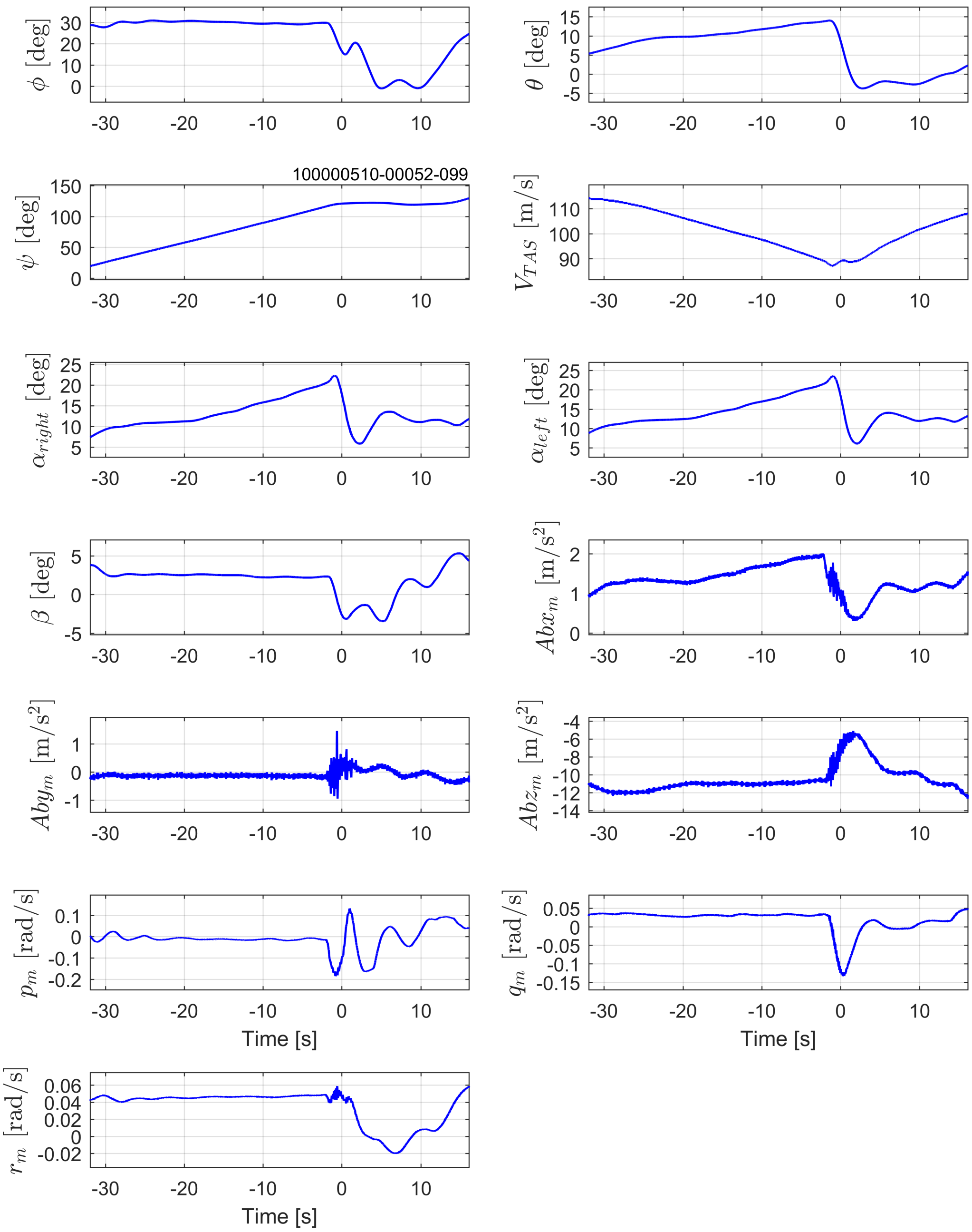
100000510-00052-099
ϕ [deg]
θ [deg]
ψ [deg]
V_{TAS} [m/s]
α_{right} [deg]
α_{left} [deg]
β [deg]
Abx_m [m/s^2]
Aby_m [m/s^2]
Abz_m [m/s^2]
p_m [rad/s]
q_m [rad/s]
r_m [rad/s]
Time [s]

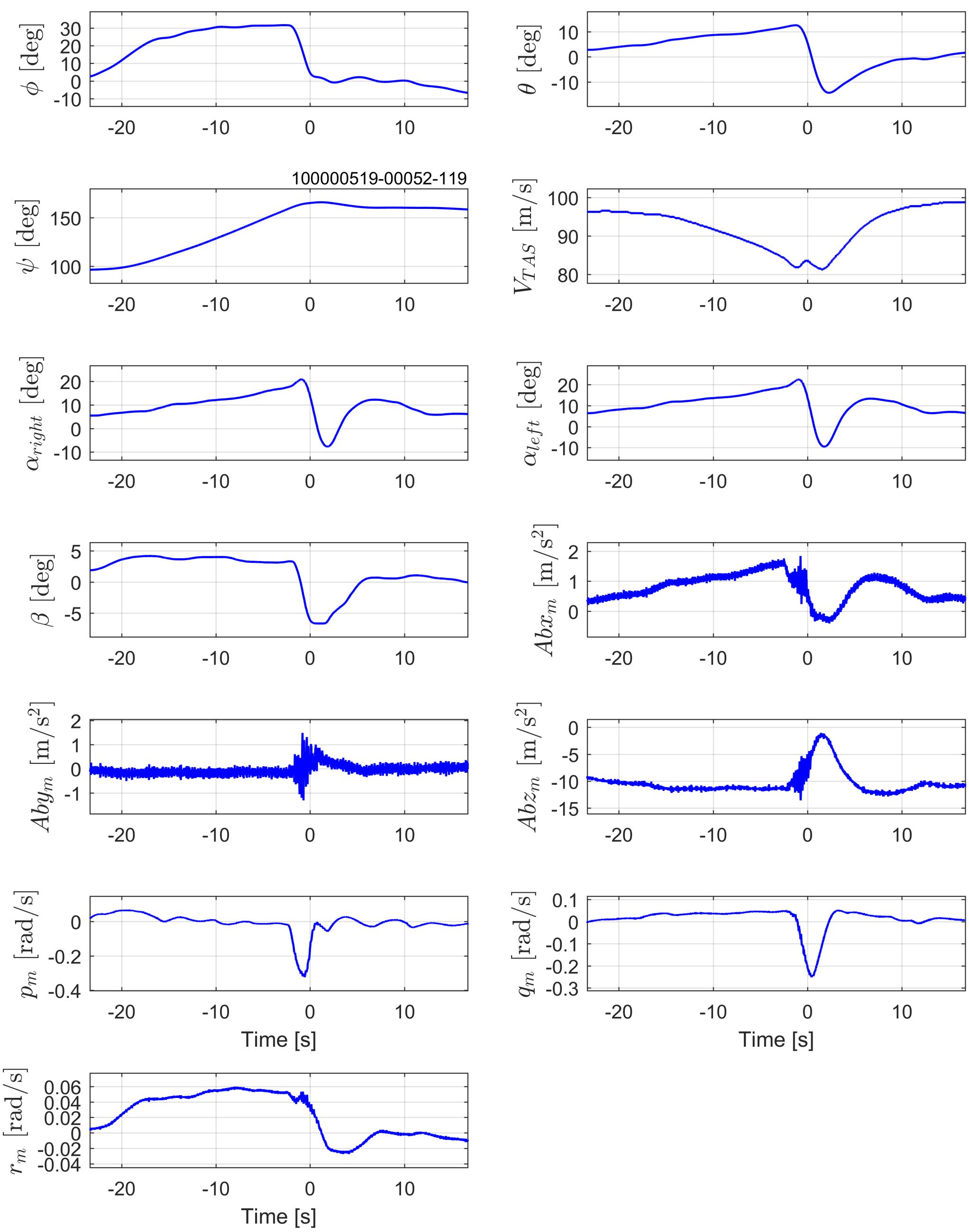

ϕ [deg]
θ [deg]
100000519-00052-119
ψ [deg]
V_{TAS} [m/s]
α_{right} [deg]
α_{left} [deg]
β [deg]
Abx_m [m/s^2]
Aby_m [m/s^2]
Abz_m [m/s^2]
p_m [rad/s]
q_m [rad/s]
r_m [rad/s]
Time [s]

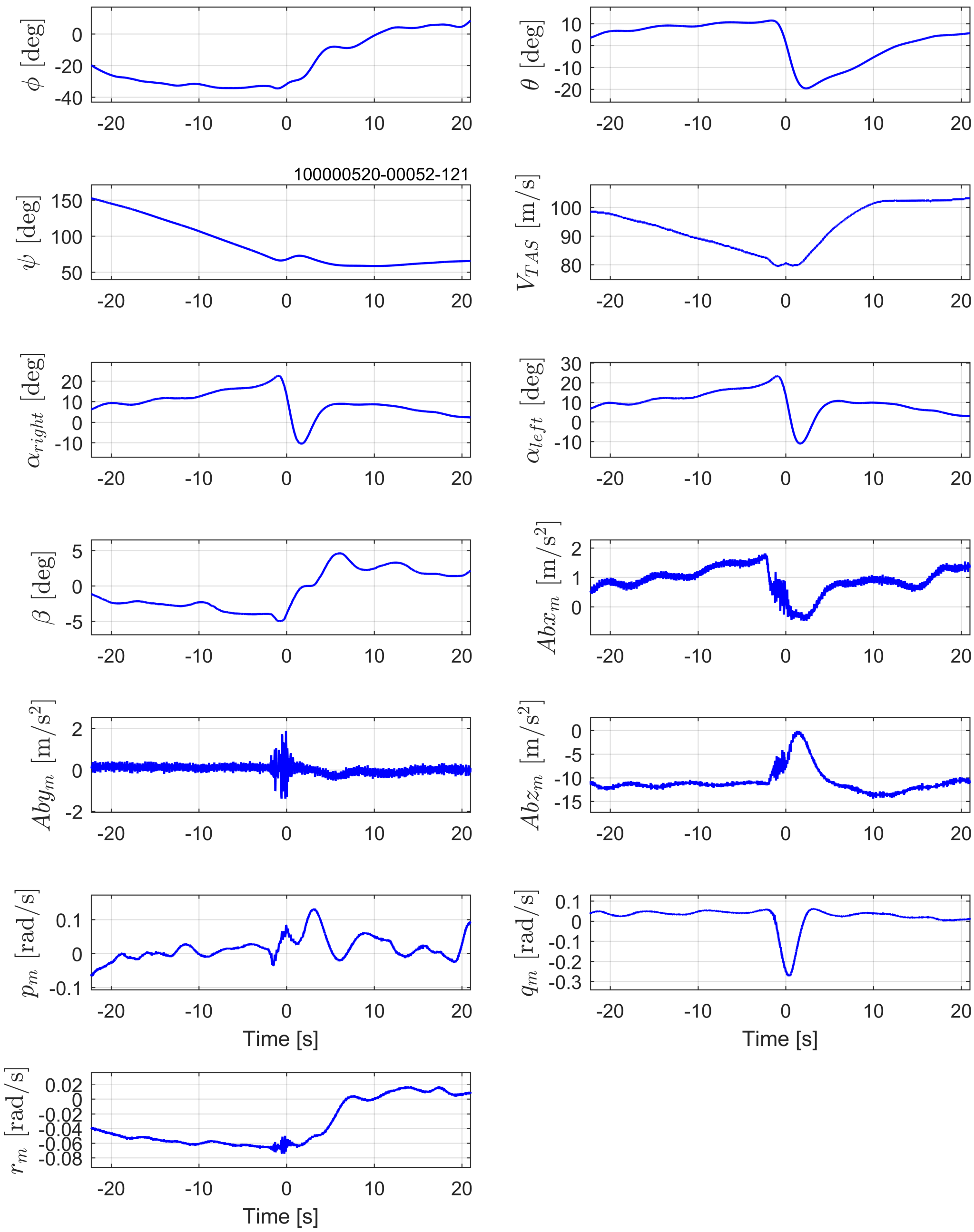
100000520-00052-121
ϕ [deg]
θ [deg]
ψ [deg]
V_{TAS} [m/s]
α_{right} [deg]
α_{left} [deg]
β [deg]
Abx_m [m/s^2]
Aby_m [m/s^2]
Abz_m [m/s^2]
p_m [rad/s]
q_m [rad/s]
r_m [rad/s]
Time [s]

A.2. 6° Flaps

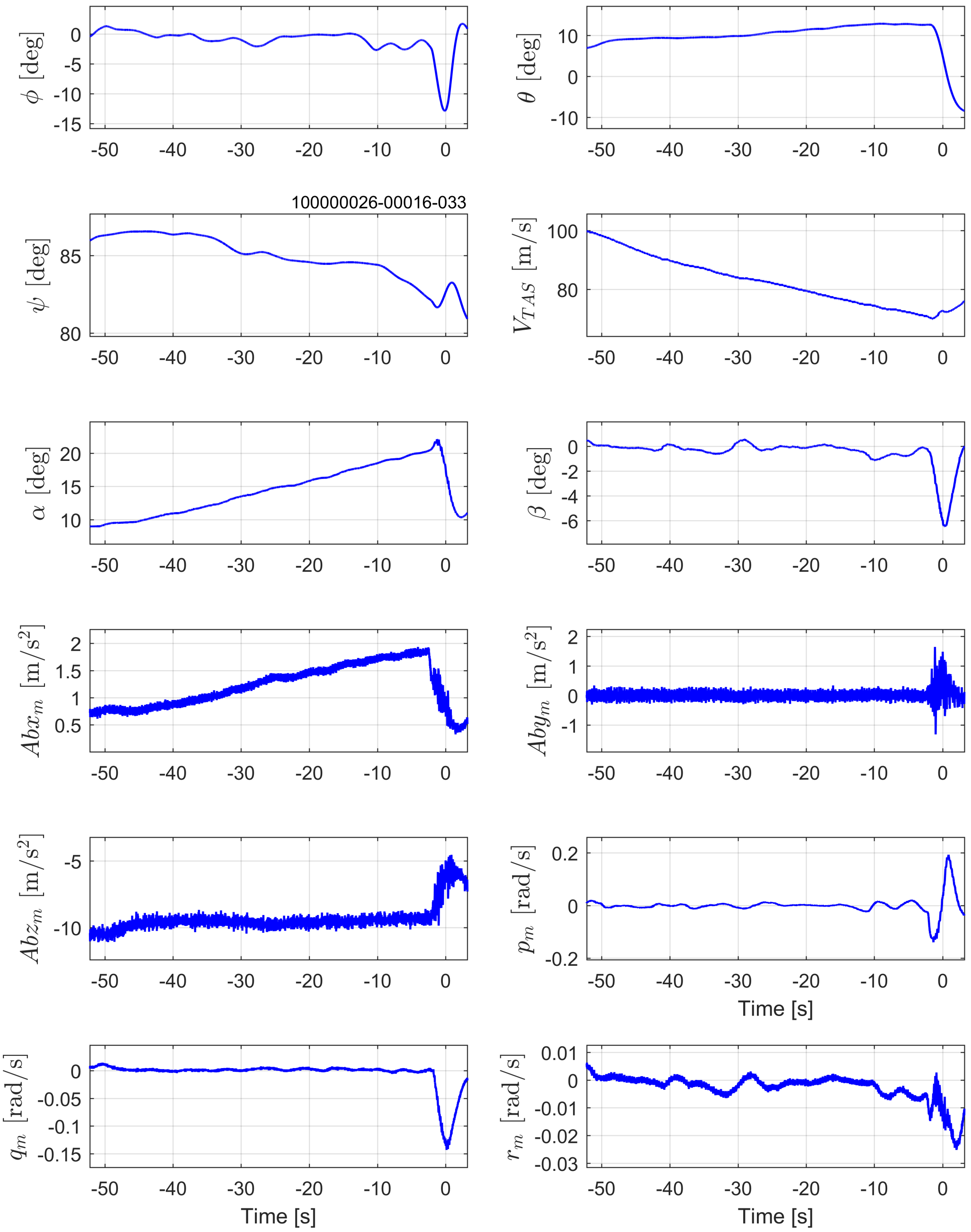

100000026-00016-033
ϕ [deg]
θ [deg]
ψ [deg]
V_{TAS} [m/s]
α [deg]
β [deg]
Abx_m [m/s^2]
Aby_m [m/s^2]
Abz_m [m/s^2]
p_m [rad/s]
q_m [rad/s]
r_m [rad/s]
Time [s]

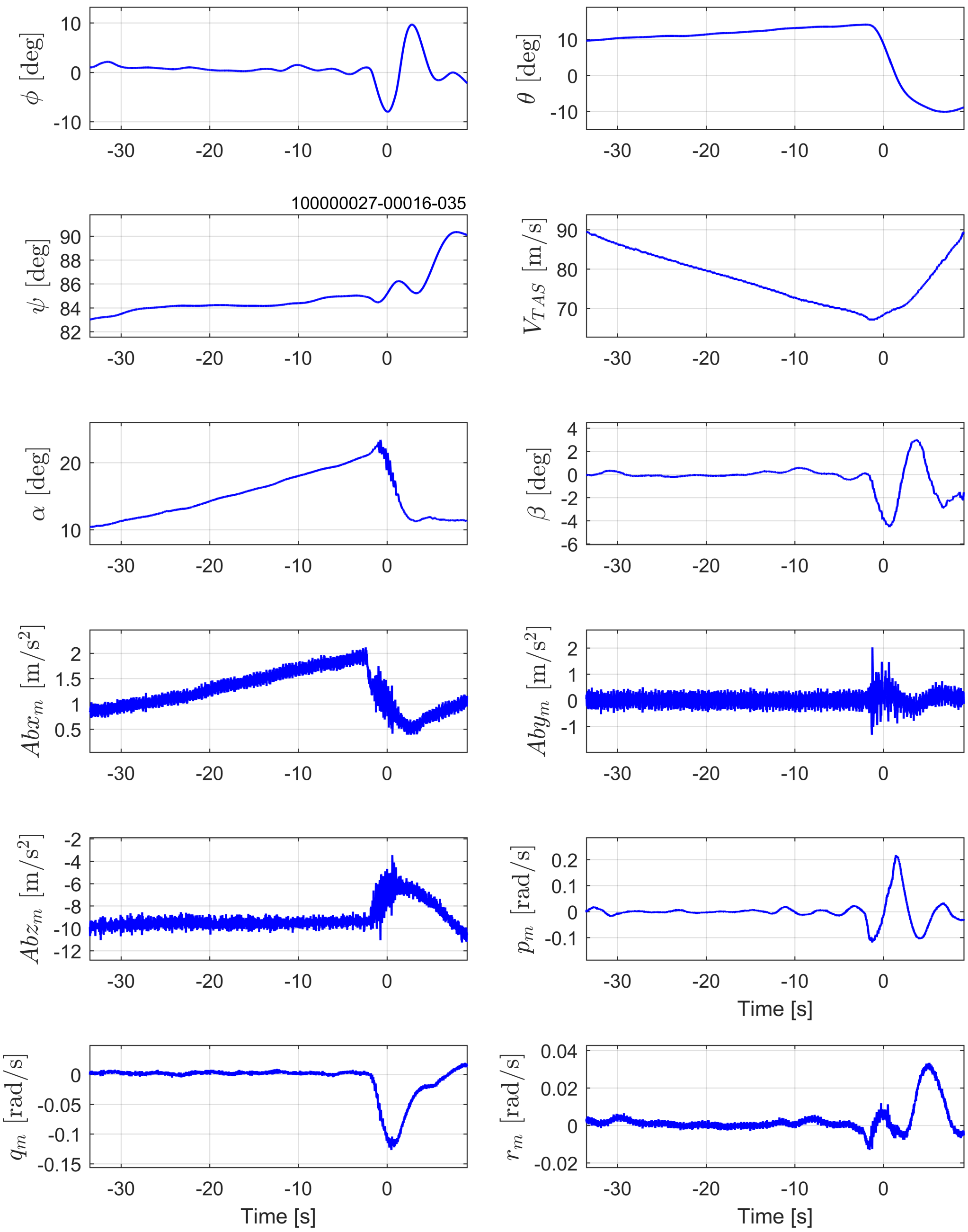
100000027-00016-035
ϕ [deg]
θ [deg]
ψ [deg]
V_{TAS} [m/s]
α [deg]
β [deg]
Abx_m [m/s^2]
Aby_m [m/s^2]
Abz_m [m/s^2]
p_m [rad/s]
q_m [rad/s]
r_m [rad/s]
Time [s]
Time [s]
Time [s]

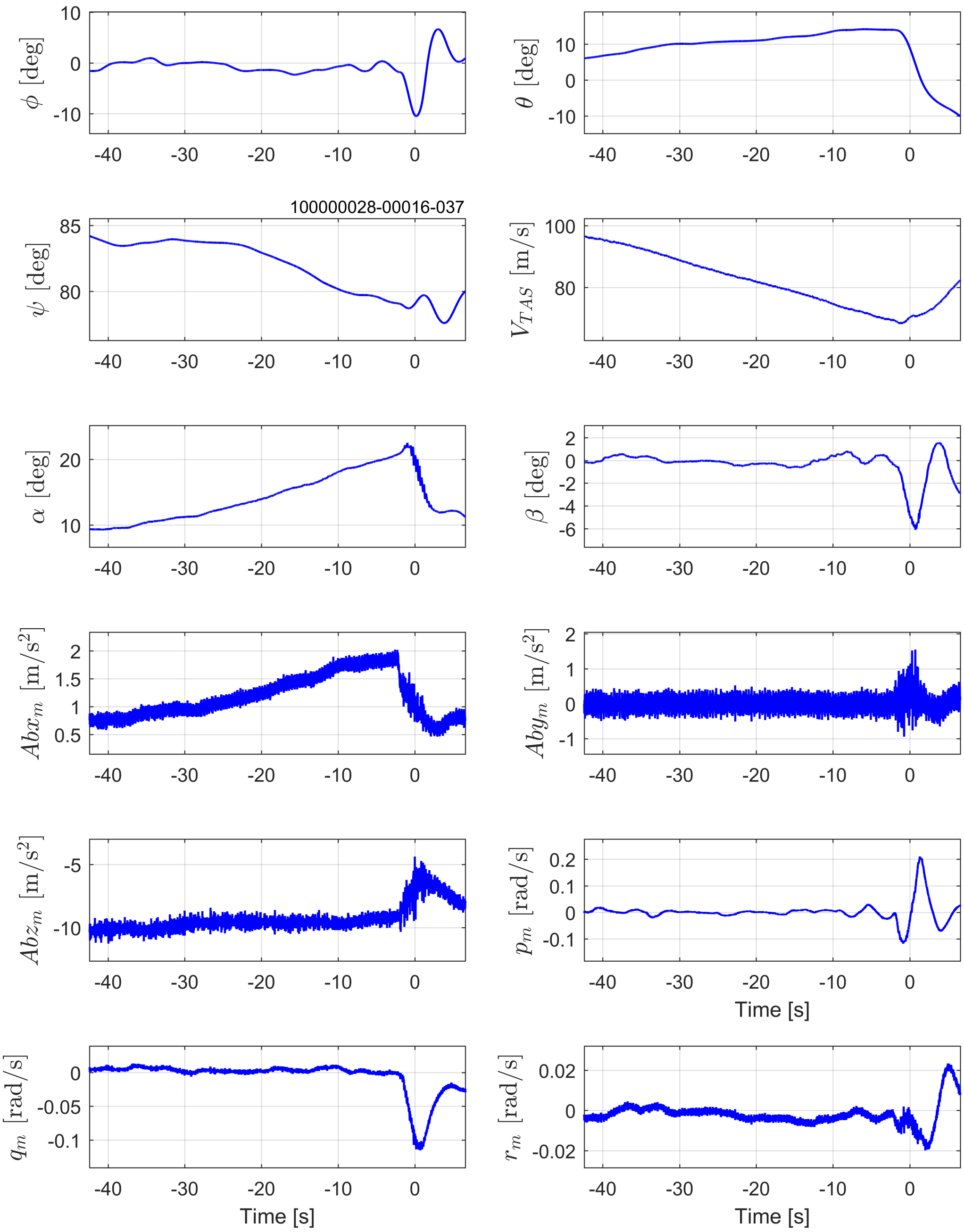
100000028-00016-037
ϕ [deg]
θ [deg]
ψ [deg]
V_{TAS} [m/s]
α [deg]
β [deg]
Abx_m [m/s^2]
Aby_m [m/s^2]
Abz_m [m/s^2]
p_m [rad/s]
q_m [rad/s]
r_m [rad/s]
Time [s]
Time [s]
Time [s]

A.3. 18° Flaps

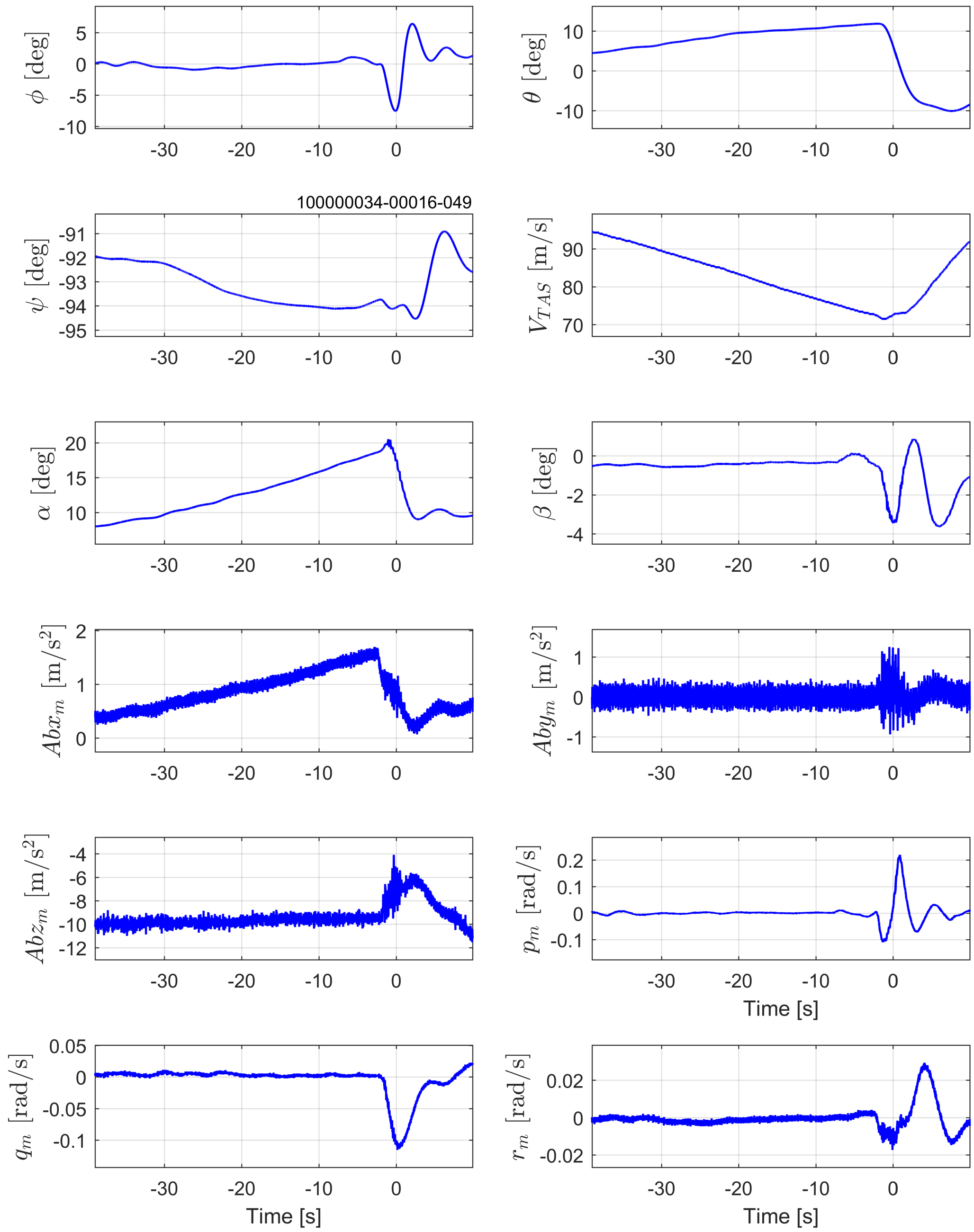

100000034-00016-049
ϕ [deg]
θ [deg]
ψ [deg]
V_{TAS} [m/s]
α [deg]
β [deg]
Abx_m [m/s^2]
Aby_m [m/s^2]
Abz_m [m/s^2]
p_m [rad/s]
q_m [rad/s]
r_m [rad/s]
Time [s]

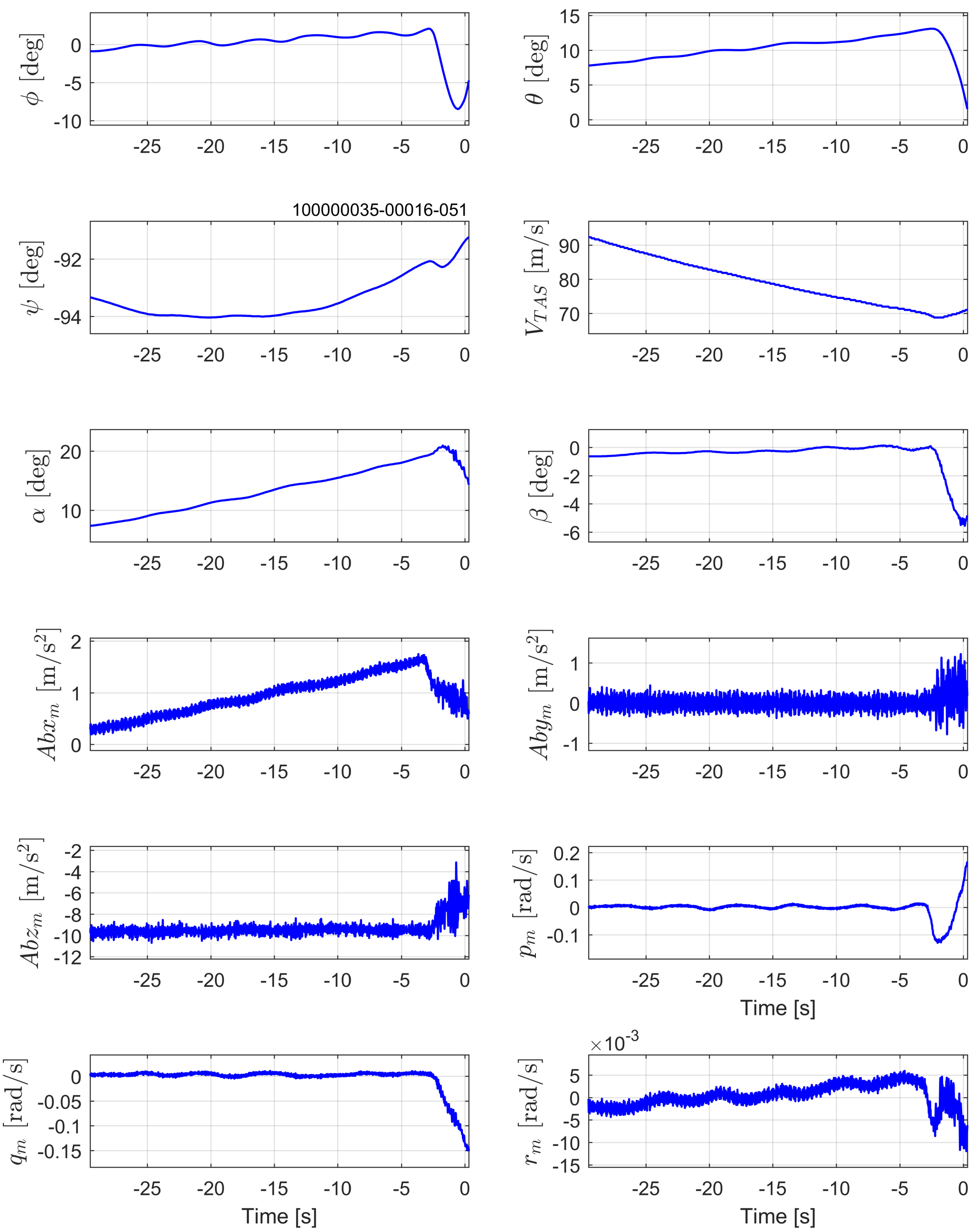

100000035-00016-051
ϕ [deg]
θ [deg]
ψ [deg]
V_{TAS} [m/s]
α [deg]
β [deg]
Abx_m [m/s^2]
Aby_m [m/s^2]
Abz_m [m/s^2]
p_m [rad/s]
q_m [rad/s]
r_m [rad/s]
$\times 10^{-3}$
Time [s]
Time [s]
Time [s]

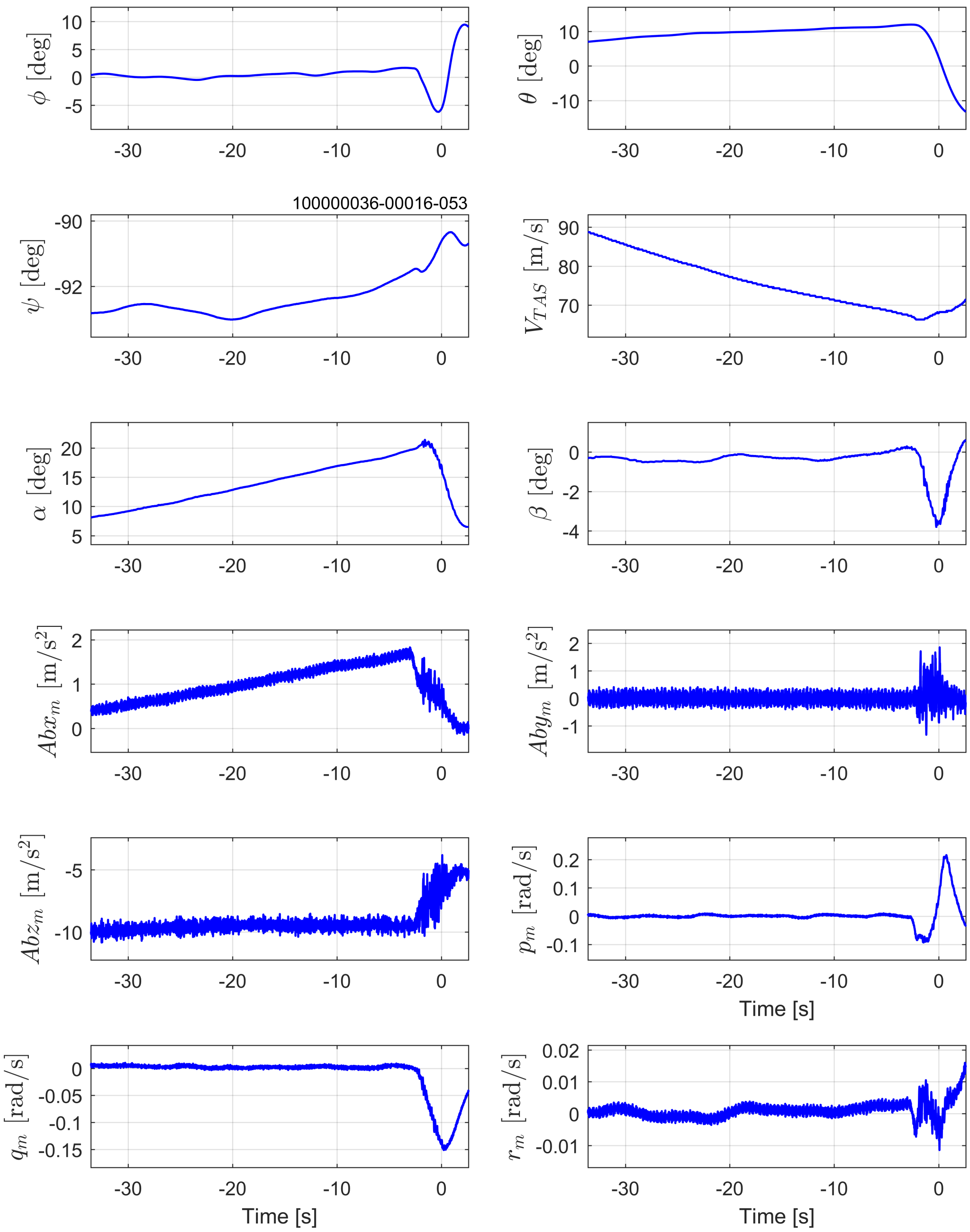

100000036-00016-053
ϕ [deg]
θ [deg]
ψ [deg]
V_{TAS} [m/s]
α [deg]
β [deg]
Abx_m [m/s^2]
Aby_m [m/s^2]
Abz_m [m/s^2]
p_m [rad/s]
q_m [rad/s]
r_m [rad/s]
Time [s]
Time [s]
Time [s]

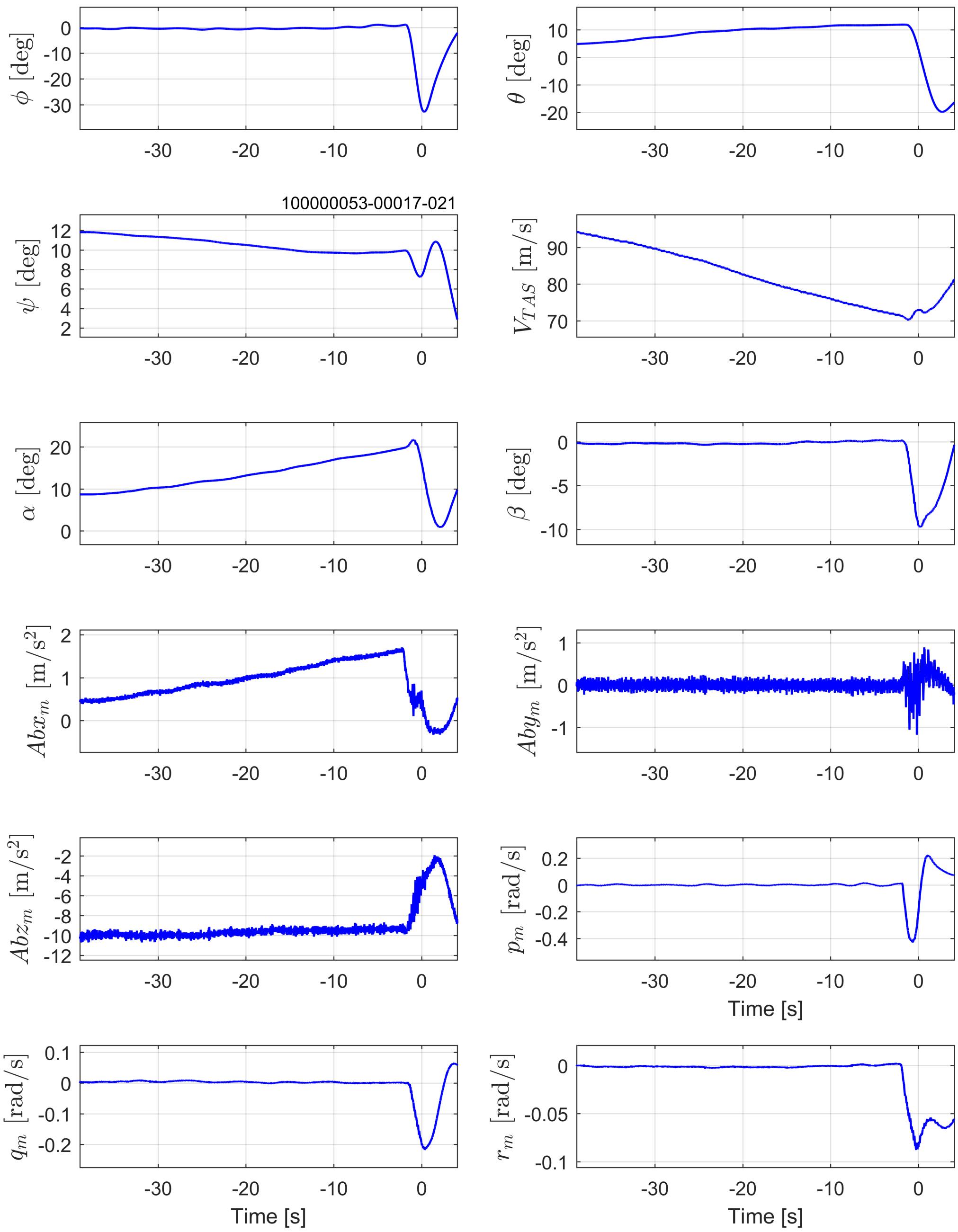

100000053-00017-021
ϕ [deg]
θ [deg]
ψ [deg]
V_TAS [m/s]
α [deg]
β [deg]
Abx_m [m/s²]
Aby_m [m/s²]
Abz_m [m/s²]
p_m [rad/s]
q_m [rad/s]
r_m [rad/s]
Time [s]

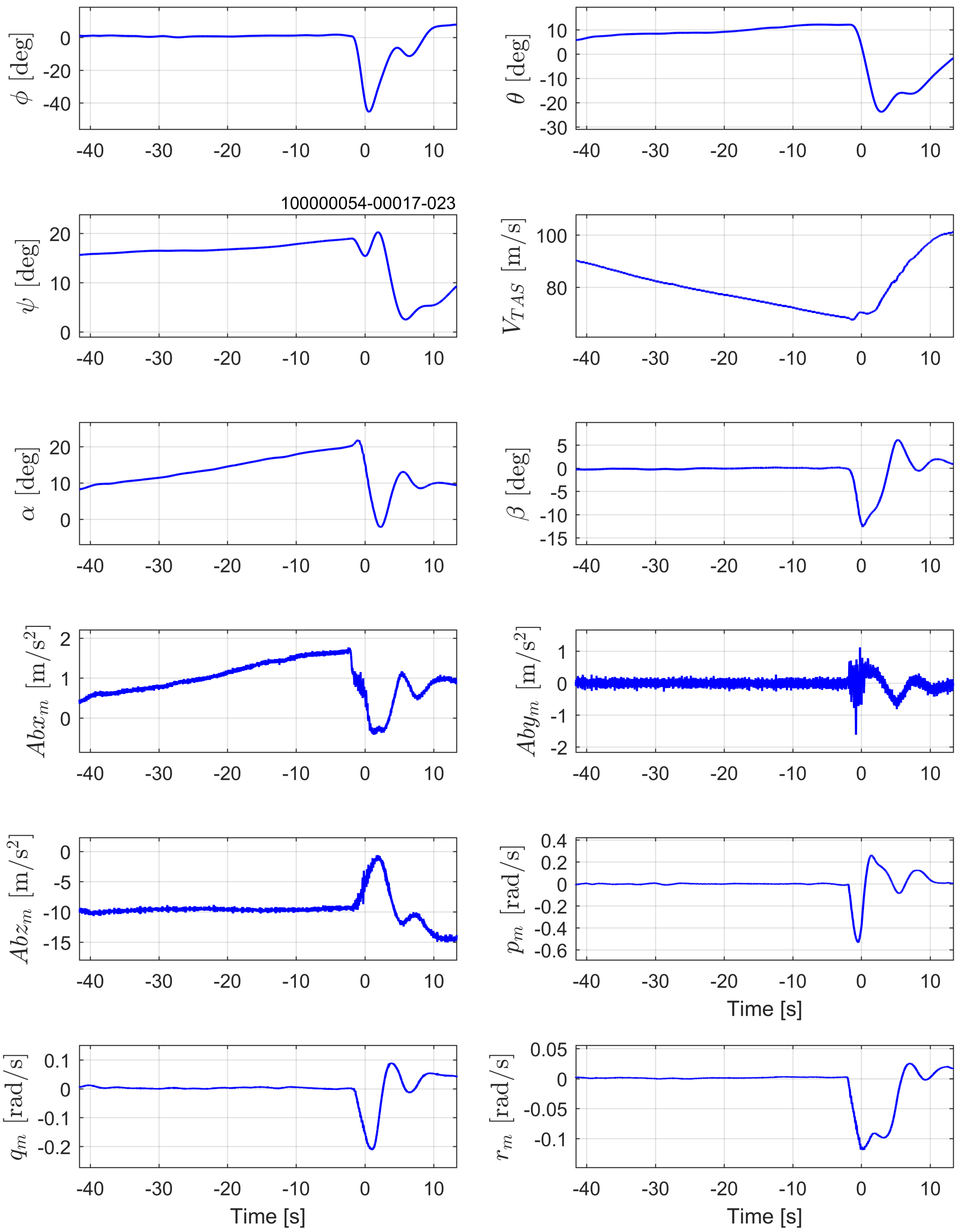
100000054-00017-023
ϕ [deg]
θ [deg]
ψ [deg]
V_{TAS} [m/s]
α [deg]
β [deg]
Abx_m [m/s^2]
Aby_m [m/s^2]
Abz_m [m/s^2]
p_m [rad/s]
q_m [rad/s]
r_m [rad/s]
Time [s]

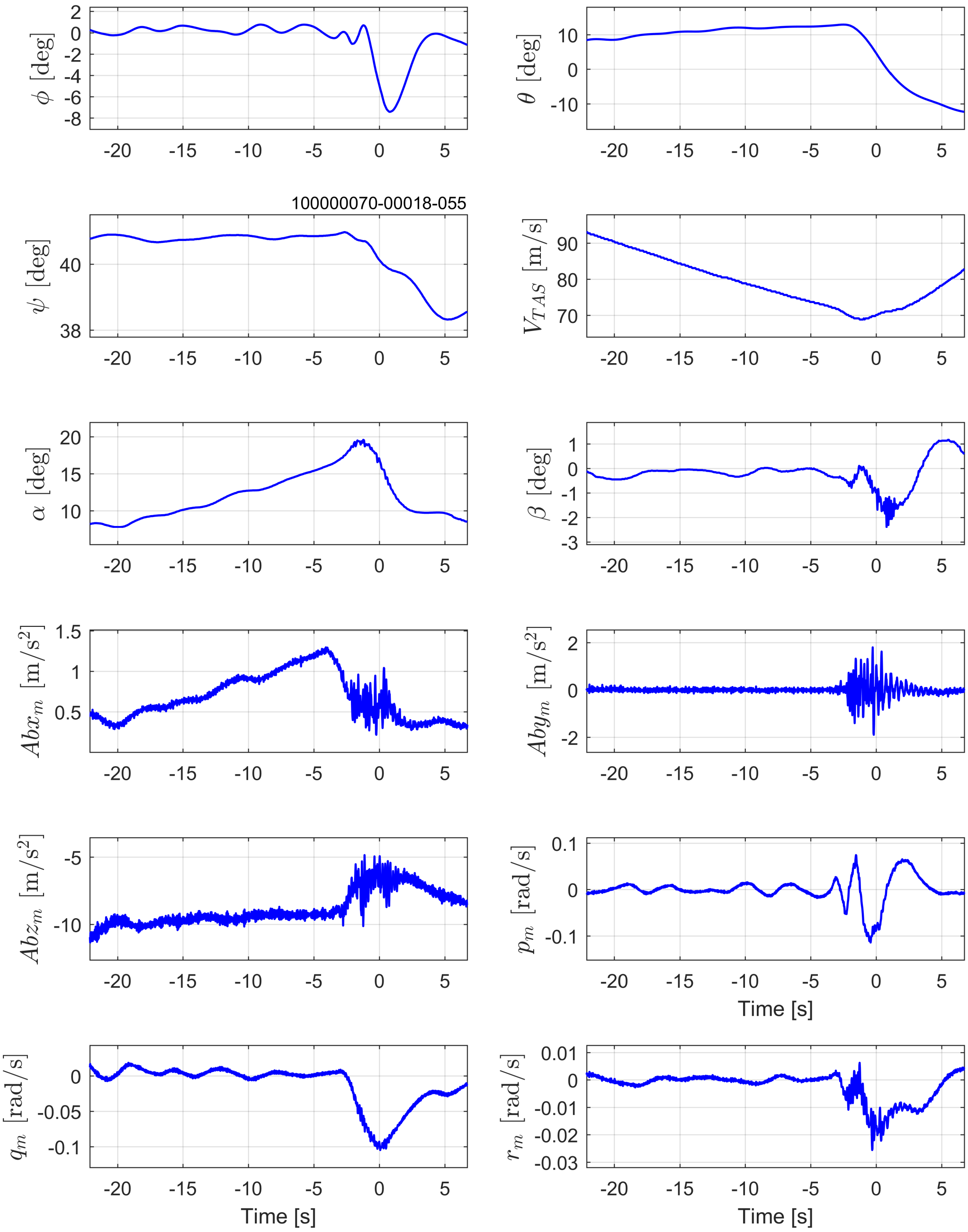
100000070-00018-055
ϕ [deg]
θ [deg]
ψ [deg]
V_{TAS} [m/s]
α [deg]
β [deg]
Abx_m [m/s^2]
Aby_m [m/s^2]
Abz_m [m/s^2]
p_m [rad/s]
q_m [rad/s]
r_m [rad/s]
Time [s]
Time [s]
Time [s]

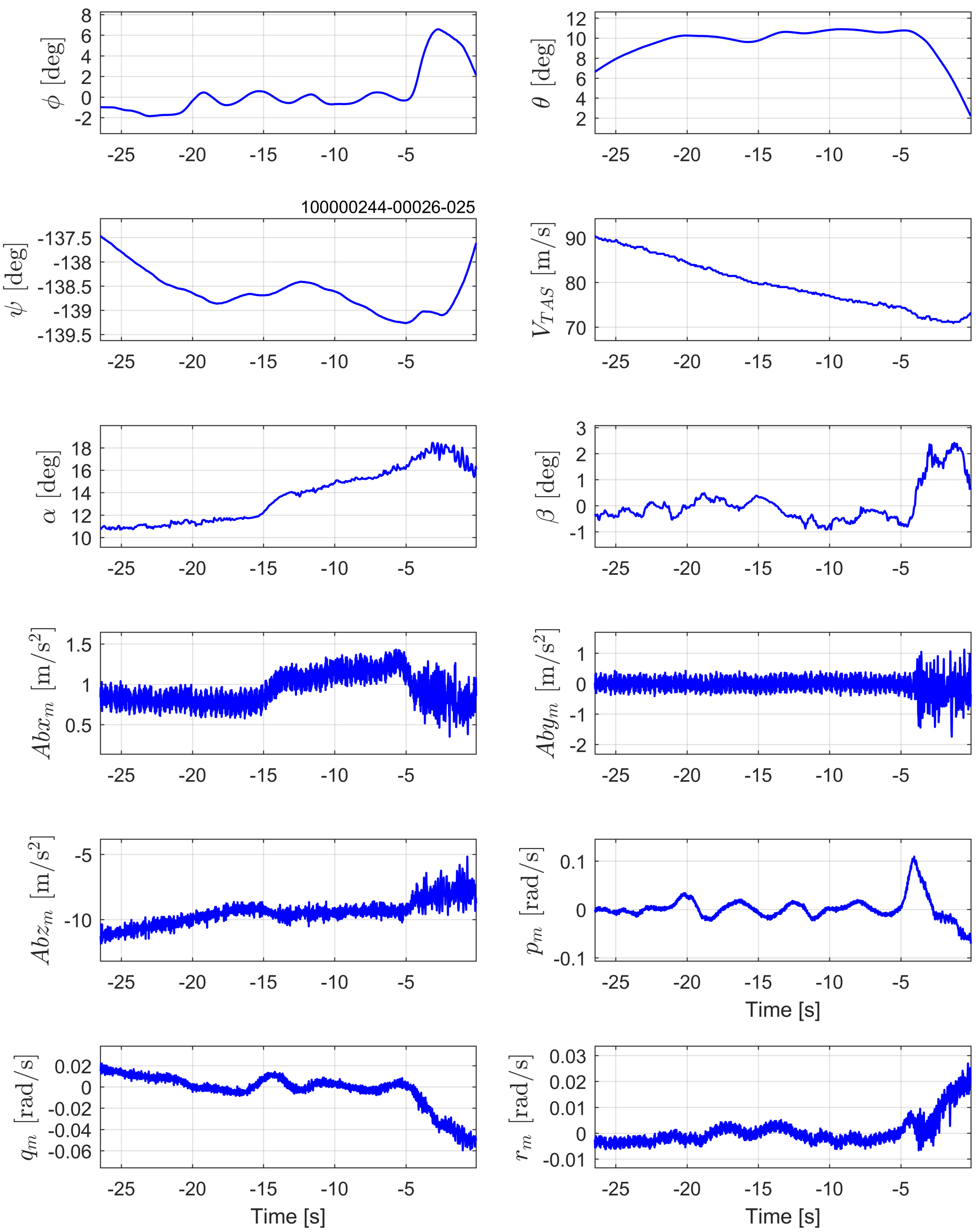
100000244-00026-025
ϕ [deg]
θ [deg]
ψ [deg]
V_{TAS} [m/s]
α [deg]
β [deg]
Abx_m [m/s^2]
Aby_m [m/s^2]
Abz_m [m/s^2]
p_m [rad/s]
q_m [rad/s]
r_m [rad/s]
Time [s]
Time [s]
Time [s]

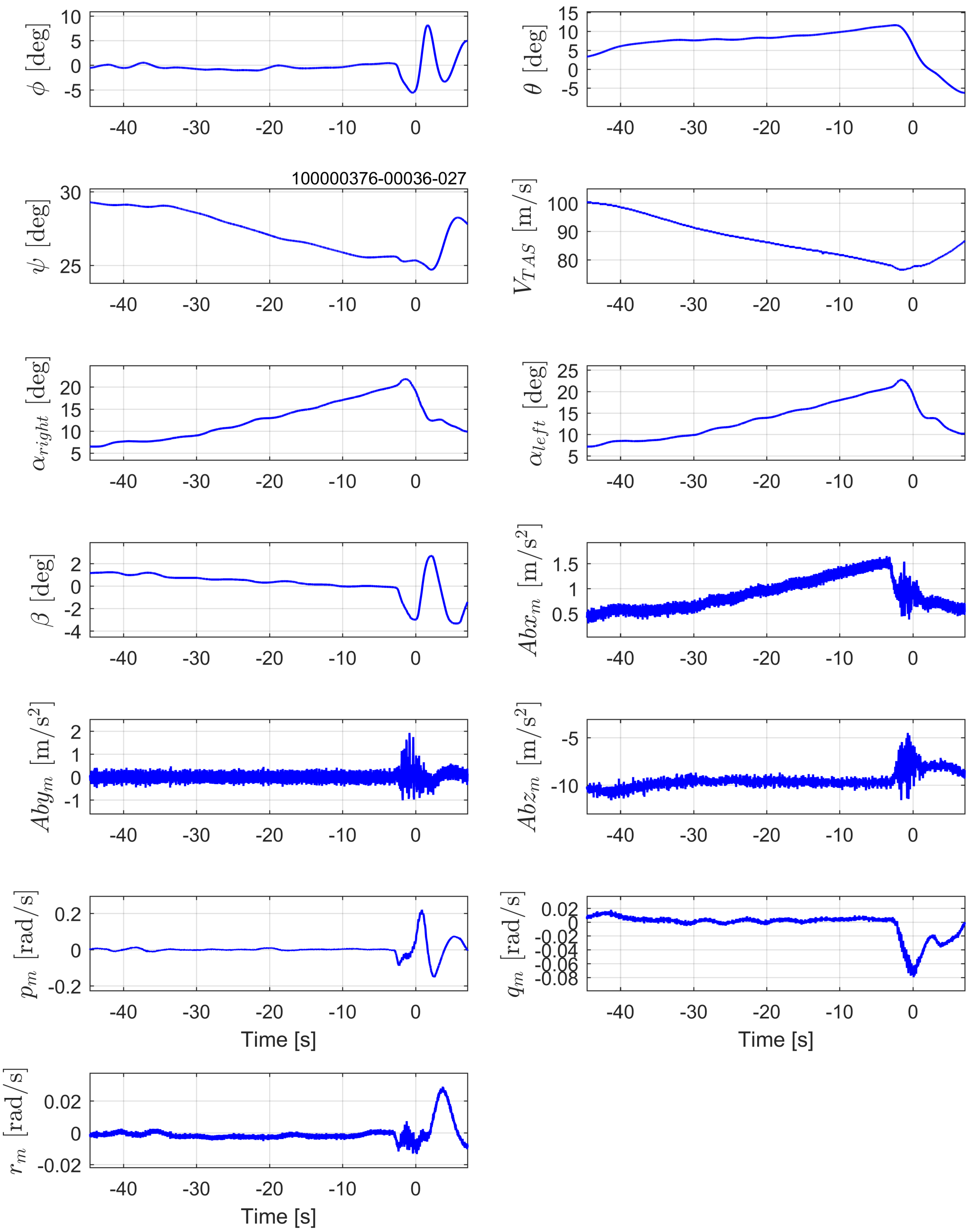

ϕ [deg]
θ [deg]
100000376-00036-027
ψ [deg]
V_{TAS} [m/s]
α_{right} [deg]
α_{left} [deg]
β [deg]
Abx_m [m/s^2]
Aby_m [m/s^2]
Abz_m [m/s^2]
p_m [rad/s]
q_m [rad/s]
r_m [rad/s]
Time [s]

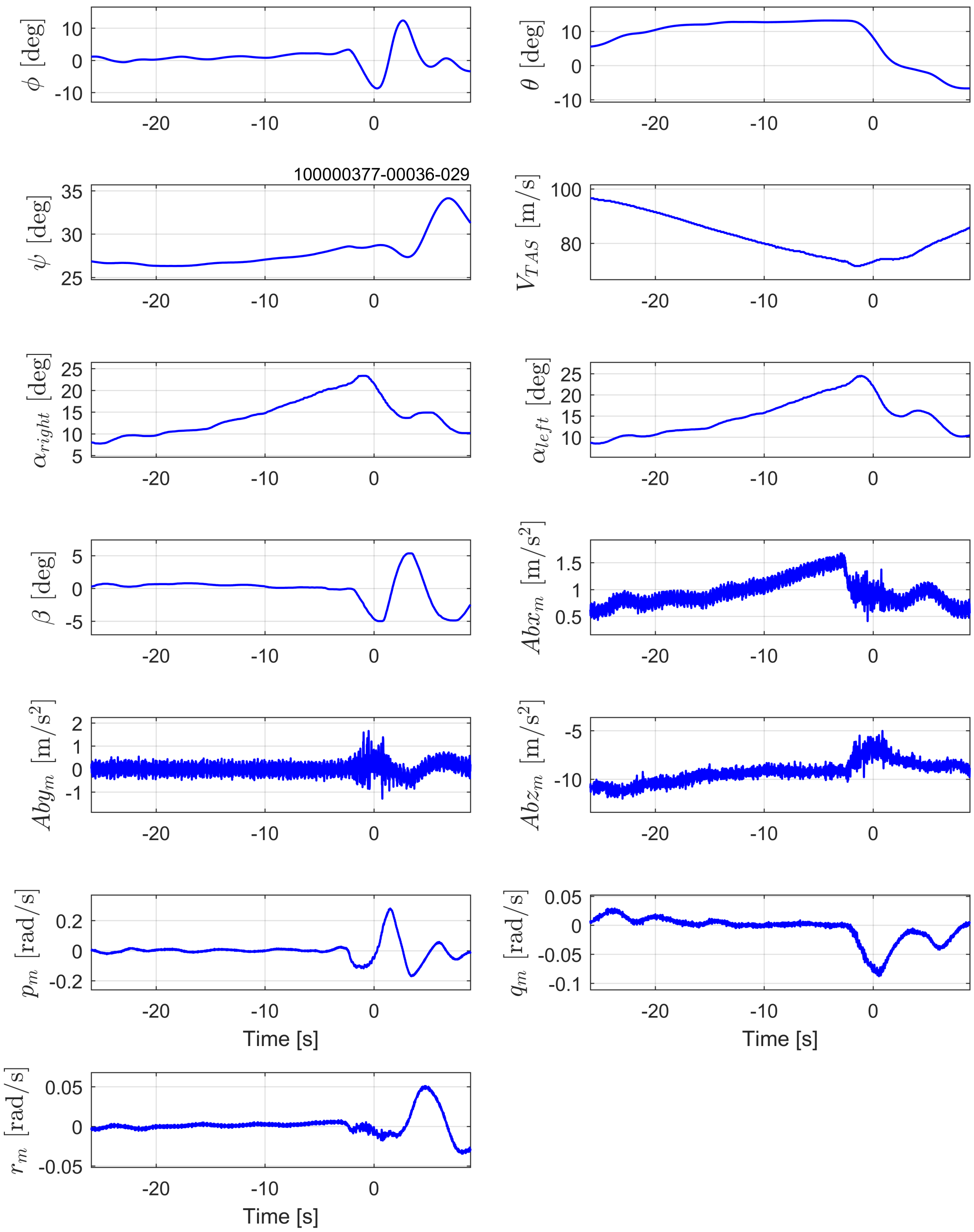
100000377-00036-029
ϕ [deg]
θ [deg]
ψ [deg]
V_{TAS} [m/s]
α_{right} [deg]
α_{left} [deg]
β [deg]
Abx_m [m/s^2]
Aby_m [m/s^2]
Abz_m [m/s^2]
p_m [rad/s]
q_m [rad/s]
r_m [rad/s]
Time [s]
Time [s]
Time [s]

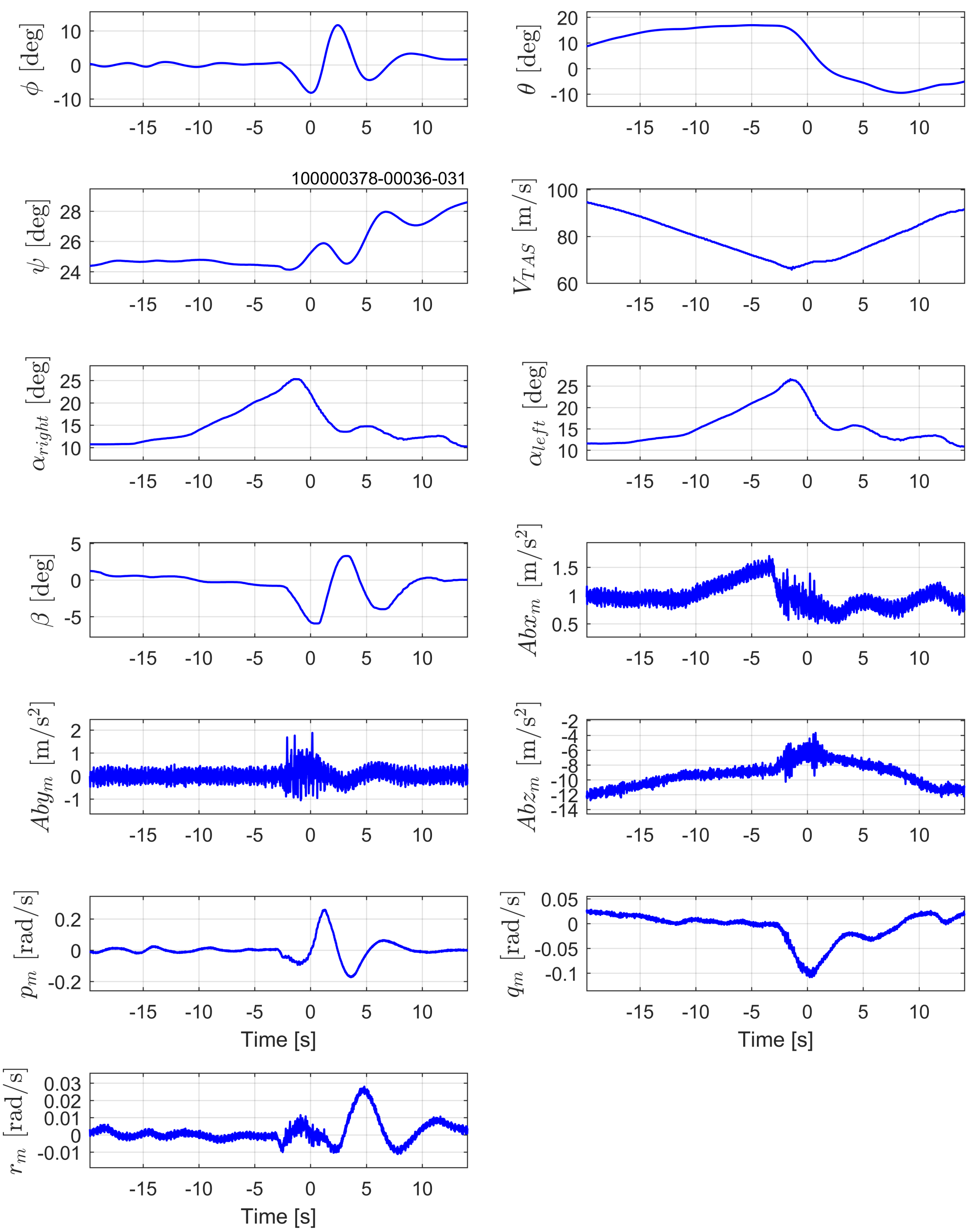
100000378-00036-031
ϕ [deg]
θ [deg]
ψ [deg]
V_{TAS} [m/s]
α_{right} [deg]
α_{left} [deg]
β [deg]
Abx_m [m/s^2]
Aby_m [m/s^2]
Abz_m [m/s^2]
p_m [rad/s]
q_m [rad/s]
r_m [rad/s]
Time [s]

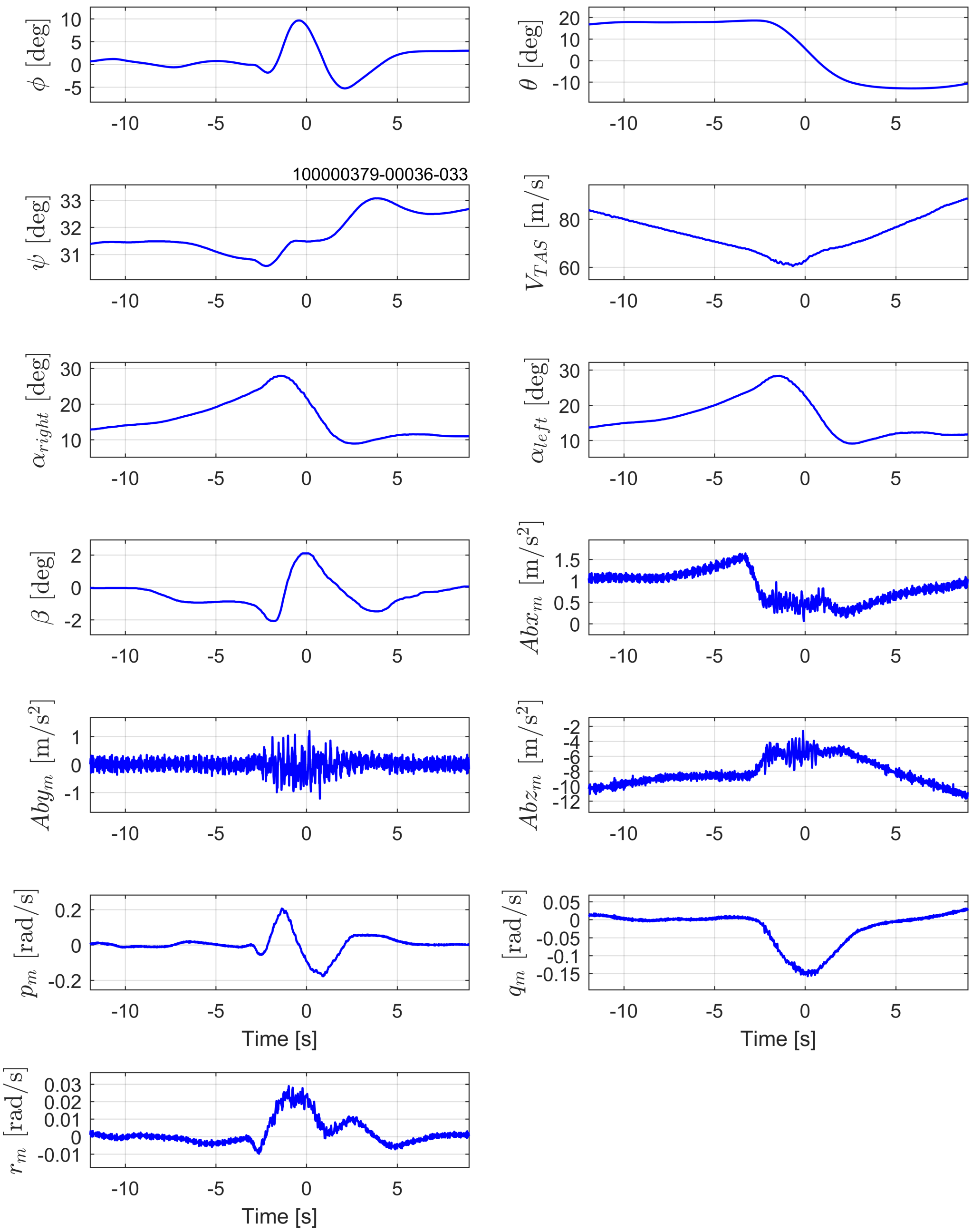
100000379-00036-033
ϕ [deg]
θ [deg]
ψ [deg]
V_{TAS} [m/s]
α_{right} [deg]
α_{left} [deg]
β [deg]
Abx_m [m/s^2]
Aby_m [m/s^2]
Abz_m [m/s^2]
p_m [rad/s]
q_m [rad/s]
r_m [rad/s]
Time [s]

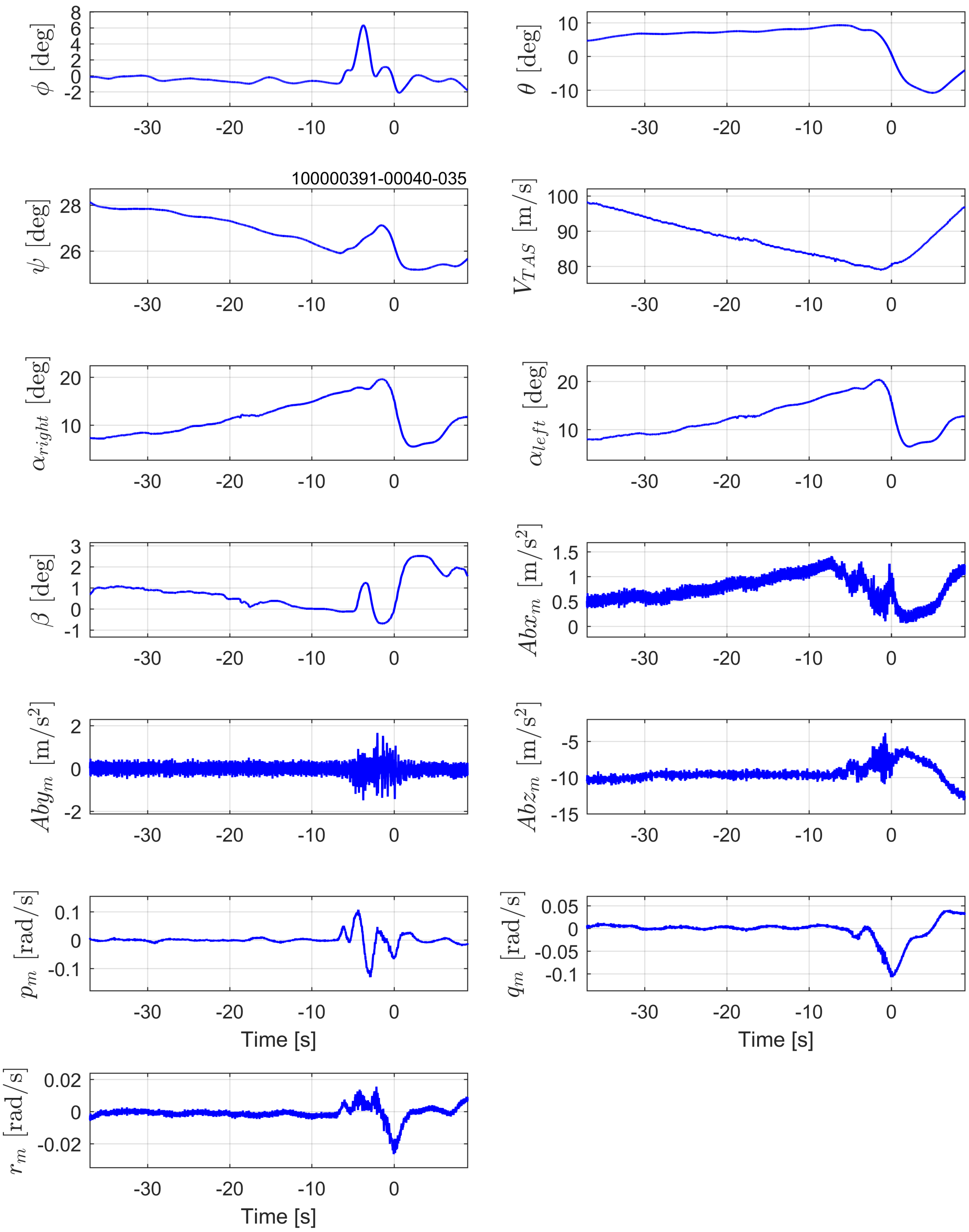
ϕ [deg]
θ [deg]
100000391-00040-035
ψ [deg]
V_{TAS} [m/s]
α_{right} [deg]
α_{left} [deg]
β [deg]
Abx_m [m/s^2]
Aby_m [m/s^2]
Abz_m [m/s^2]
p_m [rad/s]
q_m [rad/s]
r_m [rad/s]
Time [s]
Time [s]
Time [s]

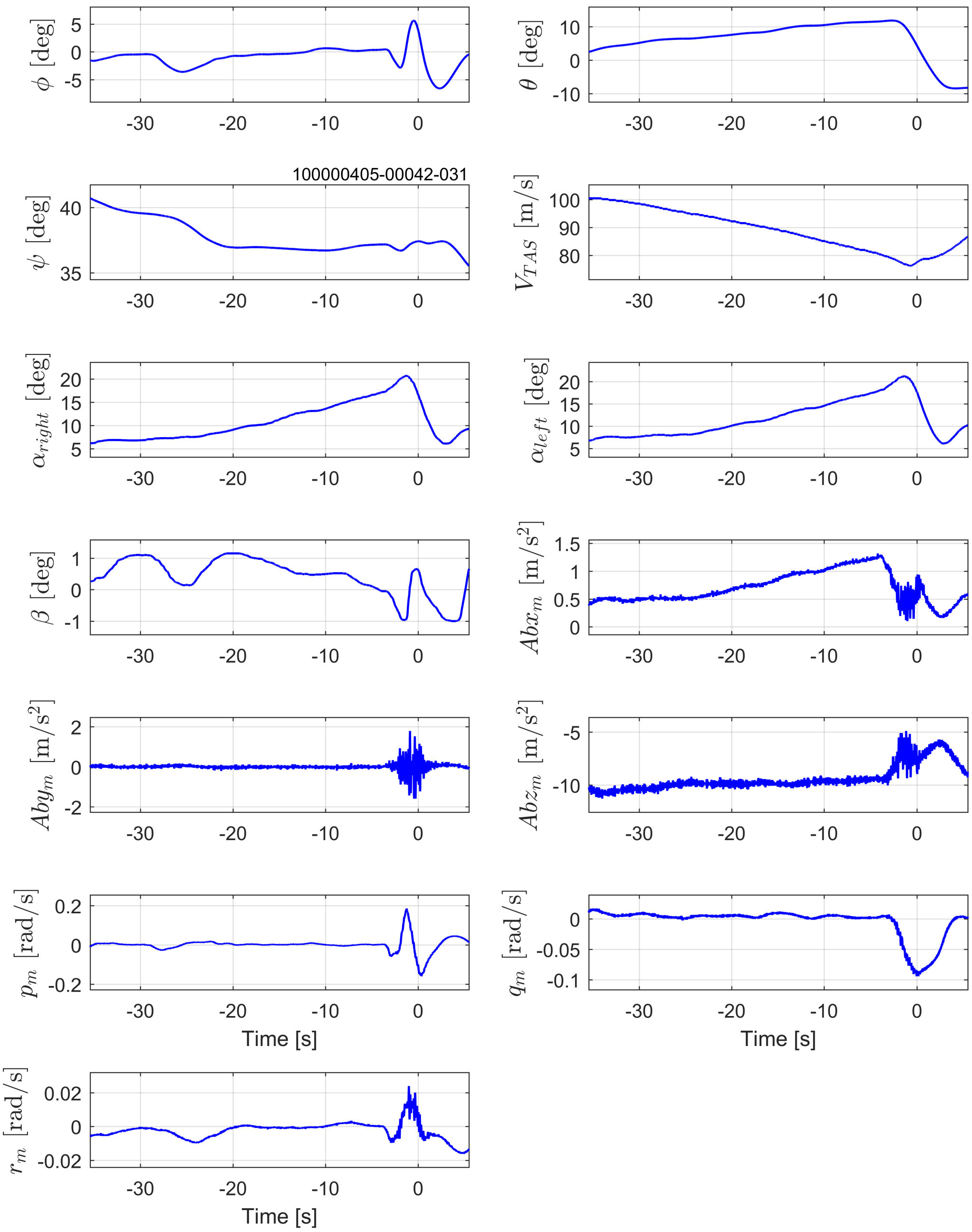
ϕ [deg]
θ [deg]
100000405-00042-031
ψ [deg]
V_{TAS} [m/s]
α_{right} [deg]
α_{left} [deg]
β [deg]
Abx_m [m/s^2]
Aby_m [m/s^2]
Abz_m [m/s^2]
p_m [rad/s]
q_m [rad/s]
r_m [rad/s]
Time [s]

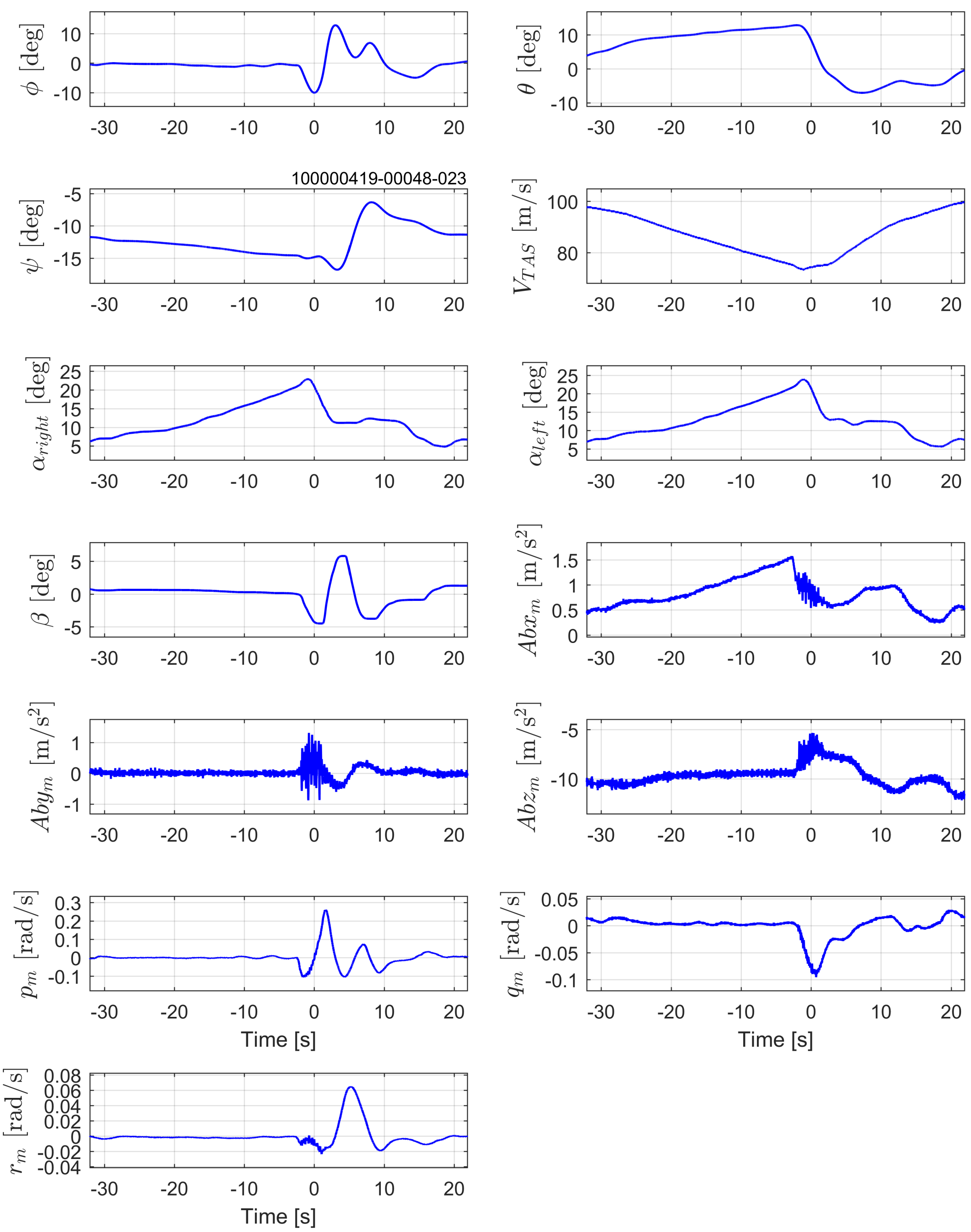

100000419-00048-023
ϕ [deg]
θ [deg]
ψ [deg]
V_{TAS} [m/s]
α_{right} [deg]
α_{left} [deg]
β [deg]
Abx_m [m/s^2]
Aby_m [m/s^2]
Abz_m [m/s^2]
p_m [rad/s]
q_m [rad/s]
r_m [rad/s]
Time [s]

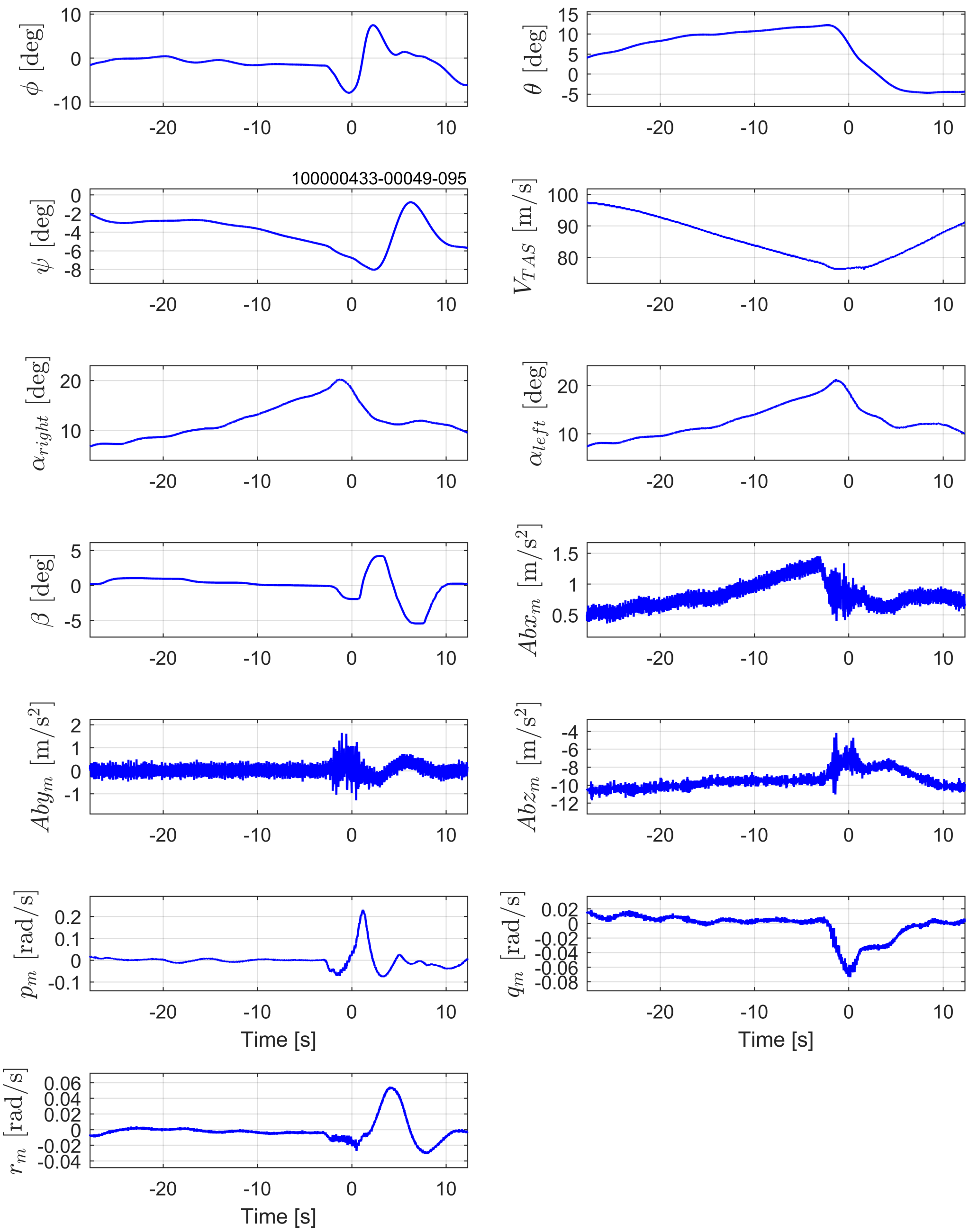
100000433-00049-095
ϕ [deg]
θ [deg]
ψ [deg]
V_{TAS} [m/s]
α_{right} [deg]
α_{left} [deg]
β [deg]
Abx_m [m/s^2]
Aby_m [m/s^2]
Abz_m [m/s^2]
p_m [rad/s]
q_m [rad/s]
r_m [rad/s]
Time [s]

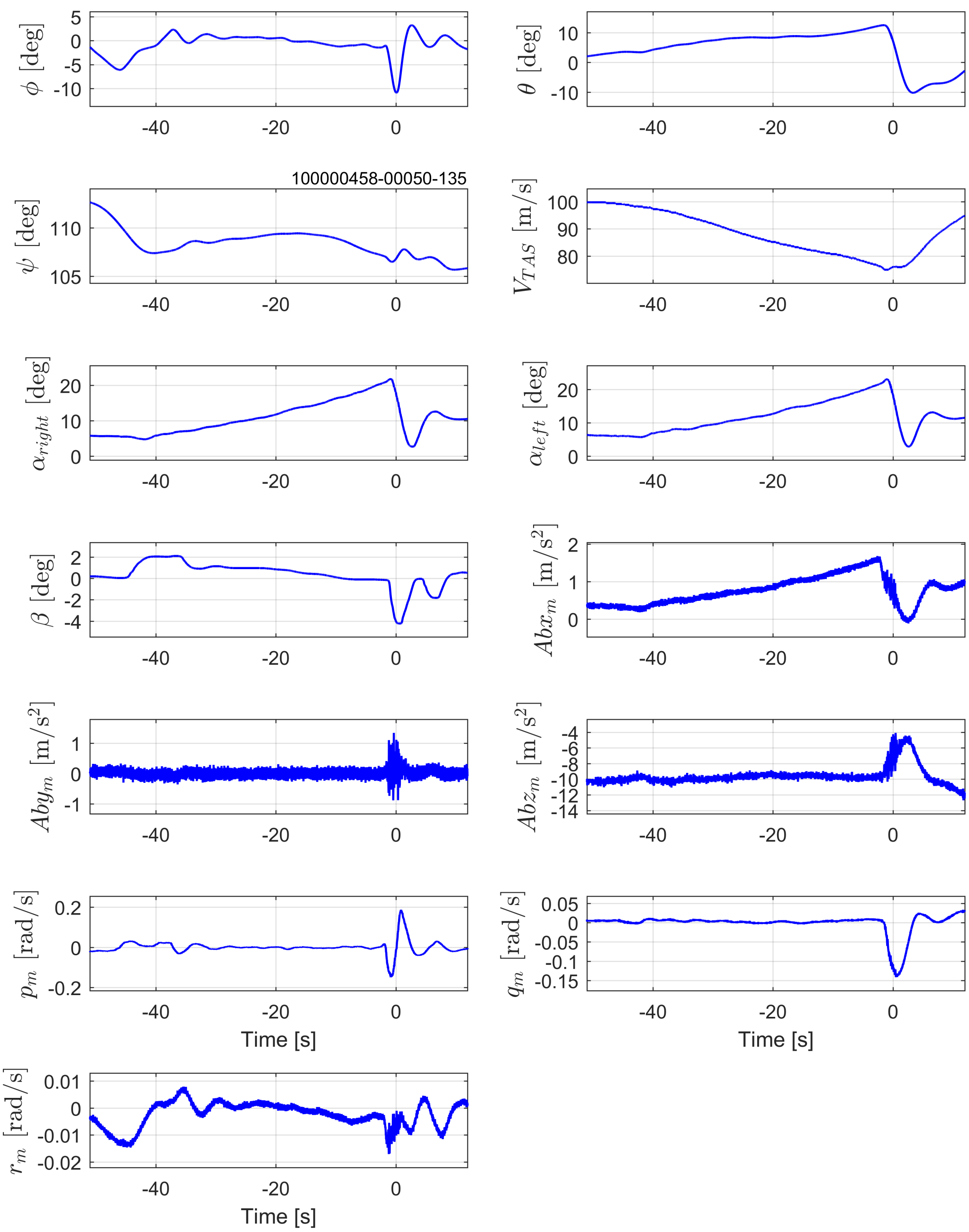
100000458-00050-135
Time [s]

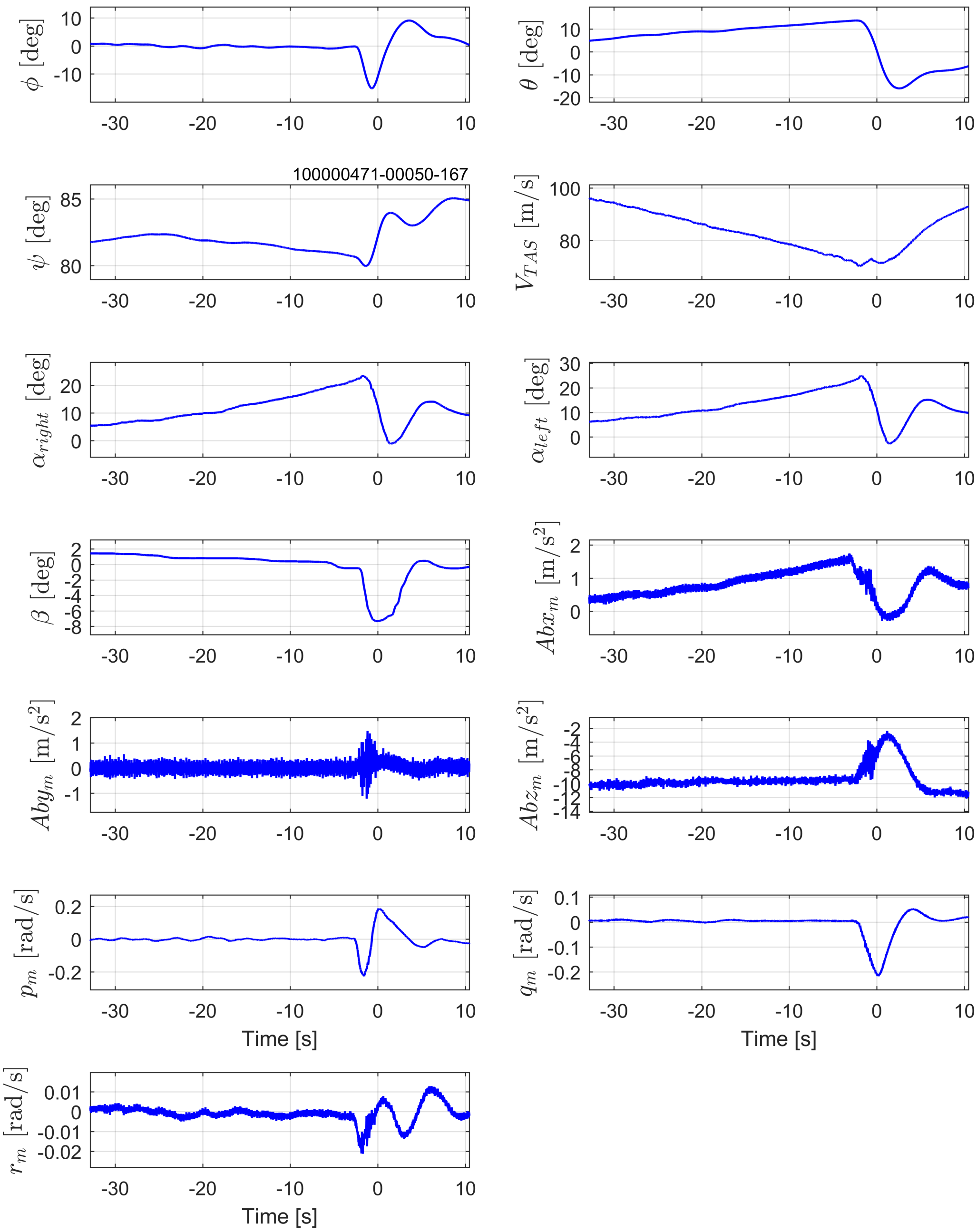

100000471-00050-167
ϕ [deg]
θ [deg]
ψ [deg]
V_{TAS} [m/s]
α_{right} [deg]
α_{left} [deg]
β [deg]
Abx_m [m/s^2]
Aby_m [m/s^2]
Abz_m [m/s^2]
p_m [rad/s]
q_m [rad/s]
r_m [rad/s]
-30 -20 -10 0 10
Time [s]

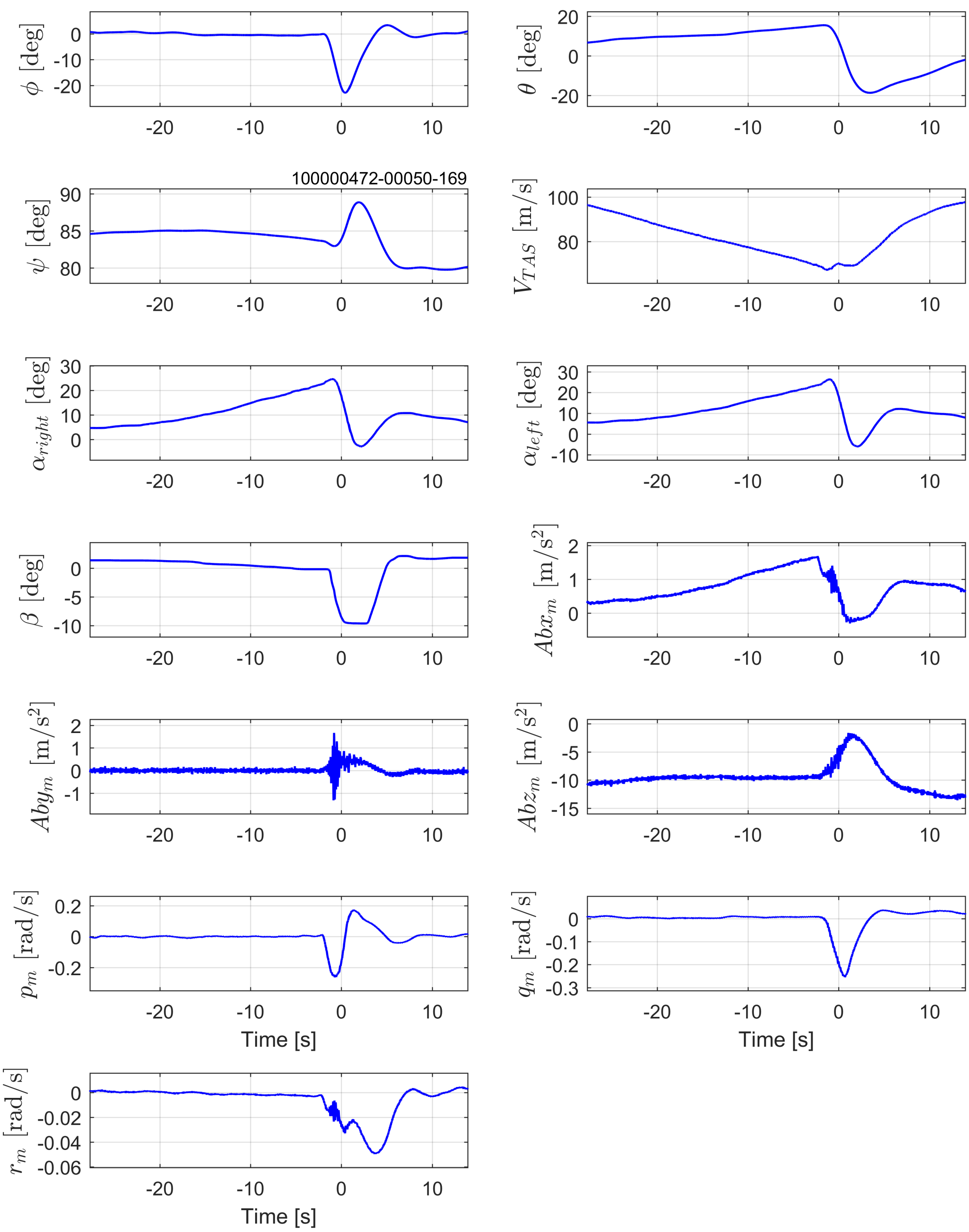
100000472-00050-169
ϕ [deg]
θ [deg]
ψ [deg]
V_TAS [m/s]
α_right [deg]
α_left [deg]
β [deg]
Abx_m [m/s²]
Aby_m [m/s²]
Abz_m [m/s²]
p_m [rad/s]
q_m [rad/s]
r_m [rad/s]
Time [s]

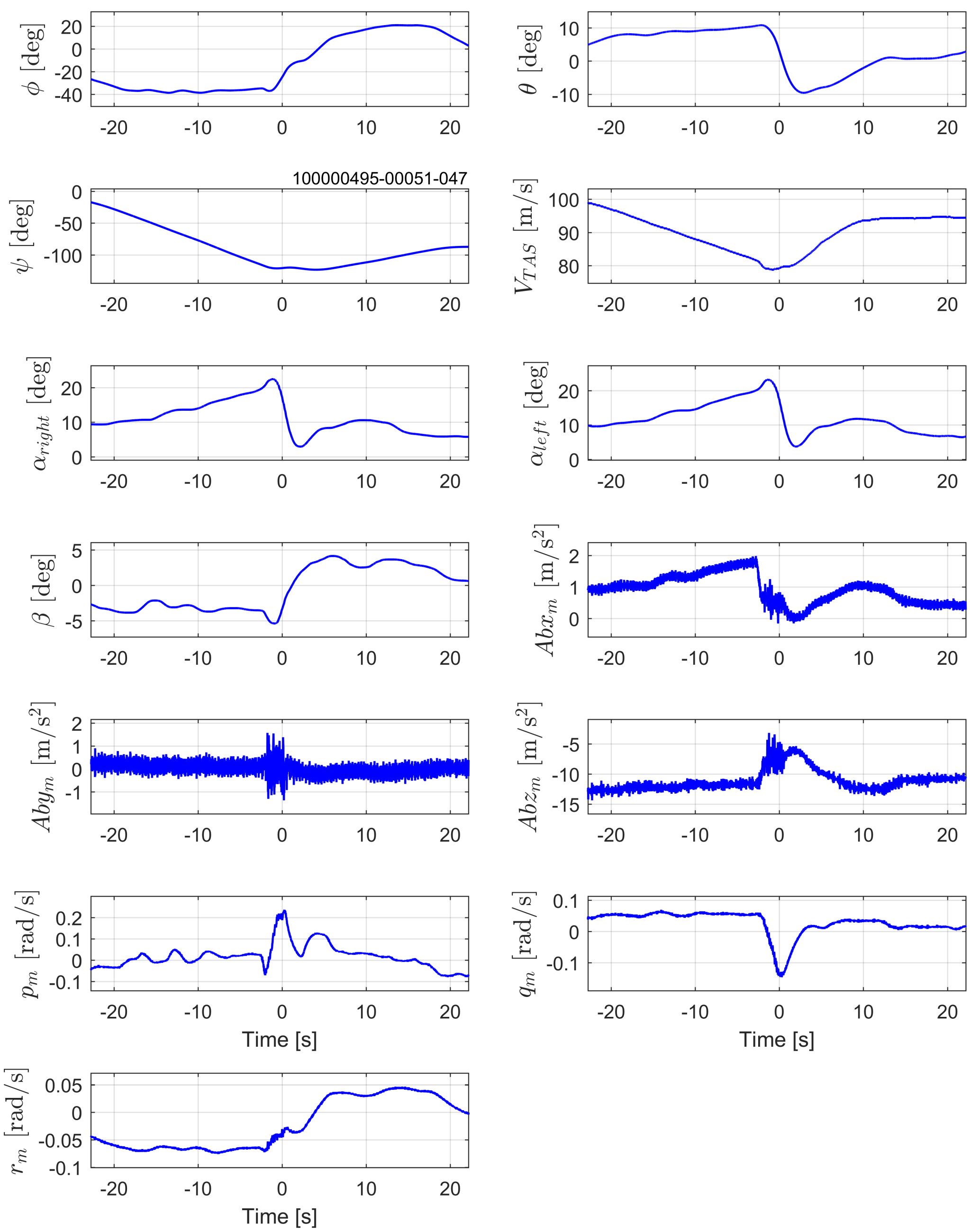
100000495-00051-047
ϕ [deg]
θ [deg]
ψ [deg]
V_{TAS} [m/s]
α_{right} [deg]
α_{left} [deg]
β [deg]
Abx_m [m/s^2]
Aby_m [m/s^2]
Abz_m [m/s^2]
p_m [rad/s]
q_m [rad/s]
r_m [rad/s]
Time [s]

A.4. 25° Flaps and Gear Down

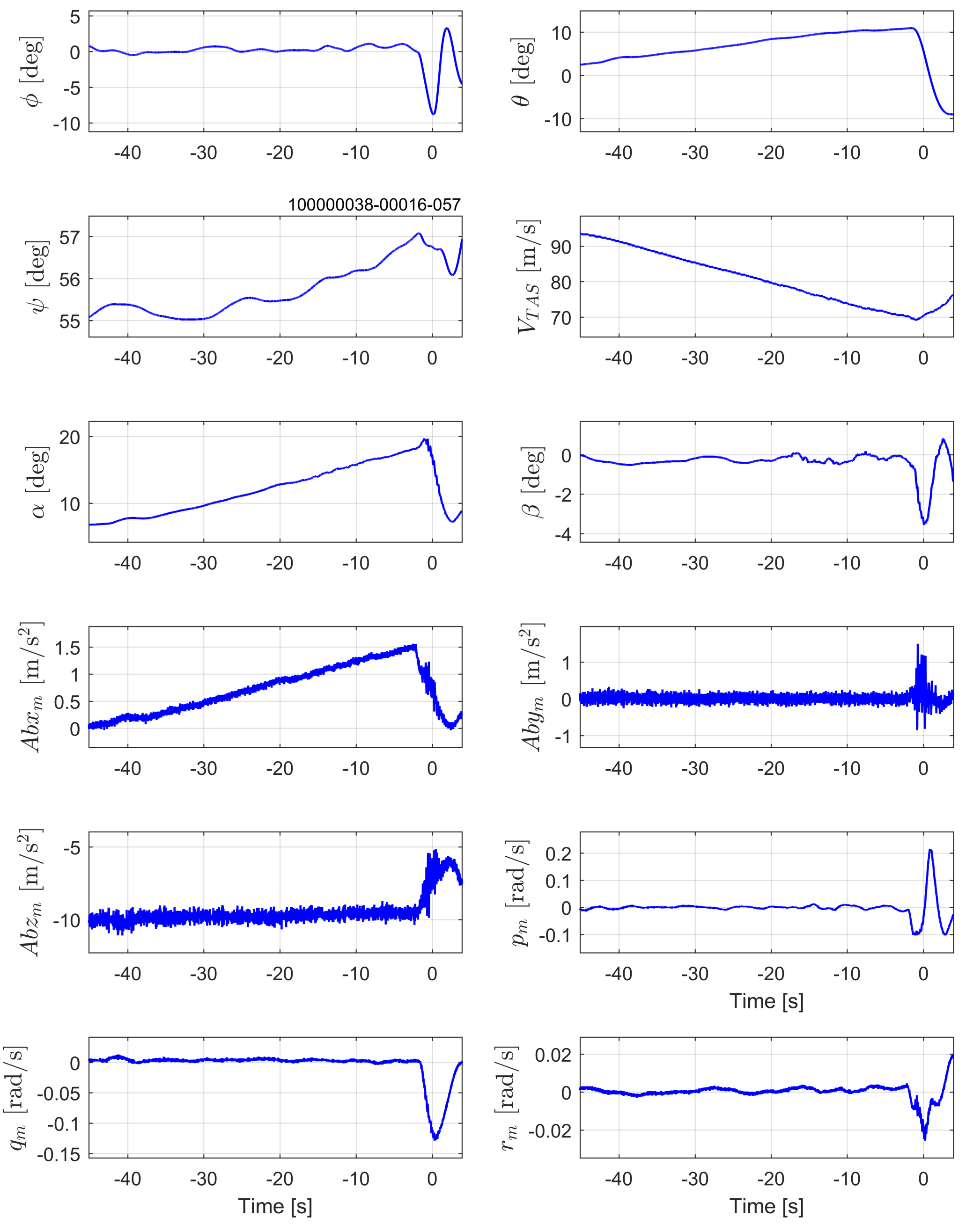

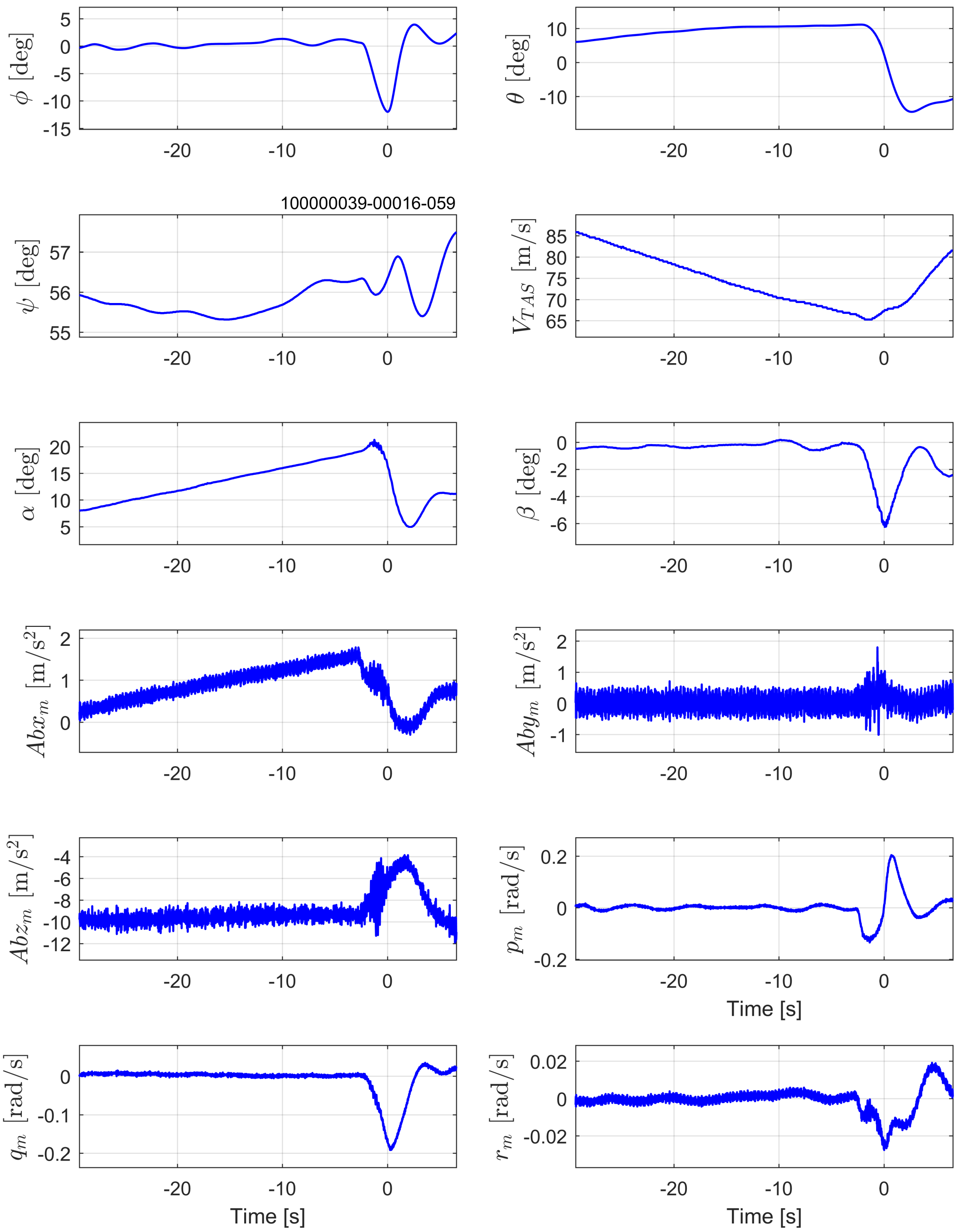
100000039-00016-059
ϕ [deg]
θ [deg]
ψ [deg]
V_{TAS} [m/s]
α [deg]
β [deg]
Abx_m [m/s^2]
Aby_m [m/s^2]
Abz_m [m/s^2]
p_m [rad/s]
q_m [rad/s]
r_m [rad/s]
Time [s]
Time [s]
Time [s]

A.5. Landing Configuration

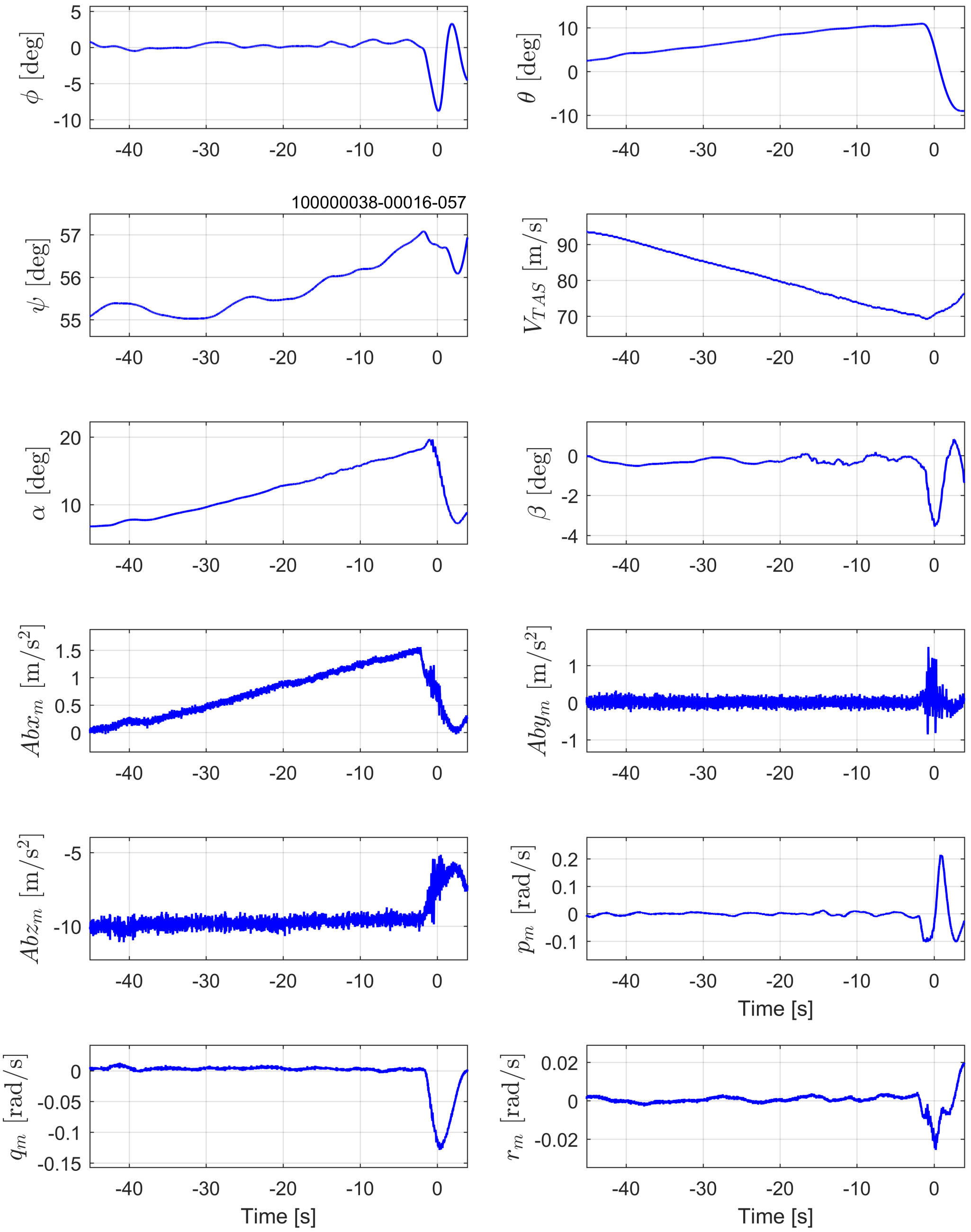

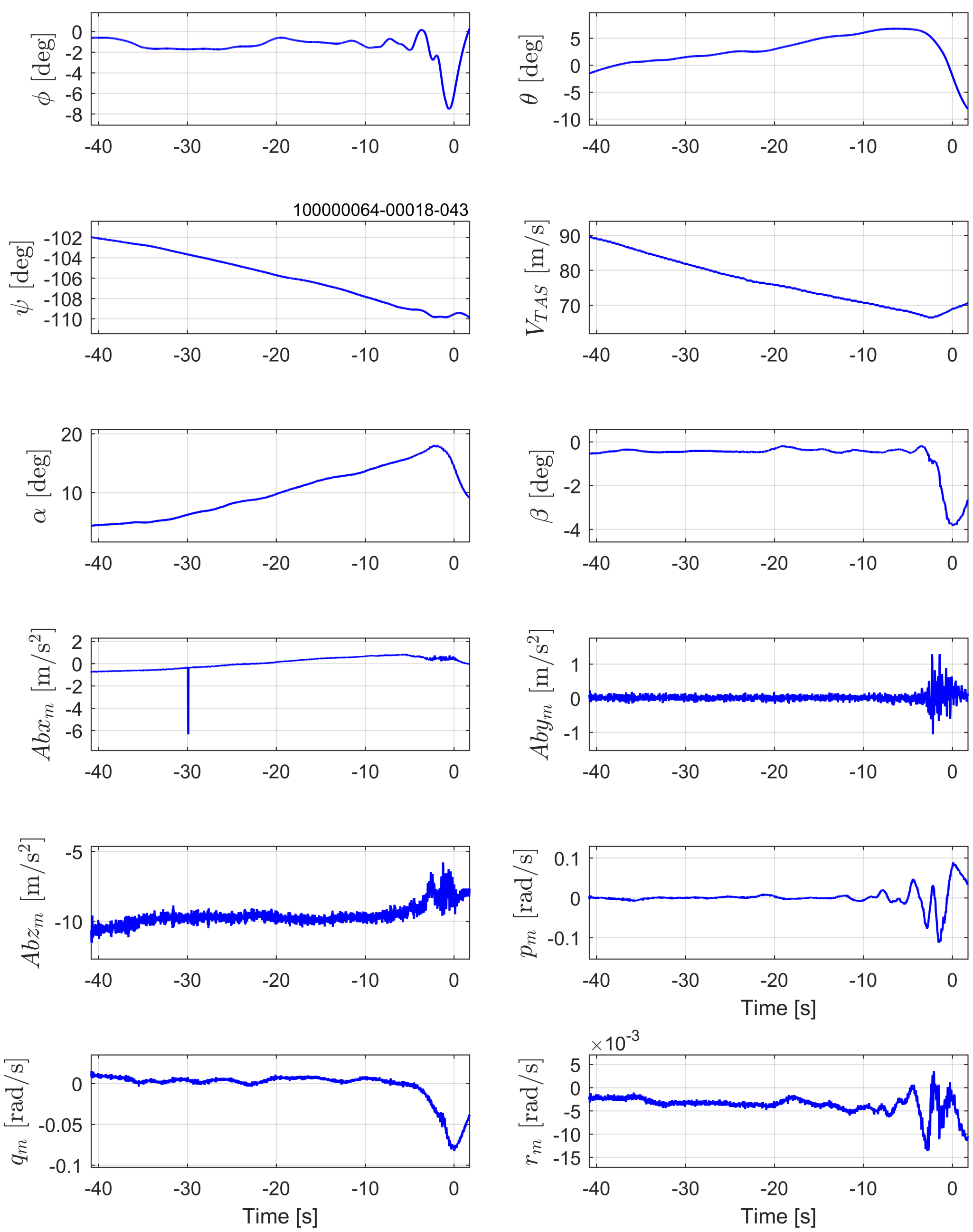

100000064-00018-043
ϕ [deg]
θ [deg]
ψ [deg]
V_{TAS} [m/s]
α [deg]
β [deg]
Abx_m [m/s^2]
Aby_m [m/s^2]
Abz_m [m/s^2]
p_m [rad/s]
q_m [rad/s]
r_m [rad/s]
$\times 10^{-3}$
Time [s]

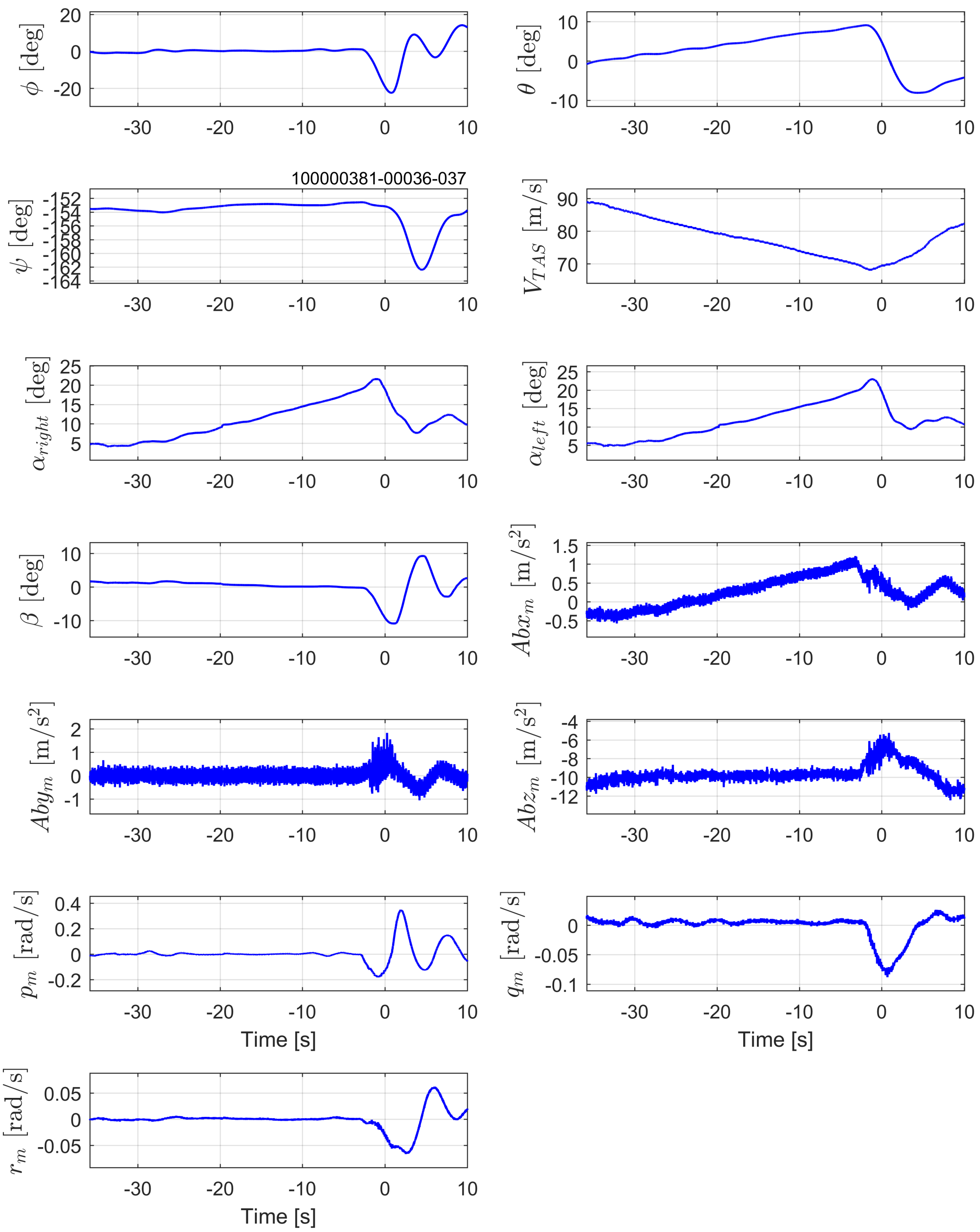
100000381-00036-037
ϕ [deg]
θ [deg]
ψ [deg]
V_{TAS} [m/s]
α_{right} [deg]
α_{left} [deg]
β [deg]
Abx_m [m/s^2]
Aby_m [m/s^2]
Abz_m [m/s^2]
p_m [rad/s]
q_m [rad/s]
r_m [rad/s]
Time [s]

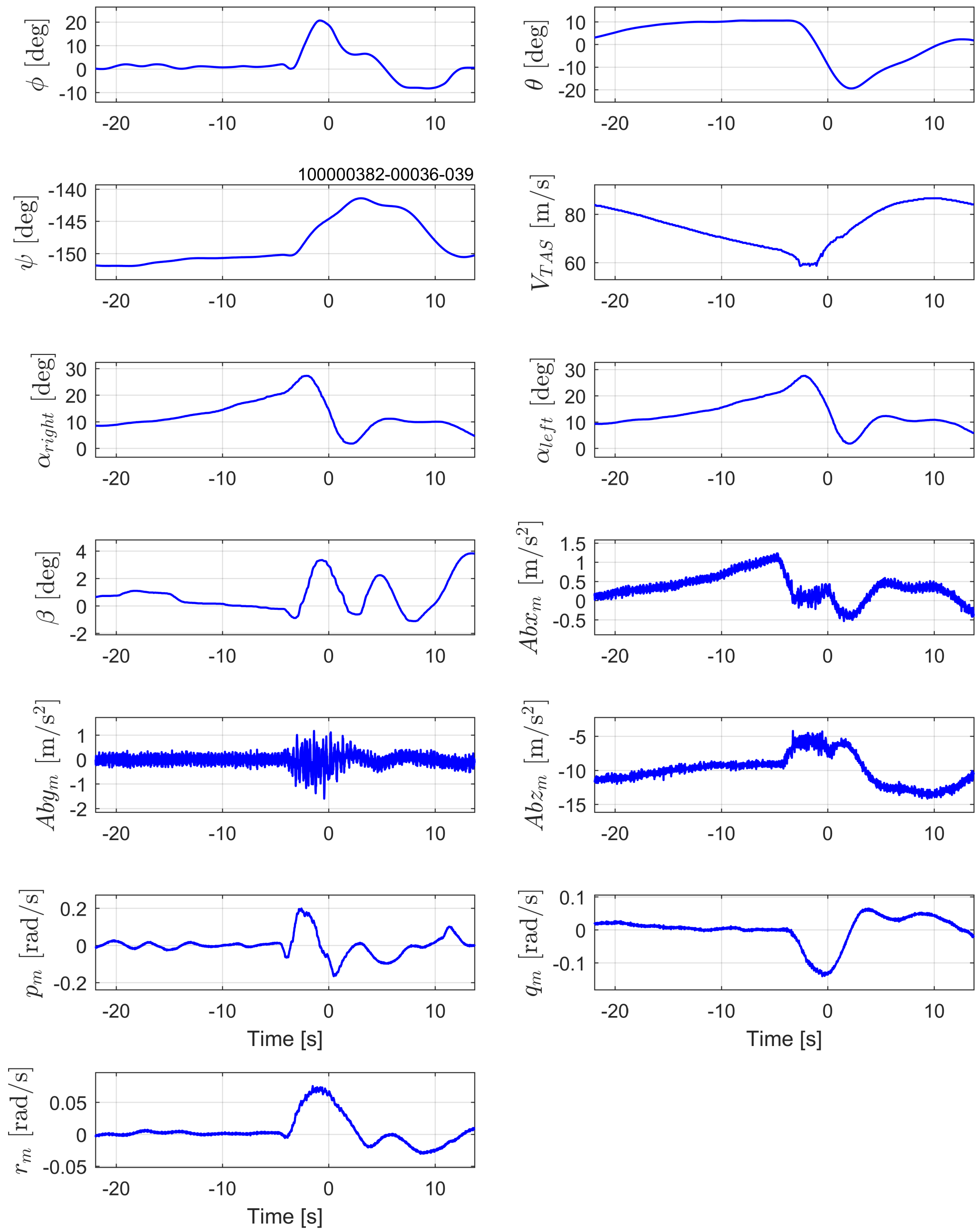
100000382-00036-039
Time [s]
Time [s]
Time [s]

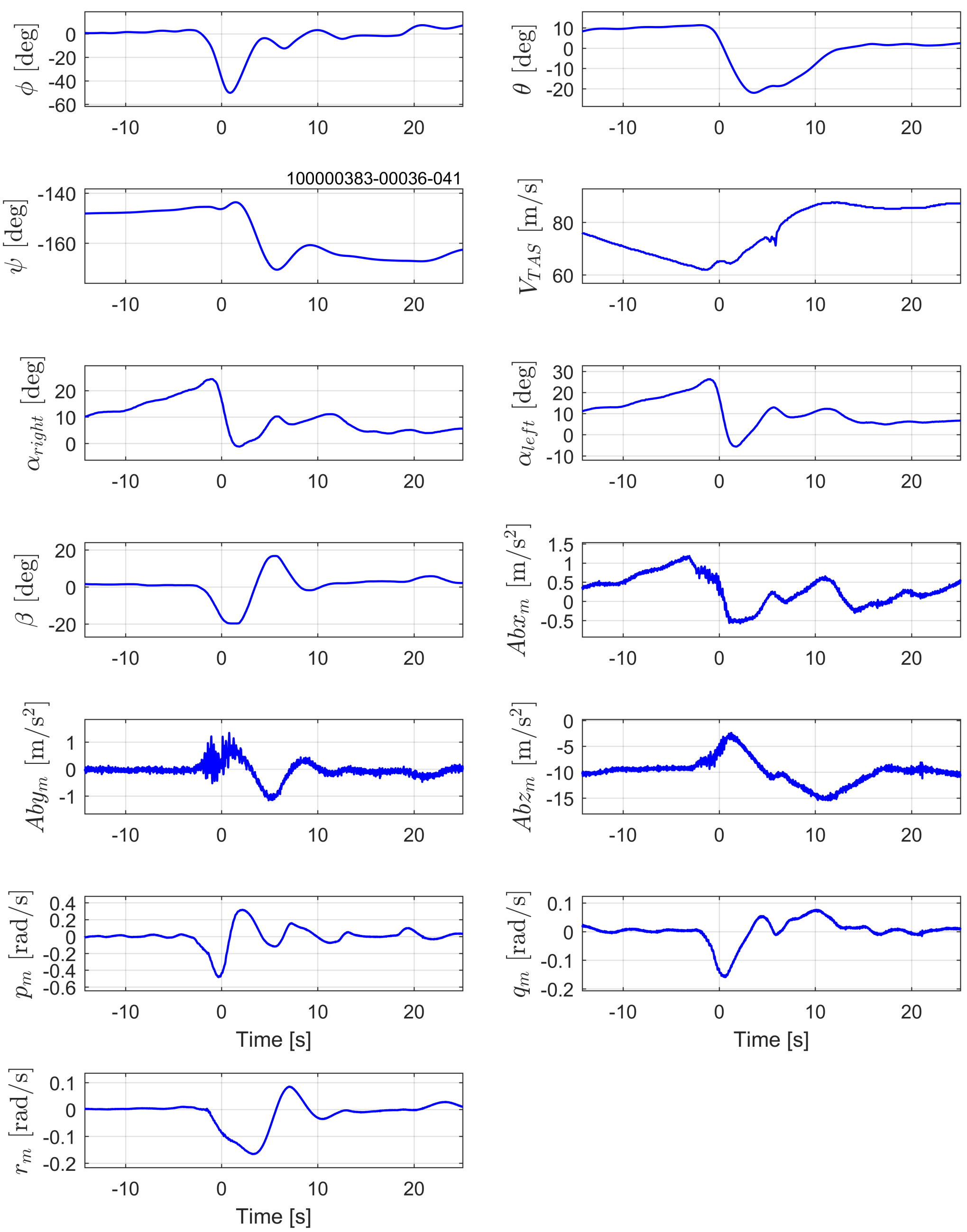

100000383-00036-041
ϕ [deg]
θ [deg]
ψ [deg]
V_{TAS} [m/s]
α_{right} [deg]
α_{left} [deg]
β [deg]
Abx_m [m/s^2]
Aby_m [m/s^2]
Abz_m [m/s^2]
p_m [rad/s]
q_m [rad/s]
r_m [rad/s]
Time [s]

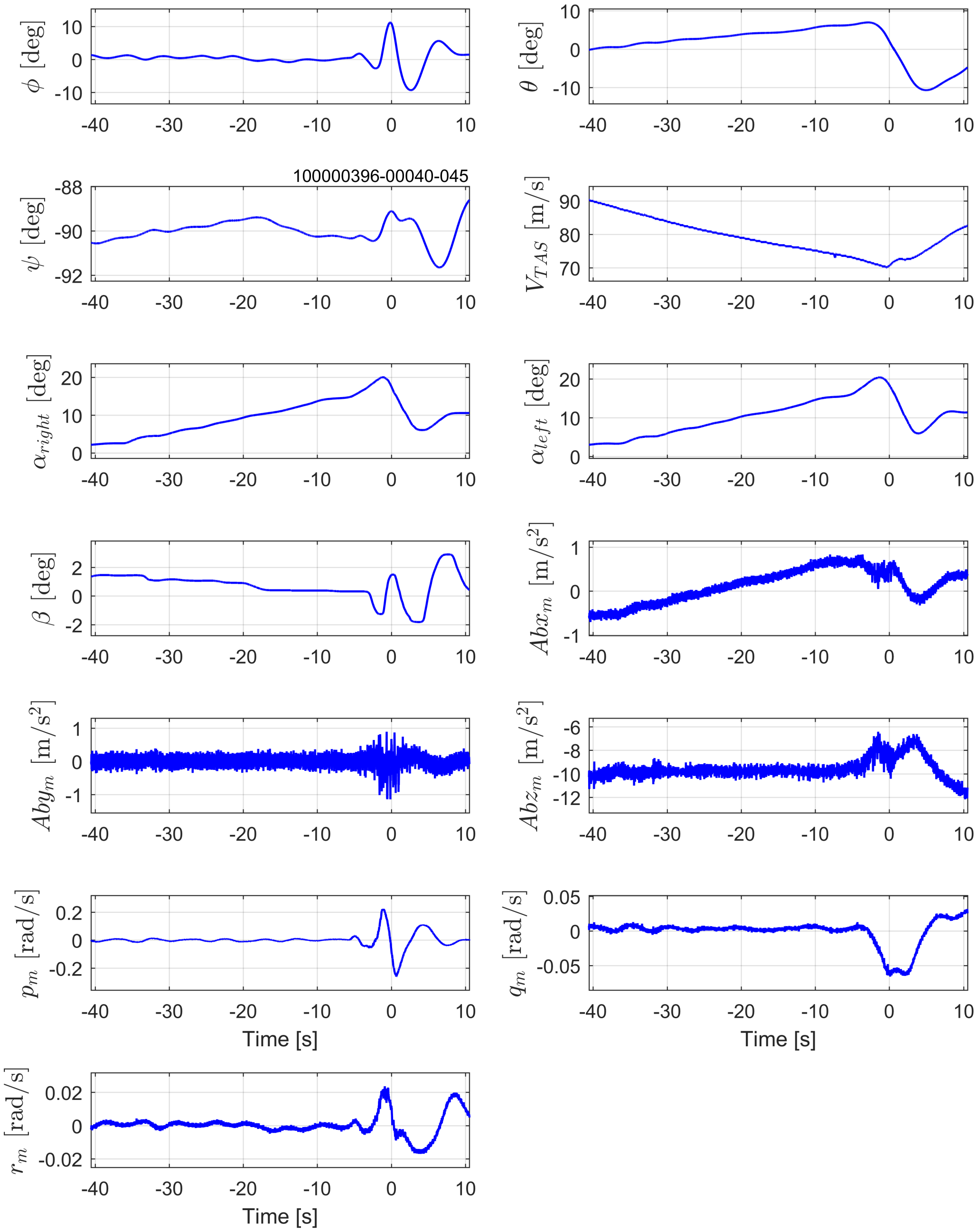

ϕ [deg]
θ [deg]
100000396-00040-045
ψ [deg]
V_{TAS} [m/s]
α_{right} [deg]
α_{left} [deg]
β [deg]
Abx_m [m/s^2]
Aby_m [m/s^2]
Abz_m [m/s^2]
p_m [rad/s]
q_m [rad/s]
r_m [rad/s]
Time [s]
Time [s]
Time [s]

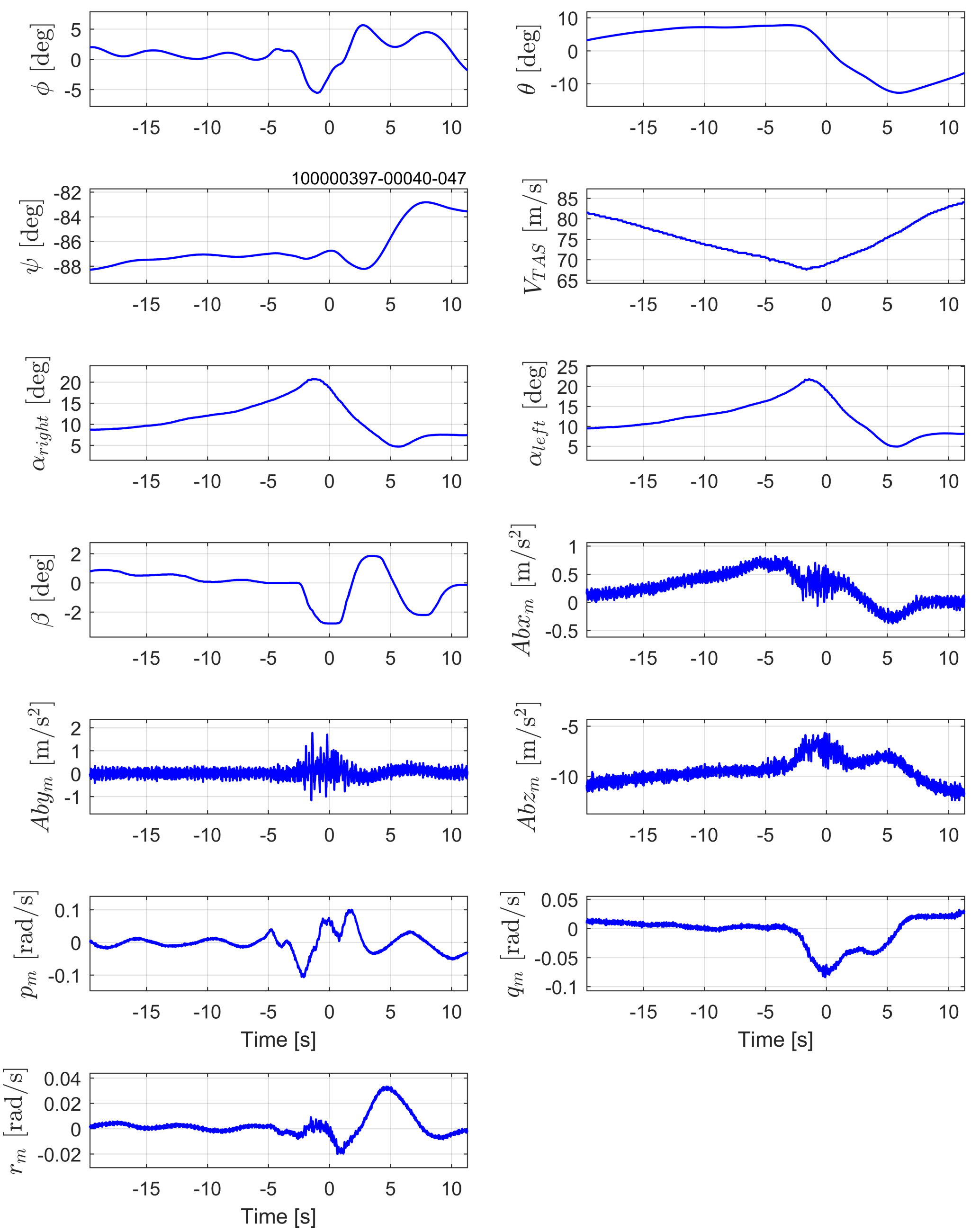
100000397-00040-047
ϕ [deg]
θ [deg]
ψ [deg]
V_{TAS} [m/s]
α_{right} [deg]
α_{left} [deg]
β [deg]
Abx_m [m/s^2]
Aby_m [m/s^2]
Abz_m [m/s^2]
p_m [rad/s]
q_m [rad/s]
r_m [rad/s]
Time [s]

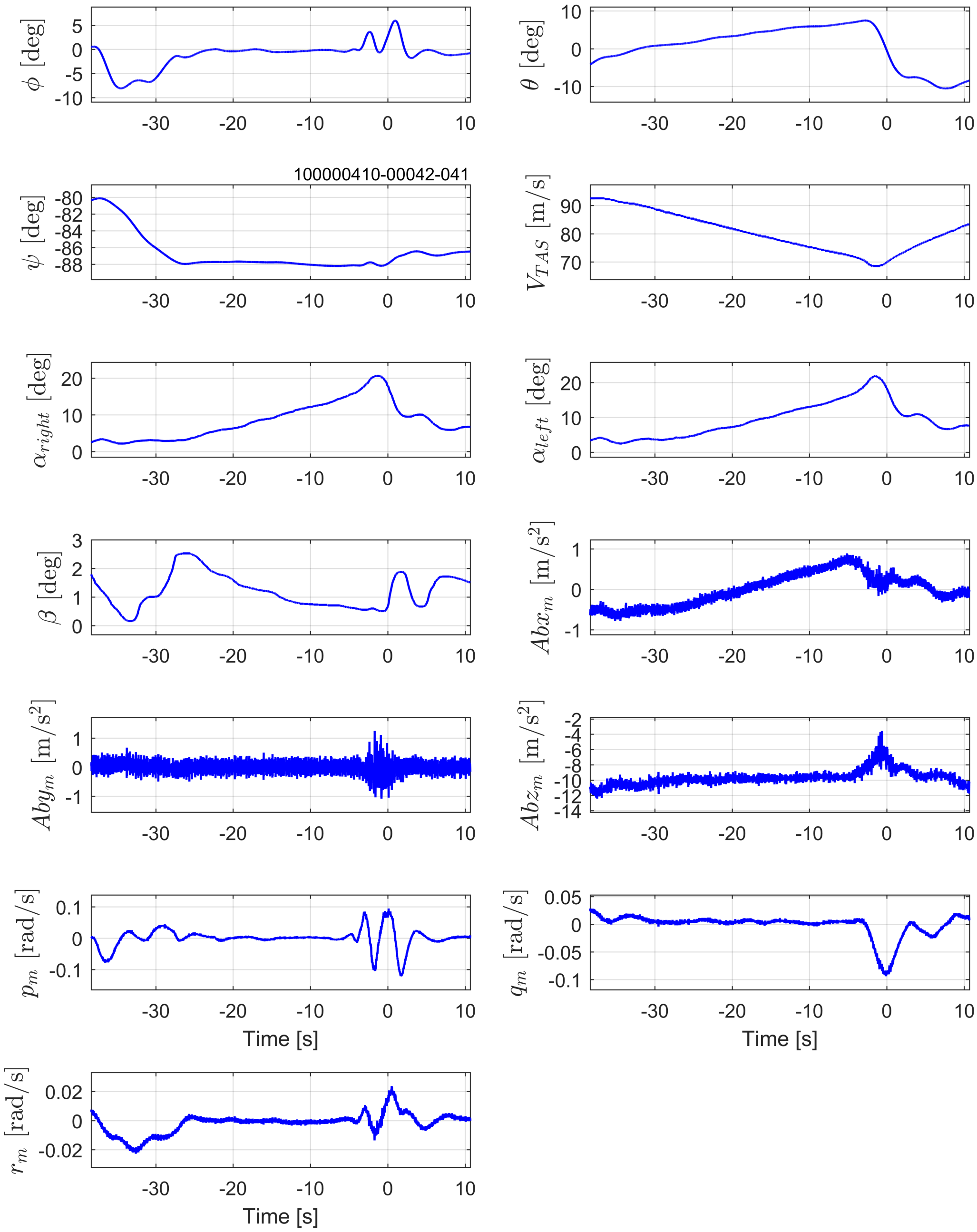
100000410-00042-041
ϕ [deg]
θ [deg]
ψ [deg]
V_{TAS} [m/s]
α_{right} [deg]
α_{left} [deg]
β [deg]
Abx_m [m/s²]
Aby_m [m/s²]
Abz_m [m/s²]
p_m [rad/s]
q_m [rad/s]
r_m [rad/s]
Time [s]

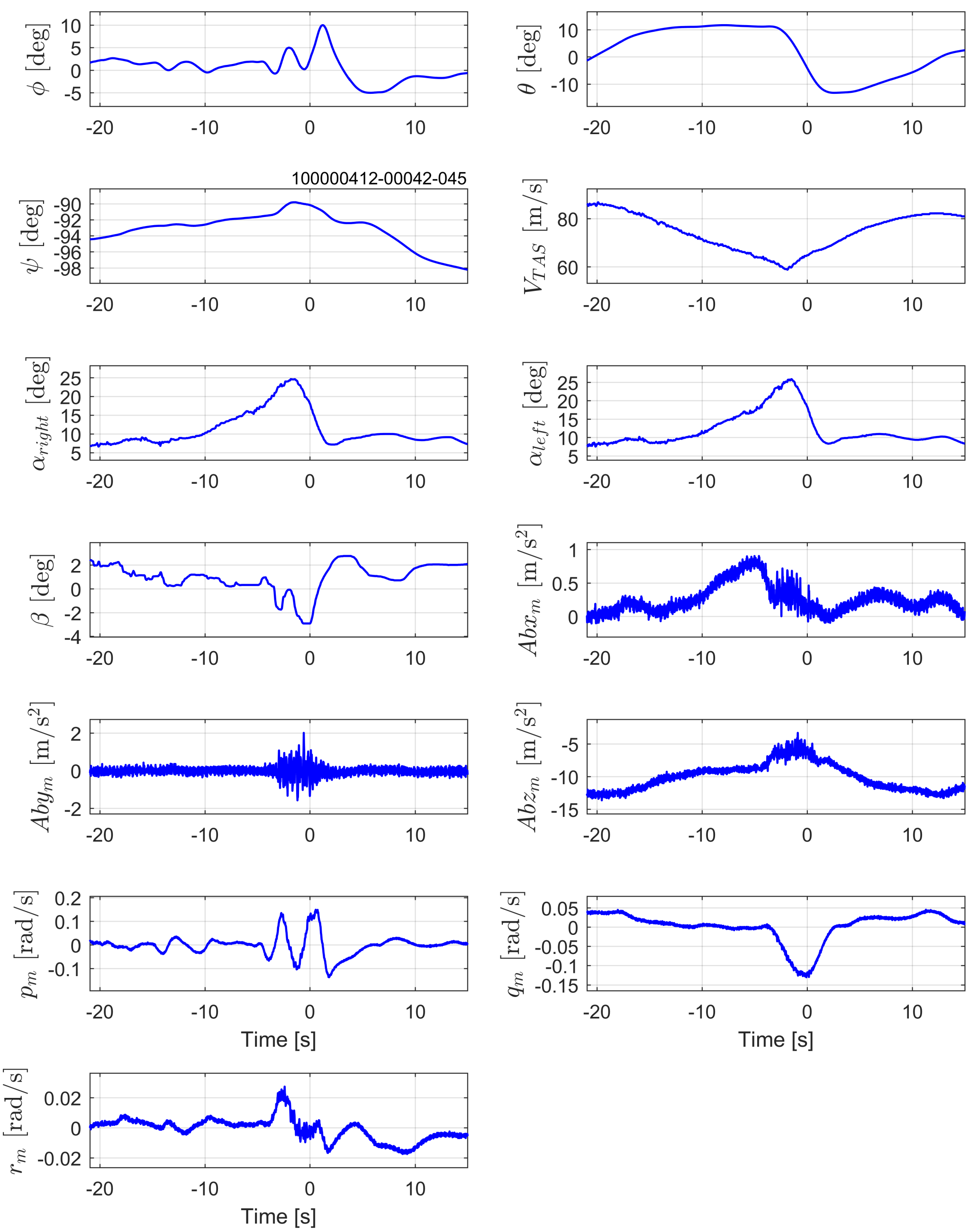
100000412-00042-045
ϕ [deg]
θ [deg]
ψ [deg]
V_{TAS} [m/s]
α_{right} [deg]
α_{left} [deg]
β [deg]
Abx_m [m/s^2]
Aby_m [m/s^2]
Abz_m [m/s^2]
p_m [rad/s]
q_m [rad/s]
r_m [rad/s]
Time [s]

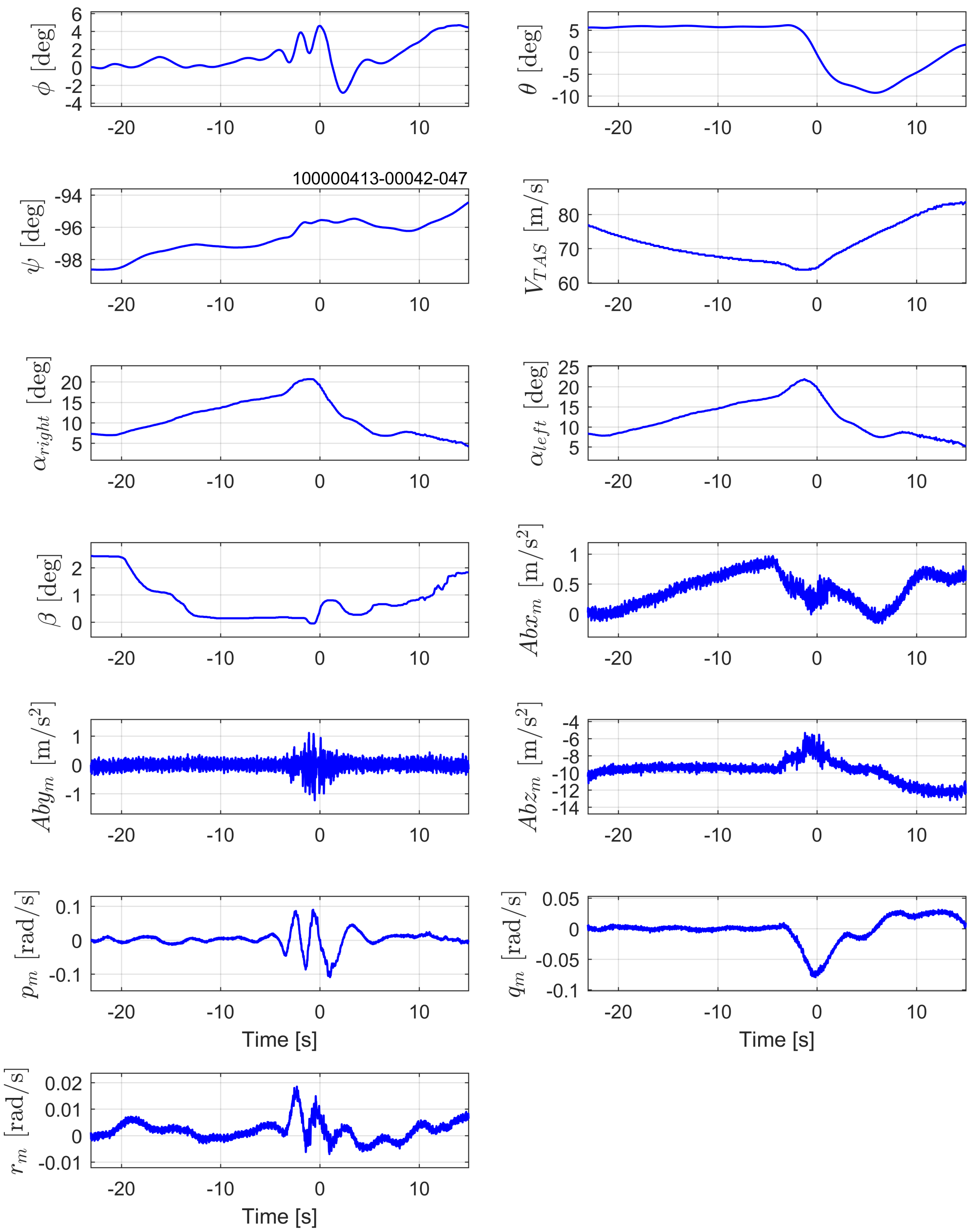
100000413-00042-047
ϕ [deg]
θ [deg]
ψ [deg]
V_{TAS} [m/s]
α_{right} [deg]
α_{left} [deg]
β [deg]
Abx_m [m/s^2]
Aby_m [m/s^2]
Abz_m [m/s^2]
p_m [rad/s]
q_m [rad/s]
r_m [rad/s]
Time [s]

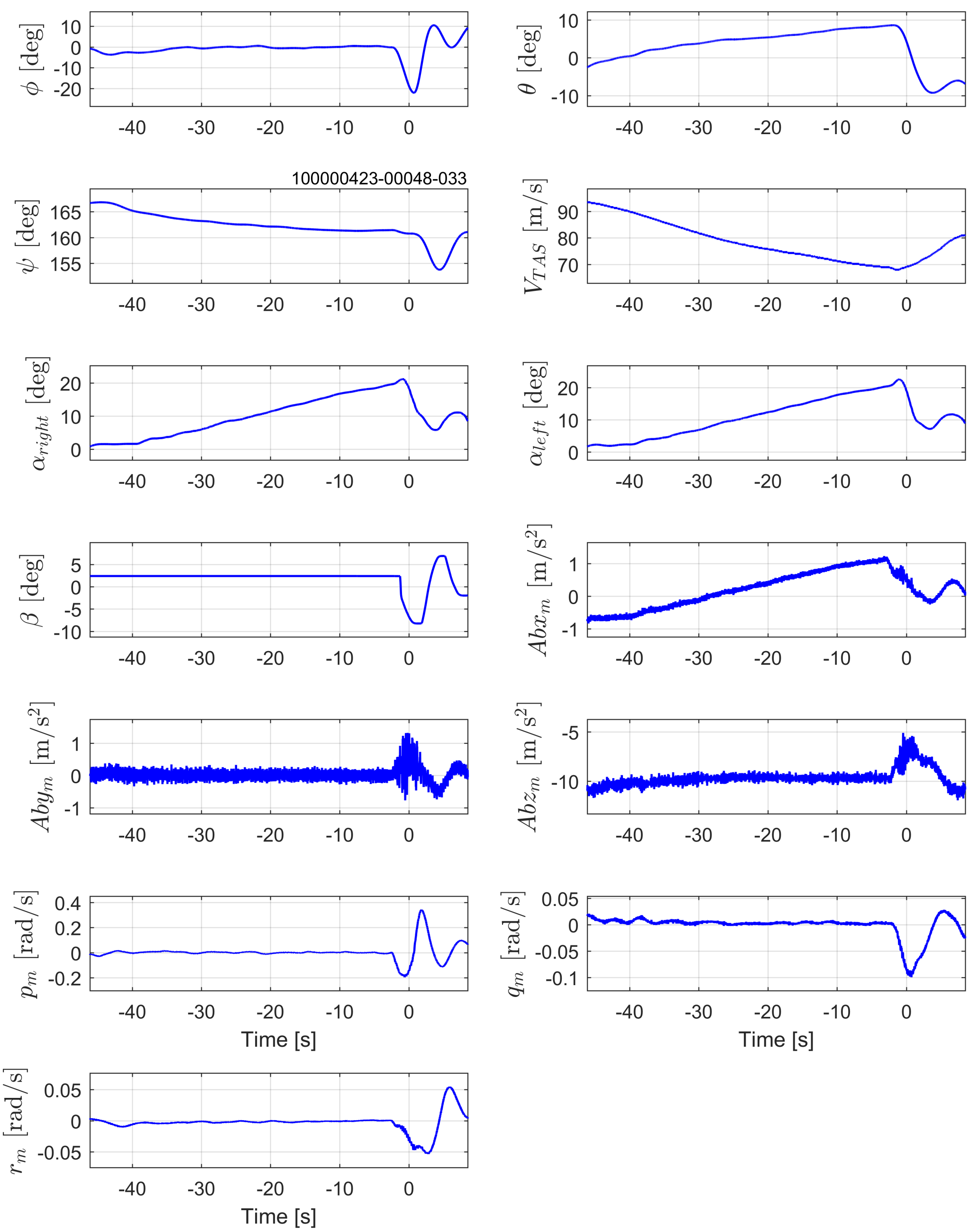

100000423-00048-033
ϕ [deg]
θ [deg]
ψ [deg]
V_{TAS} [m/s]
α_{right} [deg]
α_{left} [deg]
β [deg]
Abx_m [m/s^2]
Aby_m [m/s^2]
Abz_m [m/s^2]
p_m [rad/s]
q_m [rad/s]
r_m [rad/s]
Time [s]

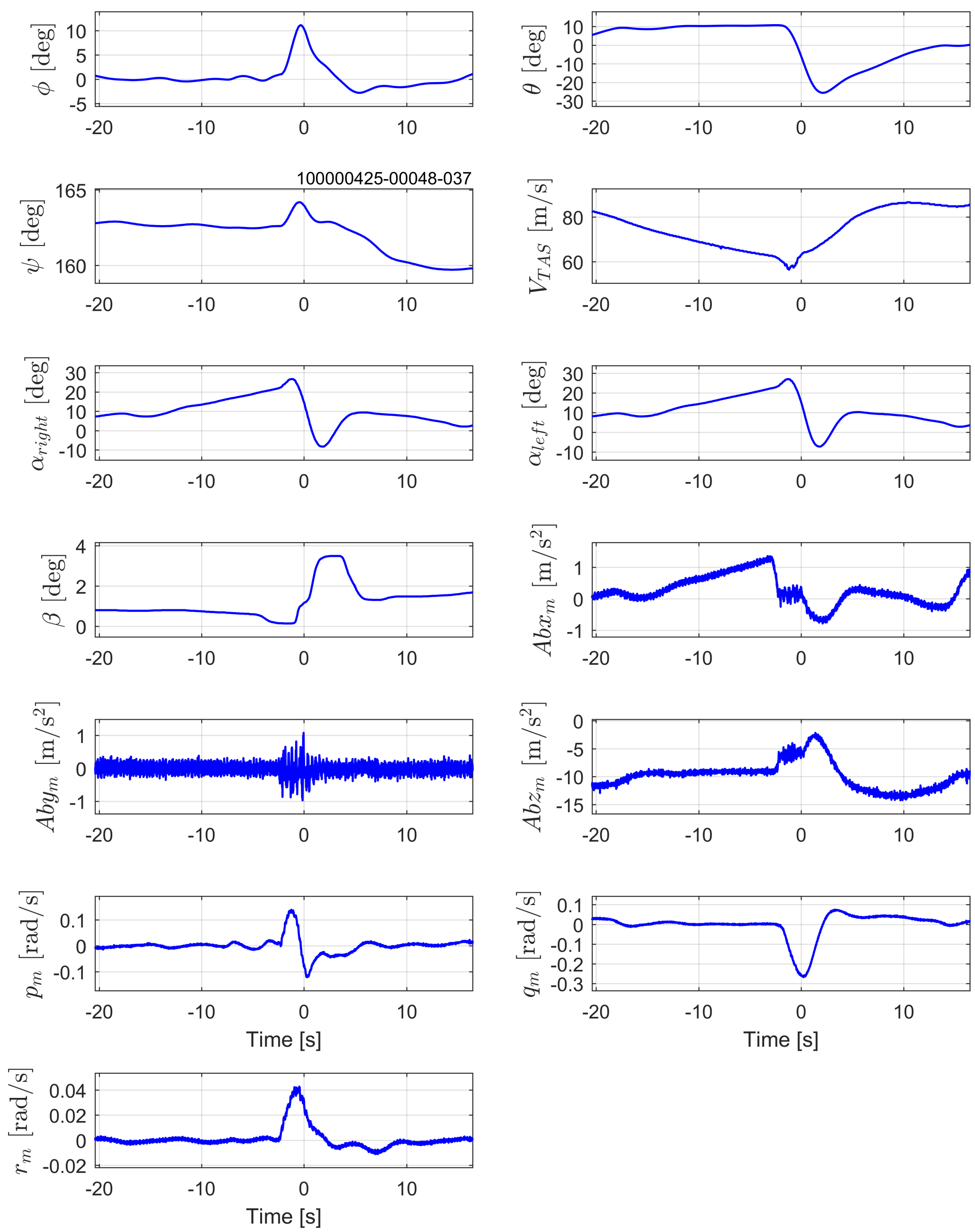

ϕ [deg]
θ [deg]
100000425-00048-037
ψ [deg]
V_{TAS} [m/s]
α_{right} [deg]
α_{left} [deg]
β [deg]
Abx_m [m/s^2]
Aby_m [m/s^2]
Abz_m [m/s^2]
p_m [rad/s]
q_m [rad/s]
r_m [rad/s]
Time [s]

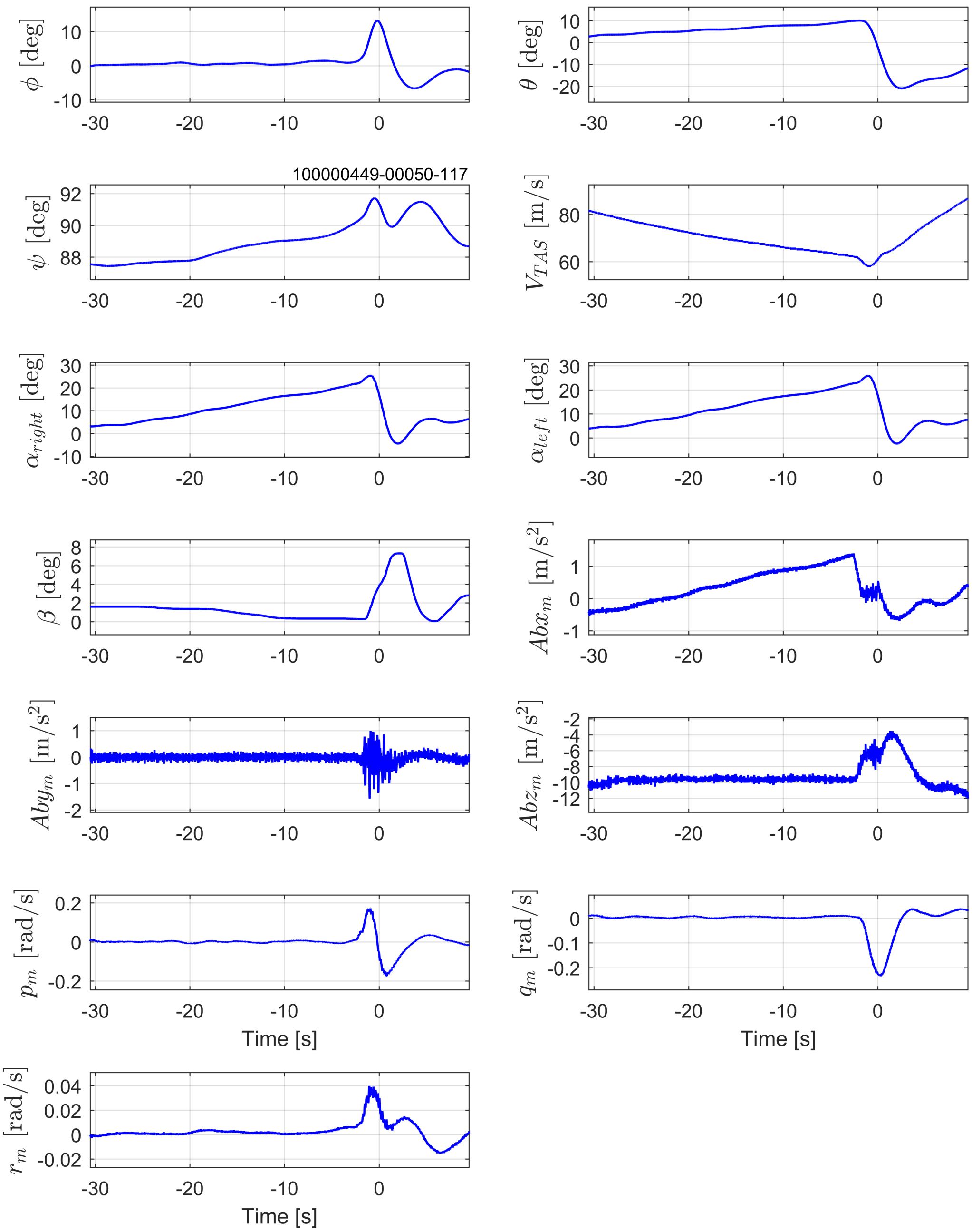
100000449-00050-117
ϕ [deg]
θ [deg]
ψ [deg]
V_{TAS} [m/s]
α_{right} [deg]
α_{left} [deg]
β [deg]
Abx_m [m/s^2]
Aby_m [m/s^2]
Abz_m [m/s^2]
p_m [rad/s]
q_m [rad/s]
r_m [rad/s]
Time [s]
Time [s]
Time [s]

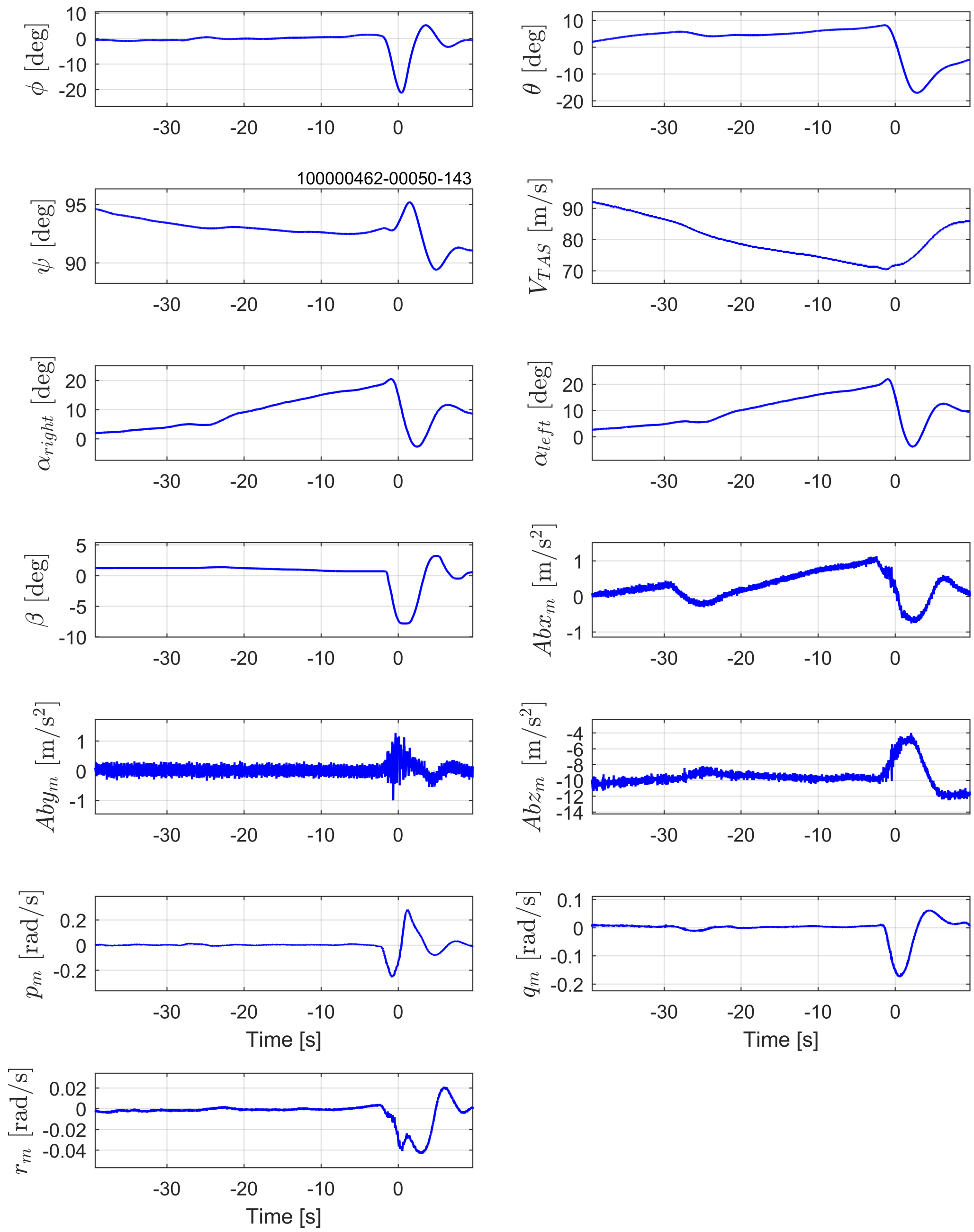

100000462-00050-143
φ [deg]
θ [deg]
ψ [deg]
V_TAS [m/s]
α_right [deg]
α_left [deg]
β [deg]
Abx_m [m/s²]
Aby_m [m/s²]
Abz_m [m/s²]
p_m [rad/s]
q_m [rad/s]
r_m [rad/s]
Time [s]

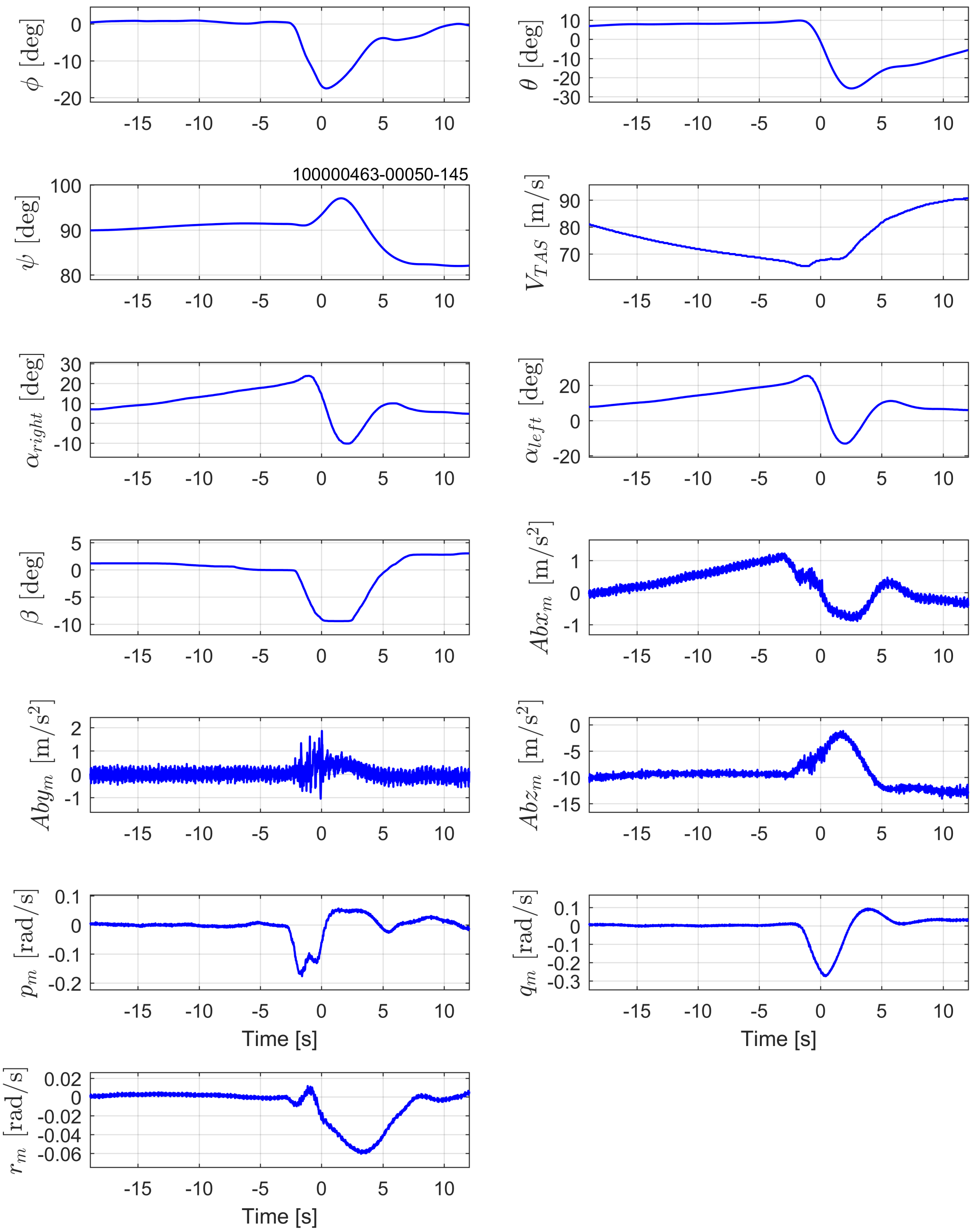

100000463-00050-145
ϕ [deg]
θ [deg]
ψ [deg]
V_{TAS} [m/s]
α_{right} [deg]
α_{left} [deg]
β [deg]
Abx_m [m/s^2]
Aby_m [m/s^2]
Abz_m [m/s^2]
p_m [rad/s]
q_m [rad/s]
r_m [rad/s]
Time [s]

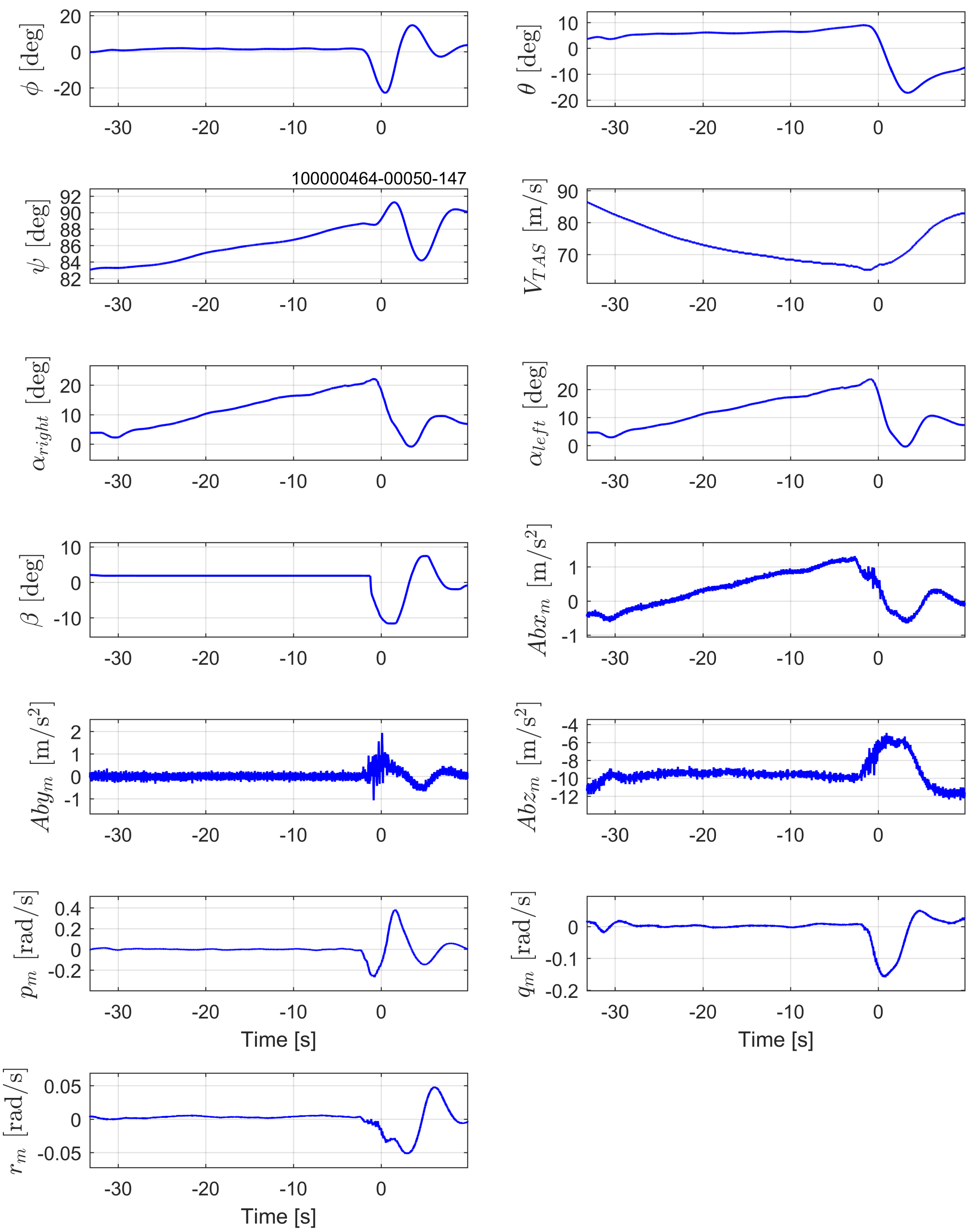
100000464-00050-147
ϕ [deg]
θ [deg]
ψ [deg]
V_{TAS} [m/s]
α_{right} [deg]
α_{left} [deg]
β [deg]
Abx_m [m/s^2]
Aby_m [m/s^2]
Abz_m [m/s^2]
p_m [rad/s]
q_m [rad/s]
r_m [rad/s]
-30 -20 -10 0
Time [s]

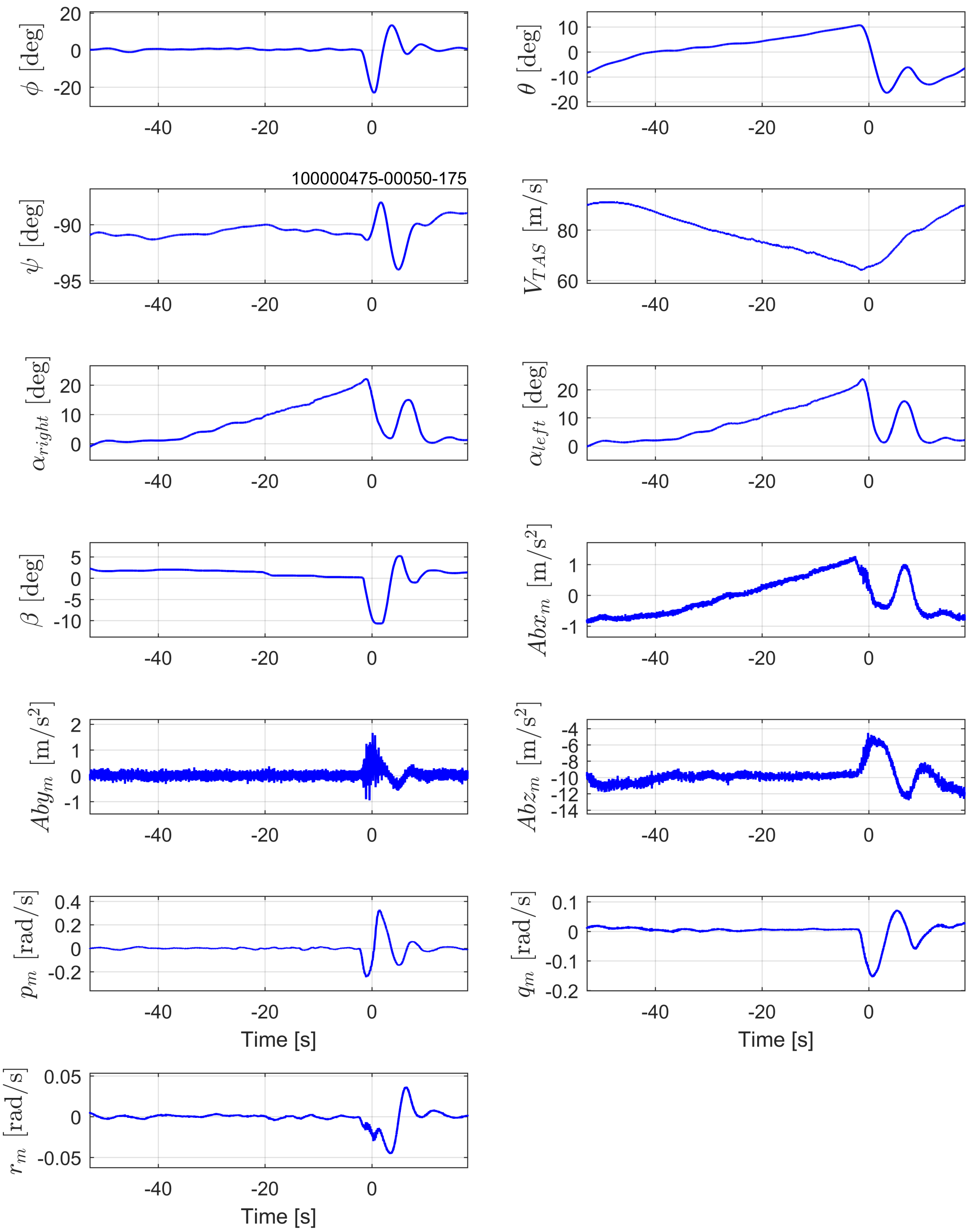
100000475-00050-175
Time [s]
Time [s]
Time [s]

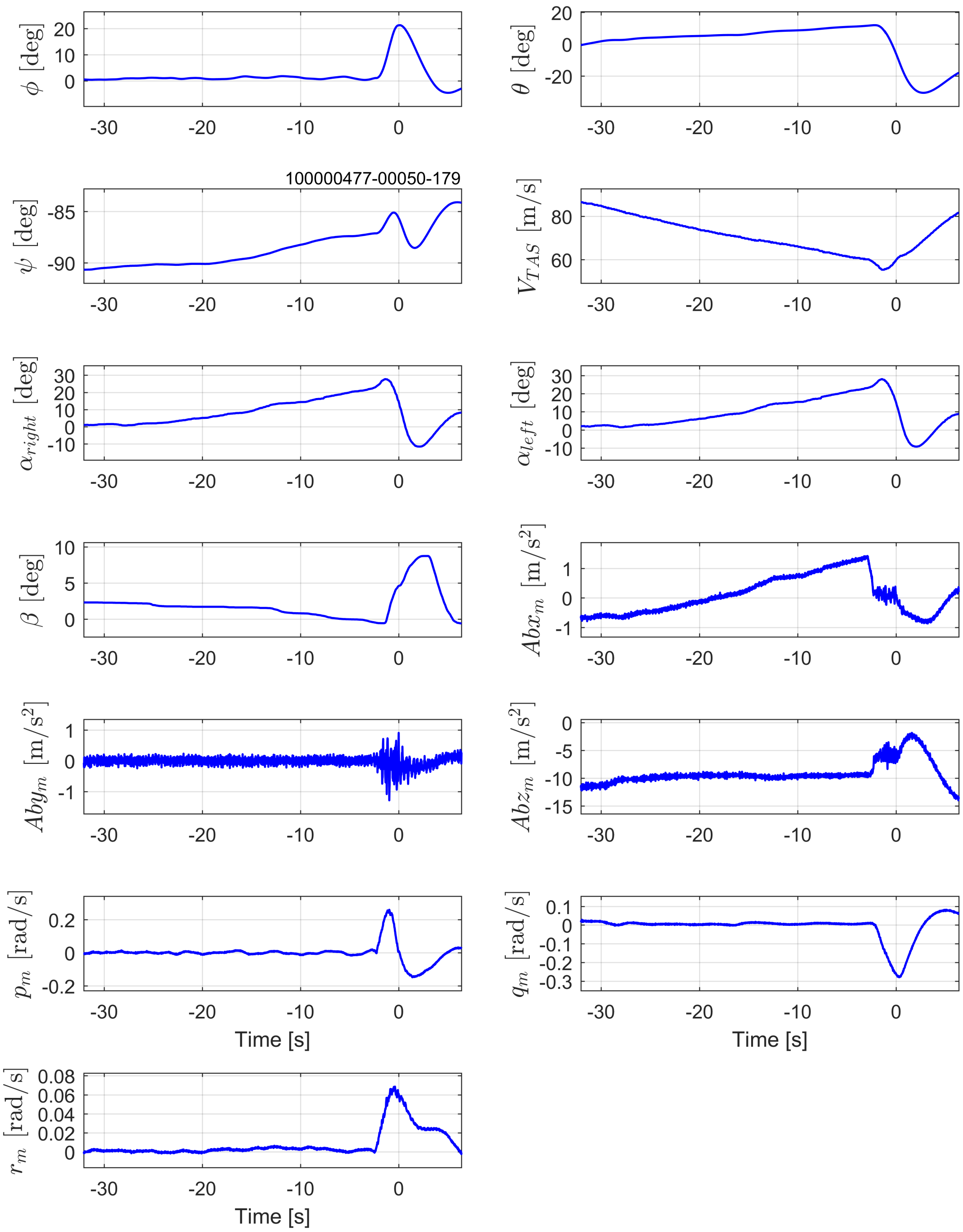

ϕ [deg]
θ [deg]
100000477-00050-179
ψ [deg]
V_{TAS} [m/s]
α_{right} [deg]
α_{left} [deg]
β [deg]
Abx_m [m/s^2]
Aby_m [m/s^2]
Abz_m [m/s^2]
p_m [rad/s]
q_m [rad/s]
r_m [rad/s]
Time [s]

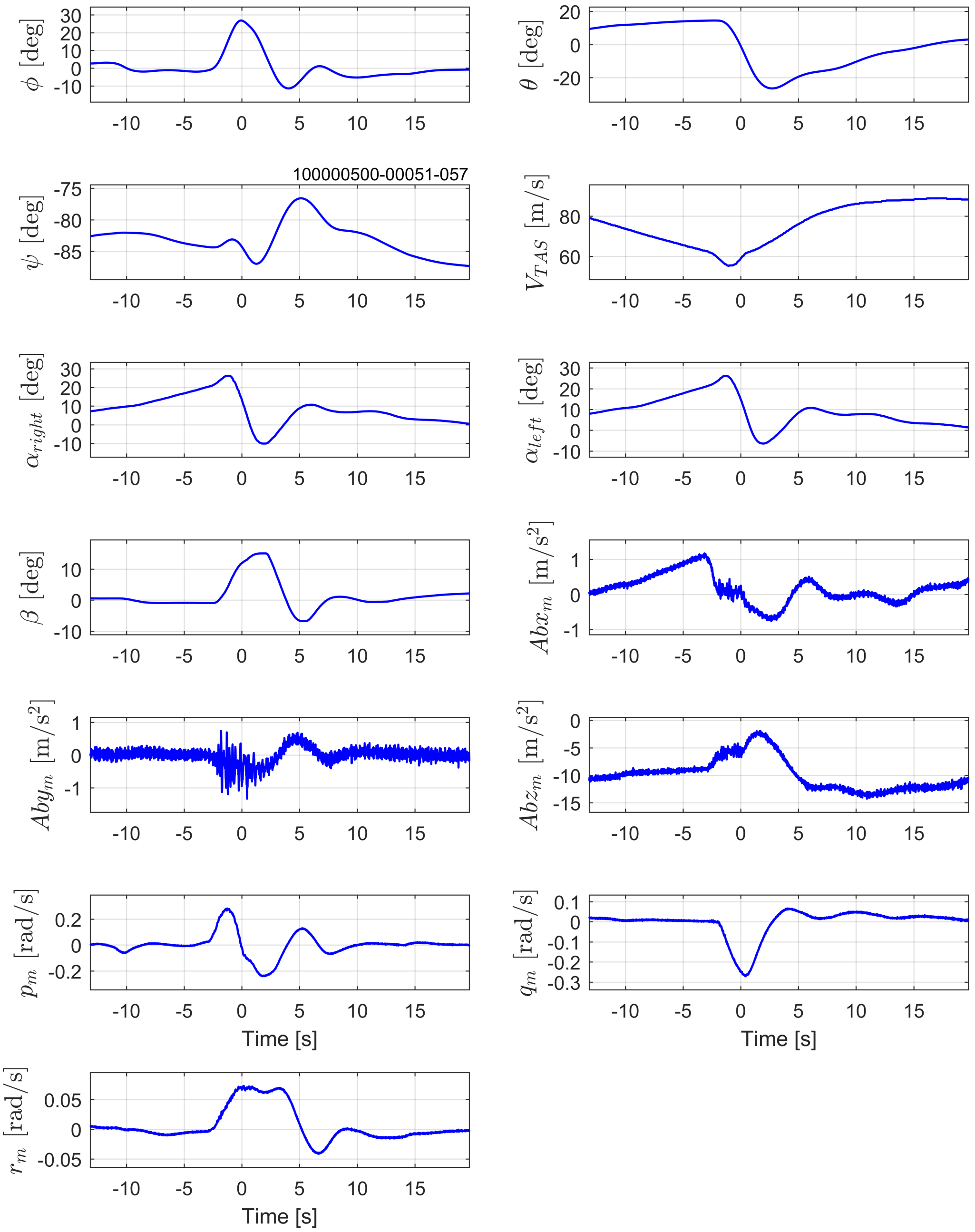
100000500-00051-057
ϕ [deg]
θ [deg]
ψ [deg]
V_{TAS} [m/s]
α_{right} [deg]
α_{left} [deg]
β [deg]
Abx_m [m/s^2]
Aby_m [m/s^2]
Abz_m [m/s^2]
p_m [rad/s]
q_m [rad/s]
r_m [rad/s]
Time [s]
Time [s]
Time [s]

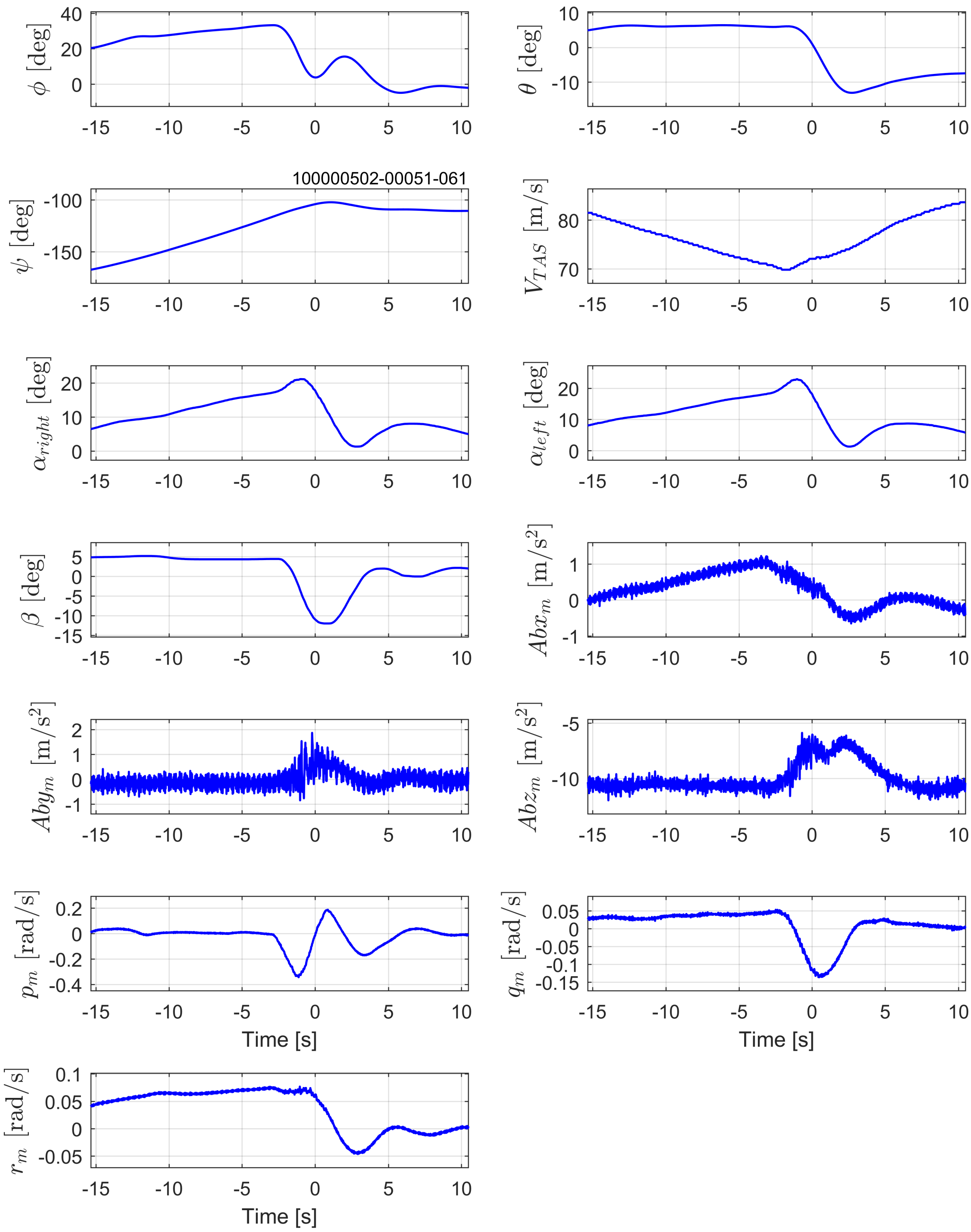
100000502-00051-061
ϕ [deg]
θ [deg]
ψ [deg]
V_TAS [m/s]
α_right [deg]
α_left [deg]
β [deg]
Abx_m [m/s^2]
Aby_m [m/s^2]
Abz_m [m/s^2]
p_m [rad/s]
q_m [rad/s]
r_m [rad/s]
-15 -10 -5 0 5 10
Time [s]

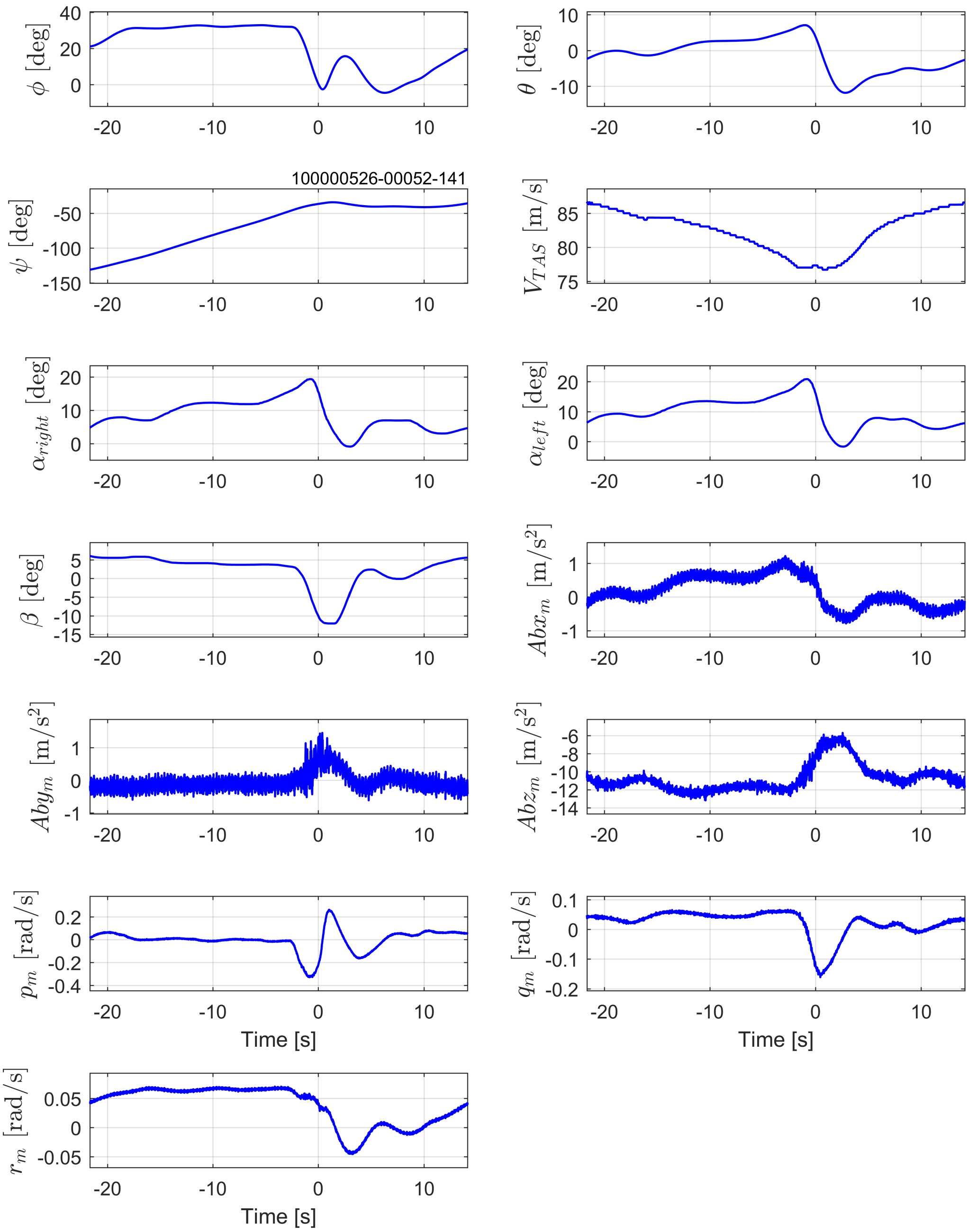

100000526-00052-141
ϕ [deg]
θ [deg]
ψ [deg]
V_{TAS} [m/s]
α_{right} [deg]
α_{left} [deg]
β [deg]
Abx_m [m/s^2]
Aby_m [m/s^2]
Abz_m [m/s^2]
p_m [rad/s]
q_m [rad/s]
r_m [rad/s]
Time [s]

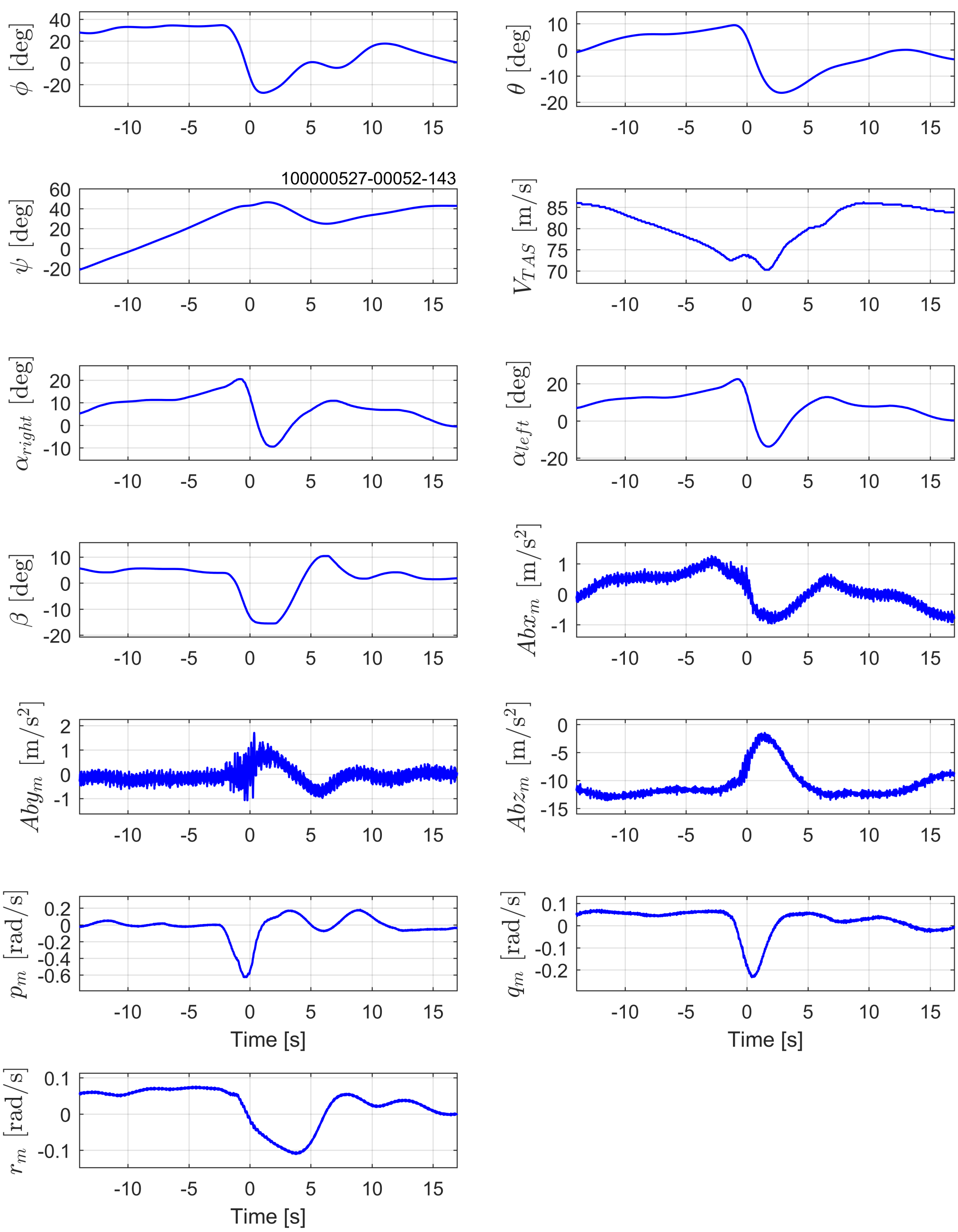
100000527-00052-143
ϕ [deg]
θ [deg]
ψ [deg]
V_{TAS} [m/s]
α_{right} [deg]
α_{left} [deg]
β [deg]
Abx_m [m/s^2]
Aby_m [m/s^2]
Abz_m [m/s^2]
p_m [rad/s]
q_m [rad/s]
r_m [rad/s]
Time [s]

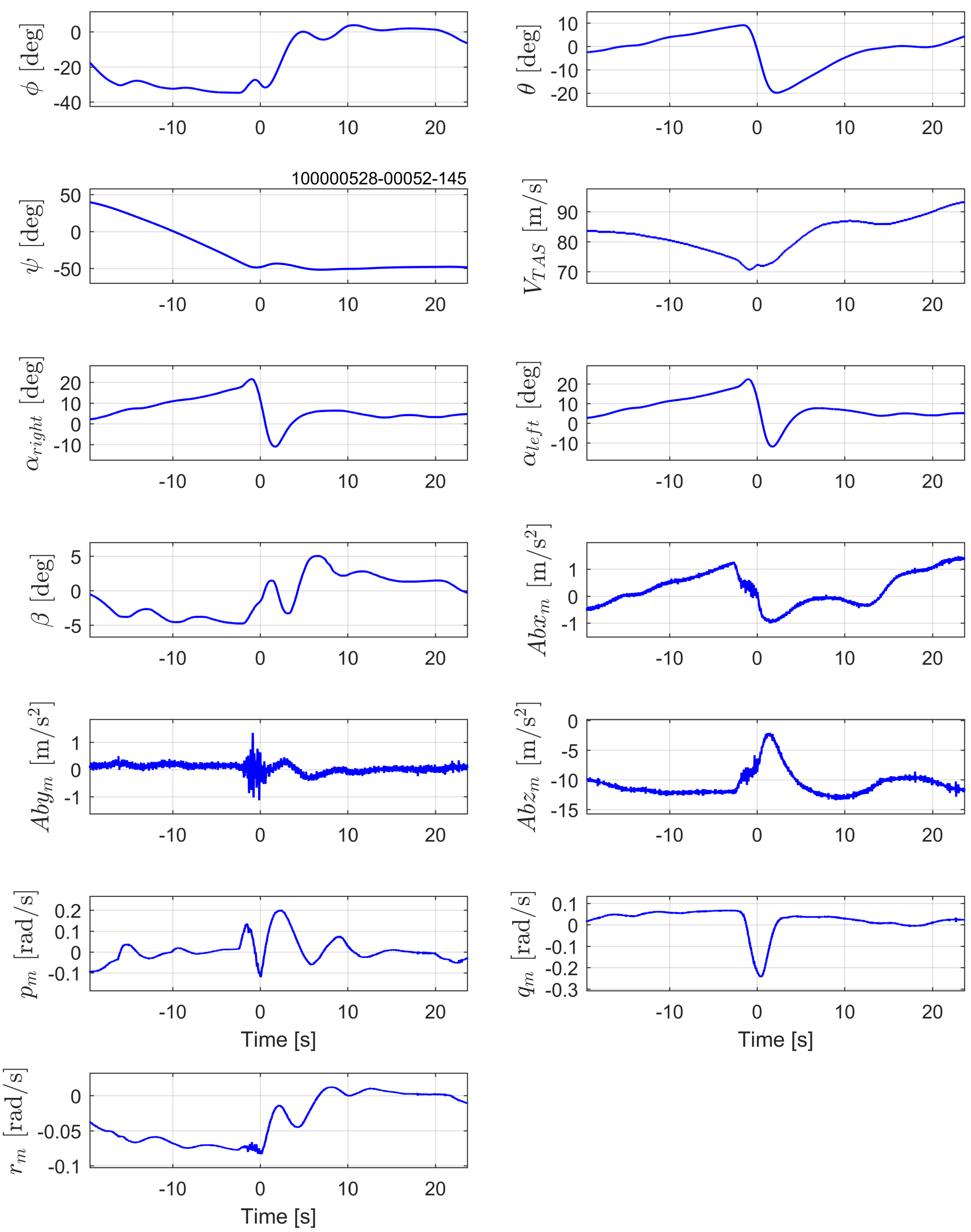

ϕ [deg]
θ [deg]
100000528-00052-145
ψ [deg]
V_{TAS} [m/s]
α_{right} [deg]
α_{left} [deg]
β [deg]
Abx_m [m/s^2]
Aby_m [m/s^2]
Abz_m [m/s^2]
p_m [rad/s]
q_m [rad/s]
r_m [rad/s]
Time [s]
Time [s]
Time [s]

B

Fokker 100 Reference Frames and Mass Model Data

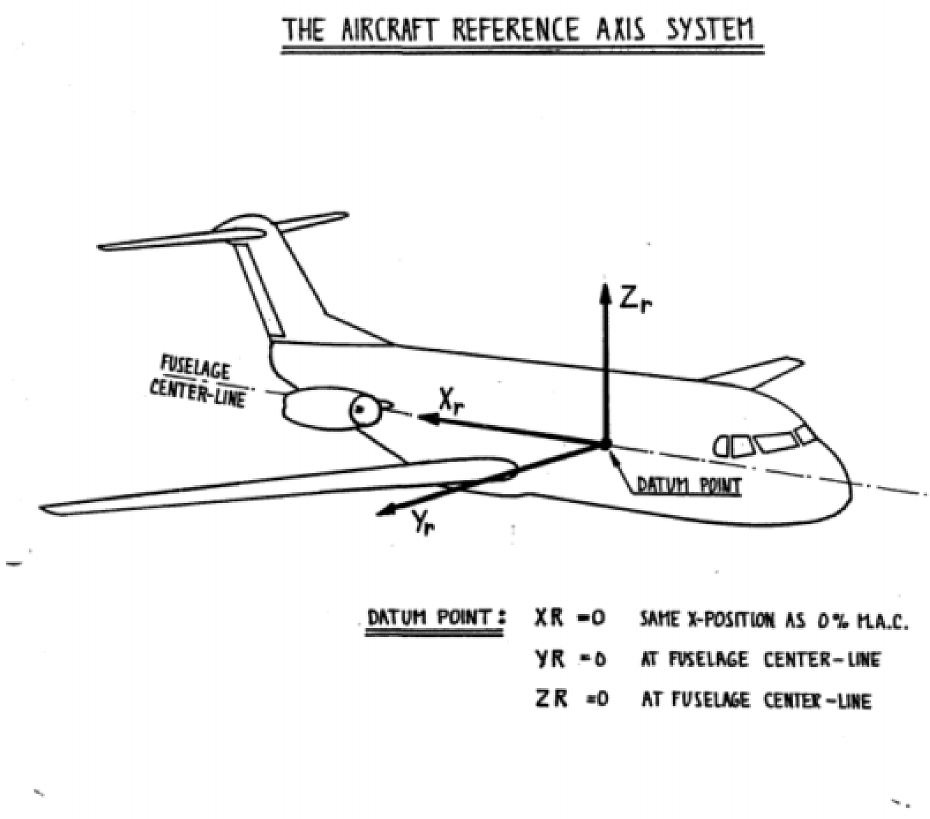

Figure B.1: Schematic overview of the Fokker 100 and the aircraft reference axis system.

Table B.1: Frames of reference regarding the Fokker 100 (Proto/Series) aircraft.

Frame	Name		Origin		X-Axis	Y-Axis	Z-Axis
		X_W [mm]	Y_W [mm]	Z_W [mm]			
F_W	Vehicle-Nose	0	0	0	AFT	RIGHT	UP
F_r	Vehicle (0% MAC)	15799	0	0	AFT	RIGHT	UP
$F_{r,40}$	Vehicle-40 (40% MAC)	17332	0	0	AFT	RIGHT	UP
F_{FUS}	Fuselage	17332	0	0	AFT	LEFT	DOWN
$F_{WNG\text{-}R}$	Wing (Right)	16334	0	-965	AFT	LEFT	DOWN
$F_{WNG\text{-}L}$	Wing (Left)	16334	0	-965	AFT	LEFT	DOWN
F_{VSB}	Vertical Stabilizer	29957	0	1575	AFT	LEFT	DOWN
$F_{HSB\text{-}R}$	Horizontal Stabilizer (Right)	32801	0	4461	AFT	LEFT	DOWN
$F_{HSB\text{-}L}$	Horizontal Stabilizer (Left)	32801	0	4461	AFT	LEFT	DOWN
$F_{ENG\text{-}R}$	Engine (Right)	23607	2681	400	AFT	LEFT	DOWN
$F_{ENG\text{-}L}$	Engine (Left)	23607	-2681	400	AFT	LEFT	DOWN
F_{NUC}	Nose Under Carriage	3770	0	-1540	AFT	LEFT	DOWN
$F_{MUC\text{-}R}$	Main Under Carriage (Right)	17649	0	-965	AFT	LEFT	DOWN
$F_{MUC\text{-}L}$	Main Under Carriage (Left)	17649	0	-965	AFT	LEFT	DOWN

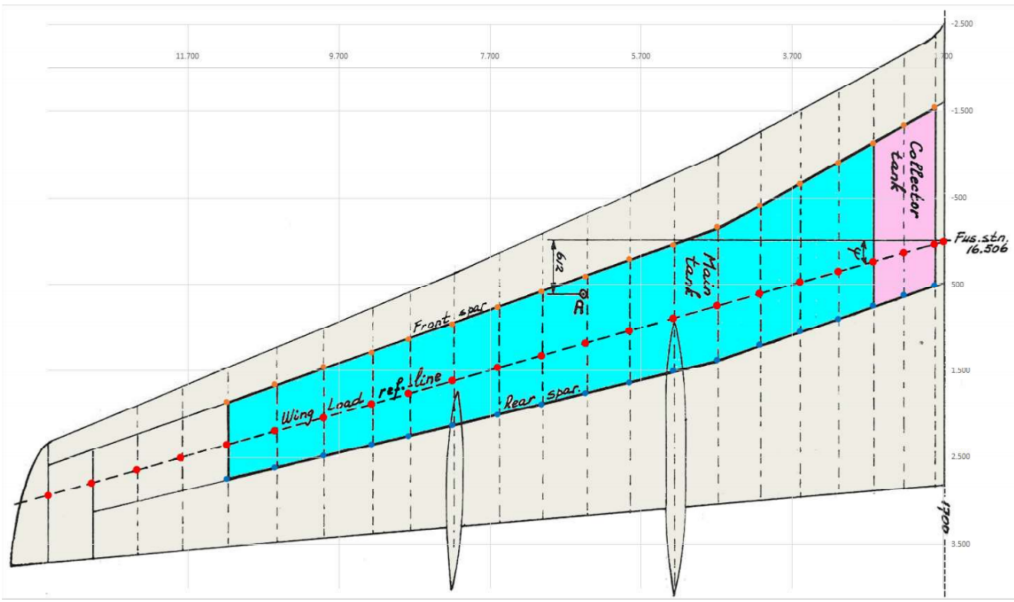

Figure B.2: Top view of the wing tank division into 2 collector tanks and 15 subtanks.

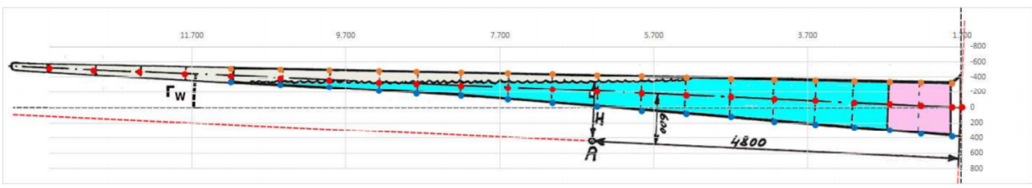

Figure B.3: Front view of the wing tank division into 2 collector tanks and 15 subtanks

C

Model Structures Drag Coefficient C_D and Pitching Moment Coefficient C_m

This appendix gives the results of the multivariate orthogonal function modelling algorithm as proposed by Morellie [70] for the two symmetric force and moment coefficients: the drag force and pitching moment. No detailed analysis and model structure determination has been further performed.

C.1. Drag Force Coefficient C_D

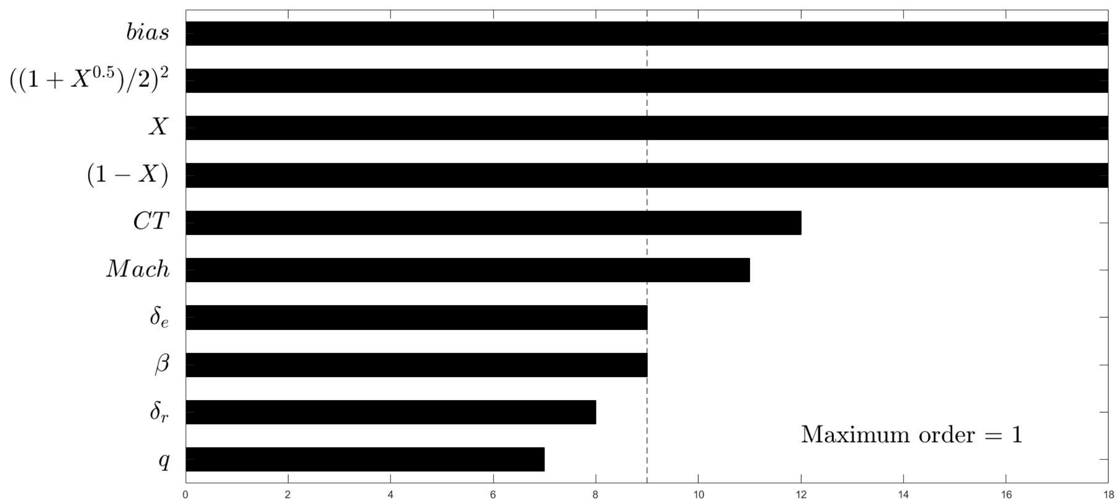

Figure C.1: Outcome of Morelli's algorithm for the drag coefficient C_D, 1st order terms and flaps = 0°

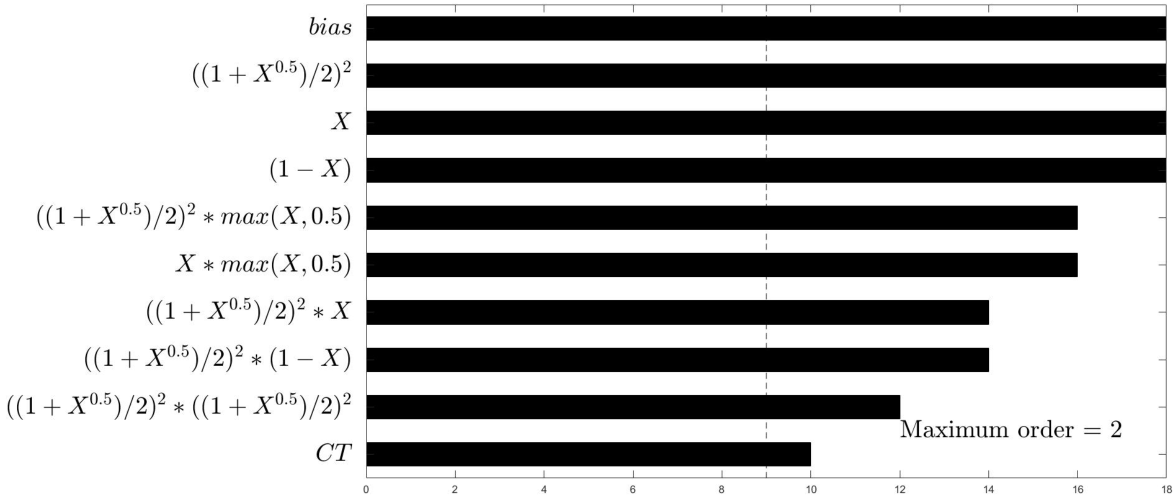

Figure C.2: Outcome of Morelli's algorithm for the drag coefficient C_D, 1st and 2nd order terms and flaps = 0°

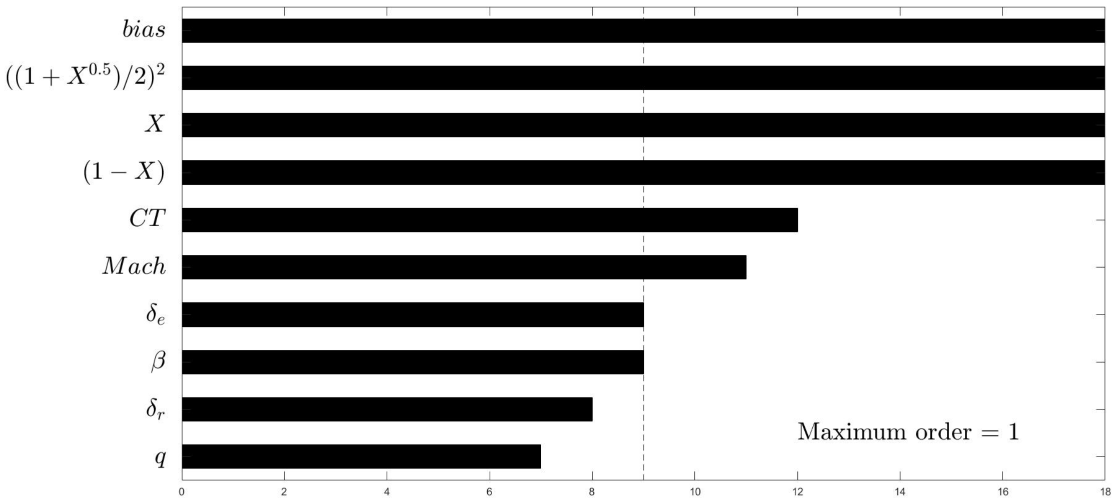

Figure C.3: Outcome of Morelli's algorithm for the drag coefficient C_D, 1st order terms and flaps = 18°

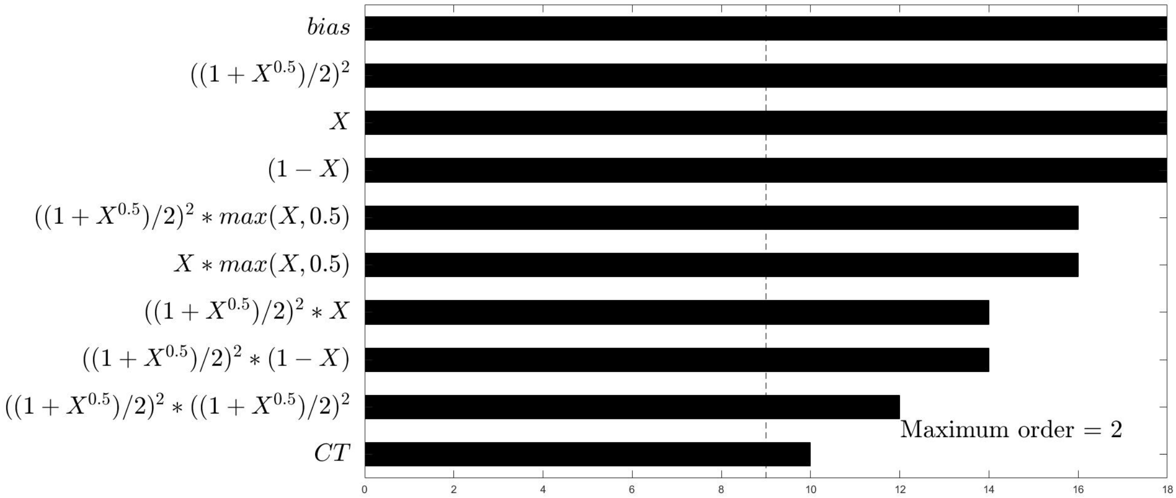

Figure C.4: Outcome of Morelli's algorithm for the drag coefficient C_D, 1st and 2nd order terms and flaps = 18°

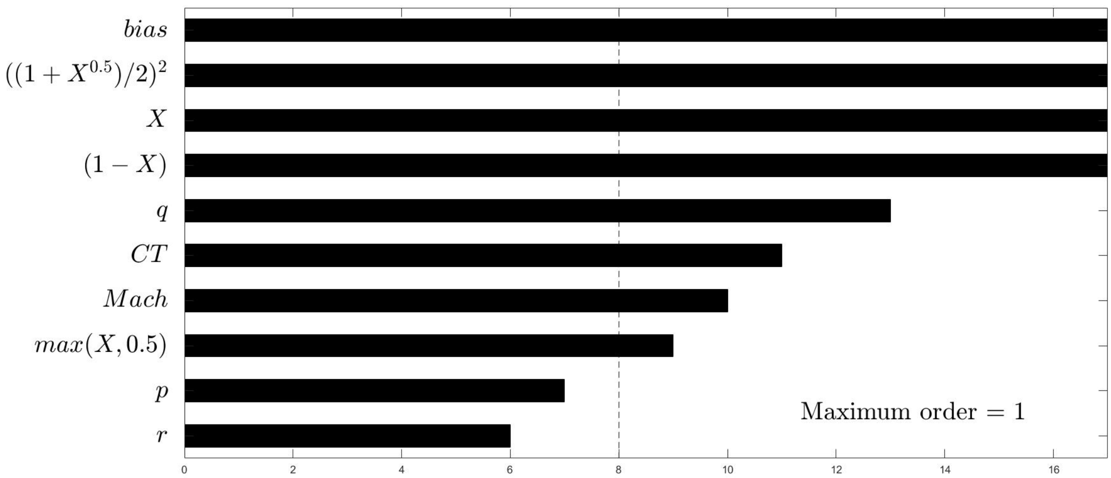

Figure C.5: Outcome of Morelli's algorithm for the drag coefficient C_D, 1st order terms and flaps = 42°

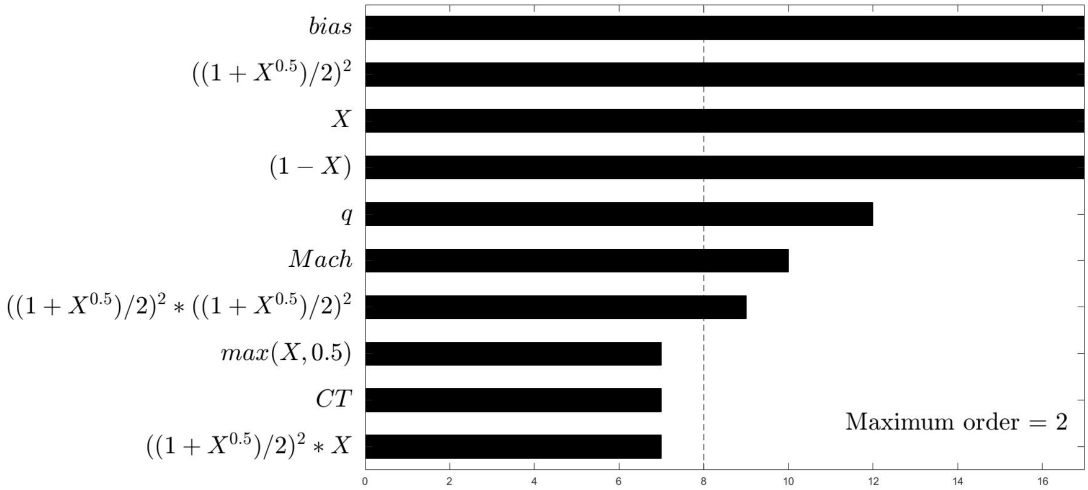

Figure C.6: Outcome of Morelli's algorithm for the drag coefficient C_D, 1st and 2nd order terms and flaps = 42°

C.2. Drag Force Coefficient C_m

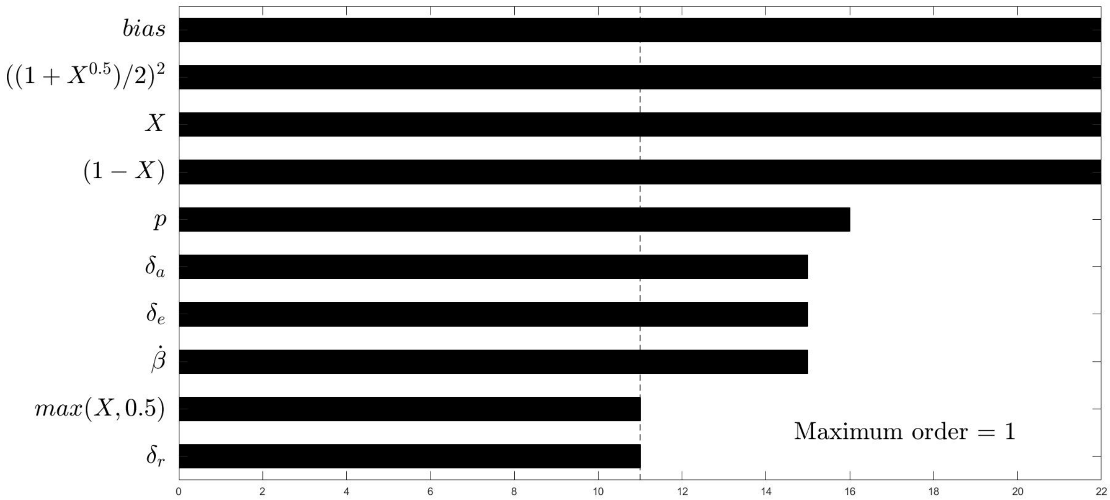

Figure C.7: Outcome of Morelli's algorithm for the drag coefficient C_m, 1st order terms and flaps = 0°

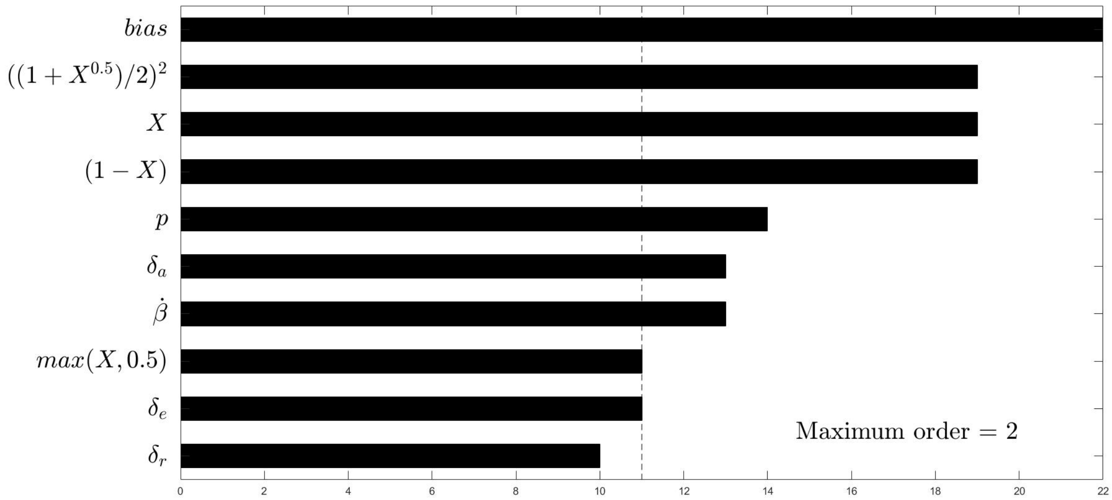

Figure C.8: Outcome of Morelli's algorithm for the drag coefficient C_m, 1st and 2nd order terms and flaps = 0°

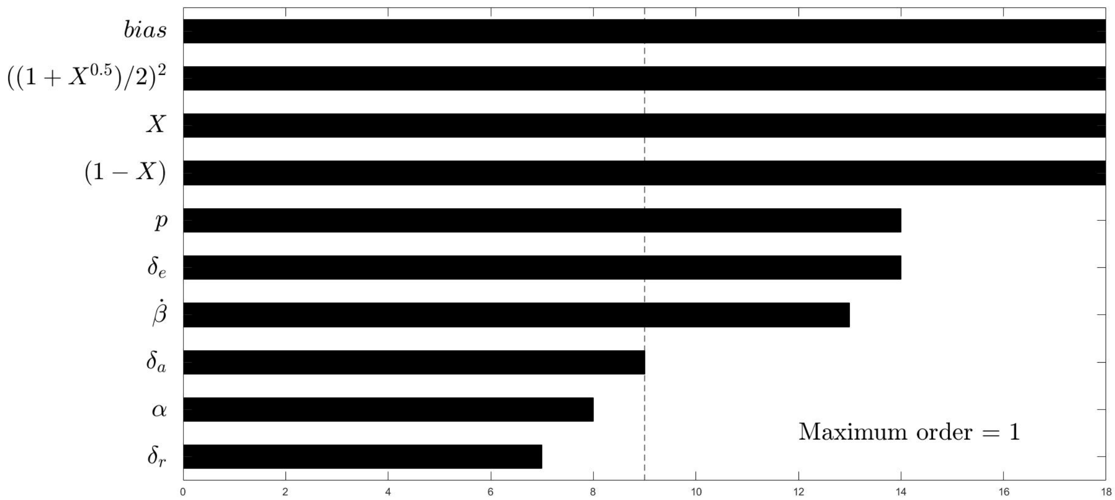

Figure C.9: Outcome of Morelli's algorithm for the drag coefficient C_m, 1st order terms and flaps = 18°

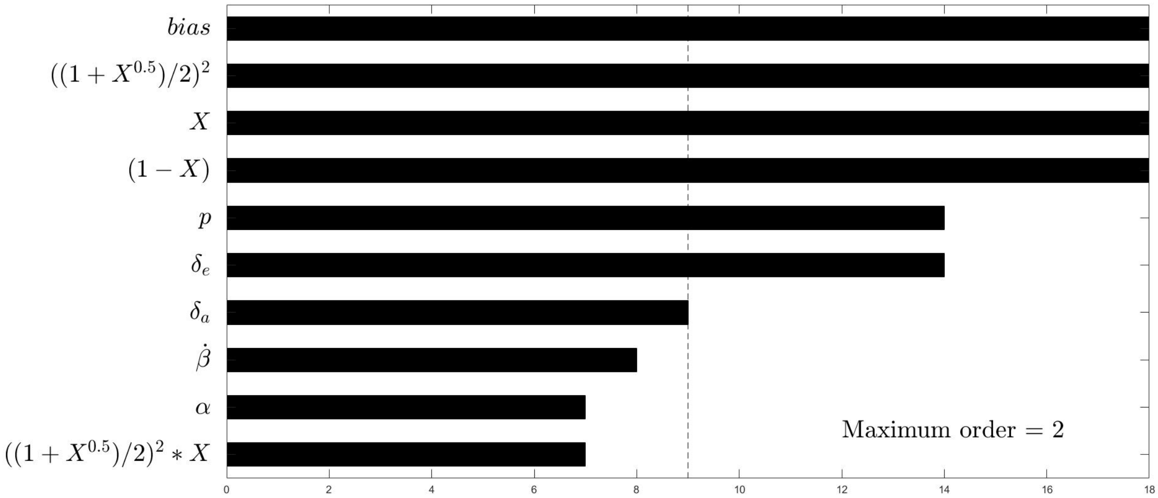

Figure C.10: Outcome of Morelli's algorithm for the drag coefficient C_m, 1st and 2nd order terms and flaps = 18°

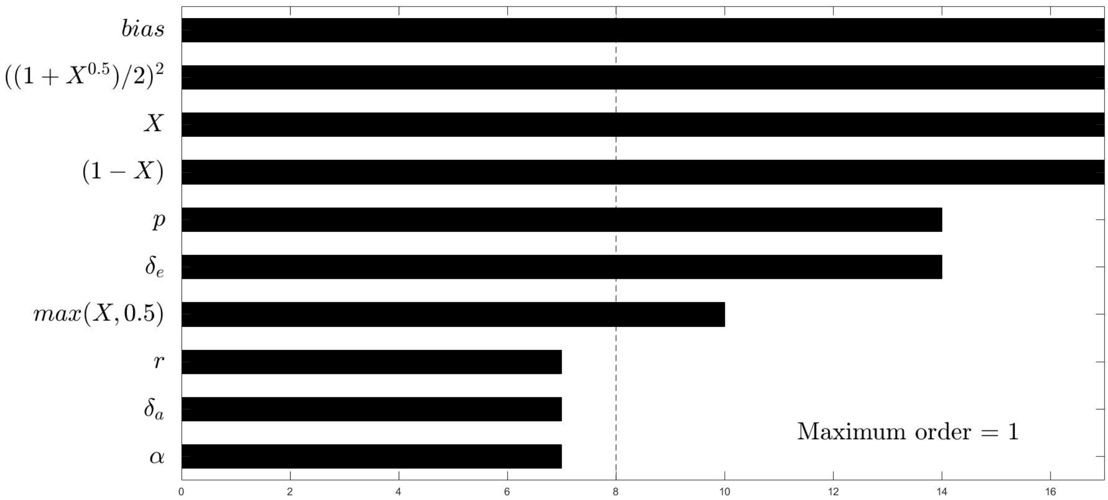

Figure C.11: Outcome of Morelli's algorithm for the drag coefficient C_m, 1st order terms and flaps = 42°

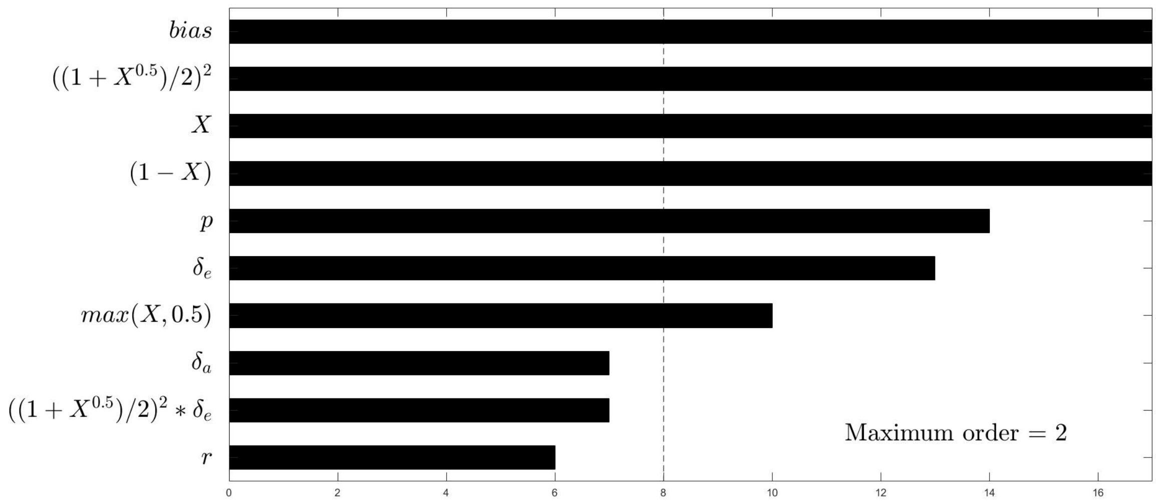

Figure C.12: Outcome of Morelli's algorithm for the drag coefficient C_m, 1st and 2nd order terms and flaps = 42°

D

Recommendations for Future Research

The Fokker 100 data set has shown its limitations. It does contain however still possibilities for more fundamental research towards the creation of stall models.

- Current research for differential Kirchhoff terms was limited to a single separation point on both the right and left wing. The use of multiple separation points per wing (panel-like method) could offer further improvements in model fit.
- Many suggestions made by authorities for pilot training is to include the startle factor. Iced wings exhibit decreased aerodynamic properties. Creating stall models of iced wings is an interesting research to work on the startle factor.
- Model and include control surface effectiveness as this decreased during stalls.
- Morelli's multivariate orthogonal function modeling algorithm showed behaviour not corresponding to Morelli's statements. More insight into the decoupling of orthogonal model terms to truly show their individual contribution could aid this model structure selection method to become more efficient. It is now still necessary to check MSE, VAF, ... by trial and error to come up with the best model fit.
- Sufficiently excite control surfaces during new flight test with the Cessna Citation II PH-LAB.
- Pilots have troubles to perform the flight manoeuvres whilst sufficiently exciting their aircraft. Designing a controller that provides dedicated excitation on top of the pilot input is an interesting subject to investigate.
- Construct a Fokker 100 buffet model to more accurately filter out buffet in measurement signals.
- With data set that have a sufficient information content, it is worth investigating if a relationship can be described between Kirchhoff's ODE and/or parameters that expresses its values as function of flap setting.
- The idea above can also be extended to aileron deflection as this changes the airfoil profile and thus its aerodynamic characteristics determining the Kirchhoff parameters.
- So far, we've used the Gramian matrix to investigate the information content in an existing data set. Turning the logic around: Can we design a proper stall flight identification manoeuvre that has a high information content based on predictions of the Gramian matrix?
- The Fokker 100 data exhibits 'wavy' behaviour in its flight data for the six aerodynamic coefficients. This is not perfectly followed by the current model structures and is not clearly observed in the measured parameters. An investigation towards identifying the cause of this behavior can provide additional and important insights.

- Investigate whether non-stationary model terms can capture the behaviour described above.

Bibliography

[1] ICATEE | International Committee for Aviation Training in Extended Envelopes. URL http://icatee.org/.

[2] The LOC-I Problem – UPRT.aero. URL https://uprt.aero/the-loc-i-problem/.

[3] Dynamic Stall, Unsteady Aerodynamics. URL https://web.archive.org/web/20071229110350/http://aerodyn.org/Dstall/dstall.html.

[4] N. Abramov, M. Goman, A. Khrabrov, E. Kolesnikov, M. Sidoruk, B. Soemarwoto, and H. Smaili. Aerodynamic Model of Transport Airplane in Extended Envelope for Simulation of Upset Recovery. In *28th Congress of the International Council of the Aeronautical Sciences 2012, ICAS 2012*, volume 2, pages 872–881, 2012.

[5] Sunjoo Advani and Joris Field. Upset Prevention and Recovery Training in Flight Simulators. In *AIAA Modeling and Simulation Technologies Conference 08-11 August 2011, Portland, Oregon*, Portland, 2011. doi: 10.2514/6.2011-6698. URL http://arc.aiaa.org.

[6] Sunjoo Advani and Joris Field. Global Implementation of Upset Prevention & Recovery Training. *AIAA SciTech Forum 4-8 January 2016, San Diego, California, USA*, (January):1–7, 2016. doi: 10.2514/6.2016-1430.

[7] Sunjoo K Advani, Jeffery A Schroeder, and Bryan Burks. What Really Can Be Done in Simulation to Improve Upset Training? In *AIAA Modeling and Simulation Technologies Conference 2 - 5 August 2010, Toronto, Ontario Canada*, Toronto, 2010. doi: 10.2514/6.2010-7791. URL http://arc.aiaa.org.

[8] Airbus. A Statistical Analysis of Commercial Aviation Accidents 1958-2018. Technical report, 2019.

[9] N. Alègre and D. Hammond. Experimental setup for the study of runback ice at full scale. *Journal of Aircraft*, 48(6):1978–1983, nov 2011. ISSN 00218669. doi: 10.2514/1.C031398.

[10] Gavin K. Ananda and Michael S. Selig. Stall/Post-Stall Modeling of the Longitudinal Characteristics of a General Aviation Aircraft. In *AIAA Atmospheric Flight Mechanics Conference*, volume 2016-Janua. American Institute of Aeronautics and Astronautics Inc., 2016. doi: 10.2514/6.2016-3541.

[11] Boeing. Statistical Summary of Commercial Jet Airplane Accidents Worldwide Operations | 1959 – 2017. Technical report, Boeing Commercial Airplanes, 2018. URL www.boeing.com/news/techissues/pdf/statsum.pdf.

[12] Paul J. Bolds-Moorehead, Van G. Chaney, Terry Lutz, and Stephane Vaux. Stalling Transport Aircraft. *44th Annual International Symposium of the Society of Flight Test Engineers 2013*, (3984):84–109, 2013.

[13] Albion H Bowers, Joseph W Pahle, R Joseph Wilson, Bradley C Flick, and Richard L Rood. An Overview of the NASA F-18 High Alpha Research Vehicle. Technical report, 1996. URL https://ntrs.nasa.gov/search.jsp?R=19970003009.

[14] A. J. Buchner and J. Soria. Measurements of the Flow Due to a Rapidly Pitching Plate Using Time Resolved High Resolution PIV. *Aerospace Science and Technology*, 44:4–17, 2015. ISSN 12709638. doi: 10.1016/j.ast.2014.04.007.

[15] Dave Carbaugh. Approach to Stall Simulator Training. In *AIAA Modeling and Simulation Technologies Conference 2010*, number August, 2010. ISBN 9781624101526.

[16] David Carbaugh. Simulator Upset Recovery Training and Issues. In *AIAA Modeling and Simulation Technologies Conference*. American Institute of Aeronautics and Astronautics (AIAA), aug 2008. doi: 10.2514/6.2008-6866.

[17] Stephen M. Casner, Richard W. Geven, and Kent T. Williams. The Effectiveness of Airline Pilot Training for Abnormal Events. *Human Factors*, 55(3):477–485, jun 2013. ISSN 00187208. doi: 10.1177/0018720812466893.

[18] Joseph R Chambers. Overview of stall/spin technology. In *AIAA Atmospheric Flight Mechanics Conference*. American Institute of Aeronautics and Astronautics (AIAA), aug 1980. doi: 10.2514/6.1980-1580.

[19] Joseph R Chambers. High-angle-of-attack aerodynamics - Lessons learned. In *AIAA 4th Applied Aerodynamics Conference June 9-11, 1986 San Diego CA*. American Institute of Aeronautics and Astronautics (AIAA), jun 1986. doi: 10.2514/6.1986-1774.

[20] Joseph R Chambers and Ernie L Anglin. Analysis of Lateral-Directional Stability Characteristics of a Twin-Jet Fighter Airplane at High Angle of Attack. Technical report, 1969.

[21] Joseph R Chambers and Sue B Grafton. Aerodynamic Characteristics of Airplanes at High Angles of Attack. Technical report, 1977. URL `https://ntrs.nasa.gov/search.jsp?R=19780005068`.

[22] Paul L Coe, A Bruce Gruhum, and Joseph R Chambers. Summary of Information on Low-Speed Lateral-Directional Derivatives due to Rate of Change of Sideslip. Technical report, 1975. URL `https://ntrs.nasa.gov/search.jsp?R=19750022117`.

[23] Dennis A Crider. The Need for Upset Recovery Training. In *AIAA Modeling and Simulation Technologies Conference and Exhibit 18 - 21 August 2008, Honolulu, Hawaii*, Honolulu, 2008. doi: 10.2514/6.2008-6864. URL `http://arc.aiaa.org`.

[24] Ethan C.E. Culler and John A.N. Farnsworth. Pitch Rate Induced Separation Delay Modeling of Dynamic Stall and Stall Flutter. In *AIAA Scitech 2019 Forum*. American Institute of Aeronautics and Astronautics Inc, AIAA, 2019. ISBN 9781624105784. doi: 10.2514/6.2019-1394.

[25] Torbjørn Cunis, Laurent Burlion, and Jean Philippe Condomines. Piece-Wise Identification and Analysis of the Aerodynamic Coefficients, Trim Conditions, and Safe Sets of the Generic Transport Model. In *AIAA SciTech Forum 8 - 12 January 2018, Kissimee, Florida*. American Institute of Aeronautics and Astronautics Inc, AIAA, jan 2018. ISBN 9781624105265. doi: 10.2514/6.2018-1114.

[26] C. Deiler and T. Kilian. Dynamic Aircraft Simulation Model Covering Local Icing Effects. *CEAS Aeronautical Journal*, 9(3):429–444, sep 2018. ISSN 18695590. doi: 10.1007/s13272-018-0291-6.

[27] C Deiler, P Ohme, C Raab, and C Mendonca. Facing the Challenges of Supercooled Large Droplet Icing: Results of a Flight Test Based Joint DLR-Embraer Research Project. *SAE Technical Paper*, 2019. doi: 10.4271/2019-01-1988.

[28] Christoph Deiler. Time-Domain Output Error System Identification of Iced Aircraft Aerodynamics. *CEAS Aeronautical Journal*, 8(2):231–244, jun 2017. ISSN 18695590. doi: 10.1007/s13272-016-0231-2.

[29] Christoph Deiler. Flight Characteristics of Iced Aircraft. In *AIAA Scitech 2019 Forum*. American Institute of Aeronautics and Astronautics Inc, AIAA, 2019. ISBN 9781624105784. doi: 10.2514/6.2019-0560.

[30] Joaquim N. Dias. Flight Path Reconstruction t Techniques Applied to Spin Tests. In *AIAA AVIATION 2014 -AIAA Atmospheric Flight Mechanics Conference*, Atlanta, 2014. American Institute of Aeronautics and Astronautics Inc. ISBN 9781624102943. doi: 10.2514/6.2014-2559.

[31] Joaquim N. Dias. High Angle of Attack Model Identification with Compressibility Effects. In *AIAA Atmospheric Flight Mechanics Conference, 2015*. American Institute of Aeronautics and Astronautics Inc., 2015. ISBN 9781624101328. doi: 10.2514/6.2015-1477.

[32] Joaquim N. Dias. Unsteady and Post-Stall Model Identification Using Dynamic Stall Maneuvers. In *Proceedings of the AIAA Atmospheric Flight Mechanics Conference, Dallas (TX)*, Dallas, 2015. American Institute of Aeronautics and Astronautics (AIAA). doi: 10.2514/6.2015-2705.

[33] Joaquim Neto Dias. Post-Stall Model Identification from Flight Test Data. In *43rd Annual International Symposium of the Society of Flight Test Engineers 2012*, pages 130–154, 2012. ISBN 9781622766024.

[34] Joaquim Neto Dias. Identification of High Angle of Attack Aerodynamic Model Using Flight Data from Spin Tests. In *44th Annual International Symposium of the Society of Flight Test Engineers 2013*, pages 382–407. Society of Flight Test Engineers, 2013. ISBN 9781629939520.

[35] Edward G Dickes, Johnn Ralstont, and Kenneth P Lawson. Application of Large-Angle Data for Flight Simulation. In *AIAA Modeling and Simulation Technologies Conference and Exhibit, 14-17 August 2000, Denver, CO*, 2000. doi: 10.2514/6.2000-4584. URL `http://arc.aiaa.org`.

[36] EASA. Loss of Control (LOC-I) in Approach and Landing | EASA. URL `https://www.easa.europa.eu/easa-and-you/general-aviation/flying-safely/loss-of-control-in-approach-and-landing`.

[37] EASA. European Aviation Safety Agency Terms of Reference for a rulemaking task Loss of Control Prevention and Recovery Training Technical consultation during NPA drafting TBD Publication date of the NPA 2015/Q2 Driver/origin: Safety and Regulatory Harmonisation. Technical report, 2015.

[38] EASA. Opinion No 06/2017. Technical report, 2017. URL `http://www.easa.europa.eu/the-agency/management-`.

[39] EASA. Easy Access Rules for Aircrew (Regulation (EU) No 1178/2011). Technical report, 2019. URL `http://eur-lex.europa.eu/,`.

[40] L E Ericsson and J P Reding. Fluid Mechanics of Dynamic Stall Part I. Unsteady Flow Concepts. Technical report, 1988.

[41] FAA. Advisory Circular Subject: Stall Prevention and Recovery Training. Technical report, 2017.

[42] FAA. Advisory Circular Subject: Upset Prevention and Recovery Training. Technical report, 2017.

[43] D. Fischenberg and R. V. Jategaonkar. Identification of Aircraft Stall Behavior from Flight Test Data. In *Proceedings of the RTO SCI Symposium on System Identification for Integrated Aircraft Development and Flight Testing, Madrid, Spain*, pages 17–1—-17–8, Madrid, 1998.

[44] Neal T. Frink, Patrick C. Murphy, Harold L. Atkins, Sally A. Viken, Justin L. Petrilli, Ashok Gopalarathnam, and Ryan C. Paul. Status of Computational Aerodynamic Modeling Tools for Aircraft Loss-of-Control. In *AIAA SciTech Forum 4-8 January 2016, San Diego, California, USA*. American Institute of Aeronautics and Astronautics Inc, AIAA, 2016. ISBN 9781624103902. doi: 10.2514/6.2016-1041.

[45] David R. Gingras, John N. Ralston, Ryan Oltman, Chris Wilkeningi, Robert Watts, and Paul Desrochers. Flight Simulator Augmentation for Stall and Upset Training. In *AIAA Modeling and Simulation Technologies Conference 2014*, number January, pages 1–14, 2014. ISBN 9781624102974. doi: 10.2514/6.2014-1003.

[46] M. Goman and A. Khrabrov. State-Space Representation of a Aerodynamic Characteristics of an Aircraft at High Angles of Attack. In *Astrodynamics Conference, 1992*, pages 759–766, Reston, Virigina, aug 1992. American Institute of Aeronautics and Astronautics. doi: 10.2514/3.46618. URL `http://arc.aiaa.org/doi/10.2514/6.1992-4651`.

[47] Peter R. Grant, Stacey Liu, Zhanhong Zane Luo, and Gregory Moszczynski. Development of Post-Stall Flight Models from Certification Flight Test and Wind-Tunnel Data. In *AIAA Modeling and Simulation Technologies Conference, 2017*. American Institute of Aeronautics and Astronautics Inc, AIAA, 2017. ISBN 9781624104510. doi: 10.2514/6.2017-1549.

[48] Jared Grauer. Position Corrections for Airspeed and Flow Angle Measurements on Fixed-Wing Aircraft. Technical Report November, 2017.

[49] Eric Groen, Joris Field, Lars Fucke, Suzanne Nooij, Mikhail Goman, Michael Mayrhofer, Larisa Zaichik, Maxim Grigoryev, and Vladimir Biryukov. SUPRA – Enhanced Upset Recovery Simulation. In *AIAA Modeling and Simulation Technologies Conference 13-16 August, 2012, Minneapolis, Minnesota*, number August, pages 1–14, 2012. doi: 10.2514/6.2012-4630.

[50] Donald E Hewes. Low-Subsonic Measurements of the Static and Oscillatory Lateral Stability Derivatives of a Sweptback-Wing Airplane Configuration at Angles of Attack from -10° to 90°. Technical report, 1959.

[51] M Hwang and J H Seinfeld. Observability of Nonlinear Systems 1. Technical Report 2, 1972.

[52] ICAO. Manual on Aeroplane Upset Prevention and Recovery Training. Technical report, 2014.

[53] ICAO. Safety Report. Technical report, 2017. URL `www.icao.int`.

[54] ICAO. Safety Report 2018 Edition. Technical report, 2018. URL `https://www.icao.int/safety/Pages/GASP.aspx`.

[55] ICAO. State of Global Aviation Safety ICAO Safety Report 2019 Edition. Technical report, 2019.

[56] Steven R. Jacobson. Aircraft Loss of Control Causal Factors and Mitigation Challenges. In *AIAA Guidance, Navigation, and Control Conference*, 2010. ISBN 9781600869624. doi: 10.2514/6.2010-8007.

[57] Blessing Kavai. Loss of Control Inflight Accident Data. In *AFI LOC-I and UPRT Seminar*, Johannesburg, 2017. IATA.

[58] Jacob Kay, John N Ralston, and Stanley F Lash. Development of Non-Linear, Low-Speed Aerodynamic Model for the F-16/Vista. *American Institute of Aeronautics and Astronautics*, 1997. doi: 10.2514/6.1997-3576. URL `http://arc.aiaa.org`.

[59] Vladislav Klein, Thomas P. Ratvasky, and Brent R. Cobleigh. Aerodynamic Parameters of High Angle-Of_Attack Research Vehicle (HARV) Estimated From Flight Data. Technical report, 1990. URL `https://ntrs.nasa.gov/search.jsp?R=19900019262`.

[60] Martin Laban. *Laban - 1994 - On-Line Aircraft Aerodynamic Model Identification*. PhD thesis, 1994.

[61] A A Lambregts, G Nesemeier, J E Wilborn, and R L Newman. Airplane Upsets: Old Problem, New Issues. In *AIAA Modeling and Simulation Technologies Conference and Exhibit 18 - 21 August 2008, Honolulu, Hawaii*, Honolulu, 2008. doi: 10.2514/6.2008-6867. URL `http://arc.aiaa.org`.

[62] Jordan M. Leung, Gregory Moszczynski, and Peter R. Grant. A state estimation approach for high angle-of-attack parameter estimation from certification flight data. In *AIAA Scitech 2019 Forum*. American Institute of Aeronautics and Astronautics Inc, AIAA, 2019. ISBN 9781624105784. doi: 10.2514/6.2019-0013.

[63] Thomas Longridge, Judith Bürki-Cohen, Tiauw H Go, and Andrew J Kendra. Simulator Fidelity Considerations for Training and Evaluation of Today's Airline Pilots. In *Proceedings of the 11th International Symposium on Aviation Psychology, Columbus, OH, 5-8 March 2001*, pages 5–8, 2001.

[64] Dirk M Luchtenburg, Clarence W Rowley, Mark W Lohry, Luigi Martinelli, and Robert F Stengel. Unsteady High-Angle-of-Attack Aerodynamic Models of a Generic Jet Transport. *Journal of Aircraft*, 52(3), 2015. doi: 10.2514/1.C032976. URL `http://arc.aiaa.org`.

[65] Peter C. Luteijn. *Influence of a Swept-Wing Configuration On Global Nonlinear Model Identification of Aerodynamic Stall*. PhD thesis, TU Delft, 2020.

[66] Jack Kevin Ly. *Angle of Attack Determination Using Inertial Navigation System*. PhD thesis, 2017.

[67] S.C.E. Marschalk. *Stall Buffet Modeling using Swept Wing Flight Test Data*. PhD thesis, TU Delft, 2019.

[68] Phillip D Mckeehen, Thomas J Cord, and Ba T Nguyen. Modified VISTA/F-16 Piloted Simulation Study. In *AIAA Flight Simulation Technologies Conference, San Diego, CA, July 29-31, 1996*, 1996. doi: 10.2514/6.1996-3508. URL `http://arc.aiaa.org`.

[69] Sanggyu Min, Evan Harrison, Hernando Jimenez, and Dimitri Mavris. Development of Aerodynamic Modeling and Calibration Methods for General Aviation Aircraft Performance Analysis - A Survey and Comparison of Models. In *15th AIAA Aviation Technology, Integration, and Operations Conference AIAA Aviation Forum 22-26 June, 2015 Dallas, TX*. American Institute of Aeronautics and Astronautics Inc, AIAA, 2015. ISBN 9781624103698. doi: 10.2514/6.2015-2853.

[70] Eugene A Morelli, Kevin Cunningham, and Melissa A Hill. Global Aerodynamic Modeling for Stall/Upset Recovery Training Using Efficient Piloted Flight Test Techniques. In *AIAA Atmospheric Flight Mechanics Conference; August 19, 2013 - August 22, 2013; Boston, MA; United States*, 2013. URL `https://ntrs.nasa.gov/search.jsp?R=20140002791`.

[71] Gregory J. Moszczynski, Matthew Giamou, Jordan M. Leung, Jonathan Kelly, and Peter R. Grant. An Observability-Based Approach to Flight Path Reconstruction of Uninformative Coupled Aircraft Trajectories: A Case Study Considering Stall Maneuvers for Aircraft Certification. In *AIAA Scitech 2019 Forum*. American Institute of Aeronautics and Astronautics Inc, AIAA, 2019. ISBN 9781624105784. doi: 10.2514/6.2019-0012.

[72] Gregory J. Moszczynski, Jordan M. Leung, and Peter R. Grant. Robust Aerodynamic Model Identification: A New Method for Aircraft System Identification in the Presence of General Dynamic Model Deficiencies. In *AIAA Scitech 2019 Forum*. American Institute of Aeronautics and Astronautics Inc, AIAA, 2019. ISBN 9781624105784. doi: 10.2514/6.2019-0433.

[73] J. A. Mulder, Q. P. Chu, J. K. Sridhar, J. H. Breeman, and M. Laban. Non-Linear Aircraft Flight Path Reconstruction Review and New Advances. *Progress in Aerospace Sciences*, 35(7):673–726, 1999. ISSN 03760421. doi: 10.1016/S0376-0421(99)00005-6.

[74] Austin M Murch, John V Foster, Flight Dynamics Branch, and Flight Dynamics Branch. Recent NASA Research on Aerodynamic Modeling of Post- Stall and Spin Dynamics of Large Transport Airplanes. In *45th AIAA Aerospace Sciences Meeting and Exhibit 8 -11 January 2007, Reno, Nevada*, pages 1–20, Reno, 2007.

[75] Luat T. Nguyen. Evaluation of Importance of Lateral Acceleration Derivatives in Extraction of Lateral-Directional Derivatives at High Angles of Attack. Technical report, 1974.

[76] Yuanbo Nie and Tobias Bellmann. Aircraft Upset and Recovery Simulation with the DLR Robot Motion Simulator Loss of Control. In *AIAA SciTech 5 - 9 January 2015, Kissimee, Florida AIAA Modeling and Simulation Technologies Conference*, pages 1–10.

[77] Yuanbo Nie, Erik-jan Van Kampen, and Ping Chu. Geometry Based Quick Aircraft Modeling Method for Upset Recovery Applications. In *AIAA SciTech 5 - 9 January 2015, Kissimee, Florida AIAA Modeling and Simulation Technologies Conference*, pages 1–16, 2015.

[78] NLR. Preventing Loss of Control In-Flight. Technical report. URL `www.nlr.nl`.

[79] Matthew J O'rourke, John N Ralston, Jeffery W Bell, and Stanley F Lash. PC-Based Simulation of the F-16/MATV. *American Institute of Aeronautics and Astronautics*, 1997. doi: 10.2514/6.1997-3728. URL `http://arc.aiaa.org`.

[80] Christian Raab, Per Ohme, and Christoph Deiler. Support of Icing Flight Tests by Near Real-Time Data Analysis. *CEAS Aeronautical Journal*, 8(4):561–577, dec 2017. ISSN 18695590. doi: 10.1007/s13272-017-0260-5.

[81] Christian Raab, Per Ohme, and Christoph Deiler. Support of Icing Flight Tests by Near Real-Time Data Analysis. *CEAS Aeronautical Journal*, 8(4):561–577, dec 2017. ISSN 18695590. doi: 10.1007/s13272-017-0260-5.

[82] John N. Ralston, David R. Gingras, Chris Wilkening, and Paul Desrochers. The Application of Potential Data Sources for Simulator Compliance with ICATEE Recommended Stall Modeling Requirements. In *AIAA Modeling and Simulation Technologies Conference 2012*, number August, pages 1–22, 2012. ISBN 9781624101830. doi: 10.2514/6.2012-4568.

[83] T S R Reddy and K R V Kaza. Analysis of an Unswept Propfan Blade With a Semiempirical Dynamic Stall Model. Technical report, NASA, 1989. URL `https://ntrs.nasa.gov/search.jsp?R=19890005741`.

[84] Leonard E. Ryan, Paul G. Scott, and Robert F. Browning. The Effects of Simulator Landing Practice and the Contribution of Motion Simulation to P-3 Pilot Training. Technical report, 1978.

[85] S. Saderla, R. Dhayalan, and A. K. Ghosh. Non-Linear Aerodynamic Modelling of Unmanned Cropped Delta Configuration from Experimental Data. *The Aeronautical Journal*, 121(1237):320–340, 2017. ISSN 00019240. doi: 10.1017/aer.2016.124.

[86] Deepakkumar M. Sharma and Kamal Poddar. Investigations on Quasi-Steady Characteristics for an Airfoil Oscillating at Low Reduced Frequencies. *International Journal of Aerospace Engineering*, 2010:1–11, 2010. ISSN 1687-5966. doi: 10.1155/2010/940528.

[87] J. Singh and R. V. Jategaonkar. Identification of Lateral-Directional Behavior in Stall From Flight Data. *Journal of Aircraft*, 33(3):627–630, 1996. ISSN 00218669. doi: 10.2514/3.46993.

[88] M.H. Smaili, B.I. Soemarwoto, N.B. Abramov, M.G. Goman, A.N. Khrabrov, E.N. Kolesnikov, and L. Fucke. Pushing Ahead-SUPRA Airplane Model for Upset Recovery. Technical report, 2017. URL www.nlr.nl.

[89] S. C.E. Smets, C. C. de Visser, and D. M. Pool. Subjective Noticeability of Variations in Quasi-Steady Aerodynamic Stall Dynamics. In *AIAA Scitech 2019 Forum*, San Diego, 2019. American Institute of Aeronautics and Astronautics Inc, AIAA. ISBN 9781624105784. doi: 10.2514/6.2019-1485.

[90] Tim T Teng, Tony S Zhang, Stacey Liu, and Peter R Grant. Representative Post-Stall Modelling of T-tailed Regional Jets and Turboprops for Upset Recovery Training. In *AIAA SciTech 5 - 9 January 2015, Kissimee, Florida AIAA Modeling and Simulation Technologies Conference*, number January, pages 1–19, 2015.

[91] The Mathworks Inc. fmincon, 2020.

[92] J. R. van der Ploeg, M. Roza, and M. Laban. Ventus – Towards a Cost-Effective Phenomenological Post-Stall Aerodynamic Model Add-on for Upset Recovery Training. In *AIAA Scitech Forum 9-13 January 2017, Grapevine, Texas*. American Institute of Aeronautics and Astronautics Inc, AIAA, 2017. ISBN 9781624104510. doi: 10.2514/6.2017-1756.

[93] J. Van Ingen. Dynamic Stall Modeling for the Cessna Citation II. (October):145, 2017. URL http://resolver.tudelft.nl/uuid:f76439ef-ab2a-4173-8d78-3122a2696e91.

[94] B. L. Walcott, M. J. Corless, and S. H. Żak. Comparative study of non-linear state-observation techniques. *International Journal of Control*, 45(6):2109–2132, 1987. ISSN 13665820. doi: 10.1080/00207178708933870.

[95] Greg Welch and Gary Bishop. An Introduction to the Kalman Filter. Technical report, 2001. URL http://www.voluntarybenefitsmagazine.com/article/population-risk-management-and-workplace-health-centers.html{%}5Cninternal-pdf://1153/population-risk-management-and-workplace-health-centers.html.

[96] Wei Zhong, Wen Zhong Shen, Tong Guang Wang, and Wei Jun Zhu. A new method of determination of the angle of attack on rotating wind turbine blades. *Energies*, 12(20), 2019. ISSN 19961073. doi: 10.3390/en12204012.